WASHINGTON UNIVERSITY

SEVER INSTITUTE OF TECHNOLOGY

DEPARTMENT OF CHEMICAL ENGINEERING

BUBBLE VELOCITY, SIZE AND INTERFACIAL AREA MEASUREMENTS IN BUBBLE COLUMNS

By

Junli Xue

Prepared under the direction of

Prof. M. P. Duduković, Prof. M. H. Al-Dahhan & Prof. R. F. Mudde

---

Thesis presented to the Sever Institute of Washington University

in partial fulfillment of the requirements of the degree of

DOCTOR OF SCIENCE

December 2004

Saint Louis, Missouri

WASHINGTON UNIVERSITY
SEVER INSTITUTE OF TECHNOLOGY
DEPARTMENT OF CHEMICAL ENGINEERING

ABSTRACT

BUBBLE VELOCITY, SIZE AND INTERFACIAL AREA MEASUREMENTS IN BUBBLE COLUMNS

By Junli Xue

ADVISOR: Professor M. P. Duduković, Professor M. H. Al-Dahhan and
Professor R. F. Mudde

December 2004
Saint Louis, Missouri

The knowledge of bubble properties, including bubble velocity, bubble size, gas holdup, and specific interfacial area, is of importance for the proper design and operation of bubble columns. A four-point optical probe was adopted in this study to measure bubble properties in such systems. An improved algorithm for data processing was developed, which extends the capability of the probe and improves the accuracy of the measurement. The new algorithm provides both the magnitude and direction angles of the bubble velocity vector. The results from the probe and the algorithm were validated against video imaging and it was established that the bubble velocity distribution, bubble chord length distribution, local gas holdup, and specific interfacial area obtained by the four-point optical probe are reliable.

The four-point optical probe measurements of bubble properties were taken in an air-water system using a 16.2cm (6.4”) diameter bubble column at elevated pressure, up to 1.0 MPa, and at high superficial gas velocity, up to 60 cm/s, equipped with three different gas spargers.

It was established that gas holdup radial profiles evolve from flat at low superficial gas velocity to highly parabolic at high superficial gas velocity. Specific interfacial area profiles, bubble mean velocity profiles, and bubble frequency profiles exhibit the same trends. Bubble velocity distributions change from unimodal to bimodal with increase in superficial gas velocity. However, only unimodal bubble size distributions were observed. The effects of pressure, spargers, and elevation in the column are also illustrated.

This study establishes the four-point probe as a useful tool for study of bubble properties in actual bubble columns.

Contents

Tables

Figures

Acknowledgements

The accomplishments presented in this thesis would not have been possible without the support of many people. I wish to express my deepest gratitude to my advisors Prof. M. P. Dudukovic, Prof. M. H. Al-Dahhan and Prof. R. F. Mudde for their guidance, encouragement and constructive criticism. I would like to thank the members of my committee, Prof. P. A. Ramachandran, Prof. R. A. Gardner, Prof. Sureshkumar and Dr. B. A. Toseland of Air Products and Chemicals, Inc. for investing their valuable time in examining my thesis and providing me with useful comments. Especially Dr. B. A. Toseland for the numerous discussions and comments that helped me to better focus on the real goals of my research in keeping it relevant to industrial practice.

I would like to acknowledge partial support from DOE Contract FC 2295 PC 95051 via Air Products and Chemicals Inc. and CREL industrial sponsors, which financially made this work possible.

I want to thank the members of CREL for their help. My special thanks goes to Dr. P. Chen and Dr. Rafiq for sharing their knowledge with me and their valuable discussions and suggestions.

During the course of my study numerous devices and pieces of equipment needed to be designed and machined. I am very thankful to Mr. Pat Harkins and Jim Linders for their fine work in machining of these devices. I am also thankful to Steve Picker whose large experience helped me in solving various technical issues effectively.

Furthermore, I would like to thank Professor James Ballard of the Technical Writing Center for helping me to improve the language in my thesis.

I wish to thank the secretaries of the Department of Chemical Engineering for their prompt help in numerous administrative issues. I wish to thank to faculty, associates and students of the Department of Chemical Engineering for making my overall graduate school experience enjoyable.

And last but not least, my deepest gratitude is to the each and every member of my family for their absolute support. Especially, I am grateful to my wife Yingjian Zhao and my son Jiarui Xue for sharing all ups and downs, for their support and most of all, for their understanding.

Nomenclature

a	gas-liquid specific interfacial area, m^2/m^3
b	the length of minor axis of an ellipsoidal bubble, cm
c	the length of major axis of an ellipsoidal bubble, cm
D	column diameter, cm
d_s	Sauter mean bubble diameter, mm
d_e	volume equivalent bubble diameter, mm
D_H	the hydraulic equivalent diameter of the flow channel, cm
Eo_b	bubble Eotvos number
g	acceleration of gravity, m/s^2
L_i	the bubble chord length pierced by the ith tip of the probe, cm
Mo	Morton number
$\vec{n}$	bubble's normal vector
H_I	the initial liquid phase height, cm
H_D	dynamic height of the gas-liquid system, cm
L	the axial distance between peripheral tips and the central tip of the probe, cm
r	the radial distance between peripheral tips and the central tip, mm
Re_b	Bubble Reynolds number
r/R	radial position in the bubble column
ΔT	measurement time, s
Δt_i	time intervals between a bubble hitting the central tip T_0 and it hitting tip T_i, s
T_i	the time interval during which the ith, i=0,1,2,3, tip of the probe is inside the bubble, s
th	bubble discarding threshold
v	the bubble velocity, cm/s
V	the total volume of the gas-liquid mixed phase, m^3

We_b bubble Weber number

z axial position, cm

Greek Letters

α aspect ratio of the ellipsoidal bubble, α=(length of vertical axis)/(length of horizontal axis)

δv bubble selection tolerance

ε_g gas holdup

φ the angle of the projection of the bubble velocity vector on the xy plane to the x axis, degree

θ the angle between the bubble velocity vector and the probe's axial direction, degree

ϕ the angle between the velocity vector and the normal vector of the gas-liquid interface, degree

ρ density, Kg/m^3

σ surface tension, N/m

μ viscosity, mPa·s

ν kinematic viscosity, m^2/s

Subscripts

g gas phase

l liquid phase

T time based

V volume based

Chapter 1 Introduction

1.1 Motivation

Bubble column reactors are used extensively to perform a wide variety of gas/liquid or gas/liquid/solid reactions, such as oxidation, hydrogenation, chlorination, aerobic fermentation, waste water treatment, and coal liquefaction (De Swart and Krishna, 1995; Jager and Espinoza, 1995; Shollenberger *et al.*, 1997; Eisenberg *et al.*, 1994; Davis, 2002). The main advantages of bubble columns over other multiphase reactors (stirred vessels, packed towers, trickle bed reactors etc.) include simple construction, low maintenance due to the absence of moving parts, excellent heat transfer properties, easy temperature control, and reasonable interphase mass transfer rates at low energy input.

The knowledge of bubble properties, including bubble velocity, bubble size, gas holdup, and specific interfacial area, is of considerable importance for the proper design and operation of bubble columns. For example, the overall mass transfer rate per unit volume of the dispersion in a bubble column is governed by the liquid-side volumetric mass transfer coefficient ($k_l a$), assuming that the gas-side resistance is negligible. In a bubble column reactor, the variation in $k_l a$ is primarily due to variations in the specific interfacial area, a. The specific gas-liquid interfacial area, a, is related to the gas holdup, ε_g, and the bubble size distribution, while the gas holdup is determined by the bubble size distribution, bubble velocity (i.e., bubble residence time), and bubble frequency. In the same way, bubble properties play key roles in determining the heat transfer rate in bubble columns (Yang *et al.*, 2000). Furthermore, bubble size distribution and bubble velocity distribution are key parameters in evaluating the drag forces on bubbles and in using the bubble population balance in Computational Fluid Dynamics (CFD).

However, the measurement of bubble size, bubble velocity, and specific interfacial area in two and three-phase systems has always been a challenging problem. The problem is even much more complex when the system being considered is no longer in the bubbly flow regime, but rather in the chaotic churn-turbulent flow regime and at high pressure, conditions which are of industrial interest.

The appeal of non-invasive techniques has led to attempts to capture the bubble size distribution bubble velocity distribution by video imaging techniques (Patel, Daly and Buckar, 1990; Idogawa, 1997; Luewisutthichat, Tsutsumi and Yoshida, 1997a; Mihai and Pincovschi, 1998; Marques *et al.*, 1999). However, video imaging can be used only in 2-D transparent columns at low gas holdup, where light can penetrate the system. In real 3-D columns, even with transparent walls, this technique provides no hope of capturing anything beyond the reactor wall. Video imaging also cannot be used in systems where the columns are operated at high temperature and high pressure and thus cannot be made of transparent materials. Thus, invasive techniques are still the state of the art when it comes to bubble size and bubble velocity measurements in practical 3-D multiphase systems.

In recent years, optical and conductivity microprobes have been most frequently employed to investigate bubble properties (Vince *et al.*, 1982; Matsuura and Fan, 1984; Lee, De Lasa and Bergougnou, 1986; Saxena, Rao and Saxena, 1990; Chabot *et al.*, 1992; Kuncova, Zahradnik and Mach, 1993; Groen *et al.*, 1996; Farag *et al.*, 1997; Luo *et al.*, 1998; A. Cartellier, 1998; Mudde and Saito, 2001). Conductivity probes utilize the difference in electrical conductivity between the liquid phase and the gas phase. Optical fiber probes make use of the difference in the refractive index between the gas phase and the liquid phase and provide a sequence of voltage pulses when a bubble passes by the probe. In comparison with conductivity probes, optical probes offer significant advantages: 1) They can be used in conductive as well as non-conductive (organic) systems, which are important in the petrochemical industry. 2) The presence of a liquid film on the sensor tip reduces the effectiveness of a conductivity probe but not that of an

optical probe. Therefore the sensitivity of optical probes is higher than that of conductivity probes (van der Lans, 1985). 3) Optical probes achieve a much better signal/noise ratio than conductivity probes.

At present, optical probes have been used mainly to determine bubble size and velocity for individual bubbles in bubbly flows of modest gas holdup. There is no firm experimental data or theory that can guide us as to how to use these probes and interpret their signals in churn-turbulent flow with significant bubble coalescence and re-dispersion and with a wide distribution of bubble sizes. The goal of this work is to explore what bubble phase information can be obtained in churn-turbulent flows using optical probe and make necessary modifications to the data processing algorithm.

For many years now, Washington University's Chemical Reaction Engineering Laboratory (CREL) has used Computer Tomography (CT) and Computer Automated Radioactive Particle Tracking (CARPT) to investigate the gas holdup distribution and the liquid phase recirculation in bubble columns. The gas holdup obtained by the optical probe in the current study can be compared with values already obtained by CT for validation. Moreover, gas holdup is qualitatively determined by the bubble velocity and the bubble size distribution. Hence, by investigating these bubble properties, the mechanism for changes in the gas holdup profiles with changing operating conditions can be disclosed. Furthermore, in bubble columns the liquid recirculation derives from and interacts with bubble properties. Hence, the combination of the measurement results from CARPT with bubble properties obtained by the probe can give a clearer understanding of the hydrodynamics in bubble columns.

In CFD, the population balance model, applied to gas bubbles, is needed to provide a statistical formulation to describe the gas phase in bubble columns. The bubble size and velocity distribution functions are employed in the population balance model. So far, either a 'mean' bubble size is assumed or the bubble size distribution is predicted from the bubble breakup and coalescence model. This can be much improved by comparing

the experimental results for the bubble velocity and size distribution obtained by the probe with the predictions generated by the model. Furthermore, two-fluid model based codes (e.g., FLUENT, CFX, CFDLIB) cannot predict well the observed gas holdup radial profiles, even in 3D simulations. With the bubble velocity and size distribution obtained by the probe, the prediction of the gas holdup profile in CFD can be improved, which would substantially increase the capability of CFD modeling of bubble column reactors. This improvement, however, is beyond the scope of this thesis.

1.2 Research Objectives

The overall objective of this work is to investigate the bubble velocity distribution, bubble chord length distribution, local gas holdup, and specific interfacial area as a function of operating conditions (i.e., superficial gas velocity, pressure etc.) in both bubbly flow and in churn-turbulent flow in bubble columns. Four major research goals are:

(1) Modify the data processing algorithm to improve the capability of the four-point optical probe to set up a practical tool for investigating bubble properties in bubble columns in both bubbly flow and churn-turbulent flow.

(2) Validate the four-point optical probe and the developed novel data processing algorithm versus video imaging in validation setups, e.g., a 2-D bubble column, at different conditions.

(3) Use this probe in a 6.4” bubble columns to study the bubble velocity distribution, bubble chord length distribution, gas holdup, and the specific interfacial area at superficial gas velocity up to 60 cm/s, pressure up to 1.0 MPa, and for different spargers. These operating conditions are the same as those at which the CT and CARPT experiments were carried out in CREL (Bong Cheng Ong, 2003). These data are nonexistent in the literature.

(4) Obtain deeper understanding of the hydrodynamics of bubble columns by analyzing such data.

Chapter 2 Background

2.1 Bubbles' Behavior in (Slurry) Bubble Columns

The research presented in the literature has captured some aspects of the behavior of bubbles in bubble columns and slurry bubble columns. The following are the results pertinent to this study.

2.1.1 Bubble Shape, Motion, and Size Distribution

Bubbles in motion are generally classified by shape as spherical, oblate ellipsoidal, and spherical/ellipsoidal cap, etc. (Figure 2-1). The actual bubble shape depends on the relative magnitudes of the forces acting on the bubble, such as surface tension and inertial forces (Bhaga and Weber, 1981). When the bubble size is small (for example, volume equivalent bubble diameter d_e<1mm in water), the surface tension force predominates and the bubble is approximately spherical.

For bubbles of intermediate size, the effects of both surface tension and the inertia of the medium flowing around the bubble are important. As a result, intermediate-size bubbles exhibit very complex shapes and motion characteristics. While called ellipsoidal bubbles, they often lack fore-and-aft symmetry and, in extreme circumstances, cannot be described by any simple regular geometry, due to significant shape fluctuations (Bhaga and Weber, 1981). This complex shape results from the superposition of various modes of fluctuations that are of different amplitudes and take place at different frequencies (Hibino, 1969). The dominant mode of shape fluctuations has been noted to be quite periodic and characterized by the extension/contraction of the bubble height/width or vice versa, i.e., variation in the bubble aspect ratio (Bhaga and Weber, 1981).

Large bubbles, whose volumes are larger than 3 cm^3 (i.e., d_e>18mm) in general, are dominated by inertial or buoyancy forces, with negligible effects of surface tension and viscosity of the liquid media. The bubble is approximately a spherical cap with an included angle of about 100^o (provided liquid viscosity μ_l<50 mPa·s) and a relatively flat or sometimes indented base. The fluctuation in the overall shape becomes suppressed, i.e., the main feature of the bubble's shape fluctuation is the oscillation of the bubble base, especially in the edge region (Bhaga and Weber, 1981).

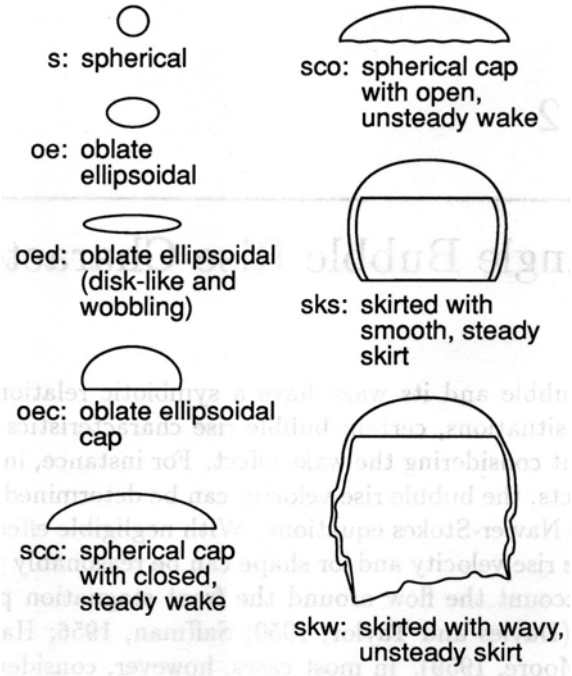

Figure 2-1. Sketches of Various Bubble Shapes Observed in Infinite Newtonian Liquid (Bhaga and Weber, 1981)

In multiphase flow systems, bubble size distribution is not constant but changes due to breakup and/or coalescence of bubbles caused by bubble-bubble interactions (Domenico *et al.*, 1999). The rates of these two processes are associated with the generated bubble size and the property of surrounding liquid. In a coalescence-promoting liquid, such as water and pure organic liquids, bubbles generated are apt to coalesce, so that the bubble size in the fully developed flow region is larger than the initial bubble size generated

from the sparger. When a coalescence hindering liquid, such as electrolytes and alcohols, are added to an aqueous solution, the initial bubbles generated at the sparger essentially do not change in size in the course of rising to the free surface. Accordingly, higher gas holdup and specific interfacial area than those encountered in a coalescence-promoting liquid can be achieved in a coalescence hindering liquid (Hikita et al., 1980; Heijnen and van't Riet, 1984). It has been reported that whatever the liquid phase, in multiphase flow systems the bubble size distributions are very asymmetric and can be represented well by the log-normal distribution (Luewisutthichat, Tsutsumi and Yoshida, 1997a; Rajarathinam and Nafis, 1996; Chanson, 1997).

No broadly applicable model for the determination of rates of coalescence and breakup has yet been presented, due to both the inaccurate understanding of the physical mechanisms that lead to bubble breakup and coalescence, and the enormous difficulty in obtaining reliable data, especially at high gas flow rates. The latter is the reason why bubble size distribution measurements are not so common in literature, and, often, different techniques lead to different measured values. Actually, bubble size in bubble columns, including 2D bubble columns, cannot be measured directly, i.e., without any assumptions on bubble shape, by any available technique so far, except at some extreme conditions, e.g., single bubble rise or a extremely thin 2D bubble column (Spicka et al., 1999). Methods now available to derive the bubble size distribution include:

(1) Video imaging (Bhaga and Weber, 1981; Domenico et al., 1999; Spicka et al., 1999).

(2) Point probes (Burgess and Calderbank, 1975; Manabu et al., 1995; Wu and Ishii, 1999; Sanaullah, Zaidi and Hills, 2001; Vince et al., 1982; Yu and Kim, 1988; Chabot et al., 1992; Farag et al., 1997; Mudde and Saito, 2001; Xue et al., 2003).

(3) Dynamic gas disengagement technique (Krishna, Wilkinson and van Dierendonck, 1991; Daly, Patel and Bucker, 1992; Deshpande, Dinkar and Joshi, 1995).

The bubble size distribution obtained by the dynamic gas disengagement method is not reliable, due to unrealistic assumptions and too many approximations, e.g., the bubble size is obtained from the correlation of bubble size and the terminal rise velocity in a still medium and the bubble rise velocities were calculated very roughly (Daly, Patel and Bukur, 1992).

Video imaging has been frequently employed to study the behavior of bubbles in bubble columns and other gas-liquid contactors. However, it can be used only in transparent systems, e.g., 2D systems and 3D systems with very low gas holdup. At high gas holdup, video imaging can investigate only the near wall section. Furthermore, to employ video imaging, the wall of the multiphase systems investigated must be made of transparent material, i.e., glass or Plexiglas, which hinders its application to high pressure systems. Hence, video imaging is not suitable for practical systems, which are usually 3D, with high gas holdup and opaque walls.

Various point probes can be used in opaque systems. They can be employed at high gas holdup and in high pressure systems. However, the model assumed for the bubble shape is an important factor affecting the accuracy of the measurement results for the bubble size distribution. In general the measurement by point probes requires the transformation of bubble chord length distribution, obtained by probes, to bubble size distribution. Usually, simple symmetric geometric models are employed to represent bubbles' shapes. The following axially symmetric geometric shape models were customarily used as approximations of real bubbles:

(1) In the case of small bubbles, bubbles are modeled as spheres (Batchelor, 1967; Harmathy, 1960).

(2) Large bubbles (e.g., over 1.5mm diameter in air-water systems) are represented as ellipsoids with a larger horizontal than vertical dimension (Harmathy, 1960; Clark and Turton, 1988).

(3) Very large bubbles, with strong wakes in liquids, are cap-shaped (Hills and Darton, 1975; Batchelor, 1967), and can be modeled as the top lesser section of an ellipsoid or sphere (refer to Figure 2-1).

(4) In fluidized beds, the bubble shape is often termed “spherical cap” (Reuter, 1966; Rowe and Widler, 1973), and is modeled by the top greater section of a sphere or ellipsoid.

The shape of splitting and coalescing bubbles is very complicated. Data interpretation in such circumstances is very difficult, for the shape is not well defined. Furthermore, in many situations, e.g., in churn-turbulent flow, due to the bubble shape fluctuation mentioned above, the shape of many bubbles is highly irregular and is not constant, so that it cannot be represented by any simple geometric model at all.

In gas-liquid upflow, bubbles move faster than the surrounding liquid (due to buoyancy), and large bubbles rise more quickly than small bubbles. The motion of bubbles is very complex. The rise path and change in orientation of the bubble are known to be strongly related to the bubble shape (Fan and Tsuchiya, 1990). The motion of spherical bubbles is usually rectilinear. Once the bubble becomes deformed into an oblate ellipsoid, instability sets in, and results in a spiral or zigzag trajectory. Luewisutthichat, Tsutsumi and Yoshida (1997b) found that both the bubble shape and bubble velocity of oblate ellipsoidal bubbles exhibit chaotic features. In turn, the fluctuation of the bubble shape is likely to cause oscillation of the drag force, leading to the chaotic fluctuation of bubble velocity in the streamwise direction. Therefore, in spite of the periodic macroscopic motion, bubbles exhibit highly chaotic fluctuations in both the lateral and axial components along the zigzag path of the bubble ascent. At the same time, the bubble orientation changes in such a way that the bubble major axis tends to be perpendicular to the direction of instantaneous motion (Haberman and Morton, 1953).

As the bubble size increases further, the bubble changes from an ellipsoidal to spherical-cap shape, the radius of the spiral or the amplitude of the zigzag path gradually decreases as bubble size increases, and the motion eventually becomes rectilinear style, but with a oscillating component. This rule is generally valid in systems of low Morton number, $\mathrm{Mo} = \frac{g\mu^4}{\rho\sigma^3}$, where g is the acceleration of gravity, ρ, σ and μ are the density, surface tension and viscosity of the liquid.

2.1.2 Gas Liquid Flow Patterns and Flow Regimes (Hydrodynamics)

Two different types of flow regimes are generally encountered in bubble column operation, namely, bubbly flow and churn-turbulent flow. Bubbly flow transits to churn-turbulent flow as the gas superficial velocity increases above a critical value. Chen, Reese and Fan (1994) studied macroscopic flow structures in 3-D bubble columns, at various operating conditions in an air-water system at atmospheric pressure, using Particle Image Velocimetry (PIV). They described three different flow regimes: the dispersed bubble, vortical-spiral flow, and turbulent flow regimes (Figure 2-2).

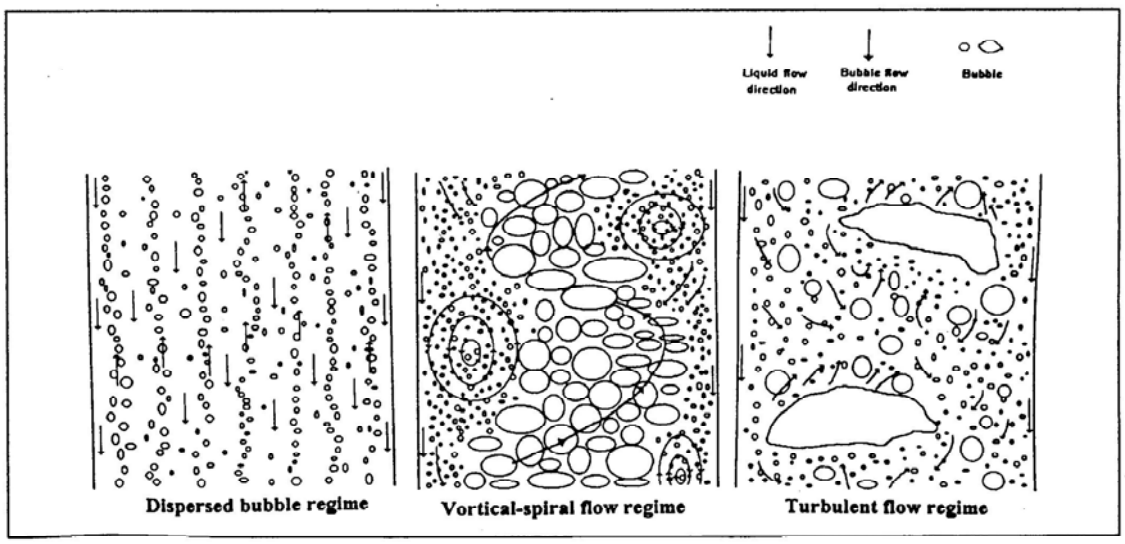

Figure 2-2. Flow Regimes in a 3-D Bubble Column (Chen, Reese and Fan, 1994)

At low gas velocities, bubble streams are observed to rise rectilinearly with relatively uniform size distribution along the column radius. Bubble coalescence and breakup are insignificant in this dispersed bubble regime.

With a further increase in superficial gas velocity, bubbles start forming a central bubble stream, which moves in an oscillating spiral manner. Bubble coalescence and breakup become evident as the gas velocity reaches a certain value (about 2.1 cm/s in an air-water system, according to Chen, Reese and Fan, 1994). In the meantime, the rotating frequency of the central bubble stream is intensified as the gas velocity increases, which results in a more clearly observable spiral motion of the central bubble stream. The central bubble stream, which consists of coalesced bubbles and bubble clusters, not only spirals upward but also swings laterally back and forth. In the region between the central bubble stream and the column wall, tiny bubbles are observed to move up and down. This phenomenon indicates the dynamic nature of this region. The general macroscopic flow structure of a 3-D column in the vortical-spiral flow regime is displayed in Figure 2-3.

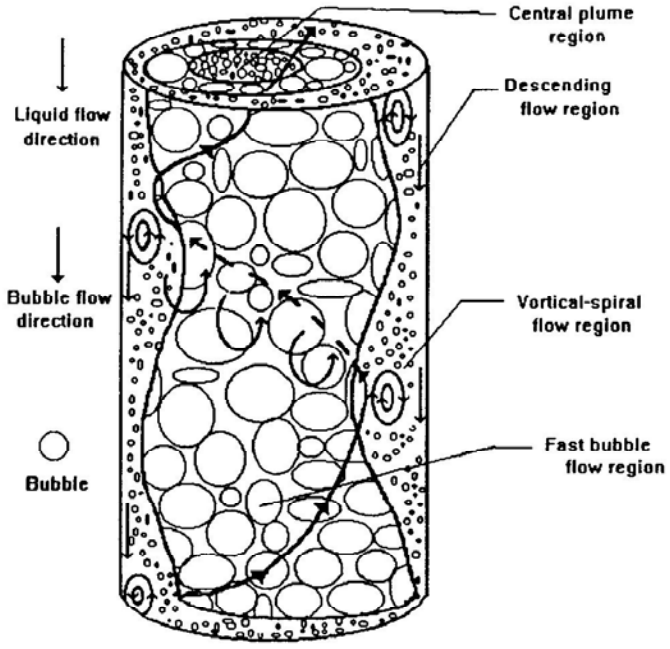

Figure 2-3. Flow Structure in the Vortical-Spiral Flow Regime in a 3-D Gas-Liquid Bubble Column (Chen, Reese and Fan, 1994)

For still higher gas velocity ranges (4.2~4.9 cm/s, Chen, Reese and Fan, 1994), large bubbles start forming by intensive bubble coalescence, and moving in a sort of “discrete” manner, i.e., discrete large bubbles are separated by a certain distance. The spiral flow pattern of the central bubble stream gradually breaks down.

Krishna, Wilkinson and van Dierendonck (1991) inferred from gas disengagement experiments that there are both large and small bubbles in churn-turbulent flow; large bubbles constitute the so-called “dilute” phase, and rise rapidly through the core of the column, which causes the radial gas holdup profile to be almost parabolic. This non-uniform gas holdup profile drives liquid circulation, i.e., the liquid rises in the center and falls by the wall. The smaller bubbles form the “dense” phase and closely follow the liquid, thereby undergoing recirculation with the liquid. Large bubbles rise fast through the column virtually in plug flow, while small bubbles display a wide residence time distribution. Beyond a certain transition gas velocity, the small bubble holdup remains constant, while the large bubble holdup keeps increasing with the gas velocity. Such a ‘bimodal’ bubble size distribution is reported by Krishna, Wilkinson and van Dierendonck (1991) as a characteristic feature of the churn-turbulent flow regime.

However, Deshpande, Dinkar and Joshi (1995) provided another explanation for the gas disengagement experimental results. They thought that the initial faster gas disengagement is partly due to internal liquid recirculation instead of due to only the presence of very large bubbles, and, hence, claimed that the bimodal bubble size distribution is not necessarily proven by results of gas disengagement experiments.

As mentioned before, the video imaging method is limited to 2D systems and 3D systems of very low gas holdup. Fan et al. (1999) found that under high-pressure conditions bubble coalescence is suppressed, bubble breakup is enhanced, and the distributor tends to generate smaller bubbles. All these factors contribute to small bubble sizes and narrow bubble size distributions. However, their observation was conducted in bubble columns

of small diameter (2” and 4”) and at low gas holdup. Hence, there are no visual or video observations available for 3D bubble columns, of larger size and operated at high superficial gas velocity and high pressure, to clarify the existence or lack of the bimodal bubble size distribution in churn-turbulent flow. By measuring the bubble chord length distribution with a four-point optical probe in a bubble column of 6.4” diameter and at high superficial gas velocity (up to 60 cm/s) and high pressure (up to 10 bar) in this research, it is expected that this issue can be clarified.

2.1.3 Effect of Operating Conditions on Hydrodynamics

The superficial gas velocity is one of the most important factors that affect the hydrodynamics in bubble columns. As the superficial gas velocity increases, the flow condition in bubble columns changes from bubbly flow to churn-turbulent flow; at the same time, the liquid recirculation is enhanced; the Sauter mean bubble diameter increases, and the bubble size distribution becomes wider (Olmos *et al.*, 2001). The gas holdup radial profile is flat in bubbly flow, and it is parabolic in churn-turbulent flow; in bubbly flow the gas holdup increases more rapidly with gas velocity than in churn-turbulent flow (Chen, Reese and Fan, 1994; Kemoun *et al.*, 2001; Lin *et al.*, 2001).

Pressure and temperature affect the behavior of bubbles mainly by varying physical properties of fluids (gas density, liquid viscosity, surface tension). In detail, gas density increases with pressure and decreases with temperature, the liquid surface tension decreases with both pressure and temperature, the liquid viscosity decreases with temperature, and the effect of pressure on liquid viscosity is negligible. It was found that the Sauter mean bubble diameter decreases with an increase in pressure or temperature; the rise velocity of bubbles decreases with an increase in pressure and a decrease in temperature (Fan *et al.*, 1999; Lin, Tsuchiya and Fan, 1998). At elevated pressure, the transition from bubbly flow to churn-turbulent flow is delayed (Letzel *et al.*, 1997). The effect of pressure on gas holdup in the homogeneous regime is insignificant (Kolbel *et al.*, 1961; Deckwer *et al.*, 1980). In churn-turbulent flow, gas holdup increases

with pressure, and the radial profile of the gas holdup becomes more parabolic (Jiang *et al.*, 1995; Fan *et al.*, 1999; Chen *et al.*, 1999b). Consequently, the volumetric mass transfer coefficient increases also with pressure (Stegeman *et al.*, 1996). Some researchers (Wilkinson and Haringa, 1994; Jiang *et al.*, 1995; Luo *et al.*, 1998) believe that as pressure is increased, the bubble size at the distributor is reduced; bubble coalescence is suppressed; and large bubbles tend to break up, so that higher pressure (gas density) leads to smaller bubbles, and hence to an increase in gas holdup. However, in bubbly flow, this could not be confirmed by studies at Sandia National Laboratory (Shollenberger et al., 1997). Generally an increase in temperature leads to higher gas holdup (Bach and Pilhofer, 1978; Zou et al., 1988; Wilkinson and van Dierendonck, 1990). The reasons are: (1) Both the surface tension and the liquid viscosity decrease if the temperature increases, and lower surface tension and liquid viscosity leads to a higher gas holdup. (2) A higher temperature also increases the vapor pressure of the liquid. If the feed gas to a bubble column is not saturated, the evaporation of the liquid phase can lead to a substantial increase in the volumetric gas flow rate, which subsequently increases the gas holdup.

It was reported that column diameters larger than about 15 cm do not affect gas holdup much (Chen *et al.*, 1998). On the other hand, the liquid recirculation in a large diameter column is stronger than that in a small diameter column (Joshi *et al.*, 1998; Chen *et al.*, 1998).

The gas distributor also has important effects on bubbles in bubble columns. Jamialahmadi and Muller-Steinhagen (1993) found that in the bubbly flow regime, bubble size was a strong function of the orifice diameter and the wettability of the gas distributor, and a weak function of superficial gas velocity. In the churn-turbulent flow regime, this functionality was reversed, i.e., the effect of the sparger on the gas holdup and the liquid velocity profile is weak in the fully developed flow region in bubble columns. Mikkilineni and Knickle (1987) studied the effect of various porous-plate gas distributors (polyethylene, polypropylene, SiC, Al_2O_3, etc.) on gas holdup and flow

pattern in the bubbly flow regime in a bubble column. They reported the following: (1) Gas holdup increased with the pore size and distributor thickness, (2) Hydrophobic distributor plates gave higher gas holdup than the hydrophilic ones because the hydrophilic plates promote bubble coalescence, which results in decreased gas holdup, due to different wetting characteristics, and (3) The bubble size was dependent on the pore size, gas velocity, and column height and not on the distributor thickness and material.

The situation in slurry bubble columns is more complicated. Whether a rising bubble behaves as if it were in a “homogeneous” or “heterogeneous” medium depends primarily on the ratio of the particle diameter to bubble diameter, i.e., the effect of solid particles on bubble characteristics is entirely different in different particle size ranges. In case of small particles (less than 100 μm as reported by Luewisutthichat, Tsutsumi and Yoshida, 1997), no significant difference in bubble size and velocity distribution was observed in comparison with two-phase systems. A liquid-solid mixture of small, light particles is often regarded as a pseudo-homogeneous medium. On the other hand, in large particle systems (larger than 500 μm), increased bubble coalescence and breakup due to the presence of large particles take place, resulting in a broader bubble size distribution with larger Sauter mean diameter, causing a drop in gas holdup (Darton and Harrison, 1974; Lee, Soria and De Lasa, 1990; Luewisutthichat, Tsutsumi and Yoshida, 1997).

2.1.4 Specific Interfacial Area

Gas-liquid mass transfer in multiphase reactors, e.g., bubble columns, is most frequently characterized by the overall volumetric mass transfer coefficient k_La. The specific interfacial area, a, varies significantly with the hydrodynamic conditions in reactors. For the commonly used local two fluid models in Computational Fluid Dynamics (CFD), prediction of the interfacial area is one of the major weaknesses. Thus, experimental data for the distribution of interfacial area in the entire reactor are of great interest for the validation of two fluid models, and for locating zones of low mass transfer in real

reactors (Kiambi et al., 2001). Furthermore, the specific interfacial area is one of the key parameters that determine the heat and mass transfer in multiphase systems. Hence, it is crucial for the design, simulation, and scaleup of bubble columns.

Various physical and chemical methods have been applied to measure the specific interfacial area in multiphase flows.

The physical methods include gas disengagement (Patel, Daly and Bukur, 1990), video imaging (Akita and Yoshida, 1974; Luewisutthichat, Tsutsumi and Yoshida, 1997; Lage and Esposito, 1999; Pohorecki, Moniuk and Zdrojkowski, 1999), Laser Doppler Anemometry (LDA) (Kulkarni et al., 2001), and probes (Kiambi et al., 2001; Wu and Ishii, 1999). In all the physical methods except video imaging and some probes, the specific interfacial area for unit of the bubble column volume, a, is determined from the gas holdup and bubble size distribution. The gas-liquid interfacial area can be related to the gas holdup, ε_g, and the Sauter mean diameter (the volume-surface mean diameter of bubbles), d_s, by:

$$a = \frac{6\varepsilon_g}{d_s} \tag{2-1}$$

The Sauter mean diameter is calculated by:

$$d_s = \frac{\sum_{i=1}^{n} n_i d_{b,i}^{\ 3}}{\sum_{i=1}^{n} n_i d_{b,i}^{\ 2}} \tag{2-2}$$

where $d_{b,i}$ is the volume-equivalent diameter of the mid-sized bubbles within the i-th size-class, and n_i is the number of bubbles with size $d_{b,i}$.

Equation (2-1) is based on the assumption of spherical bubbles, which is not true for most practical multiphase systems. Hence, Equation (2-1) is an oversimplification for practical multiphase systems. Besides, as mentioned before, the volume-equivalent bubble diameter is very difficult to measure accurately in multiphase systems. Hence, Equation (2-1) can be treated only as a rough estimate of specific interfacial area.

Kataoka, Ishii and Serizawa (1986) derived the equation for the specific interfacial area, a, in gas-liquid systems as:

$$a = \frac{1}{\Delta T} \cdot \overline{\frac{1}{\left|\vec{v}\right| \cdot \cos\phi}} = \frac{1}{\Delta T} \cdot \sum_{N} \frac{1}{v \cdot \cos\phi} \tag{2-3}$$

where N is the total number of the gas-liquid interfaces passing by the probe during the measurement time ΔT, and ϕ is the angle between the velocity vector and the normal vector of the gas-liquid interface (bubble's surface). Equation (2-3) provides the probe technique with the capability to measure specific interfacial area directly.

The chemical methods (Stegeman et al., 1996; Vazquez et al., 2000; Kulkarni et al., 2001) are based on the study of reactions of known kinetics in which the absorption rate is a function of the interfacial area. The gas-liquid reaction systems are selected in such a way that the absorption is accompanied by fast chemical reaction. As a result, the overall rate of absorption (Ra) is proportional to the interfacial area, and is given by the following equation (Danckwerts, 1970):

$$Ra = a\left(\frac{2}{m+1} D_A k_{mn} [A^*]^{m+1} [B_0]^n\right)^{1/2} \tag{2-4}$$

where [A*] is the saturation concentration of solute gas (A) in the liquid phase, $[B_0]$ is the concentration of liquid phase reactive species (B), m and n are the reaction orders with respect to A and B, respectively, k_{mn} is the rate constant, and D_A is the diffusivity of A in

the liquid phase. Some of the chemical systems with these characteristics reported in the literature include: CO_2-Aqueous NaOH, CO_2-Aqueous diethanolamine, H_2- Hydrazine, O_2-Sodium sulfite. In all the cases, the bracketed term in Equation (2-4) $(2/(m+1)D_A k_{mn}[A^*]^{m+1}[B_0]^n)=F$ is measured using a model contactor, where a is known a priori, over a wide range of $[A^*]$, $[B_0]$, and temperature. These well characterized reaction systems with known F are then used in bubble columns, where the measurement of Ra directly gives a ($a = Ra/\sqrt{F}$).

The chemical methods have several shortcomings: (1) They can derive only the overall value of interfacial area rather than the distribution of specific interfacial area in multiphase systems. (2) The addition of chemicals to conduct the chemical reaction may change the properties of the investigated system, including the specific interfacial area. And (3) they are inconvenient to use, due to the complexity of the principle.

The value of 'a' is expected to depend upon column diameter, D, axial position, z, radial position, sparger design, gas velocity, the regime of operation, and the nature of gas-liquid system.

Akita and Yoshida (1974) suggested an empirical correlation for the specific interfacial area in bubbly flow in a bubble column for different liquid phases:

$$a = \frac{1}{3D_H}\left(\frac{gD_H^2\rho_L}{\sigma}\right)^{0.5}\left(\frac{gD^3}{\nu_L^2}\right)^{0.1}\varepsilon_G^{1.13} \qquad (2\text{-}5)$$

where g is gravity accelation, D_H is the hydraulic equivalent diameter of the flow channel, ν_L is the kinematic viscosity of liquid, σ is liquid surface tension, and ε_G is gas holdup.

Hibiki and Ishii (2002) also derived a semi-theoretical correlation from the interfacial area transport equation to provide the mean value of the interfacial area as a function of energy dissipation and physical parameters. Their expression is:

$$a = \frac{3.02 g^{0.174}}{D_H^{0.335} \nu_L^{0.239}} \left(\frac{\sigma}{\Delta\rho} \right)^{-0.174} \varepsilon_G \alpha^{0.0796} \qquad (2\text{-}6)$$

In Equation (2-6), $\Delta\rho$ is the density difference between phases, and α is the energy dissipation rate per unit mass. Equation (2-6) also applies to bubble columns in bubbly flow with different liquid phases. Hibiki and Ishii (2002) obtained an agreement between the developed semi-theoretical correlation and 459 data points, within an average relative deviation of ±22.0%.

With an increase in pressure, the specific interfacial area increases, due to an increase in gas holdup and decrease in bubble size. However, measurements of specific interfacial area at high pressure are much more complicated than those at atmospheric pressure. Wilkinson, Spek and van Dierendonck (1992) developed experimentally the relationship between the specific interfacial area at atmospheric pressure and at high pressure in bubbly flow:

$$\frac{a(\text{high pressure})}{a(\text{atmospheric})} = \frac{\varepsilon_G(\text{high pressure})}{\varepsilon_G(\text{atmospheric})} \cdot \left[\frac{\rho_G(\text{high pressure})}{\rho_G(\text{atmospheric})} \right]^{0.11} \qquad (2\text{-}7)$$

Equation (2-7) gives a way to estimate the specific interfacial area for high pressure on the basis of atmospheric data. However, the accuracy of the prediction of Equation (2-7) has not been validated.

An extensive literature survey was performed by Hibiki and Ishii (2002) for existing interfacial area values measured by various methods in forced convective bubbly flows and bubble columns. Key entries are shown in Table 2-1. It should be noted that the

experimental results obtained by different researchers and different methods varied considerably, and the difference among the values of the Sauter mean bubble diameter (and specific interfacial area) estimated by various empirical equations can easily be as much as a factor of two for apparently equal conditions.

In short, measurements of the specific interfacial area in multiphase systems are difficult, especially beyond very low gas holdup and in practical systems. As mentioned before, the methods employed so far either have serious limitations or are complicated, and the results obtained are not reliable.

Table 2-1. Existing Data Sets for Specific Interfacial Area Taken in Bubble Columns (Hibiki and Ishii, 2002)

Investigators	Geometry (mm)	Flow direction	Gas/Liquid	P (MPa)	Ug (cm/s)	U_l (m/s)	a (m^2/m^3)	Number of Data	Technique
(a) Existing data sets taken in forced convective bubbly flows									
Bensler (1990)	40×40	Vertical	Air/Water	0.1	3.5-25.3	0.503-3.00	67.0-391.6	16	Photograph
Grossetete (1995)	38.1 ID pipe	Vertical	Air/Water	0.1	8.95-18.1	0.877-1.75	75.1-145	3	Probe
Hibiki, Hogsett and Ishii (1998)	50.8 ID pipe	Vertical	Air/Water	0.1	1.78-9.36	0.60-1.30	25.8-135	9	Probe
Hibiki and Ishii (1999)	25.4 ID pipe	Vertical	Air/Water	0.1	5.66-127	0.262-3.49	40.5-551	25	Probe
Hibiki, Ishii and Xiao (2001)	50.8 ID pipe	Vertical	Air/Water	0.1	3.58-487	0.491-5.00	101-1083	18	Probe
Hibiki, Takamasa and Ishii (2001)	9.0 ID pipe	Vertical	Air/Water	0.1	1.23-6.19	0.580-1.00	31.6-93.0	5	Photograph
Kalkach-Navarro (1992)	38.1 ID pipe	Vertical	Air/Water	0.1	5.6-33.2	0.30-1.25	93.4-298	17	Probe
Kocamustafaogullari et al. (1994)	50.3 ID pipe	Horizontal	Air/Water	0.1	21.2-135	3.74-6.55	124-507	52	Probe
Liu (1989)	38.1 ID pipe	Vertical	Air/Water	0.1	2.7-34.7	0.376-1.39	38.2-591	42	Probe
Serizawa, Kataoka and Michiyoshi (1991)	30.0 ID pipe	Vertical	Air/Water	0.1	1.8-54.0	0.50-5.0	53.2-338	22	Probe
Yun (1996)	Annulus, D_H=17	Vertical	Steam/Water	0.1, 0.71	0.290-13.8	0.456-1.79	11.6-161	49	Probe
	Bundle (2×2), 36.2 (D_H)	Vertical	Steam/Water	0.1, 0.71	1.22-15.6	0.247-0.786	20.0-247	46	Probe
	Bundle (3×3), 8.59 (D_H)	Vertical	Steam/Water	0.1	0.580-8.96	0.261-0.630	35.6-290	58	Probe
(b) Existing data setstaken in forced convective bubble columns									

Investigators	**Geometry (mm)**	**Flow direction**	**Gas/ Liquid**	**P (MPa)**	**Ug (cm/s)**	**U_l (m/s)**	**d_s (mm)**	**Number of Data**	**Technique**
Akita and Yoshida (1974)	Square D_H=0.077, 0.15 and 0.3m, H=2.5m	Upward	Air, O_2/ Water 30%, 70%, 100% glycol solution 25%, 45%, 65% glycerol solution, Methanol 0.15 M sodium sulfite solution, CCl_4	0.1 278-313K	0.0788-7.03	0	2.67-15.9	58	Photograph
Bensler (1990)	Square D_H=0.04, 0.08 and 0.12m, H=0.675m	Upward	Air/Water	0.1	0.1-5.9	0	3.05-4.83	16	Ultrasonic
Fukuma, Muroyama and Yasunishi (1987)	Circular D_H=0.15m H=1.2, 1.7 and 3.2m	Upward	Air/Water 16, 20, 50 vol% glycerol aqueous solution	0.1 293.2K	0.86-11.5	0.005-0.05	3.3-19.6	24	Probe
Hean, Hjarbo and Svendsen (1996)	Circular D_H=0.288m H=4.33 m	Upward	Air/Water	0.1 T=285K	2.23-17.0	0	4.64-7.65	10	Dynamic gas disengagement
Koide et al. (1979)	Circular D_H=5.5m H=9m	Upward	Air/Water	0.12 T=279-286K	2.4-4.4	0	11.5-17.5	6	Probe
Lage and Esposito (1999)	Circular D_H=0.0720 mH=0.5-0.8m	Upward	Air/0.5, 1, 2% isopropanol solution	0.1 T=296-299K	0.65-7.02	0	3.2-5.5	23	Photograph
Luewisutthichat, Tsutsumi and Yoshida (1997)	Square D_H=0.0196 m w=0.56m S=10mm H=2.16m	Upward	N_2/Water	0.1	1.2-3.3	0-0.00460	4	6	Photograph

Patel, Daly and Bukur (1989)	Circular D_H=0.05, 0.23m H=3m	Upward	Air/Water	0.1	1.0-9.0	0	2.5-7.2	14	Dynamic gas disengagement
Pohorecki, Moniuk and Zdrojkowski (1999)	Circular D_H=0.304m H=3.99m	Upward	N_2/Water	0.1 T=303-433K	0.2-2.0	0.0014	6.7	30	Photograph
Radhakrishman and Mitra (1984)	Circular D_H=0.032m H=1.08m	Upward	Air-CO_2/Water	0.1	3.51-7.3	0	2.87-3.12	7	Chemical
Sada et al. (1987)	Circular D_H=0.078m H=1.5m	Upward	O_2/0.8 mol/dm^3 sodium sulfite solution	0.1 T=293-303K	1.6-20.5	0	5.1-8.2	13	Chemical
Wilkinson, Haringa and Van Dierendonck (1994)	Circular D_H=0.15m H=1.5m	Upward	N_2, He, Argon, CO_2, SF_4/n-Heptane, Mono-ethylene glycol, 0.8 M sodium sulphite in water	0.1 Room temp.	2.0-18.0	0	2.81-7.56	36	Chemical
Wolff et al. (1990)	Circular D_H=0.3m H=11m D_H=0.2m H=5m	Upward	Air/Water	0.1	1.0-10.0	0	4.3-5.9	10	Probe

2.2 Type of Probes Used in Multiphase Systems

In recent years, measurements of bubble behavior have usually been carried out by various types of probes (Burgess and Calderbank, 1975; Manabu *et al.*, 1995; Wu and Ishii, 1999; Sanaullah, Zaidi and Hills, 2001; Vince *et al.*, 1982; Yu and Kim, 1988; Chabot *et al.*, 1992; Farag *et al.*, 1997; Mudde and Saito, 2001). The miniaturization of probes using fiber optics or small electrodes makes them good choices for performing direct measurements of the bubble velocity and bubble chord length, even at high gas flow rates or in opaque systems. A comparison of measurement methods based on miniature optical and conductivity probes was presented by Choi and Lee (1990). In comparison with conductivity probes, optical probes offer several advantages: (1) They can be used in conductive as well as non-conductive (organic) systems, which are important in the petrochemical industry. (2) The presence of a liquid film on the sensor tip reduces the effectiveness of a conductivity probe but not that of an optical probe, The sensitivity of optical probes is therefore higher than that of conductivity probes (van der Lans, 1985). (3) The optical probe achieves a much better signal/noise ratio than a conductivity probe.

To measure the bubble velocity, at least two probes (tips or measure points) are needed. The two probes (or tips, measure points) are placed in the macroscopic flow direction at a small distance apart (e.g., 2~3 mm). The bubble velocity is calculated by dividing the distance between these two probes by the time interval that the bubble takes to pass through the distance between them. The two-point probes used by various researchers have different configurations, as shown in Figure 2-4.

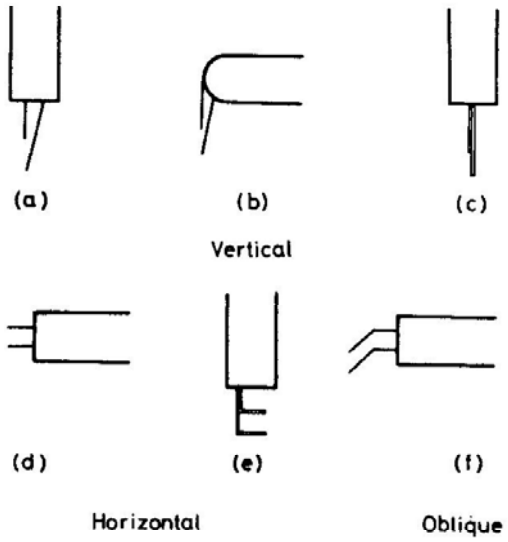

Figure 2-4. Various Tip Configurations of Two-point Probes (Choi and Lee, 1990)

A two-point conductivity probe used by Wu and Ishii (1999) is shown in Figure 2-5. The probe consists of two thin electrodes. The tip of each electrode is exposed to the multiphase system. The impedance between the probe tip and the common ground can be measured. Owing to the large difference in conductivity between the liquid phase and gas bubbles, the impedance signal rises sharply when a bubble passes through the probe. It was reported that because the diameter of the probe tips is very small (89 μm in diameter), no significant bubble deformation or fragmentation was observed through flow visualization for the studied bubble size range between 2 and 4 mm. The time delay of the two impedance signals, Δt, was utilized to characterize the time interval for the bubble surface traveling from the front probe tip to the back tip. With a known separation of the two probe tips, Δs, the bubble velocity was obtained as $v = \Delta s / \Delta t$. The bubble chord length pierced by the two tips of the probe can be obtained as $L_i = v \cdot T_i$, where T_i is the time interval that Tip i spent in the bubble. With assumptions on the bubble shape (e.g., ellipsoidal bubbles), and by using statistical algorithms, the bubble chord length distribution can be transferred to bubble size distribution. However, this method is error sensitive, and the bubble size distribution obtained is not reliable.

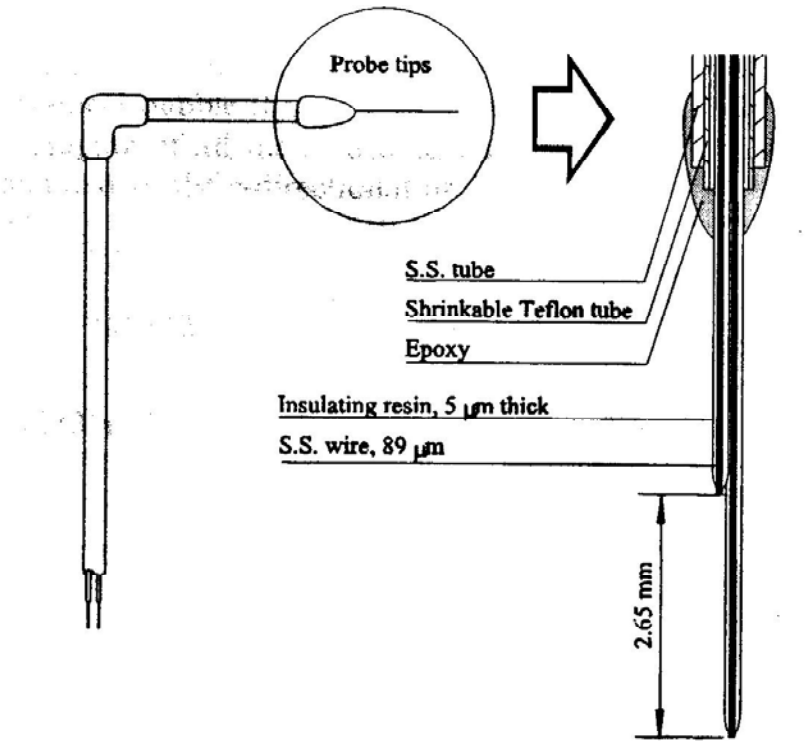

Figure 2-5. Schematic Diagram of a Double-Sensor Conductivity Probe (Wu and Ishii, 1999)

In multiphase systems bubbles hit the probe tips randomly. To eliminate the uncertainty existing in deducing the bubble size and velocity distribution due to the varying and unknown positions at which the probe contacts the bubble frontal surfaces, Burgess and Calderbank (1975) developed a five-point conductivity probe (Figure 2-6). The probe was designed by symmetrically positioning three tips around and above a central tip so that these three tips exist in a horizontal plane. A fifth tip was placed in the same horizontal plane as the central tip but somewhat distant from it. By requiring tips 2, 3, and 4 to respond almost at the same time, the probe records only those encounters where the bubble velocity and bubble vertical axis are coincident with the probe axis within fine limits. The response of the fifth tip was used to determine the horizontal dimension of the bubble, with the assumption that bubbles are ellipsoidal.

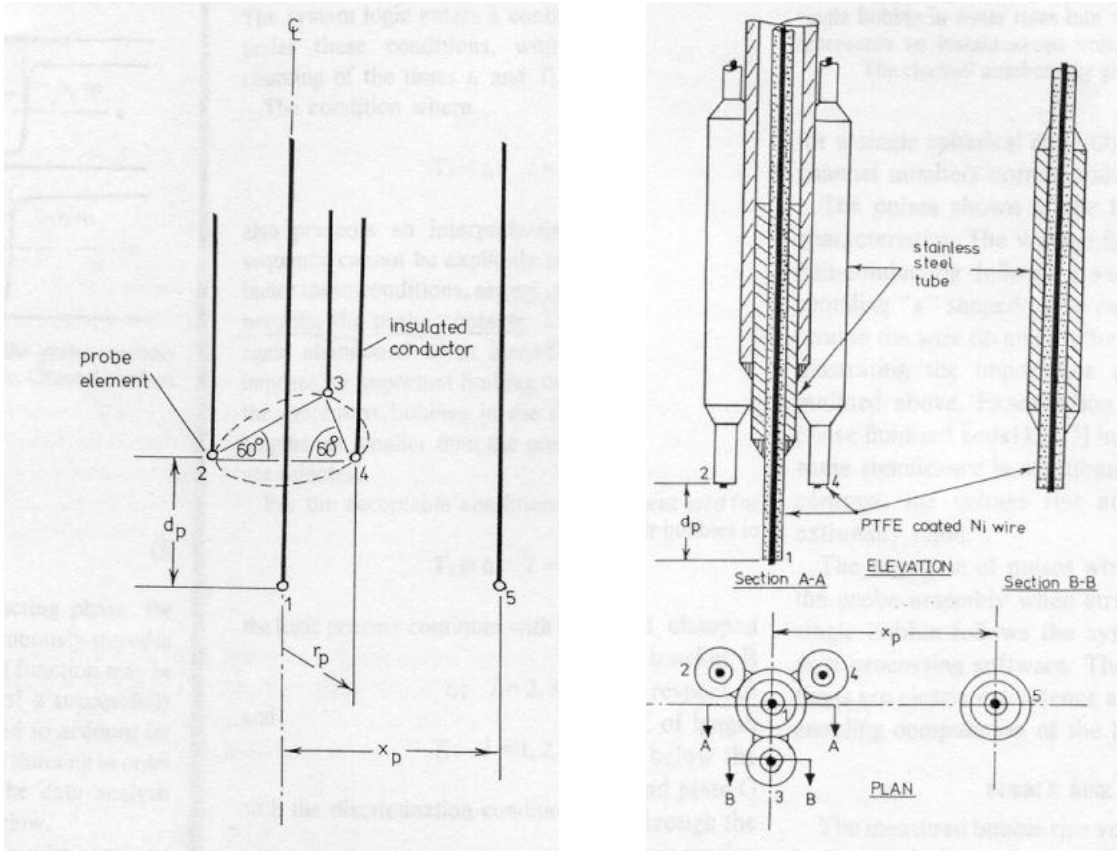

Figure 2-6. Schematic Diagram of a Five-Sensor Conductivity Probe (Burgess and Calderbank, 1975) (The probe dimensions: d_p=4.43 mm, r_p=2.4 mm, and x_p=7.02 mm)

In contrast, a two-point probe cannot provide much information on bubbles' shape. Hence, Iguchi, Nakatani and Kawabata (1997) developed a multineedle conductivity probe (Figure 2-7) to detect the profile of bubbles rising in molten metal baths. An example of the bubble profile detected is also shown in Figure 2-7. The bubble velocity was determined by the central needle of the probe, which is actually a two-point probe.

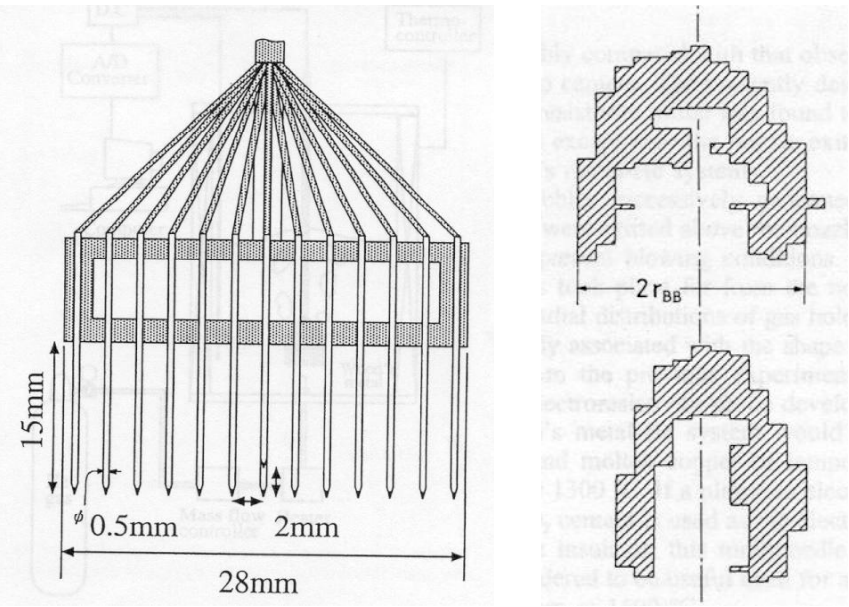

Figure 2-7. Schematic of the Multineedle Conductivity Probe and the Bubble Shape Detected (Iguchi, Nakatani and Kawabata, 1997)

Optical probes used by researchers have the same configuration as the conductivity probes shown above, except that the tips in the probe are made of optical fibers instead of conductors. Optical probes can be classified according to their operating principle into light transmission probes and light reflection probes.

A light transmission probe detects the light transmitted across the light path, while a light reflection probe detects the light reflected at the probe tip or in the phase around the probe tip. Light reflection probes have been more frequently employed because they are smaller and more accurate.

An example of light transmission probes can be found in the research of Kuncova, Zahradnik and Mach (1993). The probe assembly they used consisted of two separate probes (Figure 2-8). A decrease in light transmission at the gap between the two ends of a fiber, caused by a passing bubble, was employed as its signal. The gas holdup can be obtained as the ratio of light absorbance (500nm) in gas-liquid bed and in air,

respectively, because the absorbance is proportional to the retention of air in the probe space. An average vertical dimension of bubbles, d_v, was calculated from the local gas holdup ε_g, the bubble frequency f, and the bubble velocity v (in this study, v was calculated as v = superficial gas velocity/overall gas holdup, obviously this is an oversimplification that causes large error): $d_v = \varepsilon_g \cdot v / f$. It should be pointed out that this equation is a poor approximation to the real value of bubble size.

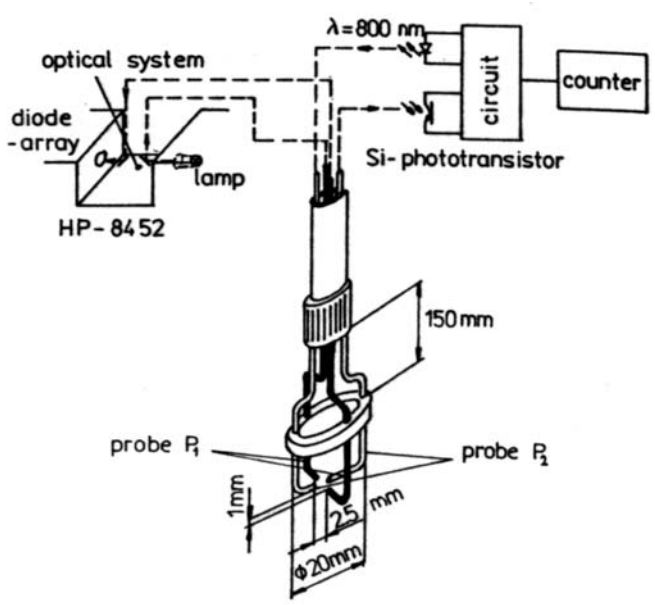

Figure 2-8. A Light Transmittance Probe (Kuncova, Zahradnik and Mach, 1993)

Kreischer, Moritomi and Fan (1990) used a light transmission probe with a configuration shown in Figure 2-9. Probes with this configuration can measure the bubble velocity by dividing the distance between the two pairs of probes by the time interval that the bubble takes to pass through the distance between them. The vertical bubble size (chord length) can be obtained by the product of the bubble velocity and the time spent by the bubble to pass through one probe. The gas holdup is calculated as the ratio of the time taken by bubbles to pass through the probe gap and the whole experimental time.

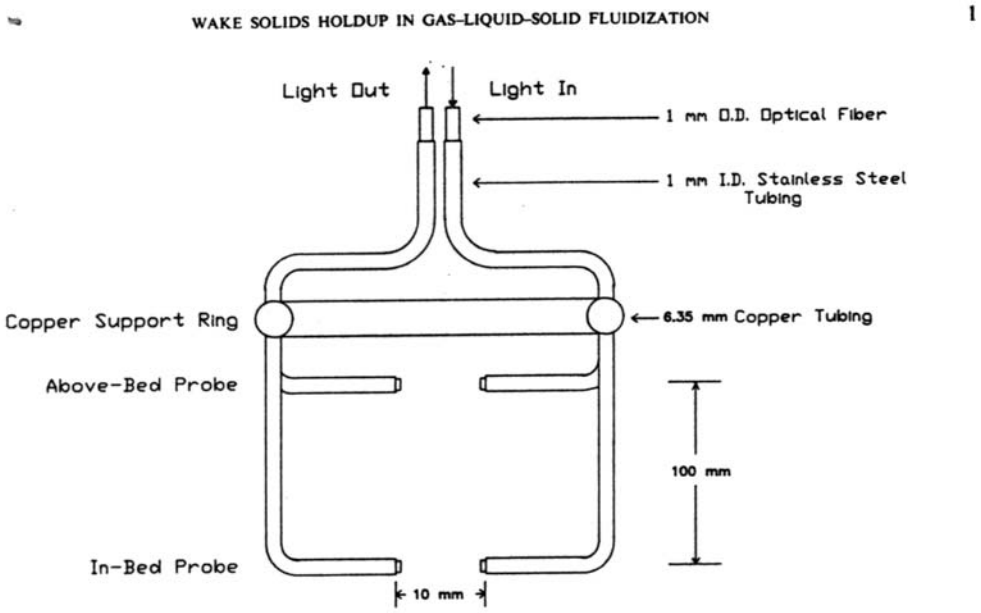

Figure 2-9. A Light Transmittance Probe (Kreischer, Moritomi and Fan, 1990)

The main limitation of all light transmission probes is their large size. The probes in Figures 2-8 and 2-9 measure up to several centimeters. These big probes are inconvenient to use in small size columns, and would disturb the flow pattern seriously.

The light reflection probes that have been employed by researchers for the bubble size distribution and bubble rise velocity measurements are of different configurations. Some light reflection probes detect the light reflected from the phase around the probe tip. Farag *et al.* (1997) used a reflective fiber optic sensor (Figure 2-10) to investigate fluid dynamic properties in turbulent fluidized beds. The sensor consists of two probes 3.2mm apart. Each probe is formed with an emitter fiber and two adjacent receiving fibers approximately 2mm apart from the emitting fiber. No light is detected as long as the probe is immersed in the dense emulsion phase. In case of a bubble passing by the probe, the light is reflected from the wall of the bubble to the receiver fibers. They found that this fiber optic probe underestimated the bubble fraction, probably due to the existence of small undetected or partially detected bubbles.

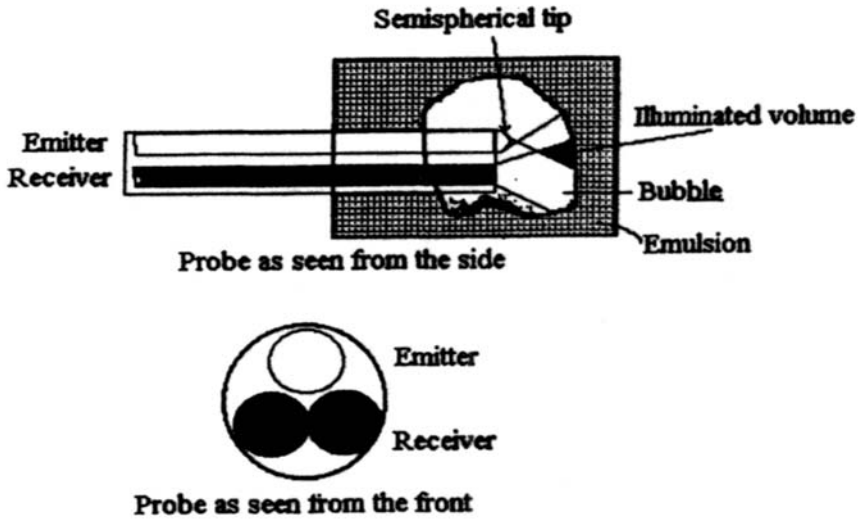

Figure 2-10. A Reflective Fiber Optic Sensor (Farag *et al.*, 1997)

Other light reflection probes detect the light reflected at the probe tip. According to Snell's Law, at the interface of two homogeneous, isotropic media of different indexes of refraction, the following equation holds: $n \cdot \sin(i) = n_0 \cdot \sin(i_0)$, where n and n_0 are the indexes of refraction of the fiber and the medium, respectively, while i and i_0 are the angles of incidence and refraction of the light measured from the normal to the surface (Figure 2-11). Hence, if $\sin(i_0) \geq n/n_0$ then $i \geq 90^o$, all the light will be reflected at the interface. This is called total reflection. The difference of the refractive index between liquid, gas, and optical fiber ensure that the light is scattered at the probe tip when it is in the liquid phase and reflected when it is in the gas (bubble) phase. For example, for a glass probe tip with an index of refraction of n_0=1.62, a total probe tip angle of 90^o, and light rays parallel to the axis (i_0=45^o) (Figure 2-11), the light rays will be reflected back if n<1.15, and will be refracted if n>1.15. By detecting the reflected light, a probe operating on this principle enables the distinction of the gas and liquid phases present at the probe tip if n_g<1.15<n_l. Light reflection probes usually consist of optical fibers bent into a U-shape to create the tip, or, alternatively, the ends of the fibers are cut, sealed, and finished into a conical tip.

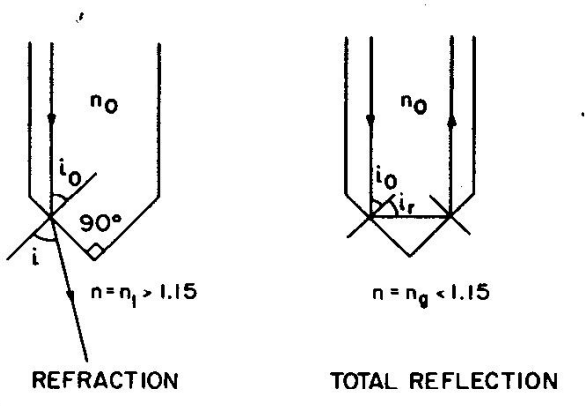

Figure 2-11. Schematic of the Snell's Law (Abuaf *et al.*, 1978)

It was found that the presence of a liquid film on the sensor tip reduces the effectiveness of a conductivity probe but not that of an optical probe. Hence, the wettability of the liquid phase with the glass optical fiber does not affect the sensitivity of optical probes very much (Frijlink, 1987). This is one of the advantages of optical fiber probes over conductivity probes. As illustrated in Figure 2-12, the light ray 'a' experiences total reflection at the glass-gas interface, i.e., $\sin(i) \geq n_{gas}/n_{glass}$. With a liquid film present, refraction to the liquid will take place, and the ray will arrive at the liquid-gas interface with angle of incidence i'. In the case of flat parallel surfaces it is easily shown that the condition of total reflection is now fulfilled at the liquid-gas interface:

$$\left.\begin{aligned} \sin(i) &\geq \frac{n_{gas}}{n_{glass}} \\ n_{glass} \cdot \sin(i) &= n_{liquid} \cdot \sin(i') = n_{gas} \cdot \sin(i'') \end{aligned}\right\} \Rightarrow \sin(i') \geq \frac{n_{gas}}{n_{liquid}} \qquad (2\text{-}8)$$

It may be said that the critical angle where the total reflection happens is transformed to the liquid-gas interface simply by Snell's law. With a curved surface, similar arguments can be used because the film thickness is very small compared to the fiber tip's radius of curvature, so that the local region of surface where the reflection happens can be treated as flat.

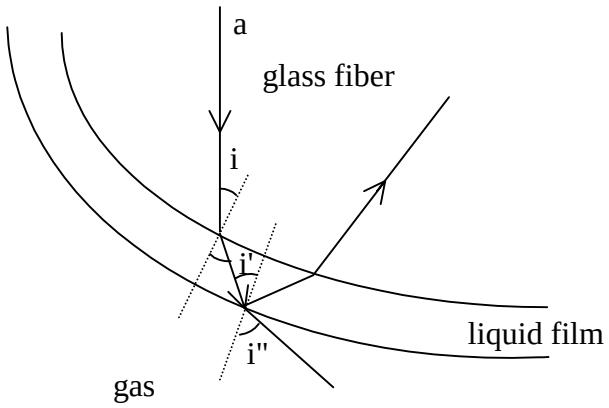

(a) Curved surface

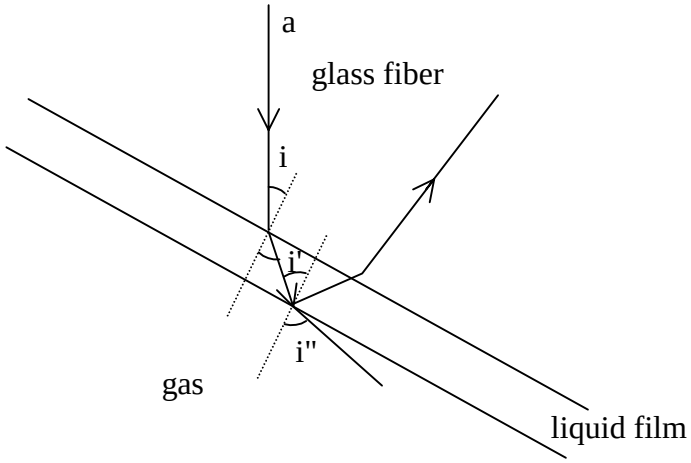

(b) Flat surface

Figure 2-12. The Effect of a Thin Liquid Film on the Probe Tip (Frijlink, 1987)

The optical fiber probes used by Abuaf, Jones and Zimmer (1978) and Vince et al. (1982) to determine the local void fraction in bubble columns had tips that were terminated as a cone with a 90^{o} apex angle (Figure 2-13). The probe in Figure 2-13 consists of two fibers (125 μm in diameter each), which were fused together at the end. The tip of the probe containing the fused ends of the fibers was ground and polished at a 45^{o} angle to the axes of the fibers, thus forming an apex angle of 90^{o}.

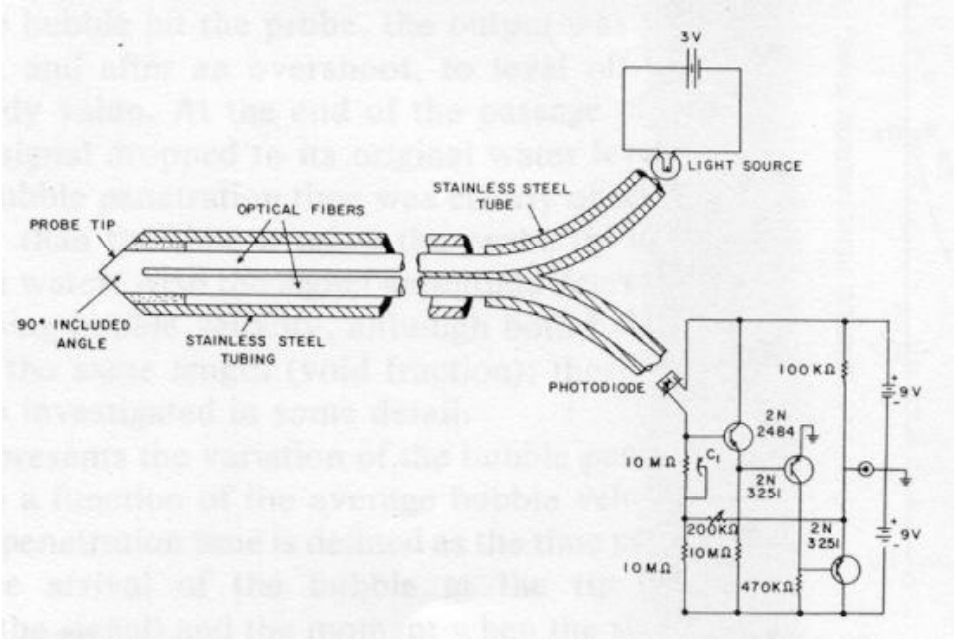

Figure 2-13. Schematic Representation of an Optical Probe (Abuaf *et al.*, 1978)

Yu and Kim (1988) used a two-point light reflection probe, whose active elements were made by bending an optical fiber into a U-shape (Figure 2-14), to determine the gas holdup, mean velocity, and mean bubble chord length in a three-phase fluidized bed.

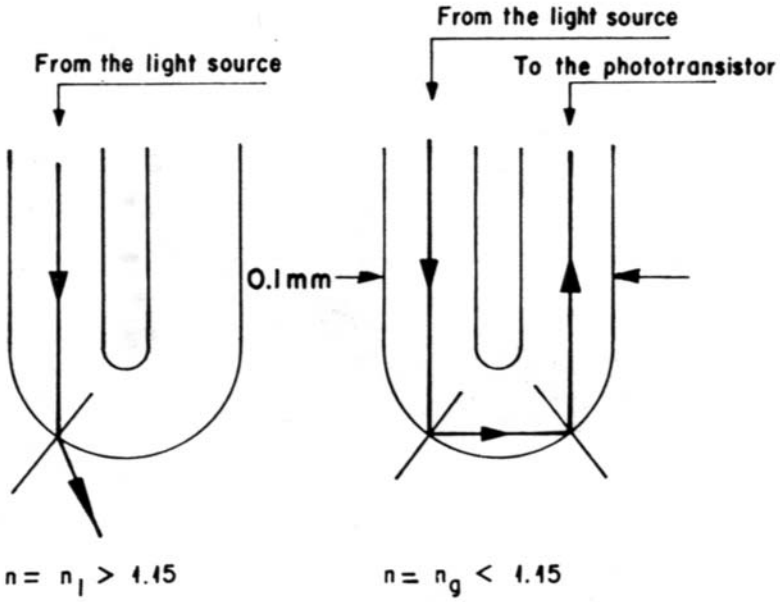

Figure 2-14. A U-Shape Light Reflective Probe (Yu and Kim, 1988)

Chabot *et al.* (1992) used a spherical bulb dual optical fiber probe (Figure 2-15) for bubble characterization in a bubble column and a slurry bubble column at high temperature. According to their research results, no bubble was observed to be significantly affected by the probes, in spite of a decrease in the bubble velocity that was important for small bubbles (for example, 2 mm diameter bubbles in oil). This is because small bubbles did not have enough inertia to be pierced by the tips of optical probes, but rather grazed the probes' tip while being slightly deflected.

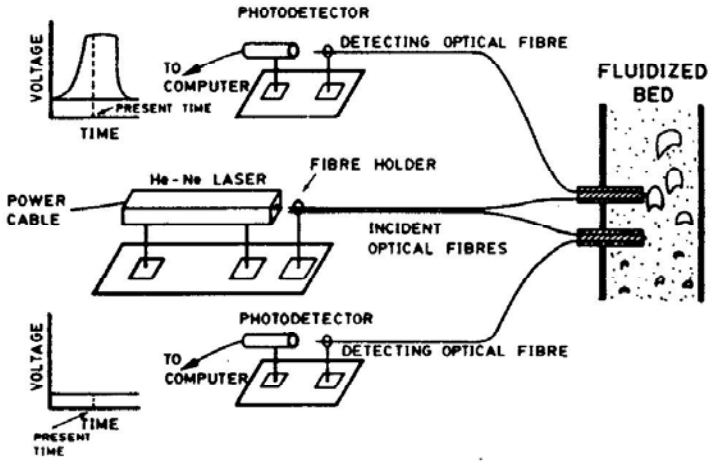

Figure 1 — Schematic diagram of the optical probe operating system.

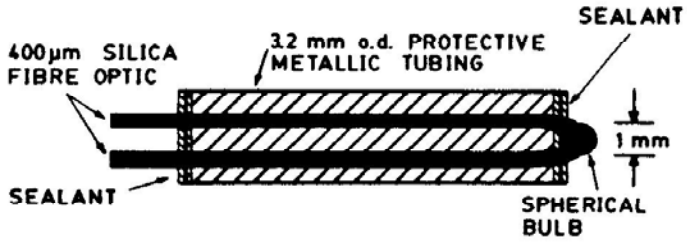

Figure 2-15. A Spherical Bulb Dual Optical Fiber Probe (Chabot *et al.*, 1992)

Saberi *et al.* (1995) made a two-point optical probe by cutting the tip of the fibers into a wedge with a 30^{o} angle. Its flat polished surface was aligned with the flow. This probe was used to measure bubble behavior in a pilot scale column with a diameter of 0.15m and height of 2.3m. It was said that the probe produced results that are of acceptable accuracy for practical calculations.

Cartellier (1998) developed a monofiber probe that can measure the bubble chord length and bubble rise velocity. This monofiber probe has a tip form of a cone + a cylinder + a cone (Figure 2-16). This complicated probe tip was made by etching. This monofiber probe was a successful miniature of a two-point probe, i.e., it combined two tips onto one single optical fiber. The application of the monofiber probe in bubbly flow showed that it is comparable to a two-point probe.

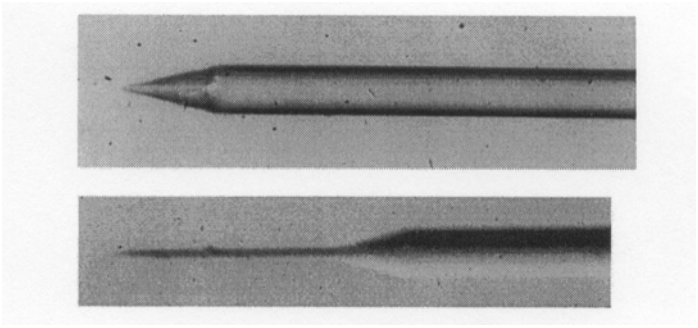

(a) Amplification of the very tip of the probe
(b) The cone+cylinder+cone probe tip

Figure 2-16. Examples of the Probe Tips Produced by Etching Optical Fibers (O.D. 140 μm) (Cartellier, 1998)

In conclusion, two-point probes have so far been employed most frequently to investigate bubble properties in multiphase systems.

Chapter 3 Suggested Algorithm for the Four-Point Optical Probe

3.1 Analysis of Measurement Errors for Two-Point Probes

As mentioned earlier, probes are the only means that can be applied in practical bubble columns to study bubble behavior, e.g., bubble velocity and bubble chord length. Two-point probes have been employed in most of the reported studies (Choi and Lee, 1990; Chabot et al., 1992; Wu and Ishii, 1999; Fan et al., 1999; Magaud et al., 2001). Lim and Agarwal (1992) analyzed the errors in bubble velocity and bubble chord length obtained by two-point probes, based on the assumption of spherical bubbles. They found that the relative error in the bubble velocity obtained by two-point probes varied with the incidence angle and the position at which the bubble hits the probe. The error can easily be over 100% in many cases. Hence, they concluded that values of both bubble velocity and bubble chord length obtained by a two-point probe are theoretically questionable, and experimental results reported using these probes must be viewed at best as qualitative. However, their analysis is limited to spherical bubbles only, and did not consider the curvature correction. Since most bubbles in bubble columns are approximately ellipsoidal, the case of ellipsoidal bubbles is analyzed in this work, and a curvature correction is included in the error analysis. It is thus quantitatively shown that measurements of bubble velocity and bubble chord length by two-point probes can be highly inaccurate. To analyze the measurement errors of two-point probes, the following assumptions are made (refer to Figure 3-1):

(1) The bubble velocity vector aligns with the bubble orientation. In other words, the bubble has a symmetry plane (e.g., spherical or ellipsoidal bubbles) that is perpendicular to the bubble velocity vector.

(2) The shape fluctuation and deformation of the bubble caused by its interaction with the probe are neglected.

(3) The bubble velocity vector (magnitude and direction) does not change during the bubble's passage past the probe.

With these assumptions, the time interval, Δt, between the time when the leading edge of a bubble hits Tip0, the longer tip of a two-point probe (Figure 3-1a), and the time when it hits Tip1, the shorter tip of a two-point probe (refer to Figure 3-1b), is:

$$\Delta t = \frac{L \cdot \cos\theta}{v} \tag{3-1}$$

where v is the magnitude of the bubble velocity vector, and θ is the angle between the bubble velocity vector and the probe's axial direction (Figure 3-1a).

A closer examination reveals that Equation (3-1) is not accurate because the curvature of the bubble's leading edge is neglected. In fact, the effect of curvature on measurements by two-point probes was neglected in most of the published studies (Choi and Lee, 1990; Chabot et al., 1992; Wu and Ishii, 1999; Fan et al., 1999; Magaud et al., 2001). This simplification strongly suggests an even larger error range for two-point probe measurements. To obtain the velocity of a bubble, the displacement of the bubble's centroid, instead of that of the bubble's leading edge, needs to be known. The centroid of an ellipsoidal bubble is on the plane formed by the major axes of the bubble, i.e., plane AB in Figure 3-1a.

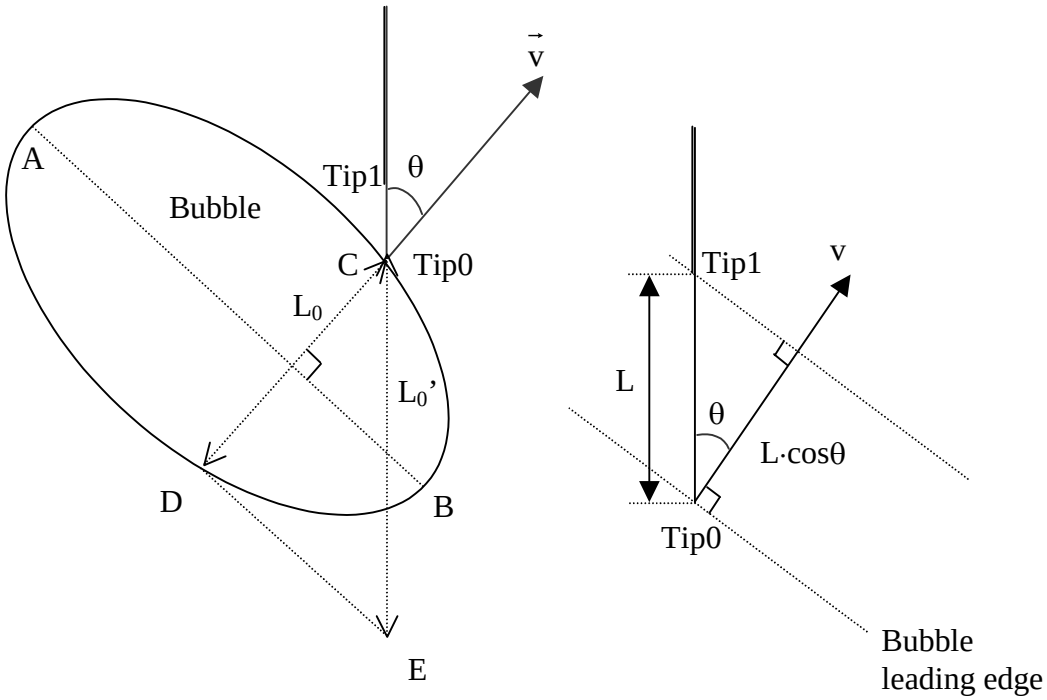

(a) **(b)**

Figure 3-1. Schematic of Bubble Behavior Measurement by a Two-Point Probe

Hence, Equation (3-1) is adjusted to account for the bubble's curvature as follows (refer to Figure 3-2):

$$\Delta t - \frac{T_0 - T_1}{2} = \frac{L \cdot \cos\theta}{v} \qquad (3\text{-}2)$$

where T_0 and T_1 are the time intervals that Tip0 and Tip1 spend in the bubble, respectively.

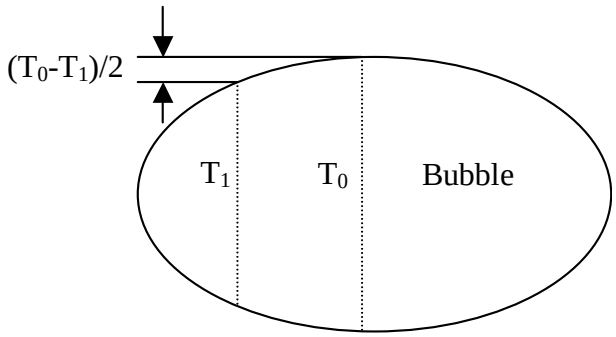

Figure 3-2. Curvature Correction

The magnitude of the vertical component of the bubble velocity vector with an angle θ to the vertical direction is then customarily obtained as (Korekazu et al., 1980; Lim and Agarwal, 1992; Choi and Lee, 1990):

$$v_z' = \frac{L}{\Delta t - \frac{T_0 - T_1}{2}} = \frac{v}{\cos\theta} \tag{3-3}$$

However, the real magnitude of the vertical component of the bubble velocity vector is (Figure 3-1b):

$$v_z = v \cdot \cos\theta \tag{3-4}$$

The relative error in the bubble vertical velocity component obtained by two-point probes therefore is:

$$\text{Error} = \frac{v_z' - v_z}{v_z} \times 100\% = (\tan\theta)^2 \times 100\% \tag{3-5}$$

The relative errors predicted by Equation (3-5) are shown in Figure 3-3a. The errors are always nonnegative, i.e., the magnitude of the bubble vertical velocity obtained by two-point probes is always larger than the real value. The value of the error increases with the value of angle θ: it can be as large as 100% at $\theta = 45^o$, and it goes to infinity at $\theta = 90^o$.

Using a typical algorithm for two-point probes, the bubble chord length is obtained by the product of the bubble vertical velocity and the time interval that the probe tip spends in the bubble. Hence, the error in the bubble velocity is transferred to the bubble chord length. The equation to obtain the chord length pierced by Tip0 is:

$$L_0' = v_z' \cdot T_0 = \frac{v}{\cos\theta} \cdot \frac{L_0}{v} = \frac{L_0}{\cos\theta} \tag{3-6}$$

where L_0 is the real chord length pierced by Tip0, and L_0' is the bubble chord length obtained by a two-point probe. Actually $L_0/\cos\theta$ represents the length CE in Figure 3-1a, while the real chord length pierced by Tip0, L_0, is the length CD.

Then the relative error in the bubble chord length pierced by Tip0 is:

$$\text{Error} = \frac{L_0' - L_0}{L_0} \times 100\% = \left(\frac{1}{\cos\theta} - 1\right) \times 100\% \tag{3-7}$$

As shown in Figure 3-3b, this error is also always positive, i.e., the bubble chord length obtained by two-point probes is always larger than the real chord length pierced by the probe tip. The error increases with the value of angle θ, and it can be as great as 40% at $\theta = 45^o$.

The above analysis indicates that measurements of bubble velocity and bubble chord length by two-point probes are subject to large errors. Reasonably accurate measurements are possible only for very small value of angle θ, i.e., for small departures of the bubble

velocity vector from the probe's axial direction (usually vertical direction). Hence, two-point probes can be used only in the situations where all bubbles move strictly in one direction, such as in forced cocurrent gas liquid flow in pipes, and are not suitable for systems having complex hydrodynamics, such as bubble columns. New probes and algorithms need to be designed to obtain these important parameters in bubble column flows.

It can be seen from Figure 3-3 that when $\theta = 0^o$, i.e., when the bubble velocity vector is aligned with the probe's axial direction, the relative errors in the bubble velocity and bubble chord length measurements by two point probes are zero. Hence, the four-point probe was originally developed to remove the errors in measurements by two-point probes by distinguishing and measuring only bubbles that move in the probe's axial direction, as explained in Section 3.2.

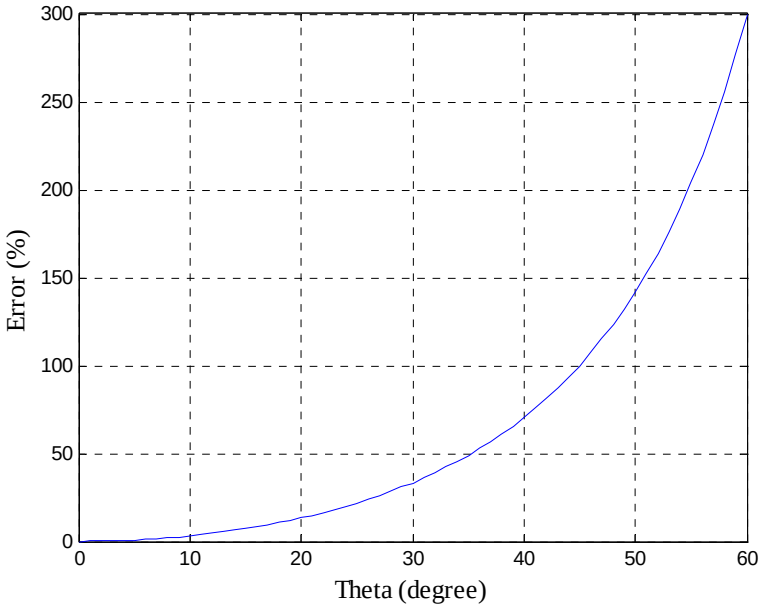

(a) Relative errors in bubble velocity

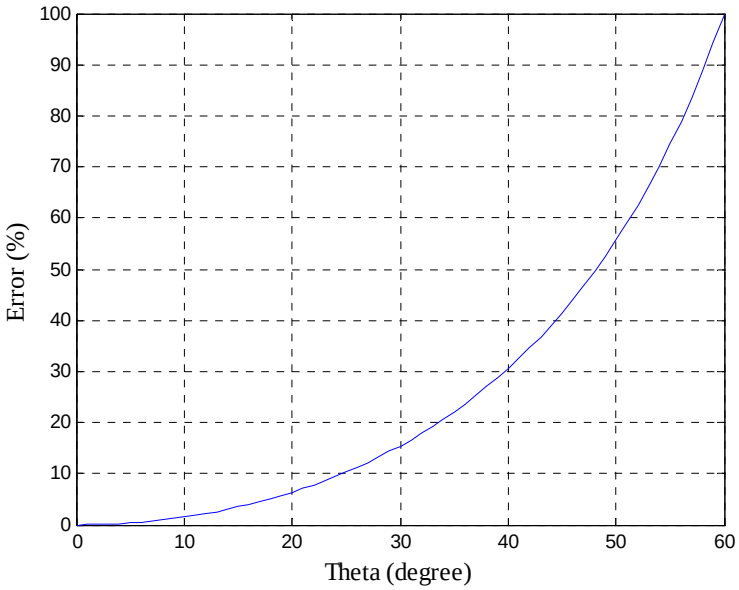

(b) Relative errors in bubble chord length

Figure 3-3. Relative Error in (a) the Bubble's Vertical Velocity and (b) the Bubble Chord Length Obtained by a Two-Point Probe

3.2 The Configuration and Principle of the Four-Point Optical Probe

3.2.1 The Configuration of the Four-Point Optical Probe

Four-point glass optical probes, developed by Frijlink (1987) and his colleagues at the University of Delft in the Netherlands, are used in this research. The optical fiber used is FP-200-UHT multimode fiber optic produced by 3M Corporation. It consists of three layers: a quartz glass core, a silicon cladding, and a protective layer of Teflon (core diameter 200±5μm, clad diameter 380±20μm, outside diameter 600±30μm).

The configuration of the four-point probe is shown in Figure 3-4. At one end of the optical fibers, the cladding and Teflon layer are removed, and the tip of the glass core is shaped into a cone or semi-sphere, like that shown in Figure 3-4e, with a hydrogen flame. This shape assures that, according to the Snell's Law (refer to Section 2.2), most light is reflected at the fiber tip when the probe is in gas phase, due to the difference in the

refractive index between the glass, the liquid phase and the gas phase. Three of the four tips of the probe are of the same length and form an equilateral triangle. The fourth, central tip is positioned through the inertial center of this triangle, and is about 2.0 mm longer than the others. The radial distance from the central fiber to each of the others that surround it is about 0.6 mm. Hence, the diameter of the four-point probe is about 1.2 mm.

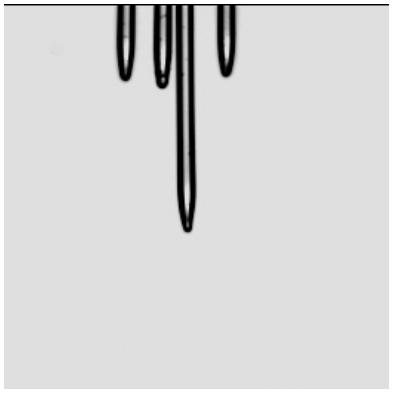

(a) Microphotograph showing side view of the four-point probe (not to scale, field of view 5×5mm)

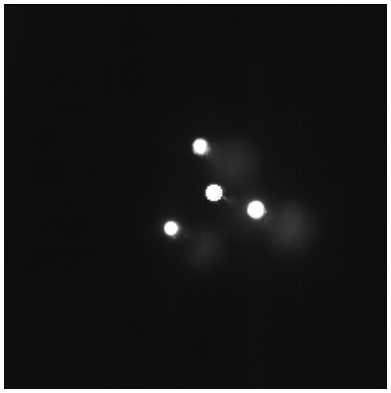

(b) Microphotograph showing bottom view of the four-point probe (not to scale, field of view 2×2mm)

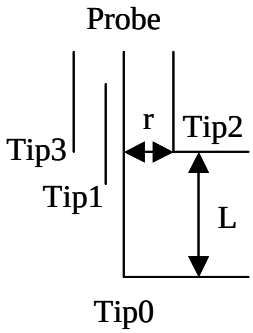

(c) Side view of the expected configuration (L ≈ 2 mm)

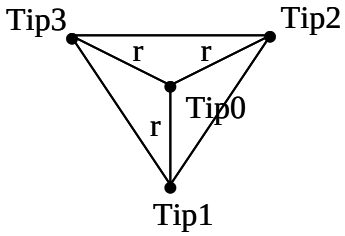

(d) Bottom view of the expected configuration (r ≈ 0.6 mm)

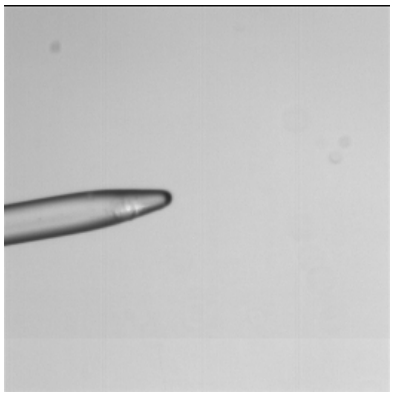

(e) Microphotograph showing the shape of the optical fiber tip (field of view 2×2mm)

Figure 3-4. Configuration of the Four-Point Optical Probe

A jig, illustrated in Figure 3-5, was used to position the four fibers with appropriate tips together in the configuration shown in Figure 3-4. After being positioned, the four fibers were glued together. The procedure is to insert the four fibers into the holes of the jig, adjust the axial distance between the tips, and put glue on the fibers while being careful that the glue does not contact the glass core of the fiber (or else the probe may not work properly). After the solidification of the glue, the probe is removed from the jig. Because the glass fiber is very fragile, one needs to be very careful with this operation.

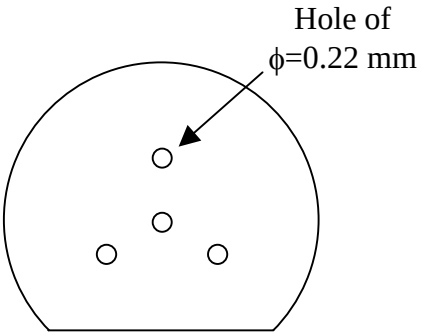

(a) Front view of the jig

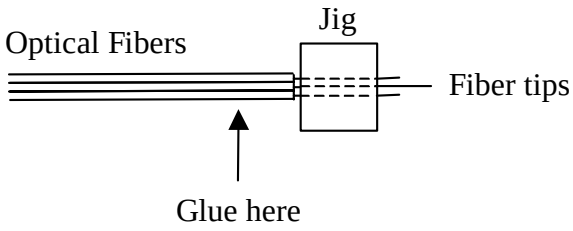

(b) Top view of the gluing operation

Figure 3-5. Jig for the Fabrication of the Four-point Probe

The four optical fibers of the probe are fitted into a stainless steel tube of 3.0mm outer diameter. The tube is bent at the end at an angle of 90^{o} (Figure 3-6). The end of the tubing where the probe tip protrudes is sealed by epoxy glue. The probe is fitted to the measuring ports on the column wall with an appropriate connector. The horizontal part of the tubing is long enough to ensure that it can be traversed over the column diameter so that the radial profile of bubble properties can be obtained. The probe is usually aligned vertically, and the tip faces downwards (Figure 3-6). The four-point optical probe made in this configuration can be used at high pressures and at temperatures up to that the glass fiber and the glue used can stand (up to 500°C). The whole assembly can be used in water, electrolytic solutions, and organic systems. These media and operating conditions cover most applications of the multiphase systems employed in industry.

The optical fiber probe is connected to an electronic unit developed by Kramers Laboratory at the University of Delft. This electronic unit generates laser beams, sends them into the optical fibers of the probe, and receives and transforms the light signals reflected from the probe tip into voltage, using photoelectric multipliers. The voltage signals are sent to the Data Acquisition Board (PowerDAQ PD2-MFS-8-1M/12) in the computer to be saved as data files. To assure the accuracy of measurements, the sampling frequency employed is usually 40 kHz, a value which had proved successful in the work of Frijilink (1987).

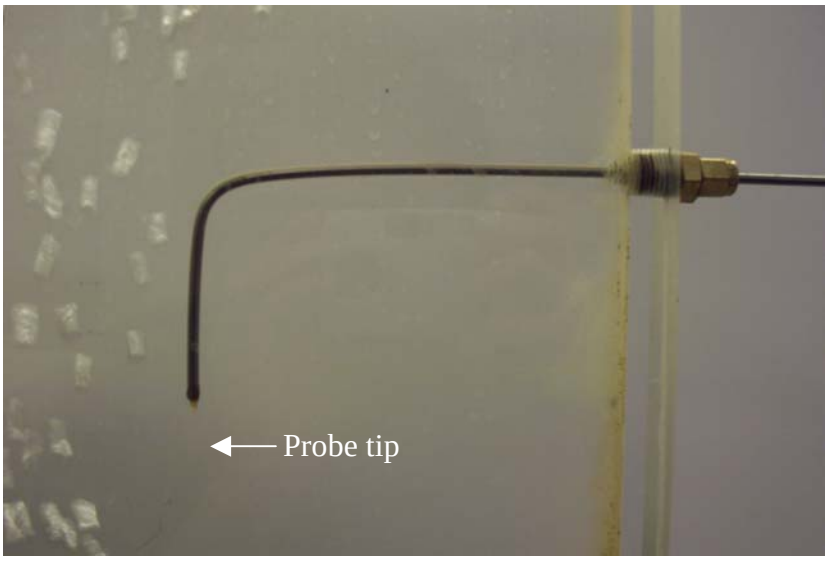

Figure 3-6. The Four-point Optical Probe Installed in a 2D Bubble Column

3.2.2 Working Principle of the Four-Point Optical Probe

A laser beam (680nm wavelength) from a Light Emitting Diode (LED) is sent into the end of the optical fibers, and then transmitted along the fibers into the tips. If the tip of an optical fiber is in the liquid phase (water in this research), most of the light will enter the liquid phase, due to the relatively small difference in the refractive index between the fiber material (silica glass) and the liquid phase. If, on the other hand, the tip of an optical fiber is in a bubble, most of the light will be reflected back into the fiber at the tip, as detailed in Section 2.2.

A Y-shape splitter, shown in Figure 3-7, is used to separate the reflected light from the incoming light. The reflected light signals are converted to voltage signals by photoelectric multipliers.

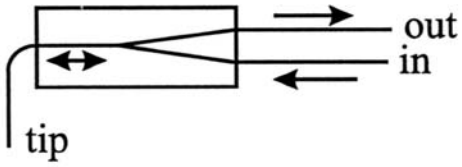

Figure 3-7. The Schematic of the Light Splitter

The voltage output is high when the probe tip is in the gas (bubble) phase, and is low when it is in the liquid phase. The response of the four-point optical probe, as illustrated in Figure 3-8, consists of four time series for the four tips of the probe's four optical fibers. As can be seen from Figure 3-8, when a bubble hits a fiber tip, the output voltage of that fiber rises from the baseline (liquid phase response) as more and more of the tip surface enters the bubble and reflects light. When the tip is completely inside the bubble the output is constant. As shown in Figure 3-8, this response increase is very fast. When the tip finally touches the bubble-water surface at the bottom of the bubble, the output voltage decreases to the baseline. This decrease is even much faster than the increase in the output voltage during the probe's initial piercing of a bubble because the surface tension will cause the bubble bottom to move upwards quickly along the fiber.

If a bubble traveling upwards hits the four-point probe, the central fiber, Tip0, which is a little longer than the others, responds first, and the other three tips (tips 1,2,3) respond a little later. For an axially symmetric bubble, e.g., an ellipsoidal bubble, requiring that the responses of tips 1, 2, 3 be almost simultaneous assures that: (1) the bubble moves in the probe's axial direction, and (2) the probe hits the center of the bubble, i.e., the trajectory of the central tip through the bubble is along the bubble's minor axis (Frijlink, 1987). If the bubble is pierced too much on the side, or the bubble does not move in the probe's axial direction, the responses of the three tips 1, 2, 3 will not be simultaneous, due to the curvature of the bubble surface.

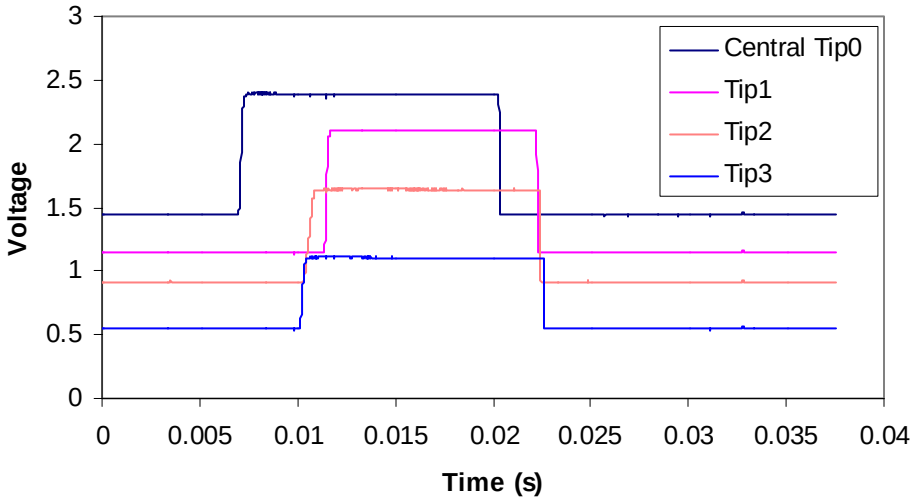

Figure 3-8. Response of the Four-Point Probe to a Bubble Pierced Through

Hence, by analyzing the output of the four-point optical fiber probe, one can distinguish and reject both bubbles that do not approach the probe in the probe's axial direction and bubbles that are not pierced by the probe in the center. In practice, a tolerance is set to accept bubbles being pierced in the vicinity of the central line. Hence, the four-point probe can measure the bubble velocity more accurately than two-point probes because only bubbles moving in a small range of angle θ close to zero, i.e., bubbles whose motion deviate little from the probe's axial direction, are measured. Hence, the theoretical error in the bubble velocity and bubble chord length obtained by the four-point probe is small, as evident from Figure 3-3 and the discussions in Section 3.1. Furthermore, the length of the bubble's minor axis can be obtained directly and more accurately by avoiding the transfer of the bubble chord length distribution measured by the probe to the bubble size distribution, as needs to be done in measurements by two-point probes (Liu, Clark and Karamavruc, 1996, 1998) which is subject to large error. This is also one of the advantages of the four-point optical probe over two-point probes. However, the disadvantage of the four-point optical probe, as used in the study of Frijlink (1987), is that in complex flow patterns only a very small fraction of bubbles will hit the probe centrally and rise in the probe's axial direction. Thus, it is uncertain that the obtained measurement reflects the bubble population that is present. This will be corrected in our

work as shown later. The diameter of the four-point probe is 1.2mm. Thus, theoretically the four-point probe can measure only bubbles whose diameter in the plane perpendicular to the probe direction is greater than 1.2mm. There is no upper limit to the bubble size that can be measured by this probe.

3.2.3 Signal Analysis

The four-point optical probe provides four time series for the detected voltage at the tips, $s_i(t)$ i=0,1,2,3 (Figure 3-9). The procedure for data processing is explained below.

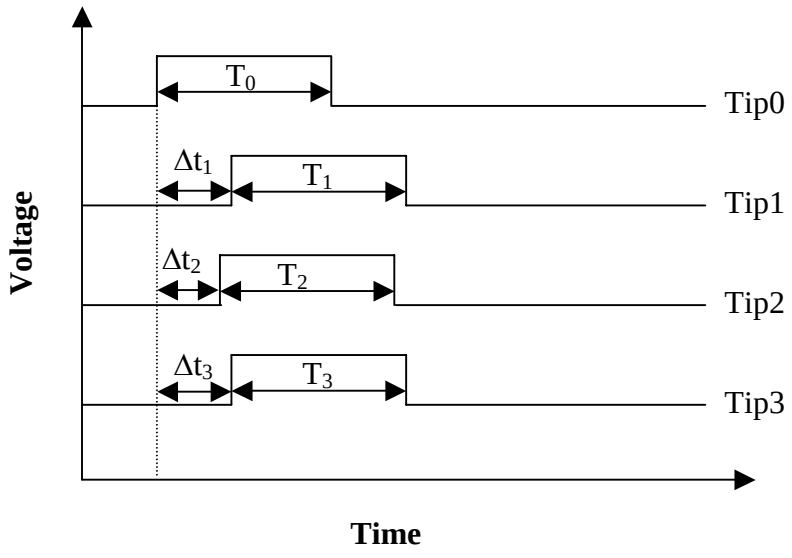

Figure 3-9. Schematic of the Response of the Four-Point Probe to a Bubble Pierced Through

First, the time series are transferred to the binary mode via an appropriate threshold (th). Different threshold is used for the extraction of bubble velocity, bubble chord length and local gas holdup. The threshold used for the calculation of bubble velocity is 60% of the difference between the baseline voltage and the peak value for bubbles. Thus, the response points where the output of the probe increases 60% of the difference between the baseline and the peak value are marked as the border of bubbles (Figure 3-10). As

shown in Figure 3-10, this threshold can discard the irregular responses caused by a bubble that slips away from the probe instead of being pierced through. These irregular peaks are difficult to define, and may cause errors in measurements. With this threshold, the responses of the probe are transferred to a binary series, in which the value 1 represents that the probe's tip is in the bubble, and the value 0 represents that the tip is in the liquid phase.

$$b_i(t) = \begin{cases} 1 & s_i(t) \geq \text{baseline} + \text{th} \times (\text{peak} - \text{baseline}) \\ 0 & s_i(t) < \text{baseline} + \text{th} \times (\text{peak} - \text{baseline}) \end{cases} \quad (3\text{-}8)$$

The value of the threshold does not affect much the obtained value of the bubble velocity, since the bubble velocity is determined by the time difference between the responses of different fiber tips to a bubble, and the effect of different threshold values is minimized during the subtraction.

However, the 60% threshold is too high for determination of the bubble chord length, because the width of the bubble peak decreases with its height (Figure 3-10), and the width at the peak root represents the bubble chord length pierced by the probe tip. Hence, a threshold of 1% is used to determine the bubble chord length, i.e. the response points where the output of the probe increases 1% of the difference between the baseline and the peak value are marked as the border of bubbles to calculate the bubble chord length (Figure 3-10).

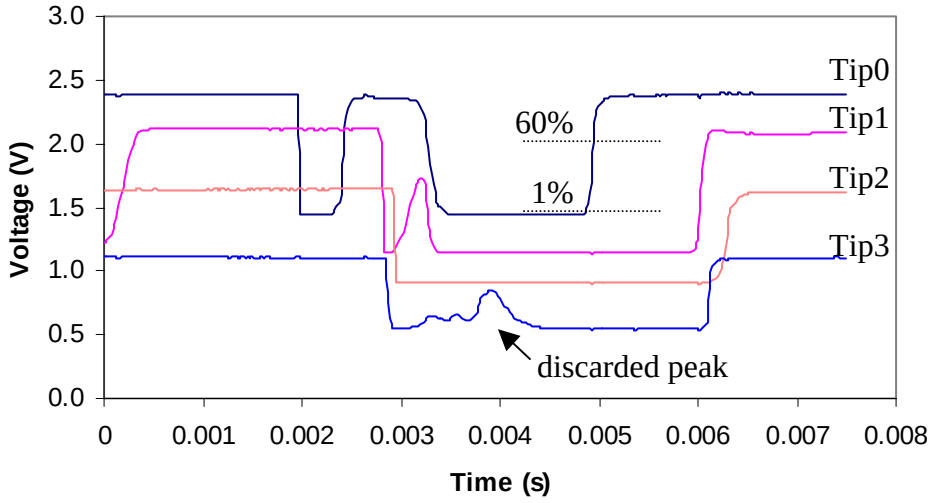

Figure 3-10. A Sample of the Probe's Responses

From the response of the probe's central tip, the local gas holdup can be obtained as:

$$\varepsilon_g = \frac{\text{Time spent by the probe's central tip in bubbles}}{\text{Total measurement time}} = \frac{\sum T_0}{\Delta T} = \frac{\sum_{j=1}^{N} b_0(t_j)}{N} \qquad (3\text{-}9)$$

where N is the total number of sample points in the response of the probe's central tip. When calculating the local gas holdup, all bubbles that hit the central tip of the probe are used, i.e., there is no rejection of any bubbles.

The threshold for the determination of gas holdup should not be too high, as this would cause bubbles that touch the tip rather than being pierced to be filtered out, thus underestimating the gas holdup. Obviously, it cannot be too close to zero either, as then unwanted noise would cause an overestimate of the gas holdup. By using various threshold values, th, and calculating the gas holdup, ε_g, the relationship between ε_g and th can be obtained, as shown in Figure 3-11 (as mentioned before, the unit of the threshold, th, is the percentage of the difference between the baseline voltage and the peak value for bubbles in Figure 3-11). Hence, a minimum threshold can be found, below which noise is

influencing the void fraction estimate. The signal to noise ratio is a little different for each measurement by the optical probe. Hence, this procedure is repeated to find the suitable th for each measurement. In this study, it was found that the suitable threshold is usually less than 0.5%. This very low value of the threshold is due to the high signal/noise ratio of the optical probe, which is much better than that of electrical conductivity probes.

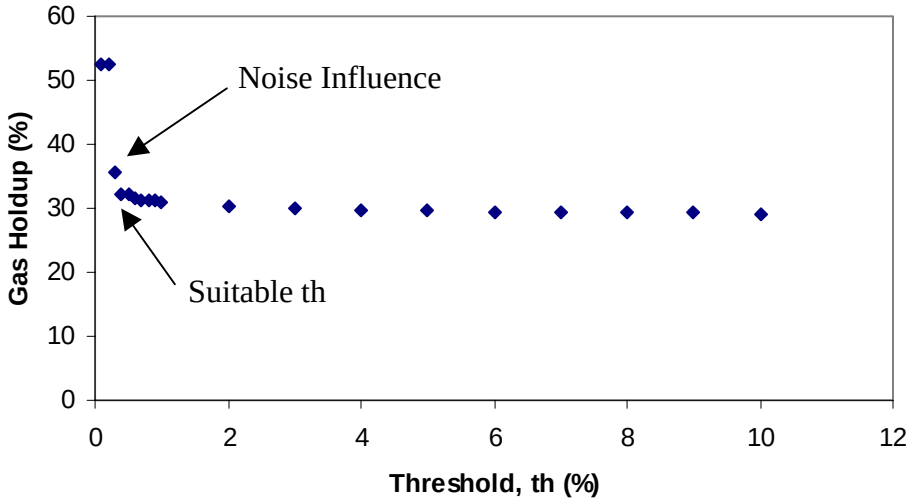

Figure 3-11. Relationship between Gas Holdup and the Threshold Selected

A data processing algorithm for the four-point optical probe was developed by Frijilink (1987) and his colleagues to get the bubble velocity and bubble chord length. This algorithm ensures that all bubbles that do not fit the selected criterion, i.e., that do not move in the probe's axial direction and are not being pierced centrally (Figure 3-12b), are rejected. First, the instants when a bubble hits a probe tip i, t_i, are determined, and the time intervals Δt_i, i=1,2,3, are calculated:

$$\Delta t_i = t_i - t_0 \qquad (3\text{-}10)$$

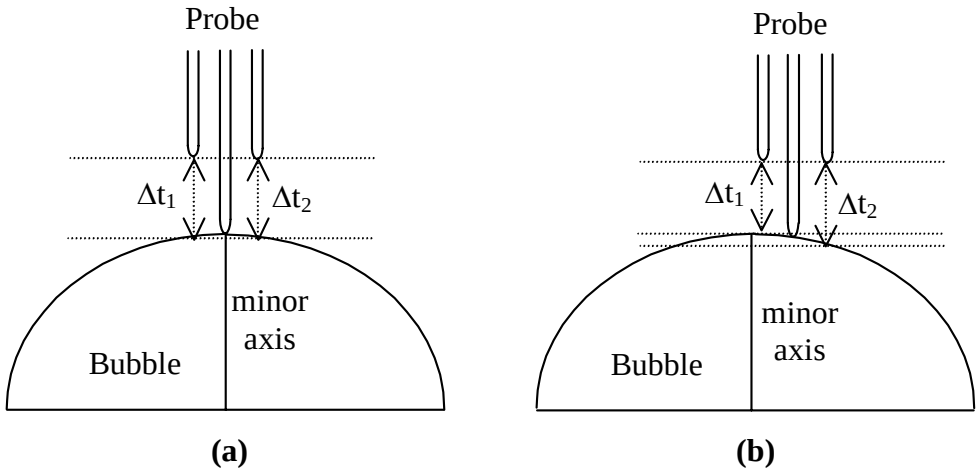

Figure 3-12. Schematic of the Selection Function of the Four-point Probe

For an axially symmetric bubble moving approximately in the probe's axial direction and being pierced centrally, the differences between Δt_i, i=1,2,3, should be very small (Figure 3-12a). Hence, the next step is to evaluate whether the differences in the bubble velocities calculated from these three time intervals are less than a given tolerance δv (for example 10%). If the maximum difference between these three velocities and the mean of them is greater than δv, then this particular bubble is discarded. Otherwise, the bubble velocity is obtained as the mean of the three values:

$$v_i = \frac{L}{\Delta t_i - \frac{T_0 - T_i}{2}} \quad i = 1, 2, 3 \tag{3-11a}$$

$$v = \frac{(v_1 + v_2 + v_3)}{3} \tag{3-11b}$$

if for i=1,2,3, $\left|\frac{v_i - v}{v}\right| < \delta v$, then a valid bubble is detected, or else it is rejected.

The length of the bubble's minor axis, d_B, is then equal to the product of the bubble velocity and the time interval that the central tip spends inside the bubble, T_0:

$$d_B = v \cdot T_0 \tag{3-12}$$

3.2.4 Measurement Errors of the Four-Point Optical Probe (Old Algorithm)

According to the data processing algorithm described in Section 3.2.3, the four-point probe used in this work measures only bubbles that move almost in the probe's axial direction and are being pierced in the vicinity of the bubble's central line by the central tip of the probe. However, the movement of bubbles in bubble columns is rather complicated. Actually bubbles do not move vertically and straight, but rather in a zigzag or spiral pattern. Hence, if the probe is installed vertically in bubble columns, most bubbles will move in directions that deviate from the probe's axial direction, i.e., the vertical direction.

Of course, it is not necessary that the probe be installed vertically. To reduce the deviation of the bubble motion from the probe's axial direction, it would be desirable to place the probe in the direction of the motion of most bubbles, if such exists, at each point in bubble columns. Unfortunately, it has been found that bubble motion in bubble columns, including the movement direction, keeps changing with the liquid flow direction all the time. There is no fixed preferred flow direction at most places in bubble columns (Chen, Reese and Fan, 1994). As a result, it is practically impossible to align the probe with the flow direction of bubbles, and many bubbles rise with a velocity direction that deviates from the probe's axial direction. Furthermore, the position where the probe hits the bubble's leading edge is random. Hence, the selection function of the probe is difficult to apply efficiently. For example, in a 2-D column used, the bubble selection with this probe (with tolerance $\delta v=10\%$, see Equation 3-11) caused more than 99% of bubbles that hit the probe to be discarded. This high selectivity causes difficulty in data processing and interpretation. Therefore, to avoid a high discard ratio of bubbles during the measurements, the effect of increasing the tolerance δv was studied so that bubbles with movement that does deviate somewhat from the probe's axial direction are also accepted. To do this in a systematic manner, an error analysis was performed.

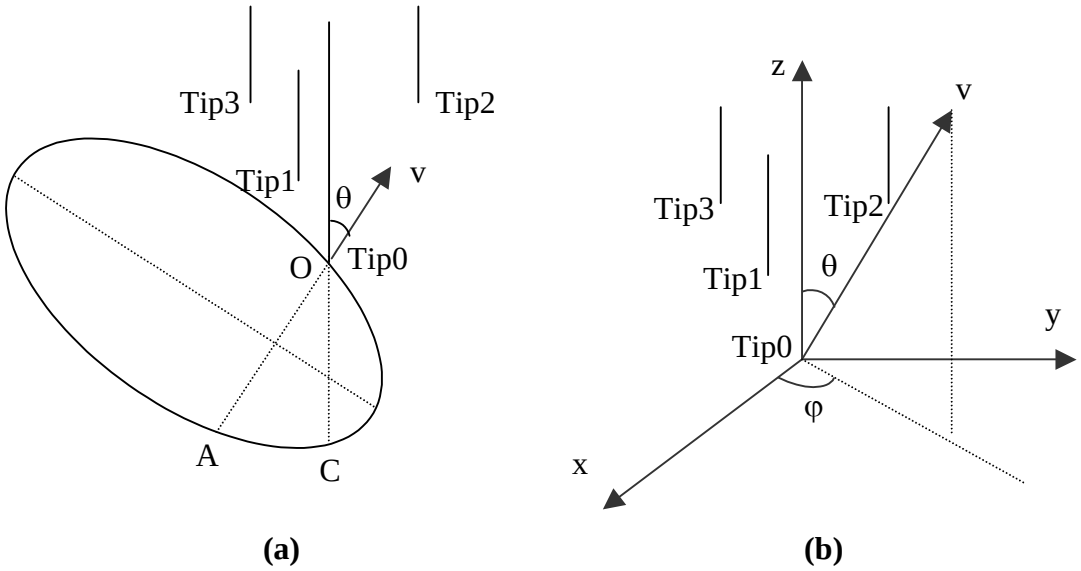

(a) **(b)**

Figure 3-13. Schematic of the Probe Tips and Bubble Velocity Vector

Assume that the bubble velocity vector is perpendicular to the major axes of the bubble. Figure 3-13 shows the schematic diagram of the four-point probe measurement. In the coordinate system shown in Figure 3-13b, the coordinates of the four tips of the probe are:

$$\text{Tip } 0 : (0, 0, 0)$$
$$\text{Tip } 1 : (r, 0, L)$$
$$\text{Tip } 2 : \left(-\frac{r}{2}, \frac{\sqrt{3}}{2} r, L\right)$$
$$\text{Tip } 3 : \left(-\frac{r}{2}, -\frac{\sqrt{3}}{2} r, L\right)$$

where L is the axial distance between peripheral tips and the central tip of the probe, and r is the radial distance between peripheral tips and the central tip (refer to Figure 3-4).

To set up the equations that describe the physical situation, a coordinate transformation was introduced as shown in Figure 3-14.

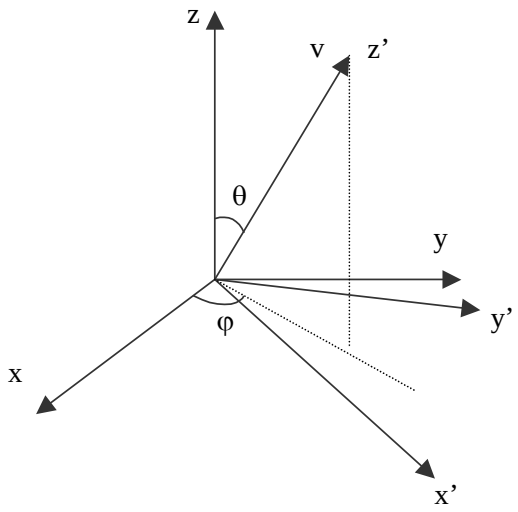

Figure 3-14. Coordinate Transformation

The xyz coordinate system was transformed to a x'y'z' system with its z'-axis in the direction of the bubble velocity vector. The relationship between coordinates x', y', z' and x, y, z is:

$$\begin{bmatrix} x' \\ y' \\ z' \end{bmatrix} = \underline{\underline{A}} \cdot \begin{bmatrix} x \\ y \\ z \end{bmatrix} = \begin{bmatrix} \cos\theta\cos\varphi & \cos\theta\sin\varphi & -\sin\theta \\ -\sin\varphi & \cos\varphi & 0 \\ \sin\theta\cos\varphi & \sin\theta\sin\varphi & \cos\theta \end{bmatrix} \cdot \begin{bmatrix} x \\ y \\ z \end{bmatrix} \tag{3-13}$$

Here, $\underline{\underline{A}}$ is the coordinate transform matrix, θ is the angle of the bubble velocity vector with respect to z axis, and φ is the angle between the projection of the bubble velocity vector on the xy plane and the x axis (Figure 3-13b).

Hence, the z' coordinates of the probe tips are:

$$\text{Tip } 0 : z_0' = 0$$
$$\text{Tip } 1 : z_1' = r \cdot \sin\theta\cos\varphi + L \cdot \cos\theta$$
$$\text{Tip } 2 : z_2' = -r/2 \cdot \sin\theta\cos\varphi + \sqrt{3}/2r \cdot \sin\theta\sin\varphi + L \cdot \cos\theta$$
$$\text{Tip } 3 : z_3' = -r/2 \cdot \sin\theta\cos\varphi - \sqrt{3}/2r \cdot \sin\theta\sin\varphi + L \cdot \cos\theta$$

Notice that the z_i' coordinate value of Tip i, i=1,2,3, is the distance between Tip i and Tip0 in the direction of the bubble velocity vector (Figure 3-13b). Hence, the time intervals between the instant when a bubble hits the central tip, Tip0, and the instant when it hits Tip i, i=1,2,3, are:

$$\Delta t_1 - \frac{T_0 - T_1}{2} = \frac{r \cdot \sin\theta\cos\varphi + L \cdot \cos\theta}{v} \tag{3-14a}$$

$$\Delta t_2 - \frac{T_0 - T_2}{2} = \frac{-r/2 \cdot \sin\theta\cos\varphi + \sqrt{3}/2r \cdot \sin\theta\sin\varphi + L \cdot \cos\theta}{v} \tag{3-14b}$$

$$\Delta t_3 - \frac{T_0 - T_3}{2} = \frac{-r/2 \cdot \sin\theta\cos\varphi - \sqrt{3}/2r \cdot \sin\theta\sin\varphi + L \cdot \cos\theta}{v} \tag{3-14c}$$

where v is the magnitude of the bubble velocity vector.

Consequently, the magnitude of the component of the bubble velocity vector in the probe's axial direction obtained by the probe is:

$$\begin{aligned} v_z' &= \frac{1}{3} \cdot \left(\frac{L}{\Delta t_1 - \frac{T_1 - T_0}{2}} + \frac{L}{\Delta t_2 - \frac{T_2 - T_0}{2}} + \frac{L}{\Delta t_3 - \frac{T_3 - T_0}{2}} \right) \\ &= v \cdot \frac{L}{3} \cdot \left(\frac{1}{r \cdot \sin\theta\cos\varphi + L \cdot \cos\theta} + \frac{1}{-r/2 \cdot \sin\theta\cos\varphi + \sqrt{3}/2r \cdot \sin\theta\sin\varphi + L \cdot \cos\theta} \right. \\ &\qquad \left. + \frac{1}{-r/2 \cdot \sin\theta\cos\varphi - \sqrt{3}/2r \cdot \sin\theta\sin\varphi + L \cdot \cos\theta} \right) \end{aligned} \tag{3-15}$$

As illustrated in Figure 3-13b, the real magnitude of the component of the bubble velocity vector in the probe's axial direction is:

$$v_z = v \cdot \cos\theta \tag{3-16}$$

Hence, the relative error in the magnitude of the component of the bubble velocity vector in the probe's axial direction is:

$$\text{Error} = \frac{v_z' - v_z}{v_z} \times 100\% = \frac{v_z' - v \cdot \cos\theta}{v \cdot \cos\theta} \times 100\% \qquad (3\text{-}17)$$

Figure 3-15 shows the errors in measurements by the probe predicted by Equation (3-17). The range of angle φ is selected as $0\sim60^o$. This range covers all the cases because of the symmetry of the three peripheral tips of the probe. The range of angle θ is selected also as $0\sim60^o$ for the convenience of display. In this range of θ and φ, the relative error in the magnitude of the bubble velocity component in the probe's axial direction can be as large as 400%. At θ values larger than 60^o, the relative errors are even larger. It can be seen from Figure 3-15 that the relative error is affected mainly by the value of angle θ. To keep the relative error smaller than 25%, θ must be smaller than 25^o.

Figures 3-16, 3-17, and 3-18 show the difference between the bubble velocity determined by Tip i, v_i i=1,2,3, and the mean of v_1, v_2, and v_3. Assume the tolerance, δv, for the bubble selection is set to be 10%, i.e., a bubble will be accepted only if the relative differences between v_1, v_2, v_3 and the mean, v, are all within ±10% (refer to Equation 3-11). From Figures 3-16, 3-17, and 3-18, it can be seen that all bubbles with a velocity vector that deviates from the probe's axial direction within 20^o will be accepted. The relative error in the bubble velocity at $\theta=20^o$ is about 15% according to Figure 3-15. If the tolerance, δv, is set to be 20%, the tolerated range of θ by the probe measurement will be larger than 30^o. At $\theta=30^o$, the relative error in the bubble velocity is about 40% according to Figure 3-15.

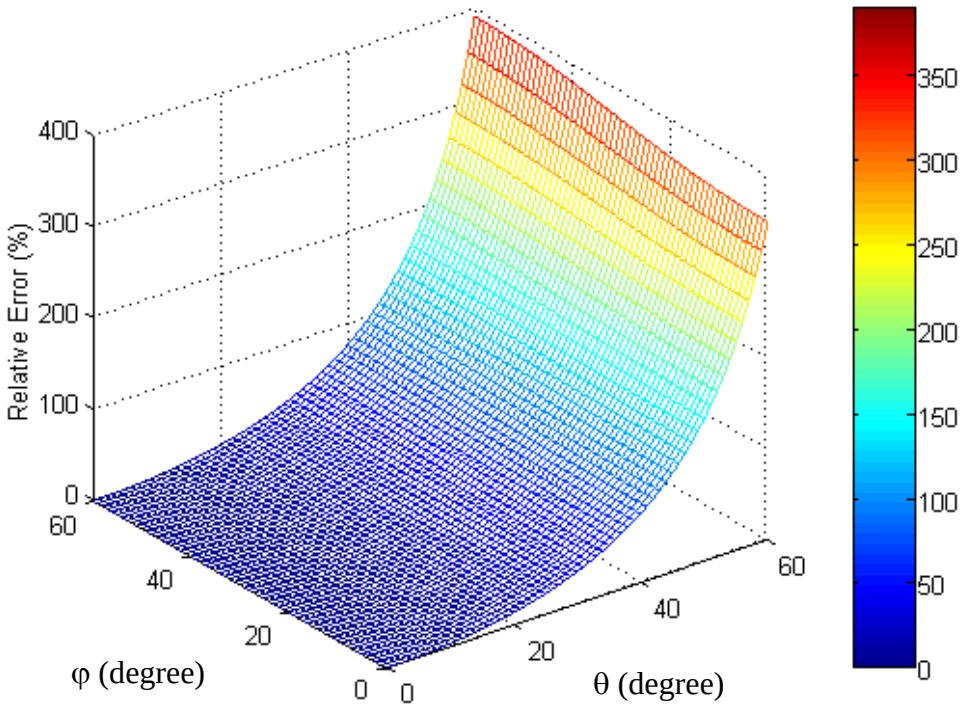

(a) Surface diagram

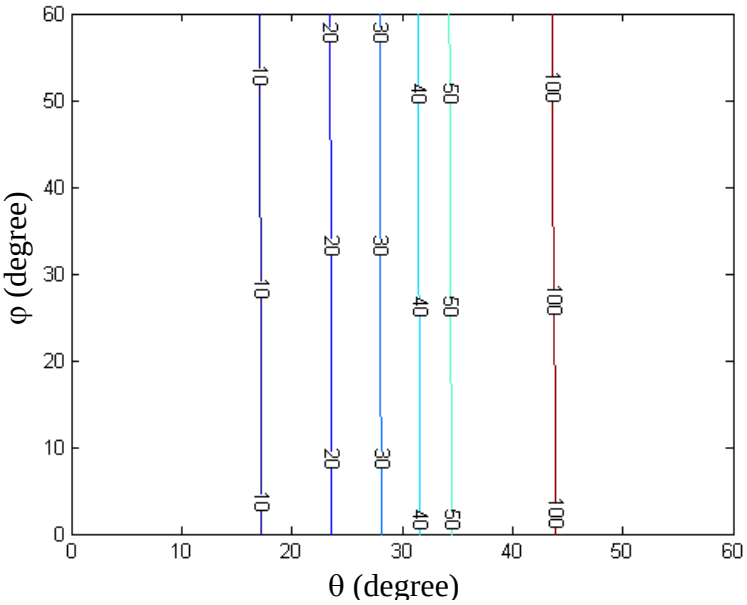

(b) Contour diagram

Figure 3-15. Relative Errors in Bubble Velocity Measurements due to the Deviation of Bubble Motion from the Probe's Axial Direction (r=0.6mm, L=1.5mm)

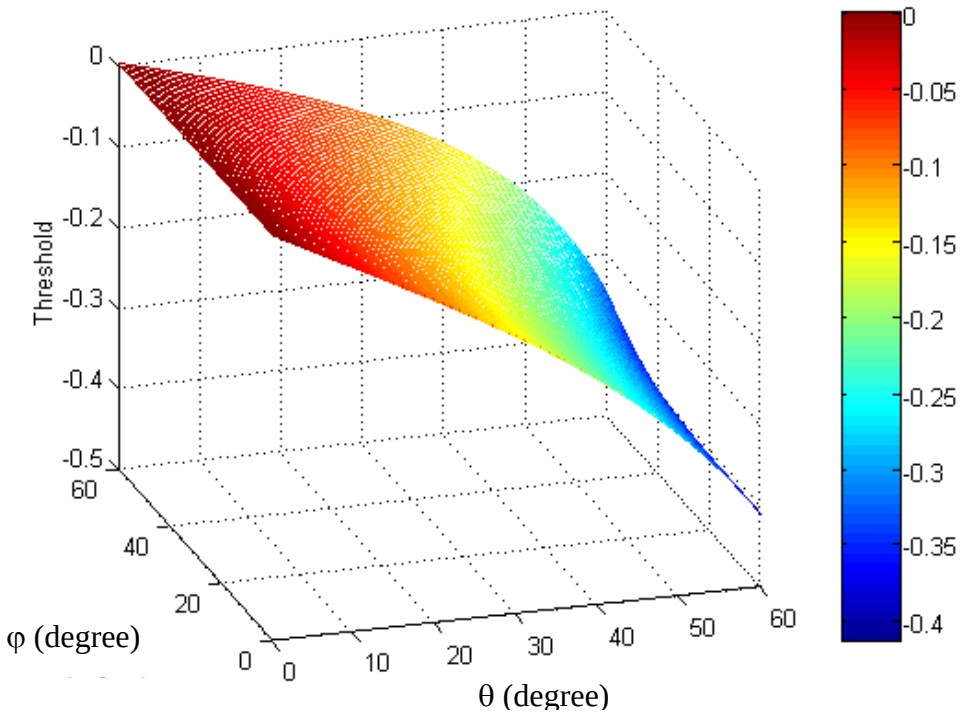

(a) Surface diagram

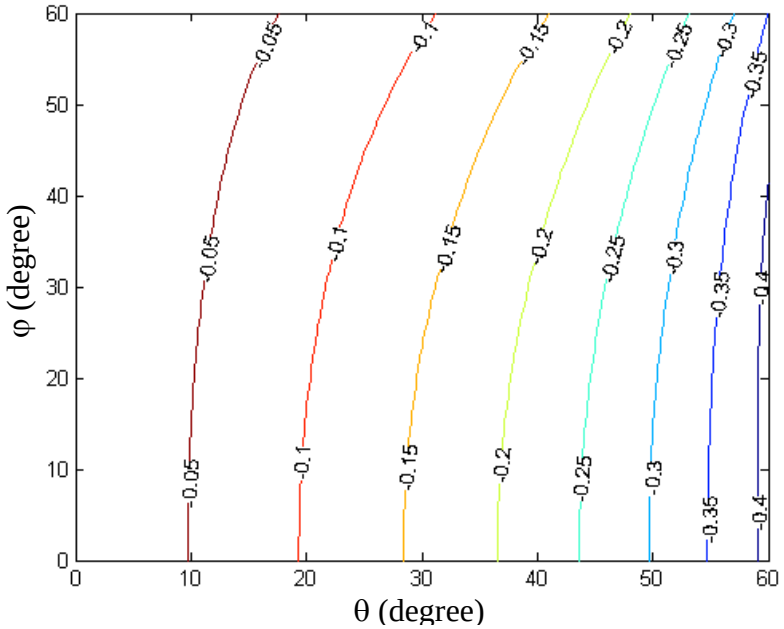

(b) Contour diagram

Figure 3-16. The Tolerance for Tip1 when Bubbles Deviated from the Probe's Axial Direction

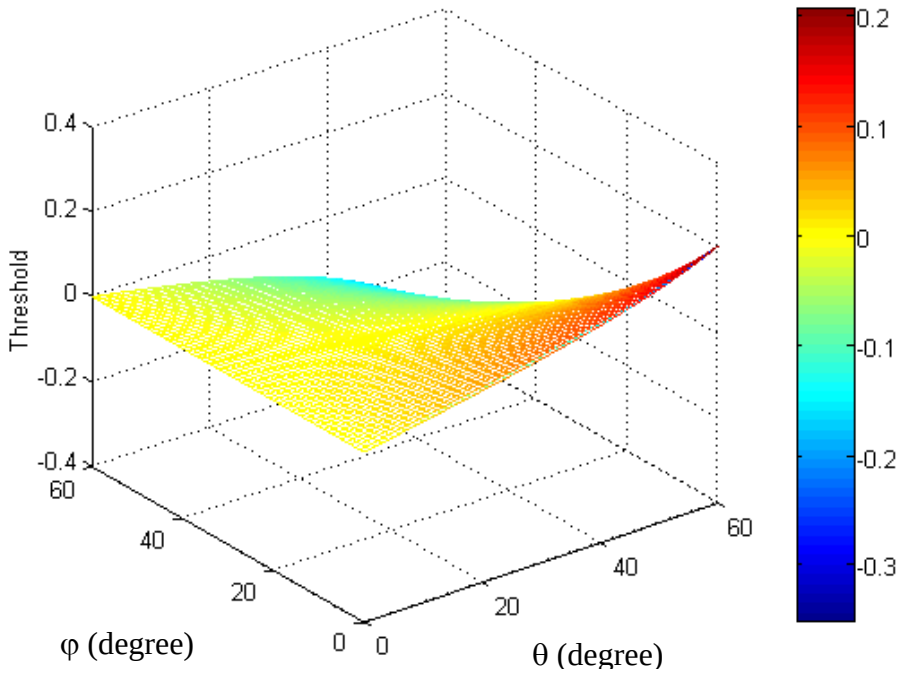

(a) Surface diagram

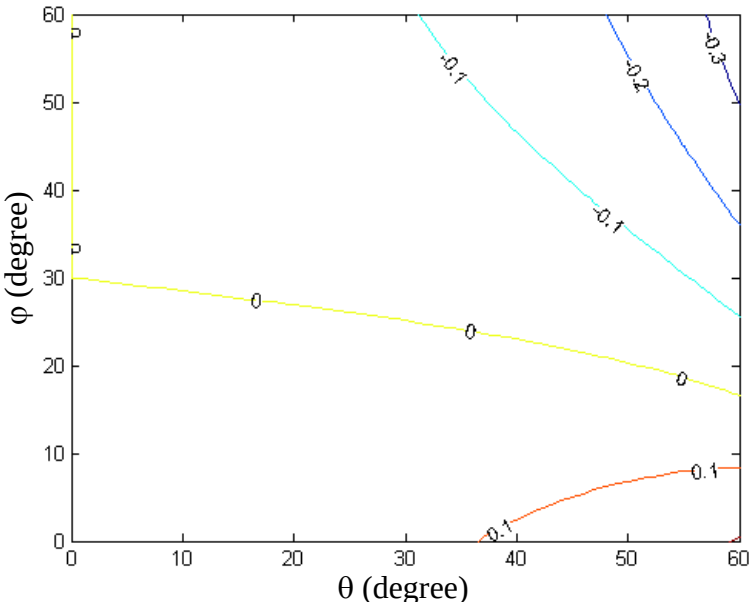

(b) Contour diagram

Figure 3-17. The Tolerance for Tip2 when Bubbles Deviated from the Probe's Axial Direction

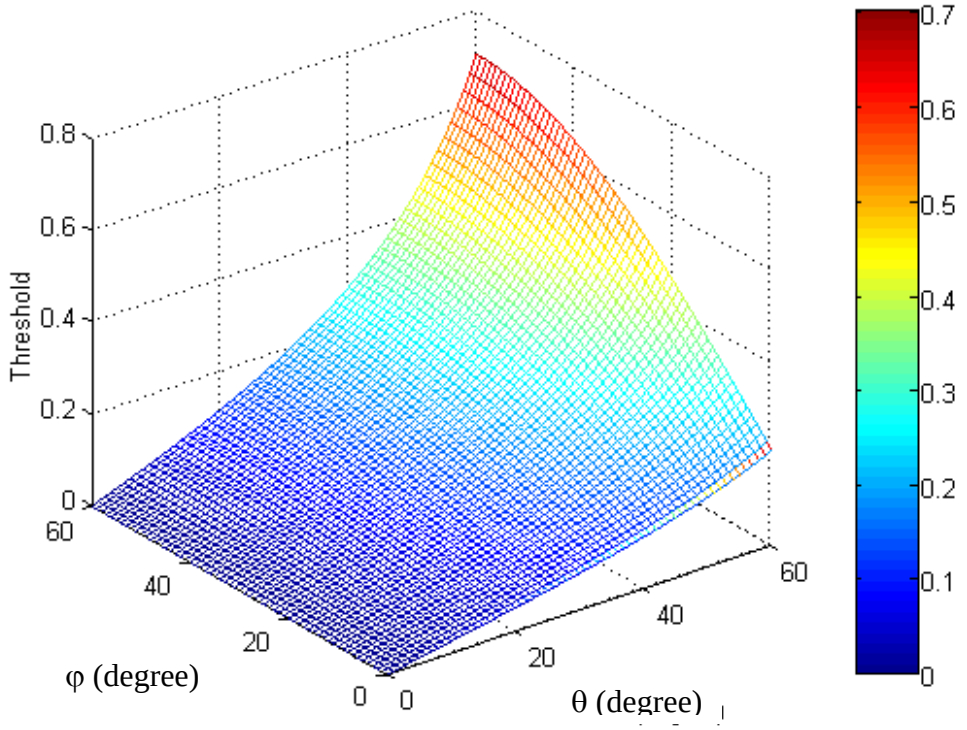

(a) Surface diagram

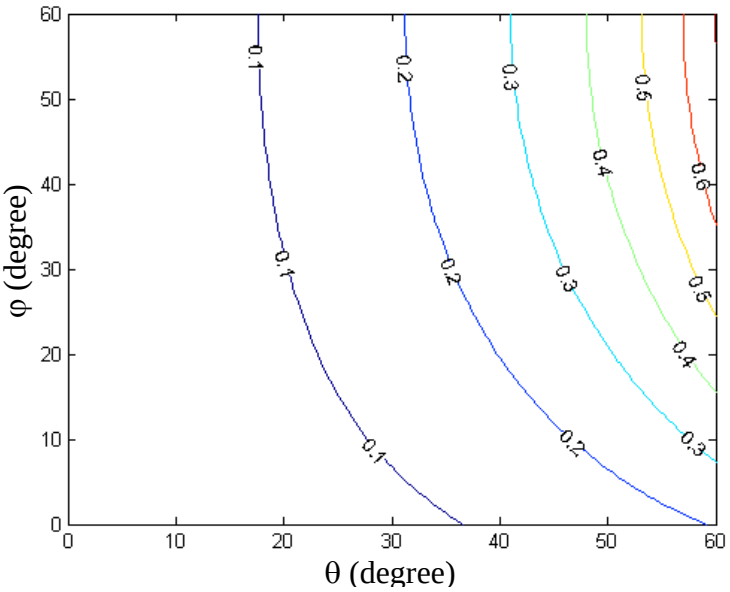

(b) Contour diagram

Figure 3-18. The Tolerance for Tip3 when Bubbles Deviated from the Probe's Axial Direction

It should be noted that the above error analysis is based on the assumption that bubbles are strictly axially symmetric, e.g., ellipsoidal bubbles, or else unpredictable errors can arise. Moreover, the definition of an irregular bubble's geometric center and centerline are meaningless. However, as we know, in bubble columns the bubbles' shapes always deviate from being strictly symmetric. Even in bubbly flow, most bubbles are not axially symmetric, as shown in Figure 3-19, let alone in transition flow and churn-turbulent flow. Due to the interaction between bubbles, usually single bubbles have a more regular shape than bubbles in clusters. At high gas holdup most bubbles are in clusters rather than moving alone. Moreover, bubbles keep fluctuating during movement, and the interaction of the bubble with the probe tip deforms the bubble shape. These factors make the bubble shape in multiphase systems, e.g., bubble columns, very difficult to define and predict. Hence, it is not wise to base the algorithm on a strict assumption of axially symmetric bubbles.

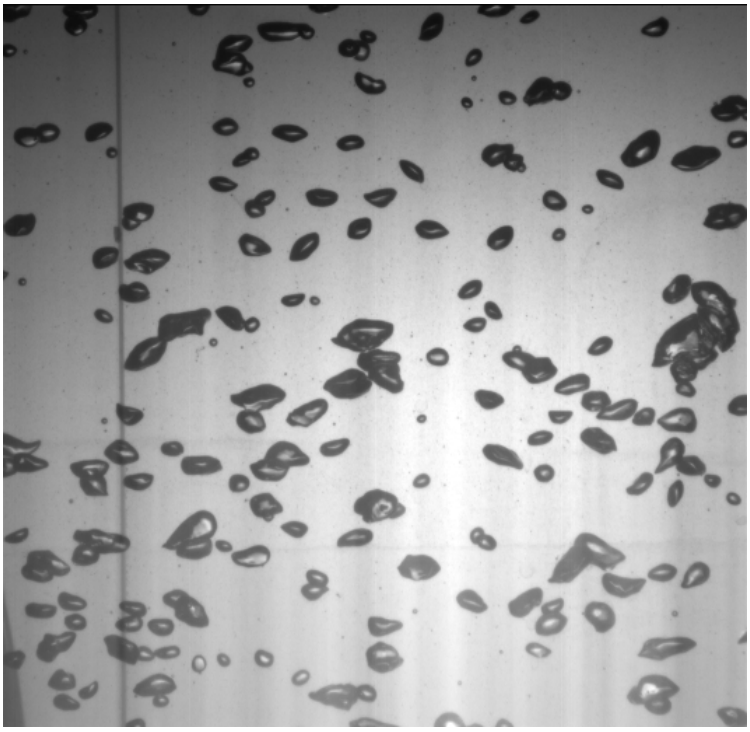

Figure 3-19. Bubbles in a 2D Bubble Column (181.5×49.0×1.3 cm) at Superficial Gas Velocity Ug=1.85 cm/s

Furthermore, the bubble selection function of this four-point optical probe needs the configuration of the probe tip to be exactly the same as that shown in Figure 3-4, i.e., three of the four tips of the probe must be of the same length and form an equilateral triangle. The fourth, central tip is positioned through the inertial center of this triangle. Due to the error in the fiber tip positioning and the stress arising during the gluing process, it is very difficult to satisfy this requirement precisely during the production of the four-point probe. In this study, most probes deviated somewhat from such exact configuration. When the three peripheral tips are not of the same length, the difference can be compensated for by measuring the distances of tips, 1, 2, and 3, from the central tip. However, by the use of the old algorithm, any deviation of the probe's four tips from the desired horizontal configuration, i.e. the central tip being positioned through the inertial center of the equilateral triangle formed by the three peripheral tips, cannot be compensated for. Such a compensation would require information on the bubble shape, e.g., the aspect ratio and size for ellipsoidal bubbles, which are the parameters that the probe was designed to measure. Hence, any deviation of the real probe from the ideal configuration is also a source of error in the bubble velocity and bubble size obtained by the old algorithm for the four-point optical probe.

Since the bubble chord length is obtained by the product of the bubble velocity and the time interval that the probe tip spends in the bubble, the error in the bubble velocity will be transferred to the bubble chord length obtained by the four-point probe. However, when the bubble velocity vector deviates from the probe's axial direction, even if the magnitude of the bubble velocity can be measured accurately, the bubble chord length pierced by the probe's central tip cannot be obtained correctly because the probe measures only the vertical component of the bubble velocity. In the case shown in Figure 3-20, the central tip of the probe passes through the central line of the bubble. The magnitude of the component of the bubble velocity vector in the probe's axial direction is $v \cdot \cos\theta$. The time interval during which the probe's central tip stays in the bubble is $\alpha a/v$ in this case, where a is the length of the major axis of the ellipsoidal bubble, and α=(length of the minor axis)/(length of the major axis) is the aspect ratio of the bubble.

The length of the bubble's minor axis is obtained as the product of these two values, i.e., $\alpha a \cdot \cos\theta$, by the existing algorithm. This value is actually the length OB in Figure 3-20, which is different from the length of the bubble's minor axis OA. Actually the length OB is physically meaningless.

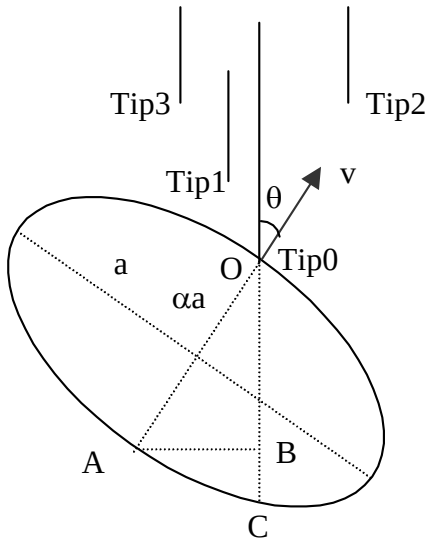

Figure 3-20. Bubble Chord Length Measured by the Probe

To sum up:

(1) The deviation of the bubble velocity vector from the probe's axial direction can cause errors in the bubble velocity and bubble size obtained by the four-point optical probe. Although the bubble selection criterion δv in Equation (3-11b) can ensure that bubbles whose velocity vectors deviate significantly from the probe's axial direction are discarded, thus reducing the magnitude of the errors caused by the deviation of the bubble velocity vector from the probe's axial direction, the application of this four-point probe in bubble columns is still not satisfactory.

(2) The original algorithm requires the bubble shape to be axially symmetric, which is far from the physical reality in bubble columns, especially in the transition and churn-turbulent flow regime.

(3) It is technically difficult to configure the probe tips accurately as required by the old algorithm.

(4) As a result of the bubble selection function of the four-point probe, only a small percentage of bubbles are measured by the probe. By selecting bubbles that hit the probe, a specific population of bubbles (e.g., bubbles moving in the probe's axial direction) in bubble columns is used to determine the bubble velocity and size distribution, instead of the whole bubble population. However, there is no firm theoretical or experimental proof which assures that the velocity and size of the whole bubble population are similar to that of this specific bubble population. Most likely, they are not similar.

To solve the problems described above, an appropriate modification of the data processing algorithm of the four-point probe is developed. This modification is described in the next section.

3.3 New Data Processing Algorithm for the Four-Point Probe

A new data processing algorithm capable of determining both the magnitude and the direction of the bubble velocity vector is proposed and developed. Moreover, the specific interfacial area now can also be determined directly from the probe's response.

To determine the bubble velocity vector, its magnitude, v, and direction angles, θ and φ (refer to Figure 3-21b), need to be measured. Hence, three equations including these three variables are needed to obtain the bubble velocity vector. If a four-point probe is considered as being comprised of three two-point probes in different directions (Figure 3-21a), the responses of the three two-point probes that comprise a four-point probe provide these three needed equations.

Figure 3-21b shows the geometry when a bubble hits the probe at an angle θ to the probe's axial direction. Assume that the bubble is ellipsoidal and the bubble velocity vector is perpendicular to the symmetry plane of the bubble (the plane formed by the major axes of the bubble). To set up the equations that describe the physical situation, the coordinate transformation shown in Figure 3-14 is made. The xyz coordinate system is transformed to x'y'z' system with its z'-axis in the direction of the bubble velocity vector. The relationship between coordinates x', y', z' and x, y, z is explained in Equation (3-13). After this coordinate transformation, the z' coordinates of the four probe tips are:

$$\text{Tip0}: z_0' = 0$$
$$\text{Tip1}: z_1' = x_1 \cdot \sin\theta\cos\varphi + y_1 \cdot \sin\theta\sin\varphi + z_1 \cdot \cos\theta$$
$$\text{Tip2}: z_2' = x_2 \cdot \sin\theta\cos\varphi + y_2 \cdot \sin\theta\sin\varphi + z_2 \cdot \cos\theta$$
$$\text{Tip3}: z_3' = x_3 \cdot \sin\theta\cos\varphi + y_3 \cdot \sin\theta\sin\varphi + z_3 \cdot \cos\theta$$

where the coordinates of the probe tips in the xyz coordinate system shown in Figure 3-21b are Tip0 (0, 0, 0), Tip1 (x_1, y_1, z_1), Tip2 (x_2, y_2, z_2), Tip3 (x_3, y_3, z_3), respectively.

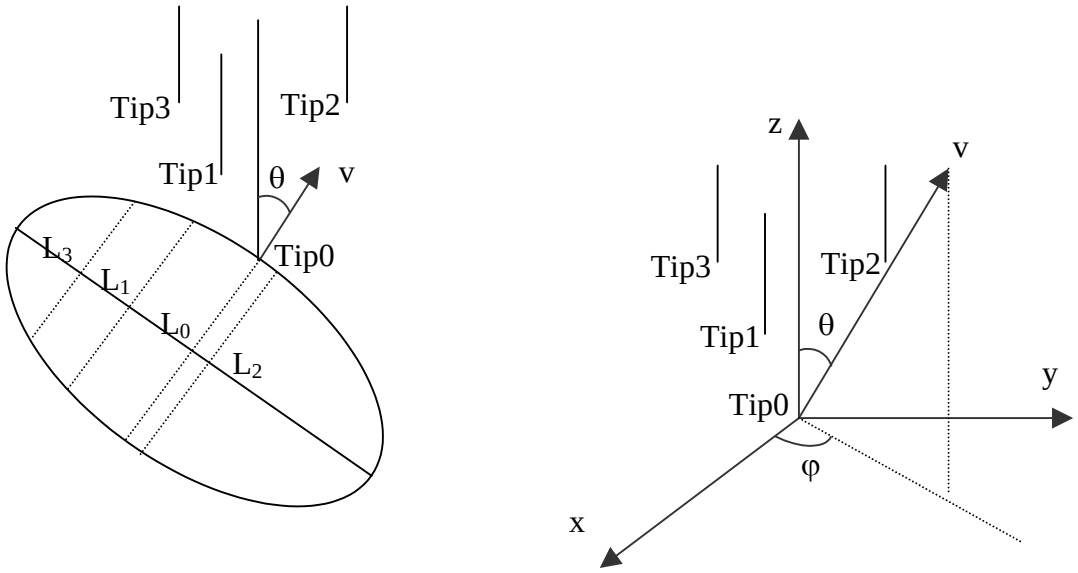

(a) **(b)**

Figure 3-21. Schematic of the Principle of the New Data Processing Algorithm

Notice that the z_i' coordinate value of Tip i, i=1,2,3, is the distance between Tip i and Tip0 in the direction of the bubble velocity vector (Figure 3-21). Accounting for the curvature correction (explained in Section 3.1, Figure 3-2), the time intervals between the instant when a bubble hits the central tip, Tip0, and when it hits Tip i, i=1,2,3 are:

$$\Delta t_1 - \frac{T_0 - T_1}{2} = \frac{x_1 \cdot \sin\theta\cos\varphi + y_1 \cdot \sin\theta\sin\varphi + z_1 \cdot \cos\theta}{v} \tag{3-18a}$$

$$\Delta t_2 - \frac{T_0 - T_2}{2} = \frac{x_2 \cdot \sin\theta\cos\varphi + y_2 \cdot \sin\theta\sin\varphi + z_2 \cdot \cos\theta}{v} \tag{3-18b}$$

$$\Delta t_3 - \frac{T_0 - T_3}{2} = \frac{x_3 \cdot \sin\theta\cos\varphi + y_3 \cdot \sin\theta\sin\varphi + z_3 \cdot \cos\theta}{v} \tag{3-18c}$$

This group of nonlinear equations for v, θ and φ does not yield analytical solutions. The equations need to be solved numerically, e.g., with a Newton-Raphson algorithm. As a result, the velocity magnitude, v, and the direction angles, θ and φ, of the bubble velocity vector are obtained. Based on these values, the bubble chord length pierced by Tip i, L_i, i=0, 1, 2, 3, can be obtained by:

$$L_i = v \cdot T_i \tag{3-19}$$

The chord length distribution obtained by the probe then needs to be transformed to the 'equivalent' bubble diameter distribution. Liu et al. (1996, 1998) developed an algorithm to transform the bubble chord length distribution obtained by a two-point probe to the bubble size distribution when bubbles are spherical, ellipsoidal or truncated ellipsoidal. To use this algorithm, the aspect ratio of the bubbles, α=(length of minor axis)/(length of major axis), in the system needs to be known or assumed in advance. Usually α is empirically set as a single value. However, in bubble columns α is not a single value but a distribution, and there is no way to estimate the mean aspect ratio in advance. Hence, this oversimplification may cause large errors in the transformation of bubble chord length distribution to bubble size distribution. Besides, Liu's algorithm is very sensitive

to errors in the bubble chord length distribution, i.e., small changes in the bubble chord length distribution obtained may cause significant changes in the bubble size distribution calculated. Hence, Liu's algorithm for the transfer of the bubble chord length distribution to the bubble diameter distribution is not really applicable to bubble columns. So far, there is no other reported algorithm for the transformation of the bubble chord length distribution to the bubble size distribution.

As to the four-point optical probe, after the bubble chord lengths are obtained, theoretically the bubble size can be calculated based on the assumption of the bubble shape. The algorithm is explained below, and is valid not only for ellipsoidal bubbles but also for any bubble whose shape can be expressed mathematically. Assume that the bubble is ellipsoidal, with the minor axis as the revolution axis, as shown in Figure 3-22a. The equation of the ellipsoid in Figure 3-22b is $y^2 + \alpha^2 x^2 = \alpha^2 c^2$, where α is the aspect ratio and c is a half of the length of the major axis. From Figure 3-22b it can be seen that in the above equation x is the distance between the chord pierced by the probe's tip to the bubble's center O, i.e., the length OC, and y equals half of the chord length, $L_i/2$.

The four bubble chord lengths obtained by the four tips of the probe give four equations:

$$\left(\frac{L_0}{2}\right)^2 + \alpha^2\left[(x_0' - x_c)^2 + (y_0' - y_c)^2\right] = \alpha^2 c^2 \qquad (3\text{-}20a)$$

$$\left(\frac{L_1}{2}\right)^2 + \alpha^2\left[(x_1' - x_c)^2 + (y_1' - y_c)^2\right] = \alpha^2 c^2 \qquad (3\text{-}20b)$$

$$\left(\frac{L_2}{2}\right)^2 + \alpha^2\left[(x_2' - x_c)^2 + (y_2' - y_c)^2\right] = \alpha^2 c^2 \qquad (3\text{-}20c)$$

$$\left(\frac{L_3}{2}\right)^2 + \alpha^2\left[(x_3' - x_c)^2 + (y_3' - y_c)^2\right] = \alpha^2 c^2 \qquad (3\text{-}20d)$$

Here, x_c' and y_c' are the coordinates of the bubble's center O in the x'y'z' coordinate system, and x_i', y_i', i=0, 1, 2, 3, are the coordinates of Tip i in the x'y'z' coordinate system (refer to Figure 3-14), which can be calculated as:

$$x_i' = \cos\theta\cos\varphi \cdot x_i + \cos\theta\sin\varphi \cdot y_i - \sin\theta \cdot z_i \quad (3\text{-}21a)$$

$$y_i' = -\sin\varphi \cdot x_i + \cos\varphi \cdot y_i \quad (3\text{-}21b)$$

The bubble size and aspect ratio can then be obtained by solving equations (3-20a-d).

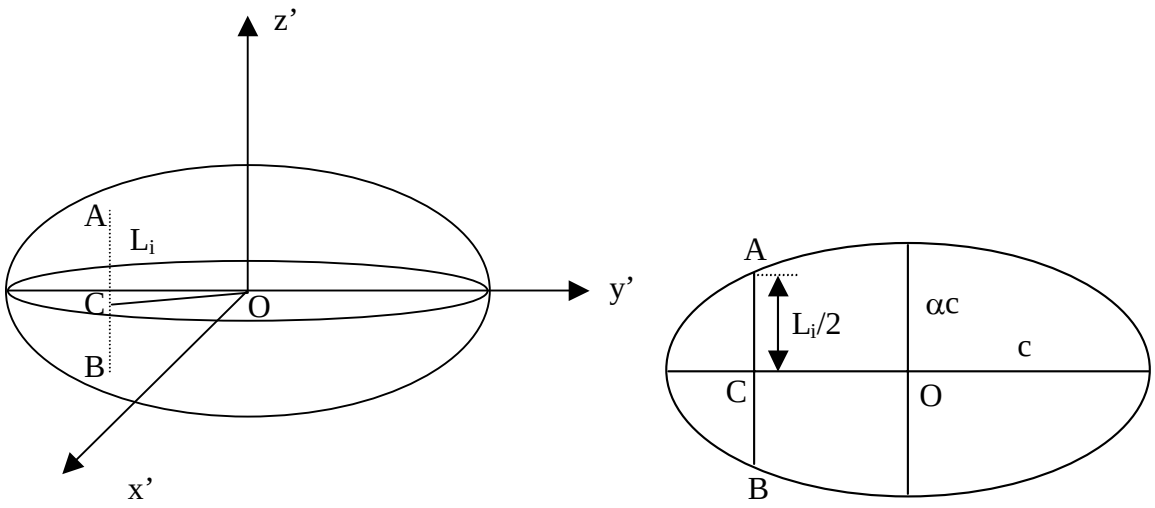

(a) **(b)**

Figure 3-22. Determination of the Bubble Size and Aspect Ratio

The advantage of this transformation algorithm over the methods suggested by Liu et al. (1996, 1998) is that the aspect ratio of the bubble, α, can be obtained experimentally instead of being assumed. This is important, since as mentioned above it may cause large errors to set α as a single value.

Unfortunately, the measurements in a 2D bubble column conducted in this study show that the proposed algorithm based on solution of Equations (3-20a-d) does not give an accurate estimate of either bubble size or aspect ratio (Appendix F). It was found that the

algorithm always underestimates the bubble aspect ratio, and is very sensitive to changes of the bubble chord lengths obtained by the probe, i.e., small changes in the bubble chord lengths may cause large variations in the calculated bubble size and aspect ratio. In 3D bubble columns, the shape of bubbles deviates much more from ellipsoidal than in the 2D bubble column at very low gas holdup. Hence, it is expected that the error in the bubble sizes and aspect ratios obtained by the four-point probe will be even larger in 3D bubble columns. As a result, this method is not recommended to investigate the bubble size and shape in bubble columns. Instead, the bubble chord length distributions obtained by the four-point probe were used to gain information on the bubble size distribution in bubble columns, e.g., to determine whether the bubble size distribution in churn-turbulent flow is bimodal or single modal.

One of the assumptions for all of the above analysis is that the bubble velocity vector aligns with the bubble orientation. Usually this is true, due to the balance of the forces on bubbles and the shape flexibility of gas bubbles. However, when the bubble's motion direction changes significantly as sometimes in churn-turbulent flow, it was observed that the bubble velocity vector might deviate from the normal vector of the bubble's symmetry plane by an angle, ϕ, as shown in Figure 3-23a. This deviation may cause errors in the bubble velocity vector and bubble chord length obtained by the four-point optical probe.

From Figure 3-23c, it can be derived that the time intervals between the instant when a bubble hits the central Tip0 and when it hits Tipi, i=1,2,3 are:

$$\Delta t_1 - \frac{T_0 - T_1}{2} = \frac{z_1' / \cos\phi}{v} = \frac{x_1 \cdot \sin\theta\cos\varphi + y_1 \cdot \sin\theta\sin\varphi + z_1 \cdot \cos\theta}{v \cdot \cos\phi} \tag{3-22a}$$

$$\Delta t_2 - \frac{T_0 - T_2}{2} = \frac{z_2' / \cos\phi}{v} = \frac{x_2 \cdot \sin\theta\cos\varphi + y_2 \cdot \sin\theta\sin\varphi + z_2 \cdot \cos\theta}{v \cdot \cos\phi} \tag{3-22b}$$

$$\Delta t_3 - \frac{T_0 - T_3}{2} = \frac{z_3' / \cos\phi}{v} = \frac{x_3 \cdot \sin\theta\cos\varphi + y_3 \cdot \sin\theta\sin\varphi + z_3 \cdot \cos\theta}{v \cdot \cos\phi} \tag{3-22c}$$

where θ is the angle between the normal vector (vector $\vec{n}$ in Figure 3-23b) of the bubble's symmetry plane to the probe's axial direction, and φ is the angle between the projection of the normal vector on the xy plane and the x axis (Figure 3-23b). As shown in Figure 3-23b, the xyz coordinate system is transformed to x'y'z' system with its z'-axis in the direction of the bubble's normal vector, $\vec{n}$.

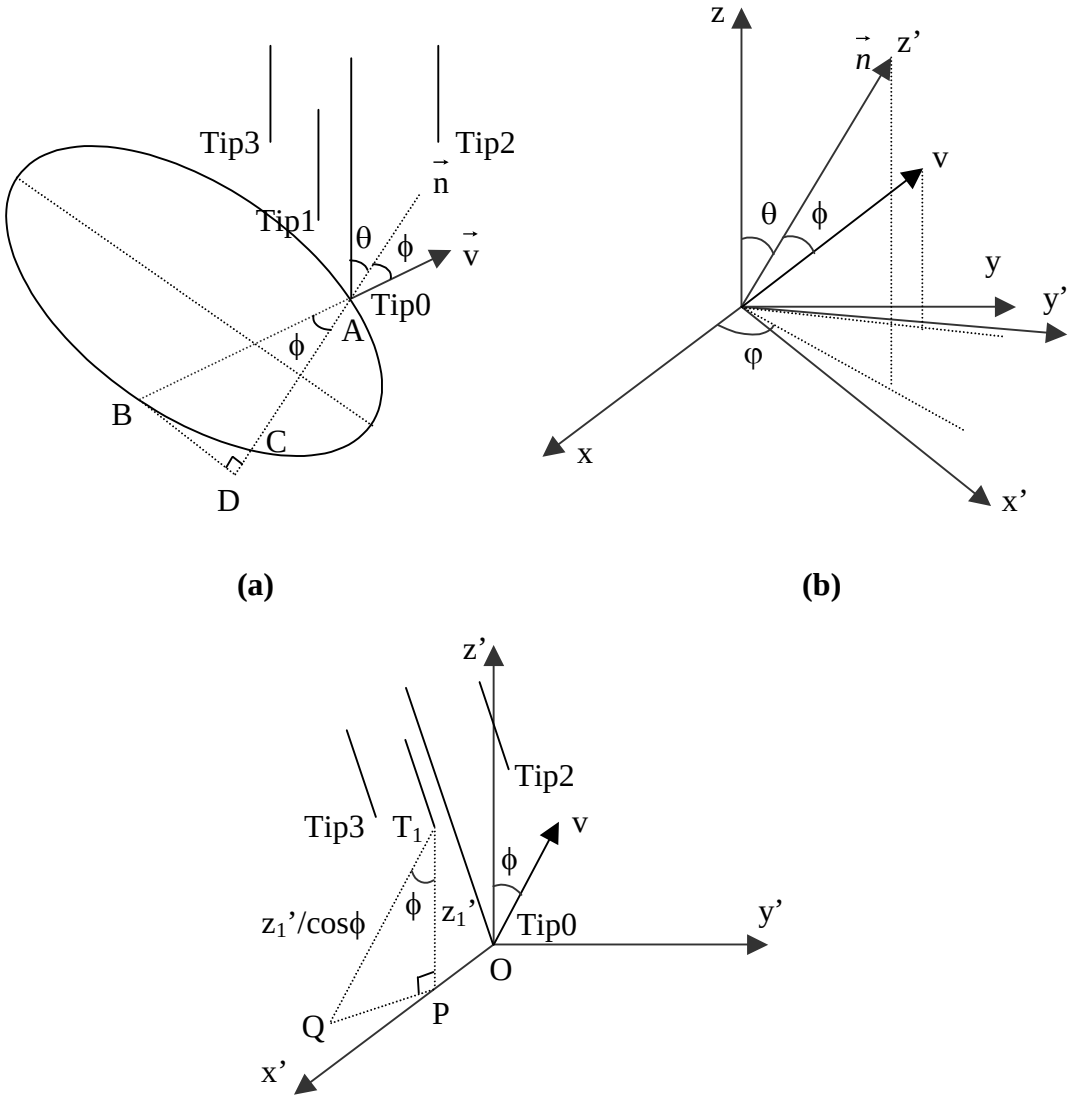

Figure 3-23. The Physical Situation of the Bubble Velocity Measurements

Since there are only three equations (equations 3-22a, 3-22b, 3-22c) for four variables, i.e., v, θ, φ and ϕ, what can be obtained is θ, φ and $v \cdot \cos\phi$ instead of v and ϕ separately. Correspondingly, the chord length obtained by the probe is $v \cdot T_i \cdot \cos\phi$. In cases of Figure 3-23a, the chord length from the point where the probe's central tip hits the bubble's surface, A, is AC, but $v \cdot T_0 \cdot \cos\phi$ is actually the length AD. Hence, in the case where the bubble velocity vector does not align with the bubble's orientation, the determined bubble velocity vector and bubble chord length contain a systematic error. However, the error is small when the value of ϕ is small.

Lim and Agarwal (1992) found that in a 2-D fluidized bed ϕ had a normal distribution with a mean of zero and standard deviation of 14^o. This fact implies that the bubble velocity aligns with the bubble orientation with a small variation. Since $\cos(14^o)=0.97$, the standard deviation of 14^o implies that the error in the bubble velocity due to ϕ is small. Kataoka, Ishii and Serizawa (1986) adopted an upper limit of 10^o~22^o for ϕ under different operating conditions in air-water bubbly and slug flow in a vertical tube of inner diameter of 6 cm. At $\phi=22^o$, $\cos\phi=0.927$. Hence, it is expected that the error in the bubble velocity magnitude due to the deviation of the bubble velocity vector from the bubble orientation is small, and the bubble velocity vector and bubble chord length obtained by Equation (3-18) and (3-19) are reliable. Coincidentally, Equation (3-22) provides a way to calculate the specific interfacial area as explained below.

Kataoka, Ishii and Serizawa (1986) derived the equation for the specific interfacial area, a, in gas-liquid systems as:

$$a = \frac{1}{\Delta T} \cdot N \cdot \overline{\frac{1}{\left|\vec{v}\right| \cdot \cos\phi}} = \frac{1}{\Delta T} \cdot \sum_N \frac{1}{v \cdot \cos\phi} \qquad (3\text{-}23)$$

where N is the total number of the gas-liquid interfaces passing by the probe during the measurement time ΔT, and ϕ is the angle between the velocity vector and the normal vector of the gas-liquid interface (e.g., the bubble's surface).

Based on Equation (3-23), the four-point optical probe can be employed to obtain the specific interfacial area. The physical situation is shown in Figure 3-24. Assume that the gas-liquid interface (bubble surface) section between the three tips, Tip1, Tip2 and Tip3, of the probe (Figure 3-24a) is flat. Considering the small size of the probe tip (1.2 mm in diameter), this is a reasonable assumption except when the probe hits a gas-liquid interface with large curvature, e.g., bubbles of very small horizontal dimension.

Note that the bubble leading edges and trailing edges both should be accounted for in the specific interfacial area, and the curvature correction mentioned above (Figure 3-2) is unnecessary (that curvature correction is valid only for measurements of the velocity of the bubble's centroid instead of the velocity of the bubble surface section).

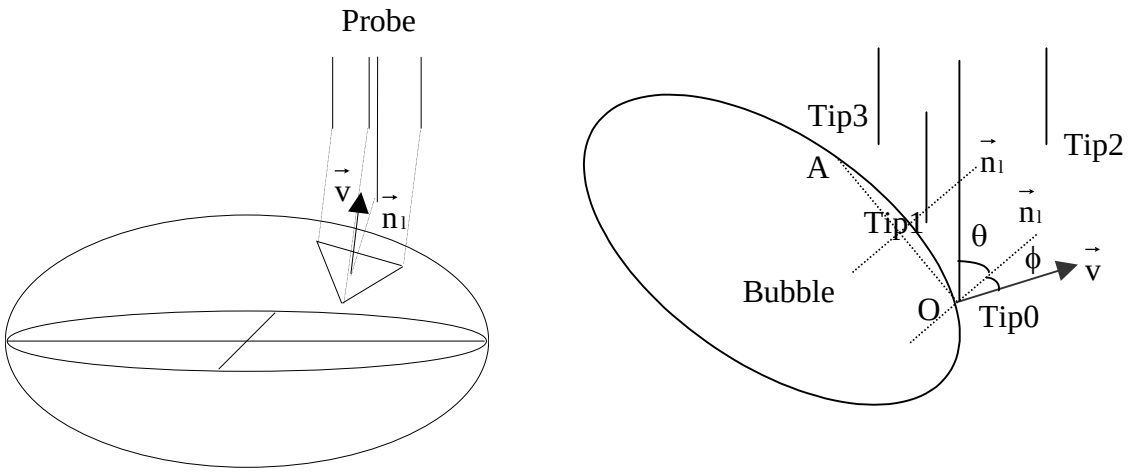

(a) **(b)**

Figure 3-24. The Physical Situation of Measurements of the Specific Interfacial Area by the Four-Point Probe

The equations to determine the velocity of the bubble surface section are:

$$\Delta t_1 = \frac{z_1' / \cos\phi}{v} = \frac{x_1 \cdot \sin\theta\cos\varphi + y_1 \cdot \sin\theta\sin\varphi + z_1 \cdot \cos\theta}{v \cdot \cos\phi} \tag{3-24a}$$

$$\Delta t_2 = \frac{z_2' / \cos\phi}{v} = \frac{x_2 \cdot \sin\theta\cos\varphi + y_2 \cdot \sin\theta\sin\varphi + z_2 \cdot \cos\theta}{v \cdot \cos\phi} \tag{3-24b}$$

$$\Delta t_3 = \frac{z_3' / \cos\phi}{v} = \frac{x_3 \cdot \sin\theta\cos\varphi + y_3 \cdot \sin\theta\sin\varphi + z_3 \cdot \cos\theta}{v \cdot \cos\phi} \tag{3-24c}$$

By solving these three equations numerically, the value of $v \cdot \cos\phi$ can be obtained, which can then be used to obtain the specific interfacial area from Equation (3-23). However, if a bubble hits the central tip of the probe but misses some of the three peripheral tips, then the bubble surface velocity vector cannot be obtained, due to the insufficient number of equations, although this bubble contributes to the specific interfacial area at the probe's central tip. To account for the contribution of these "missed" bubbles, the average value of $v \cdot \cos\phi$ of bubbles that pass all the four tips of the probe will be assigned to these "missed" bubbles. Hence, the equation for the calculation of specific interfacial area is:

$$a = \frac{1}{\Delta T} \cdot \sum_{N} \frac{1}{v \cdot \cos\phi} \cong \frac{1}{\Delta T} \cdot \frac{N}{N_{measured}} \sum_{N_{measured}} \frac{1}{v \cdot \cos\phi} \tag{3-25a}$$

$$N = N_{measured} + N_{missed} \tag{3-25b}$$

Equations (3-24) and (3-25) do not need assumptions about bubble shape. Thus, errors due to the inaccuracy in the bubble shape assumption can be avoided, leading to a robust algorithm.

In churn-turbulent flow, the shape of many bubbles is highly irregular, and cannot be described as any simple geometric shape, especially for large bubbles. Nevertheless, the Sauter mean bubble diameter (the volume-surface mean diameter of bubbles) as shown in

Equation (2-2) is widely employed to describe the bubble size. To obtain the Sauter mean diameter, bubbles' volumes need to be measured. However, it is impossible to obtain the bubble volume accurately with the current techniques. Hence, another way is needed to derive the Sauter mean diameter.

With the simplification of assuming spherical bubbles, the gas-liquid interfacial area can be related to the gas holdup, ε_g, and the Sauter mean diameter, d_s, as given by Equation (2-1). With the local specific interfacial area and gas holdup obtained by the four-point probe, the Sauter mean bubble diameter at different positions in bubble columns can be calculated by Equation (2-1). However, this should be treated only as a rough estimate of bubble size.

In conclusion, the advantages of this new data processing algorithm over the old one are:

(1) Both the magnitude and the direction of the bubble velocity vector can be obtained.

(2) The probe does not need to be aligned with the flow direction at different positions to ensure the accuracy of measurements.

(3) There is no selection of bubbles that hit the probe moving in the probe's axial direction. Hence the whole bubble population in bubble columns is used to determine the bubble velocity distribution and bubble chord length distribution, instead of just a specific population of bubbles (e.g., bubbles moving in the probe's axial direction).

(4) The specific interfacial area can be obtained in a simple way.

(5) Sauter mean bubble diameter can be reported based on sphericity assumption.

Chapter 4 Validation of Measurements by the Four-Point Optical Probe

There are many additional factors, not previously discussed, that affect the measurements of bubble properties by the four-point optical probe in multiphase systems. For example, when a bubble hits a probe tip, the interaction between the probe tip and the bubble dents the bubble's leading edge. The extent of the interaction and the dent depend on the physical properties of the liquid phase (surface tension, viscosity, polarity, and density), the properties of the probe (material, size, shape), the bubble velocity, and the bubble size. Hence, before the probe can be applied in actual bubble columns the probe measurements of bubble velocity distribution, bubble chord length distribution, local gas holdup, and specific interfacial area must be validated.

The validation of the probe is accomplished by comparing the local gas holdup, bubble velocity, and specific interfacial area obtained by the probe with those obtained by CCD cameras in the validation setups, e.g., a 2D bubble column. The measurements by the camera are believed to be accurate under these simple conditions. This chapter presents the validation results for the four-point optical probe in an air-water system. Since the deformation of bubbles when they hit the probe also depends on the physical properties of the liquid phase, it may be necessary to revalidate the probe specifically in liquids whose physical properties are very different from water, e.g., some organic systems.

4.1 Validation of the Bubble Velocity Vector

Two CCD cameras were employed to perform the video imaging analysis. The CA-D6-0256ECEW camera by DALSA provides a resolution of 260×260 pixels and a very high frame rate up to 955 frames per second (fps). The CA-D6-0256W camera provides a better resolution of 532×516 pixels and a frame rate up to 262 fps. The frame grabber and

the imaging processing software used are the PIXCI D32 and XCAP by EPIX, respectively. Two setups were used to validate the bubble velocity obtained by the four-point optical probe. Figure 4-1 shows the first experimental setup, in which a bubble train is generated via a capillary that is placed at the bottom of a rectangular container filled with tap water. The optical probe is placed about 2 cm above the capillary exit where bubbles move vertically (i.e., bubble wobbling has not caused too much deviation from a vertical trajectory). The probe tip is horizontally positioned at the center of the bubble train so that the central tip of the probe pierces the bubble in the direction of the minor axis (Figure 4-2). The bubbles' hitting the probe tip are filmed from the side (Figure 4-1). The velocity of bubbles in the same bubble train is almost identical. By using capillaries of different diameter, bubbles of different velocities and sizes can be generated.

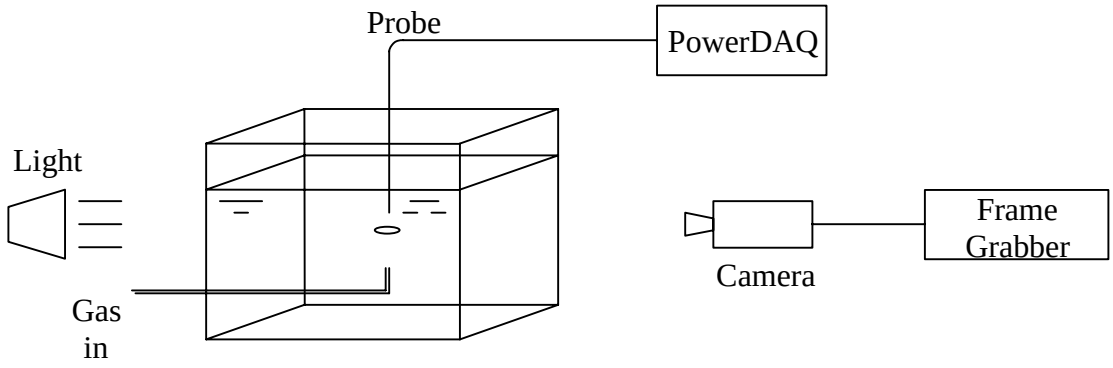

Figure 4-1. The Calibration Setup

A series of images that illustrate the process of a bubble approaching and hitting the probe tip are shown in Figure 4-2. In this case the vertical velocity of bubbles is 24.6 cm/s, and the horizontal and vertical dimensions are 2.0 mm and 5.7mm, respectively. It can be seen that the bubble shape fluctuated greatly during its ascendance. Although it is hard to distinguish the bubble shape fluctuation and the deformation caused by the interaction with the probe tip, it can be estimated that the extent of the deformation due to the probe is much smaller than the natural bubble shape fluctuation.

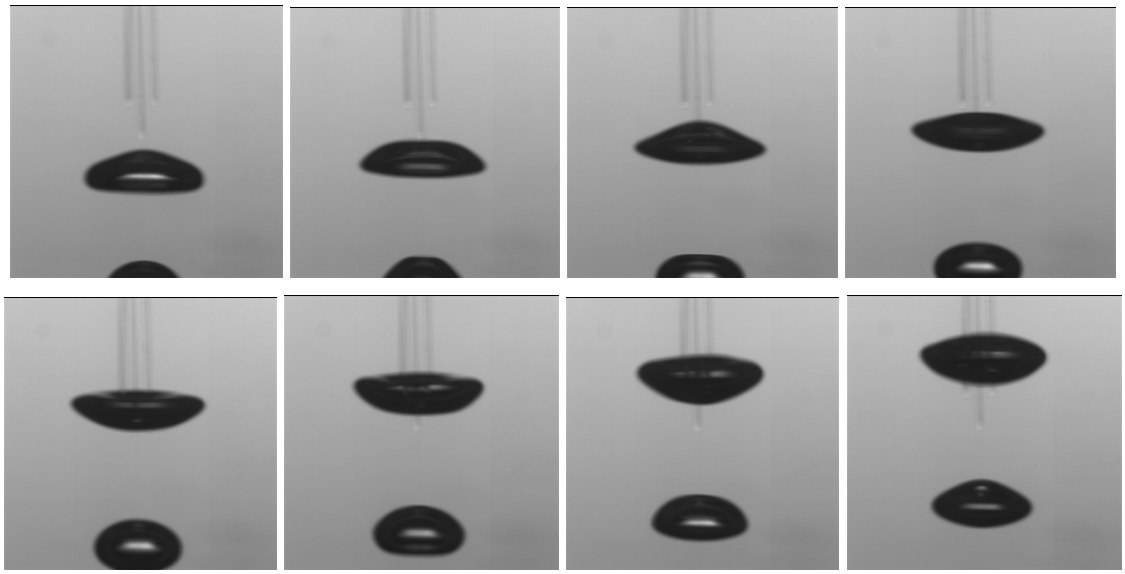

Figure 4-2. Bubble Hits the Probe Tip (field of view 1.3cm×1.3cm)

It was confirmed by video imaging that there was no obvious change in the bubble velocity in this single bubble train case when a bubble was pierced by the probe tip in the range of bubble velocities and bubble sizes studied (22.1~27.4 cm/s and 2.6~3.1 mm in volume equivalent diameter, respectively). This is illustrated in Figure 4-3. The same conclusion was reached by Mudde and Saito (2001).

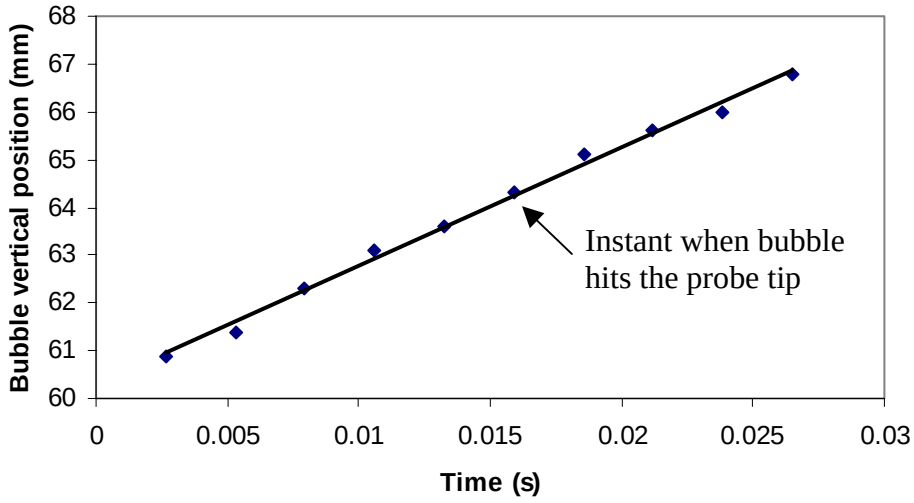

Figure 4-3. Influence of Probe and Bubble Interaction on Bubble Velocity

Examples of the bubble velocity and chord length obtained by the four-point probe and by the camera for each bubble in bubble trains of different velocities and sizes are shown in Figure 4-4. The relative errors between measurements by the probe and by the camera are also listed in Figure 4-4.

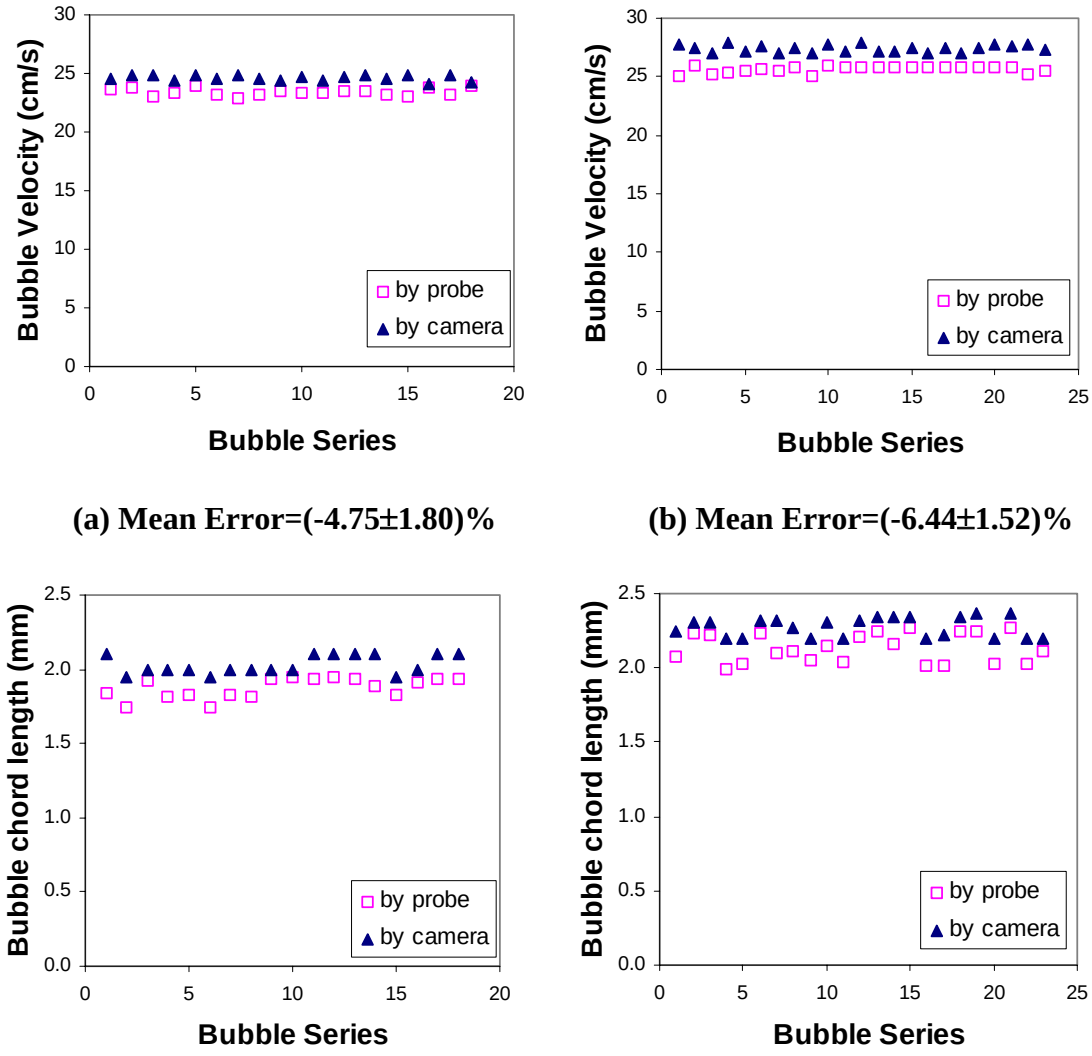

(a) Mean Error=(-4.75±1.80)% **(b) Mean Error=(-6.44±1.52)%**

(c) Mean Error=(-7.7±2.68)% **(d) Mean Error=(-6.18±2.18)%**

Figure 4-4. Comparison of Bubble Velocity and Bubble Chord Length

Error = (value by probe- value by camera)/ value by camera × 100%

As shown in Figure 4-4, it was found that the bubble velocity and chord length obtained by the four-point probe were always smaller than those obtained by the camera. This is possibly due to the deformation of the bubble leading edge by the probe tip, since it has been shown that hitting the probe tip does not slow down the bubble. The relative errors in the bubble velocity and chord length obtained by the four-point probe are within –10% in the range of bubble velocity and bubble size studied (i.e., 22.1~27.4 cm/s and 2.6~3.1 mm in volume equivalent diameter, respectively). Hence, the bubble velocity and bubble chord length obtained by the four-point probe are reliable in this single bubble train case.

The single bubble train case, as described above, is quite simple compared to the situation in bubble columns. Hence, the validation of the bubble velocity and specific interfacial area obtained by the four-point optical probe were also conducted in a transparent 2D bubble column. The configuration of this second setup was shown in Figure 4-5. The dimensions of the 2D bubble column are 181.5(h)×49.0(w)×1.3(d) cm. The gas distributor has 16 holes with diameter of 1.0 mm, evenly distributed in a line. The probe was positioned in the centerline of the column, 96.8 cm above the distributor. When validating the probe, in most cases a bubble stream was generated in the 2D bubble column using a single gas nozzle instead of the gas distributor. The single gas nozzle was introduced into the bubble column through a connector, and was about 57 cm below the four-point probe tip (refer to Figure 4-5).

The reasons for using the single gas nozzle to generate bubbles instead of the gas distributor are:

(1) The imaging analysis software can recognize only a portion of the total bubbles and measure their velocity in 2D bubble columns. This is because bubbles of larger velocity tend to form clusters that cannot be recognized by the imaging processing software due to the overlap, coalescence, and dispersion of bubbles. Hence, bubbles that move in clusters, which are of higher velocity, cannot be distinguished separately by the imaging processing software and were not measured. This omission causes errors in the bubble

velocity distribution and mean bubble velocity obtained by the camera. Hence, the imaging method can be applied only at very low gas velocity, in which case the gas holdup is very low and bubbles are sparse. However, at very low gas velocity bubbles were generated at only a portion of the holes on the gas distributor, and the generation of bubbles usually is not continuous.

(2) Bubbles of different sizes can be generated using gas nozzles of different sizes so that the probe validation can cover a range of bubble size and velocity. This is impossible using the gas distributor.

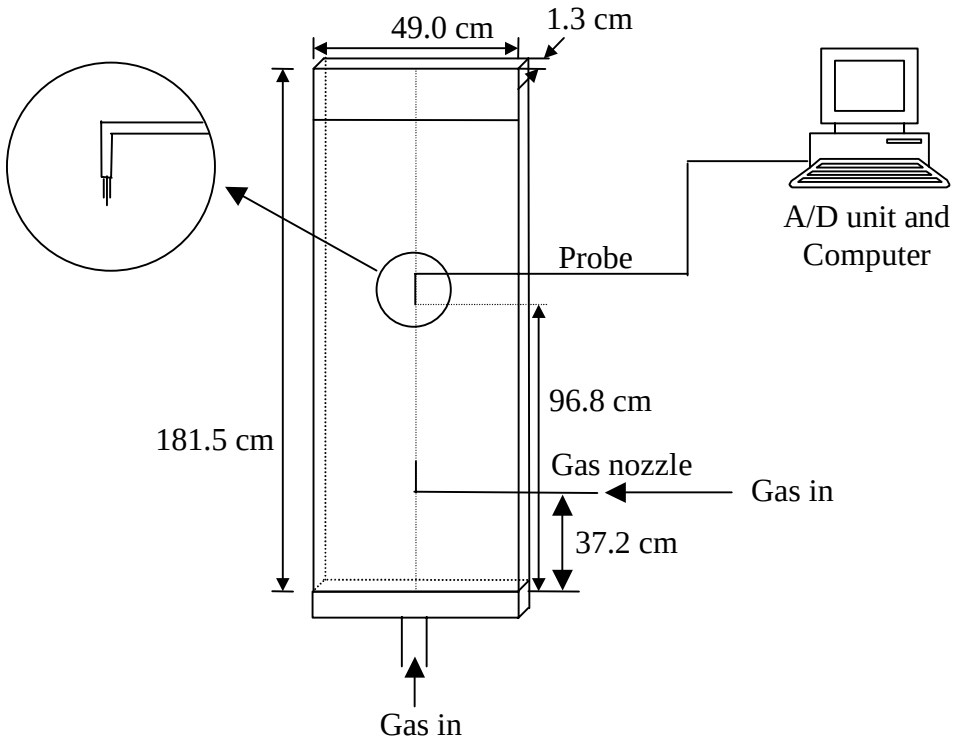

Figure 4-5. Setup of the 2D Bubble Column for the Probe Validation

In this 2D bubble column, the bubble velocity distribution and the mean bubble velocities obtained by the probe and by the camera were compared, instead of comparing the bubble velocity of each single bubble as in the single bubble train setup (Figure 4-1). This approach is chosen for the following reasons: (1) Although the bubble column was said to be 2D, it is still 1.3cm in depth. Hence, even though the probe tip and a bubble overlap on

the photo taken by the camera, it is possible that the bubble does not contact the probe tip, due to the depth of the column. One cannot distinguish this situation from real piercing; hence, it is difficult to correlate the individual bubble velocity obtained by the probe to that obtained by the camera on the one by one basis. (2) To describe the hydrodynamics in bubble columns, the bubble velocity distribution and mean bubble velocity are more valuable than the velocity of each single bubble. (3) To get the bubble velocity distribution, the velocity of hundreds or thousands of bubbles are needed, and it is too time consuming to get the bubble velocities one by one.

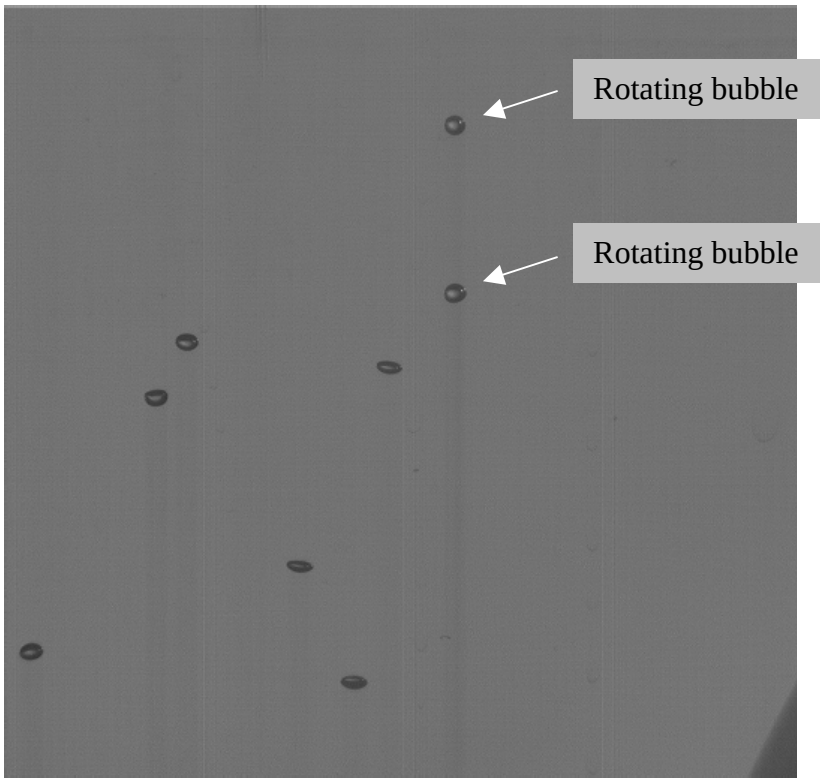

Figure 4-6. Rotation of Bubbles in the 2D Bubble Column

Furthermore, the camera cannot measure accurately the bubble chord length pierced by the probe tip in the 2D bubble column for several reasons: (1) Due to the depth of the column, the position where the probe tip hits the bubble cannot be determined on the photos. Hence, the chord length pierced by the probe tip cannot be determined by image analysis. (2) Bubbles rotate during their movement (Figure 4-6) so that the projection of

the bubbles on the photos does not represent their real dimension. (3) Again, it is too time consuming to compare the bubble chord lengths one by one. So, the bubble chord length obtained by the four-point probe was not validated directly by video imaging. It was validated indirectly as mentioned later.

Hence, the local bubble velocity distribution at the central tip of the probe was measured by the four-point probe and by the camera, respectively, and the results were compared for validation. Some examples of the bubble velocity distribution obtained by these two methods are shown in Figure 4-7. The mean bubble velocities are listed in Table 4-1. The mean bubble sizes in terms of volume-equivalent diameter, obtained by the video imaging, are listed in the captions of the diagrams.

It can be seen from Figure 4-7 that the bubble velocity distributions obtained by the probe in general match well with those obtained by the CCD camera. However, careful comparison of Figures 4-7a, 4-7b and 4-7c and the statistical parameters listed in Table 4-1 reveals that for small bubbles the mean bubble velocity obtained by the probe is larger than that obtained by the camera. For large bubbles the reverse is observed, i.e., the relative error in the mean bubble velocity obtained by the probe changes from positive to negative when the bubble size increases (Table 4-1). This may be caused by the fact that small bubbles of low velocity (momentum) tend to slip away from the probe tip instead of being pierced through (Chabot et al., 1992). Large bubbles, even when their velocity is low, still have enough momentum to be pierced through by the probe tip. Hence, more small bubbles of low velocity were not detected by the four-point probe than large bubbles. As a result, the mean velocity for small bubbles is overestimated by the four-point optical probe.

For large bubbles, the probability density function (pdf) of the bubble velocity shifts toward the low value (Figure 4-7c). This is possibly because the deformation of the bubble surface by the piercing of the probe causes the bubble velocity obtained by the probe to be lower than the real value (Figure 4-17), and the deformation is more obvious

for large bubbles than for small bubbles. Furthermore, as shown in Figure 4-7b, the bubble velocity distribution obtained by the two-point probe has larger pdf values at both low velocity and high velocity. The larger pdf values at low velocity are caused by the fact that sometimes different bubbles hit the two tips of the two-point probe successively. The algorithm for the two-point probe considers this case the same as the case when the same bubble hits the two tips successively. Because the bubbles are sparse at low gas velocity, usually the time interval when two different bubbles hit the different tips of the probe is much larger than that when a single bubble hit the two tips successively. Hence, very low bubble velocities were derived in this case. It is noticed that this peak of the pdf at low velocity is clearly separated from the normal peak in the bubble velocity distribution obtained by the two-point probe (Figure 4-7b). Hence, by removing the pdf peak at low velocity arbitrarily, the bubble velocity distribution obtained by the two-point probe match that obtained by camera better. However, there is no physical rule that supports this removal and sometimes the peak at low velocity and the normal bubble velocity peak partly overlap and it is difficult to determine the criterion for the removal. The mean bubble velocities obtained by the two-point probe displayed in Table 4-1 are obtained after the removal of the pdf peak at low velocity. As shown in Figure 4-7b and Table 4-1, the bubble velocity distribution obtained by two-point probe has higher pdf values at high velocity and higher mean bubble velocity than values detected by camera and by the four-point probe. This confirms the previous analysis that the error in the bubble velocity obtained by the two-point probe is always positive (Figure 3-3a). As illustrated in Appendix D.2, in a 3D bubble column, the two-point probe did not generate reasonable bubble velocity distributions, especially at high gas velocity. Hence, it is experimentally established that the bubble velocity distribution obtained by two-point probes is not as reliable as that by the four-point probe, especially in transition and churn-turbulent flow regime.

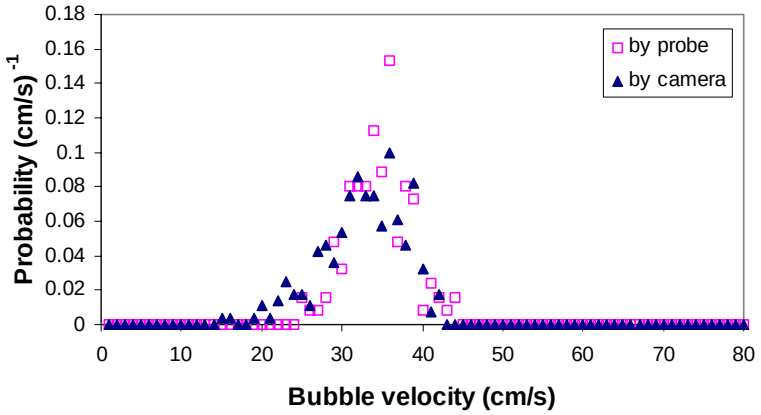

(a) Mean bubble velocity 32.2 cm/s (mean bubble size 0.23cm)

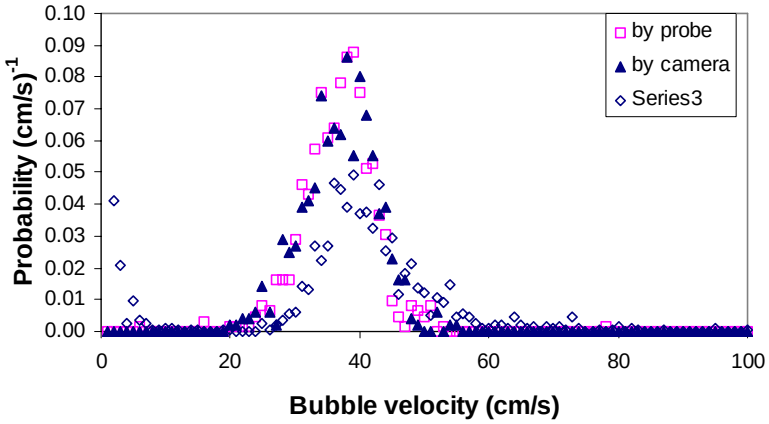

(b) Mean bubble velocity 36.5 cm/s (mean bubble size 0.36cm)

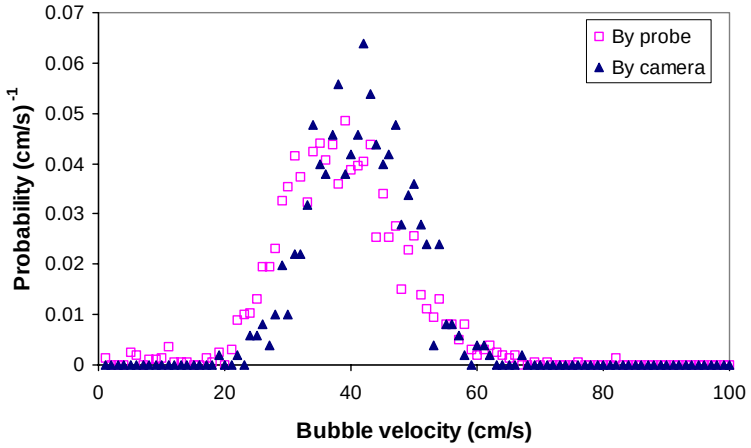

(c) Mean bubble velocity 41.2 cm/s (mean bubble size 0.62cm)

Figure 4-7. Comparison of Bubble Velocity Distributions Obtained by the Four-Point Optical Probe and by Video Imaging

Table 4-1. Statistical Parameters for the Bubble Velocity Distributions

Run	By four-point probe		By two-point probe		By the Camera		Relative error* (%)
	Mean (cm/s)	σ	Mean (cm/s)	σ	Mean (cm/s)	σ	
d_e=0.62 cm	37.9	9.79	40.2	10.6	41.2	8.44	-8.01
d_e=0.36 cm	36.3	5.62	39.5	6.37	36.5	5.54	-0.55
d_e=0.23 cm	34.1	3.77	36.3	4.19	32.2	5.13	5.90

* Relative error for the four-point probe = $(v_{probe}-v_{camera})/v_{camera}$

** σ: Standard Deviation

Figure 4-8 shows examples of the bubble direction angle distribution (angle θ in Figure 4-8a, the angle between the bubble velocity vector, v, and the vertical direction, z), obtained by the probe and by the camera, respectively. It can be seen that the distributions by the two methods roughly agree in shape, except at small values of angle θ, where higher probability values were obtained by the camera. Correspondingly, the mean bubble direction angle obtained by the camera is smaller than that obtained by the four-point optical probe (Table 4-2).

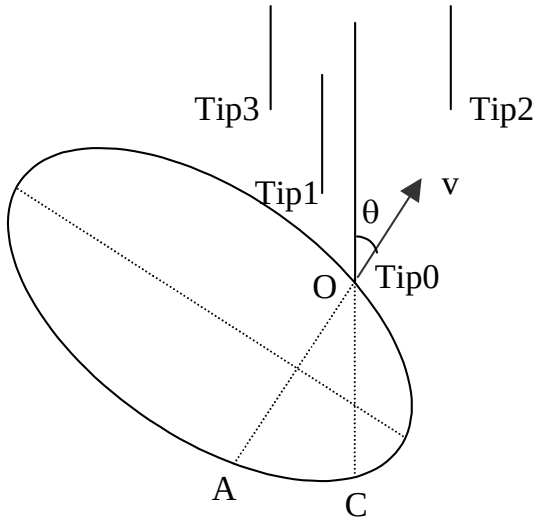

(a)

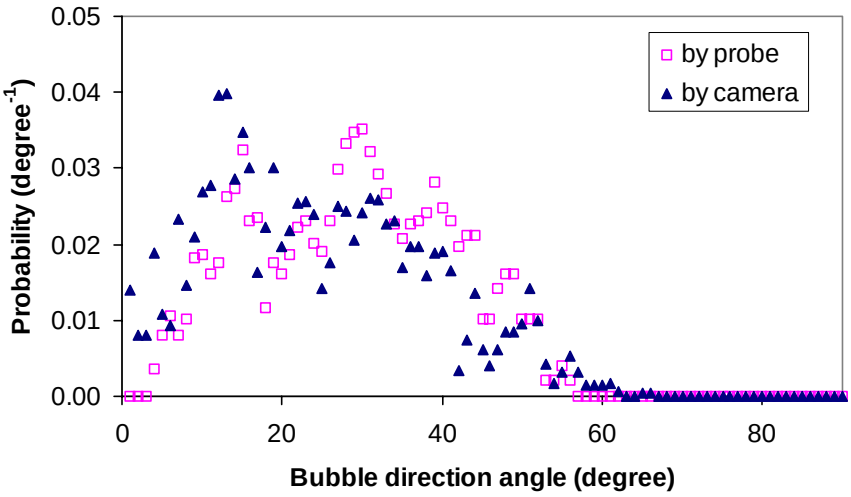

(b) d_e=0.23 cm

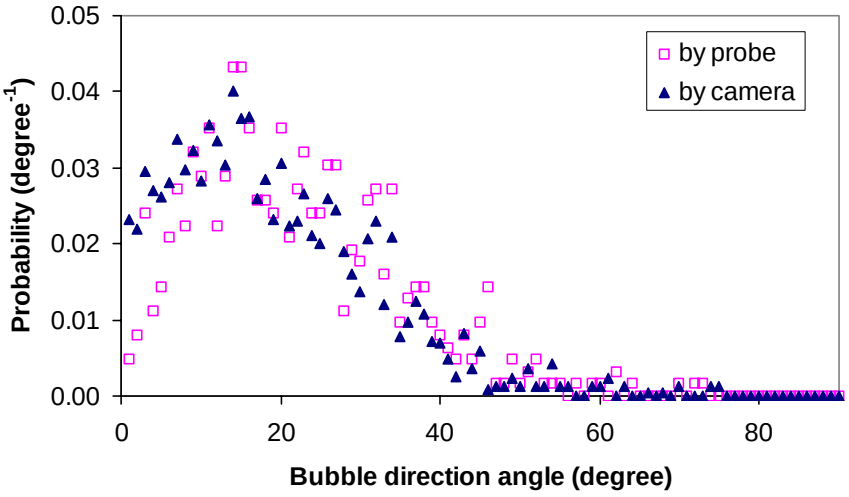

(c) d_e=0.36 cm

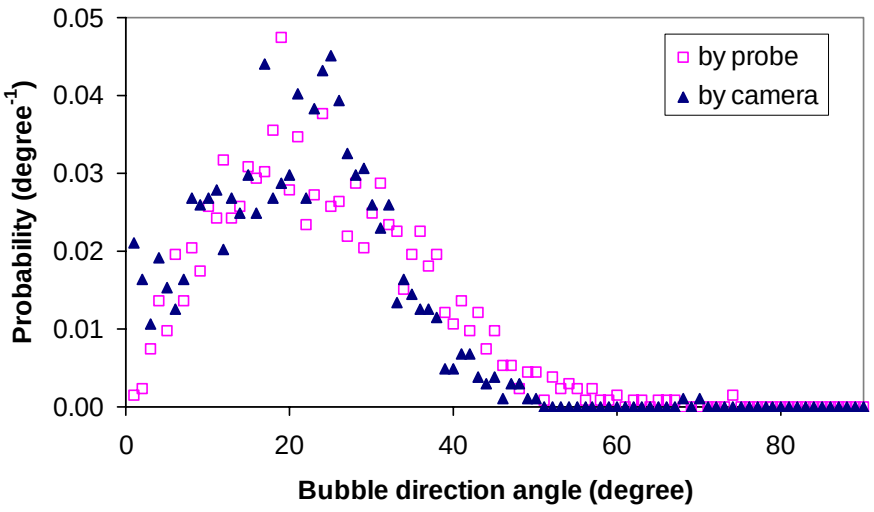

(d) d_e=0.62 cm

Figure 4-8. Comparison of Bubble Direction Angle Distributions

Table 4-2. Statistical Parameters for the Bubble Direction Angle Distributions

Run	By the Probe		By the Camera	
	Mean (degree)	Standard Deviation	Mean (degree)	Standard Deviation
d_e=0.23 cm	28.1	13.0	21.6	15.0
d_e=0.36 cm	21.6	12.8	15.4	9.27
d_e=0.62 cm	23.5	12.1	20.3	10.5

These high probability values at small θ for the camera measurements are likely caused by the fact that the depth of the 2D bubble column is 1.3 cm, so the bubbles may have had a velocity component toward the depth direction, while the camera can catch only the projection of the bubble velocity vector (direction vector) in the yz plane, the plane formed by the width and height of the 2D bubble column (refer to Figure 4-9). Since the direction angle, θ, is always larger than or equal to its projection on the yz plane, θ', i.e., $\theta' \leq \theta$, the bubble direction angle obtained by the camera is smaller than the real value, except when the bubble direction vector falls in the yz plane. This limitation results in high probability values at small direction angles indicated by the camera.

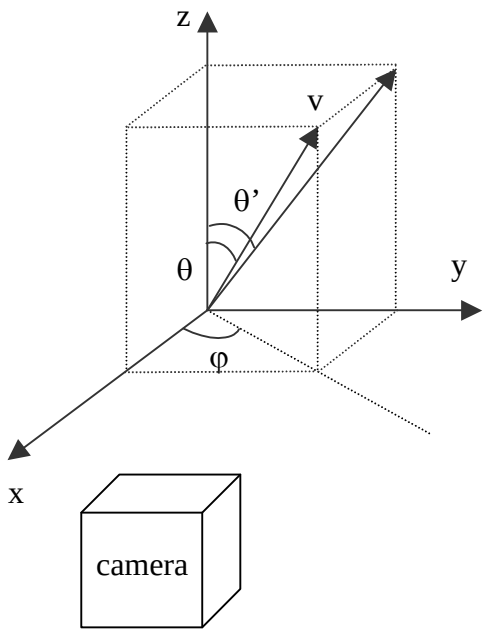

Figure 4-9. Projection of the Velocity Vector on Camera Photos

Experiments that cover bubbles of different sizes (mean diameter of 0.23cm ~ 2.33 cm) were conducted to validate the mean bubble velocity obtained by the four-point probe. The 2D bubble column illustrated in Figure 4-5 is not suitable for large bubbles because the small depth dimension (1.3 cm) makes large bubbles deform and there is also a strong wall effect on their movement, so that the large bubble behavior is very different from that in bubble columns. Hence, a transparent pipe was used to validate the velocity of large bubbles obtained by the four-point probe. The configuration of the Plexiglas pipe is shown in Figure 4-10. The pipe is 5.5 cm in the inner diameter and 105 cm in height. A single nozzle gas sparger was installed at the bottom of the pipe. Bubbles of different sizes can be generated by employing gas nozzles of different outlet sizes and by adjusting the gas velocity. It was proved by video imaging that in the central zone (3.0 cm in diameter) of the column the distortion of the imaging due to the effect of the wall curvature is negligible. The probe is positioned in the center of the pipe, about 98 cm from the bottom.

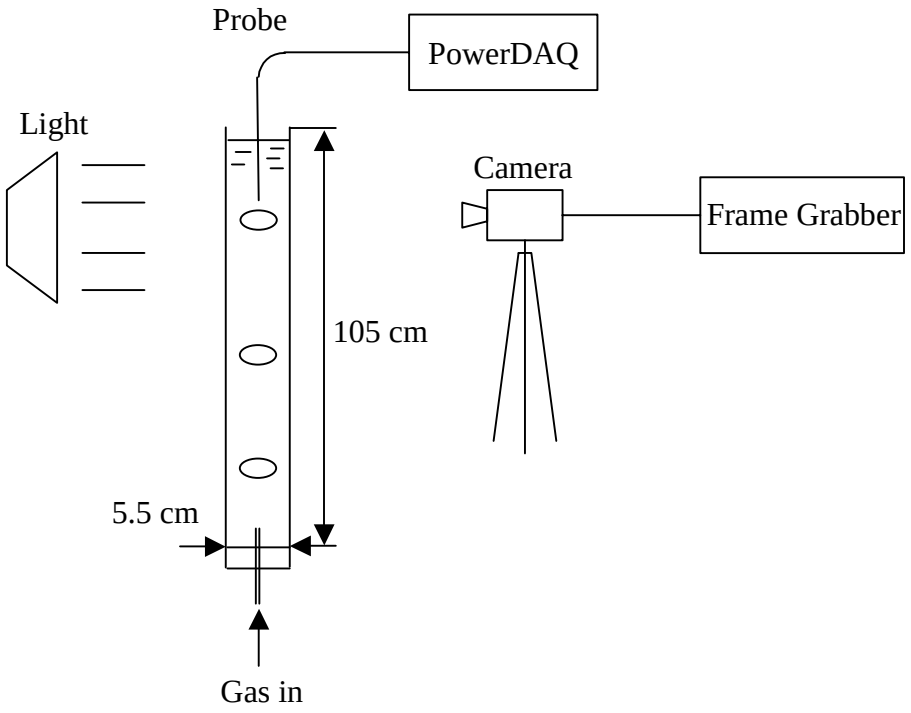

Figure 4-10. Setup for the Validation of Bubble Velocity

The validation results are shown in Figure 4-11. The relative errors in the mean bubble velocity obtained by the four-point probe were plotted against the bubble Reynolds number, Re_b, (ratio of inertial force/viscous force), and bubble Eotvos number, Eo_b (ratio of buoyancy/surface tension). The Morton number, Mo, is about 2.65×10^{-11} for the Air-water system used:

$$Re_b = \frac{\rho d_e v}{\mu} \tag{4-1a}$$

$$Eo_b = \frac{g d_e^2 \rho}{\sigma} \tag{4-1b}$$

$$Mo = \frac{g\mu^4}{\rho\sigma^3} \tag{4-1c}$$

Here, d_e is the volume-equivalent diameter of the bubble, v is the bubble velocity; ρ, σ, and μ are the density, surface tension, and viscosity of the liquid (tap water); and g is the acceleration of gravity ($g = 9.8\ m/s^2$).

Another commonly used dimensionless number, the Weber number, We_b, is not independent of Re_b, Eo_b, and Mo:

$$We = \frac{\rho d_e v^2}{\sigma} = \frac{Re^2\, Mo^{0.5}}{Eo^{0.5}} \qquad (4\text{-}2)$$

Figure 4-11 displays the relative error in the mean bubble velocity obtained by the four-point probe at different Re_b and Eo_b. It can be seen from Figure 4-11 that at bubble volume-equivalent diameter in the range of 0.23cm ~ 2.33cm (Re_b=737~10500, Eo_b=0.72~73.7), the relative error in the mean bubble velocity obtained by the four-point probe is within –11% ~ +6%, and it changes from positive to negative with an increase in bubble size and velocity. The relative errors oscillate around –10% when Re_b>4000 and Eo_b>10. Hence, the mean bubble velocity obtained by the four-point probe is reliable with the range of error –11% ~ +6% at the conditions employed in the validation.

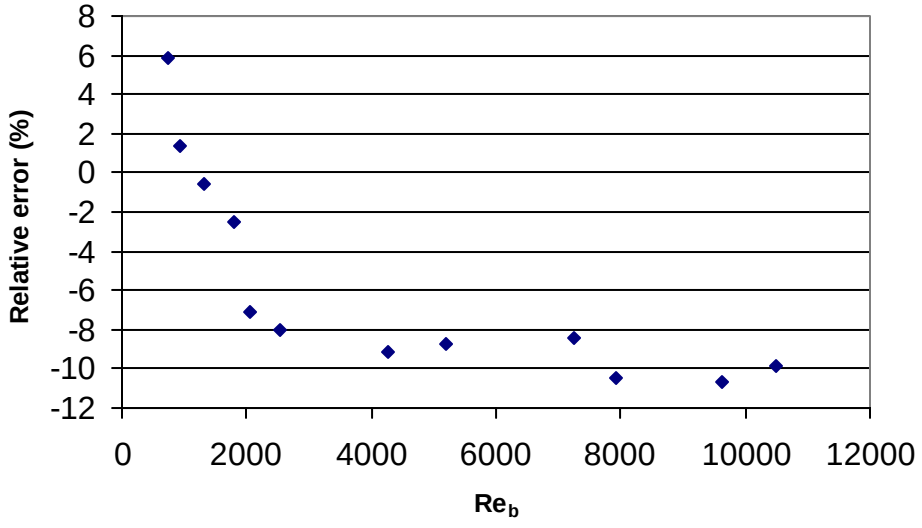

(a)

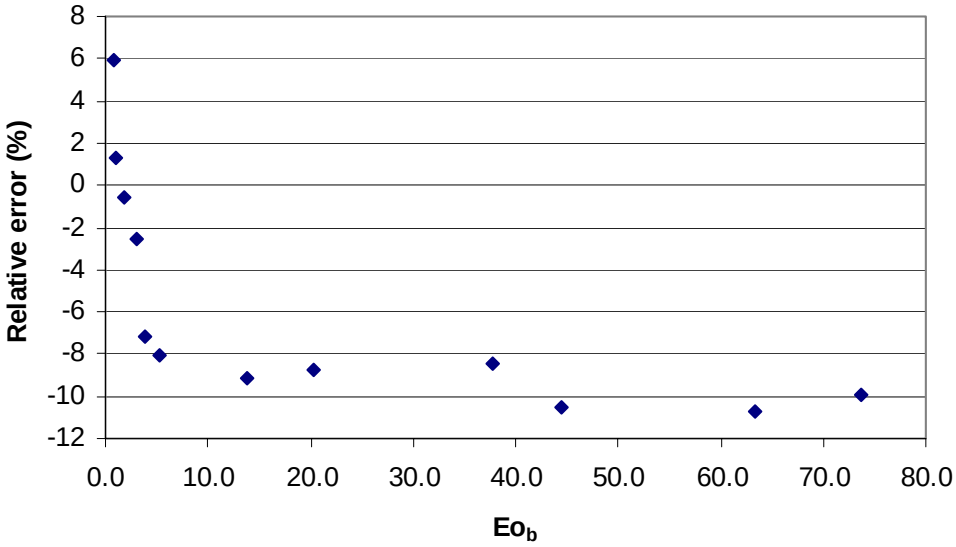

(b)

Figure 4-11. Relative Errors in the Mean Bubble Velocity vs. (a) Bubble Reynold Number and (b) Bubble Eotvos Number (Morton Number = 2.65×10^{-11})

Unfortunately, calibration of the mean bubble velocity obtained by the four-point probe in bubble columns based on Figure 4-11 is not possible. This is because the bubble volume-equivalent diameter, d_e, cannot be determined by the four-point probe. As described earlier, d_e cannot be derived from the bubble chord length obtained by the probe because the aspect ratio of the bubble is unknown. Hence, the bubble Reynolds number, Re_b, and bubble Eotvos number, Eo_b, are not available in bubble columns. Since the mean bubble velocity obtained by the four-point probe is reliable, it will be accepted without calibration.

4.2 Validation of the Specific Interfacial Area

In the case of spherical bubbles, the relationship between the specific interfacial area and the bubble size distribution is simple, and can be described by (Patel, Daly and Bukur, 1989):

$$a = \frac{6\varepsilon_g}{d_s} \tag{4-3}$$

In Equation (4-3), a is the specific interfacial area, ε_g is the gas holdup, and d_s is the Sauter mean diameter (the average volume-surface mean diameter of bubbles) as described in Equation (2-2).

It is well known that most bubbles are not spherical in most practical multiphase systems. When bubbles are not spherical, e.g., ellipsoidal, the relationship between the specific interfacial area and the bubble size distribution is much more complicated than Equation (4-3). Assume that the ellipsoidal bubble has two major axes, c, and one minor axis, b. The three axes of an ellipsoidal bubble are c, c, b, where c>b, and α=b/c is the aspect ratio of the bubble. Then the surface area of the bubble is:

$$S = 8\pi\left[c^2 + \frac{cb^2}{\sqrt{c^2-b^2}}\ln\left(\frac{c+\sqrt{c^2-b^2}}{b}\right)\right] = 8\pi c^2\left[1 + \frac{\alpha^2}{\sqrt{1-\alpha^2}}\ln\left(\frac{1+\sqrt{1-\alpha^2}}{\alpha}\right)\right] \tag{4-4}$$

The volume of the bubble is:

$$V = \frac{4\pi}{3}c^2 b = \frac{4\pi}{3}\alpha c^3 \tag{4-5}$$

Hence, the specific interfacial area is:

$$a = \sum_{i=N} 8\pi c_i^2 \left[1 + \frac{\alpha_i^2}{\sqrt{1-\alpha_i^2}} \ln\left(\frac{1+\sqrt{1-\alpha_i^2}}{\alpha_i} \right) \right] \tag{4-6}$$

where N is the average number of bubbles in unit volume.

The gas holdup is then given by:

$$\varepsilon_g = \sum_{i=N} \frac{4\pi}{3} \alpha_i c_i^3 \tag{4-7}$$

Since the aspect ratios of bubbles in bubble columns are not identical, it is evident from Equations (4-6) and (4-7) that there is no simple correlation between mean bubble size, gas holdup and specific interfacial area for ellipsoidal bubbles, let alone bubbles of irregular shape. Furthermore, for ellipsoidal bubbles Equation (4-3) does not hold even when the aspect ratio of bubbles is identical. Assuming that the size and aspect ratio of all bubbles in bubble columns are identical, Figure 4-12 shows the relative error in the specific interfacial area calculated according to Equation (4-3). It can be seen that Equation (4-3) always underestimates the interfacial area. The smaller the aspect ratio, the larger the relative error. In other words, the more the bubble shape deviates from spherical, the larger the relative error in the specific interfacial area obtained by Equation (4-3). The relative error is –55% at aspect ratio α=0.5, and becomes about –100% when α goes to zero. In the case of different bubble sizes and aspect ratios for the whole bubble population, the relative error in the specific interfacial area is the combination of that shown in Figure 4-12, and is expected to be of the same order of magnitude as that shown in Figure 4-12. It is obvious by this simulation that the error in the specific interfacial obtained by Equation (4-3) may be very large for nonspherical bubbles. Hence, Equation (4-3) is an oversimplification for practical multiphase systems, and it can be treated only as a rough estimate of the specific interfacial area and Sauter mean bubble diameter.

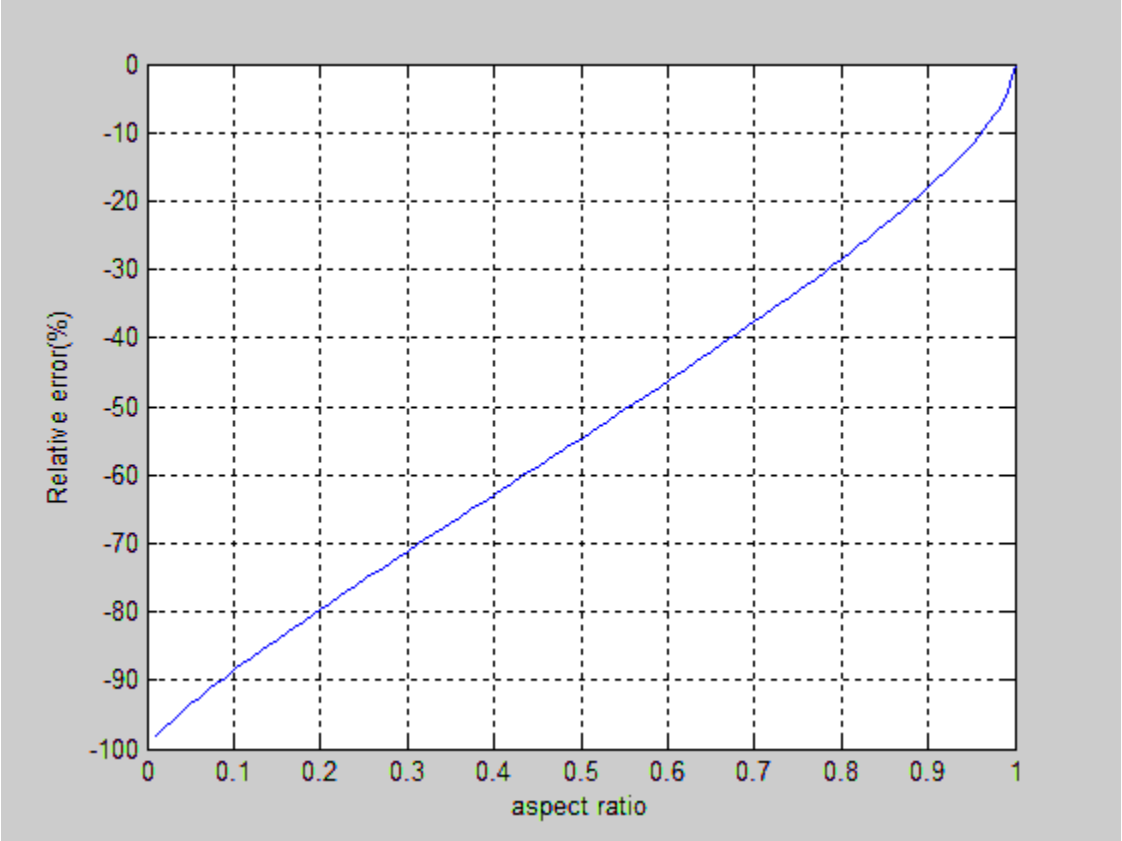

Figure 4-12. Relative Error in the Specific Interfacial Area Obtained by Equation (4-3)

However, for simplification, researchers often assume bubbles are of spherical shape in multiphase systems, e.g., bubble columns, and then employ Equation (4-3) to get the specific interfacial area from the gas holdup and Sauter mean bubble diameter. Obviously this is not accurate for almost any bubble column. However, the error caused by this simplification has never been analyzed or mentioned. Equation (4-3) was employed in this study to get the Sauter mean bubble diameter in order to compare it with the results of other researchers, and in order to qualitatively study the effect of operating conditions on the Sauter mean bubble diameter.

The validation of the specific interfacial area measurement obtained by the four-point probe against video imaging was also conducted in the 2D bubble column shown in Figure 4-5. The video imaging analysis of the specific interfacial area was performed as follows:

(1) Bubbles were assumed to be ellipsoidal, so each bubble in a photo frame was mapped to an approximate ellipsoid.

(2) With the length of the major axis, c, and the aspect ratio of the ellipsoid, α, of the approximate ellipsoid, the surface area of the bubble, a, was calculated with Equation (4-4).

(3) A small region around the central tip of the probe (about 2×2cm) is selected, and the surface area of each bubble in this small region was summed up and divided by the volume of the region to obtain the specific interfacial area in this region.

The results are listed in Table 4-3. Bubbles of different Re_b and Eo_b were generated, and the specific interfacial areas at different conditions were measured. The Re_b and Eo_b were adjusted by generating bubble streams of different mean bubble sizes. Due to the simplifying assumption of ellipsoidal bubble shape, the specific interfacial area obtained by the video imaging is expected to be smaller than the real value. This is because real bubbles are usually somewhat deformed from ellipsoidal shape, so that the surface area is larger than that of an ellipsoid of the same projected area on the photo by the CCD camera. Hence, the specific area obtained by video imaging should be treated only as a reference rather than a standard. It can be seen from Table 4-3 that the specific interfacial area obtained by the four-point probe is approximately equal to that obtained by video imaging. The relative errors are positive and within 23%. Hence, the specific interfacial area obtained by the four-point probe seems to be reasonable. Due to the inherent inaccuracy of the specific interfacial area obtained by the video imaging, no more runs were conducted.

Table 4-3. Comparison of Specific Interfacial Areas

Re_b	Eo_b	a by camera (m^2/m^3)	a by probe (m^2/m^3)
2540	5.22	15.2±1.5	17.8±1.0
2996	5.15	21.3±1.7	25.1±1.4
1211	1.76	9.83±0.62	11.7±0.7
1397	1.74	15.9±0.8	19.5±1.1
705	0.718	13.2±1.2	16.0±1.3
874	0.715	23.5±1.0	24.3±1.6

4.3 Validation of the Local Gas Holdup

The validation of the local gas holdup obtained by the probe was conducted in the setup shown in Figure 4-13. The column consists of an outer pipe with an inner diameter of 5.5 cm and a height of 105 cm, and an inner pipe with an inner diameter of 0.6 cm and a height of 100 cm. A gas nozzle was installed at the bottom of the inner pipe. Taylor bubbles are generated at the bottom, and move upward all the way through the inner pipe. By adjusting the valve on the liquid flow circuit, the liquid flow rate in the inner pipe can be controlled. Since bubbles rise with the liquid, the velocity of bubbles can also be adjusted in this way so that the gas holdup in the inner pipe can be adjusted. The probe is positioned in the center of the inner pipe, about 98 cm to the bottom.

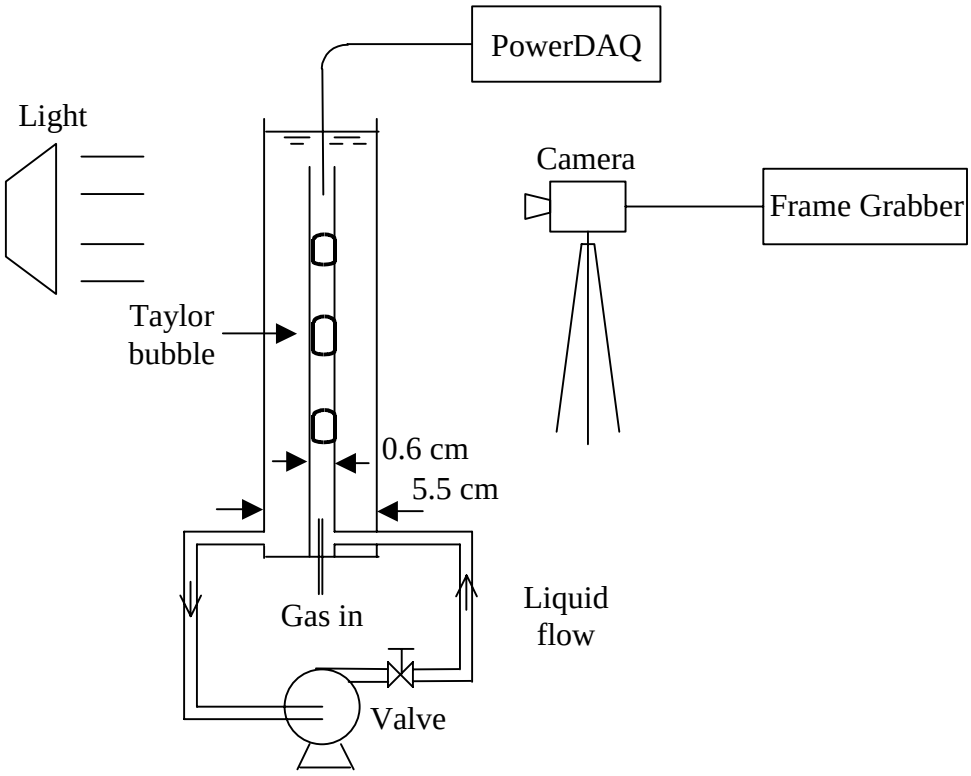

Figure 4-13. Setup for the Validation of Local Gas Holdup

It is important to recognize that the gas holdup obtained by the probe, which is time based, is a little different from the volume based gas holdup, which is commonly used. The definition of volume based gas holdup is that it is the fraction of the whole multiphase system volume that is occupied by the gas phase. Based on this definition, the overall gas holdup in bubble columns can be measured using the bed expansion method as follows:

$$\varepsilon_{g,V} = \frac{V_G}{V} = \frac{V_G}{V_L + V_G} = \frac{H_D - H_I}{H_D} \tag{4-8}$$

where V_G is the volume occupied by the gas phase (bubbles), V_L is the volume occupied by the liquid phase, V is the total volume of the gas-liquid mixed phase, H_I is the initial liquid phase height, and H_D is the dynamic height of the gas-liquid system.

The local gas holdup obtained by the probe is defined as:

$$\varepsilon_{g,T} = \frac{\text{Time spent by the probe's tip in bubbles}}{\text{Total measurement time}} = \frac{T_G}{T} \tag{4-9}$$

here, T_G is the time the probe tip spends in the gas phase (bubbles) and T is the total measuring time.

Clearly the gas holdup obtained by Equation (4-8) is volume based, and that obtained by Equation (4-9) is time based. The difference between these two definitions becomes apparent by transforming Equation (4-9) from time based to volume based. As Figure 4-14 shows, the volume based gas holdup in that simple case is:

$$\varepsilon_{g,V} = \frac{L_G}{L_G + L_L} = \frac{\sum_i L_{G,i}}{\sum_i (L_{G,i} + L_{L,i})} \tag{4-10}$$

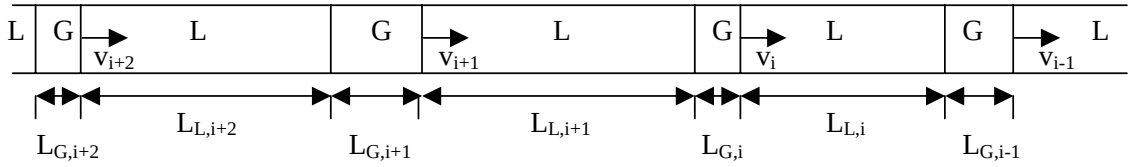

Figure 4-14. Measurement of Gas Holdup by the Optical Probe

The length of the gas phase, $L_{G,i}$, and the length of the liquid phase, $L_{L,i}$, as detected by the probe is given by:

$$L_{L,i} = v_i \cdot t_{L,i} \tag{4-11a}$$

$$L_{G,i} = v_i \cdot t_{G,i} \tag{4-11b}$$

$$\varepsilon_{g,V} = \frac{L_G}{L_G + L_L} = \frac{\sum_i L_{G,i}}{\sum_i (L_{G,i} + L_{L,i})} = \frac{\sum_i (v_i \cdot t_{G,i})}{\sum_i \left[v_i \cdot (t_{G,i} + t_{L,i})\right]} \tag{4-11c}$$

In Equation (4-11c), v_i is the velocity of the ith gas-liquid interface (bubble leading phase), $t_{G,i}$ is the time interval that the probe tip spends in the ith gas section (bubble), and $t_{L,i}$ is the time interval that the probe tip spends in the ith liquid section.

According to the calculus of random variables (Bruce, 1985), if v_i and $t_{G,i}$ are independent, then:

$$\sum_i \left(v_i \cdot t_{G,i}\right) = N\left(\bar{v} \cdot \overline{t_G}\right) \qquad \text{when} \quad N \to \infty \tag{4-12}$$

where $\bar{v}$ and $\overline{t_G}$ are the mean gas-liquid interface velocity and mean time interval that the probe tip spends in the gas sections, respectively.

From Equation (4-12) it can be derived that if v_i are statistically independent of $t_{G,i}$ and $t_{L,i}$, then:

$$\sum_i \left(v_i \cdot t_{G,i}\right) = N\left(\bar{v} \cdot \overline{t_G}\right) = \bar{v} \cdot \sum_i t_{G,i} \qquad \text{when} \quad N \to \infty \tag{4-13a}$$

$$\sum_i \left(v_i \cdot t_{L,i}\right) = N\left(\bar{v} \cdot \overline{t_L}\right) = \bar{v} \cdot \sum_i t_{L,i} \qquad \text{when} \quad N \to \infty \tag{4-13b}$$

$$\varepsilon_{g,V} = \frac{\sum_i \left(v_i \cdot t_{G,i}\right)}{\sum_i \left[v_i \cdot (t_{G,i} + t_{L,i})\right]} = \frac{\sum_i t_{G,i}}{\sum_i (t_{G,i} + t_{L,i})} = \frac{T_G}{T} \tag{4-13c}$$

Hence, Equation (4-9) is the same as Equation (4-8) only if v_i are independent of $t_{G,i}$ and $t_{L,i}$ and the number of bubbles passing by the probe tip during the measurement is large enough.

It can also be derived that:

$$\begin{aligned}\sum_i \left(v_i \cdot t_{G,i}\right) &= \sum_i \left[(\bar{v} + \Delta v_i) \cdot (\overline{t_G} + \Delta t_{G,i})\right] \\ &= \sum_i (\bar{v} \cdot \overline{t_G}) + \sum_i (\Delta v_i \cdot \Delta t_{G,i}) + \sum_i (\bar{v} \cdot \Delta t_{G,i}) + \sum_i (\overline{t_G} \cdot \Delta v_i) \\ &= \sum_i (\bar{v} \cdot \overline{t_G}) + \sum_i (\Delta v_i \cdot \Delta t_{G,i}) \\ &= N\left(\bar{v} \cdot \overline{t_G}\right) + \sum_i (\Delta v_i \cdot \Delta t_{G,i})\end{aligned} \tag{4-14}$$

where Δv_i and $\Delta t_{G,i}$ are the fluctuations in gas-liquid interface velocity and in the time interval that the probe tip spends in the gas sections, respectively.

Hence, $\sum_i (\Delta v_i \cdot \Delta t_{G,i}) = 0$ when v_i and $t_{G,i}$ are statistically independent. However, in bubble columns v_i are not independent of $t_{G,i}$ and $t_{L,i}$ because large bubbles move faster than small bubbles in bubble columns, so a large value of $t_{G,i}$ corresponds to a large v_i. Thus, a positive value of Δv_i tends to correlate to a positive $\Delta t_{G,i}$, and vice versa. This correlation implies that the fluctuation term in Equation (4-14) is positive in most cases, and Equation (4-13c) does not hold. However, it was found that in bubble columns operated in churn-turbulent flow some small bubbles also exhibit large velocities because they move with the wake of the large bubbles. In such a case, a positive value of Δv_i correlates to negative $\Delta t_{G,i}$. These two tendencies counteract, and Equation (4-13) is approximately acceptable because the behavior of small bubbles is decisive in Equation (4-13), due to the overwhelming number of small bubbles compared to large bubbles. Furthermore, the $\sum_i (v_i \cdot t_{G,i})$ term appears in both the denominator and the numerator of Equation (4-13c), counteracting the correlation of v_i and $t_{G,i}$ to some extent. Hence, it is expected that the difference between these two definitions of gas holdup is not substantial in bubble columns.

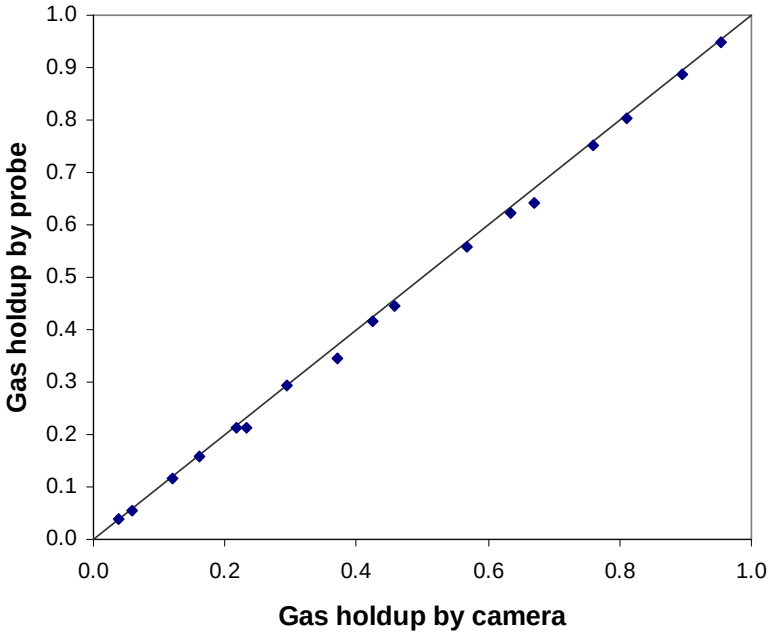

Figure 4-15. Comparison of Local Gas Holdup Obtained by Probe and by Camera

Table 4-4. Local Gas Holdup Obtained by the Probe and by the Camera

ε by probe	Standard deviation	ε' by camera	Standard deviation	Relative error (ε-ε')/ε' (%)
0.949	4.5	0.954	3.7	-0.49
0.887	3.7	0.894	4.2	-0.81
0.803	4.0	0.81	3.6	-0.86
0.751	3.1	0.759	2.9	-0.99
0.642	2.9	0.669	3.1	-4.04
0.622	3.1	0.635	2.7	-2.08
0.557	2.8	0.567	2.3	-1.69
0.445	2.2	0.457	2.2	-2.47
0.417	1.5	0.424	2.1	-1.58
0.344	1.2	0.37	1.5	-6.99
0.292	1.4	0.294	1.2	-0.68
0.212	0.9	0.232	1.1	-8.62
0.213	1.0	0.217	1.0	-2.21
0.159	0.8	0.162	0.8	-1.67
0.117	0.6	0.119	0.6	-1.51
0.0555	0.23	0.0588	0.24	-5.61
0.0384	0.19	0.0393	0.16	-2.29
Mean				-2.64

The comparison of the local gas holdup obtained by the optical probe and by the camera is shown in Table 4-4 and Figure 4-15. The relative errors are always negative within the range of –8.62%~-0.49%. The mean relative error is –2.64%. Hence, the local gas holdup obtained by the optical probe is reliable in this case.

The distributions of the time intervals that the probe's central tip spends in bubbles obtained by the probe and by the camera are displayed in Figure 4-16. It can be seen that these two distributions match well, except that the probe gave a little higher probability at small time intervals than the camera. This is because the interaction between the probe tip and the bubble's leading edge dents the bubble, and causes the chord length pierced by the probe tip to be shorter than the real value. This dent is also the reason that the probe produced lower gas holdup values than the camera. In conclusion, the time intervals that the probe's central tip spent in bubbles obtained by the probe are reliable in this case.

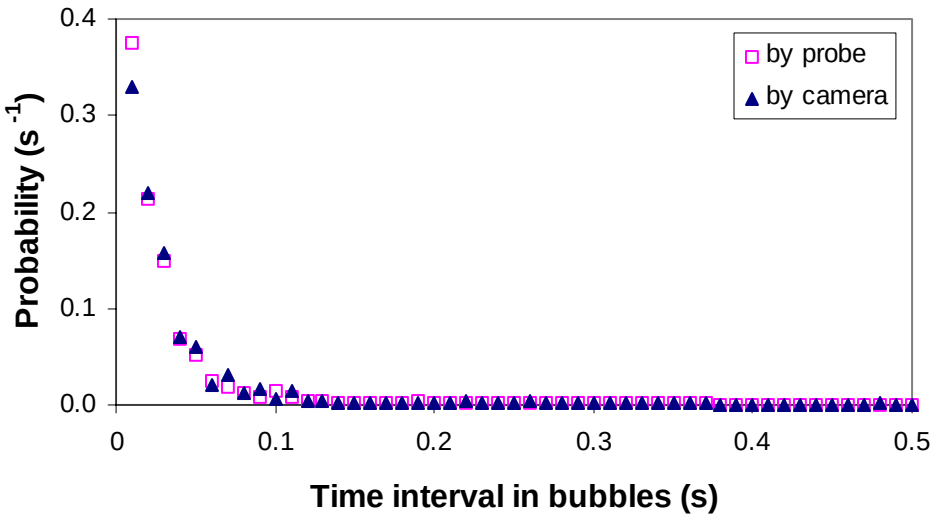

Figure 4-16. Distribution of the Time Intervals that the Probe's Central Tip Spends in Bubbles

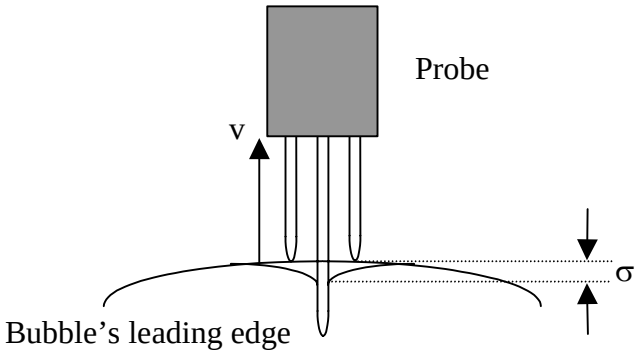

(a) Bubble moves in the probe's axial direction

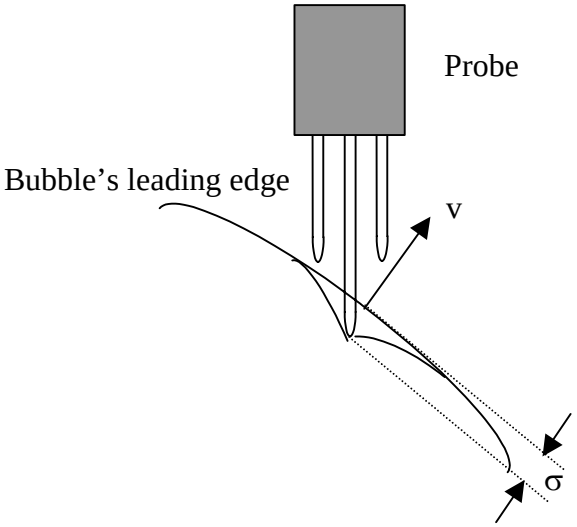

(b) Bubble movement deviates from the probe's axial direction

Figure 4-17. Deformation of the Bubble's Leading Edge due to the Interaction with the Probe Tip

In the setup shown in Figure 4-13, bubbles are forced to move in the probe's axial direction, i.e., vertical direction. However, as mentioned before, in bubble columns the direction of motion for many bubbles deviates significantly from the probe's axial direction, due to the complexity of the flow field. In this case, the deformation of the bubble's leading edge when it hits the probe tip may be more serious than that of bubbles that move in the probe's axial direction. This is because in this case the projection of the probe's tip on the bubble's leading edge is large (Figure 4-17), i.e., not only the optical fiber's tip, but also a part of the fiber body presses on the bubble's leading edge and forces it to deform. As stated before, the observed underestimation of the local gas

holdup is possibly caused by the deformation of the bubble's leading edge. Hence, it is expected that larger deformation of the bubble's leading edge causes larger error in the local gas holdup obtained by the probe.

Furthermore, in the setup shown in Figure 4-13, bubbles are restricted in the inner pipe, so there is no room for bubbles to slip away from the probe's tip. This is different from the condition in bubble columns, where small bubbles may avoid the probe tip, due to the disturbance of the flow field by the probe (Chabot et al., 1992). Hence, it is expected that the error in the local gas holdup obtained by the four-point probe in bubble columns will still be negative, and the relative errors are larger than those shown in Table 4-4. This is proved by the experiments conducted in a 3D bubble column as described later.

The 2D bubble column is not suitable for the validation of the local gas holdup obtained by the probe. This is because in the 2D bubble column, the local gas holdup obtained by the camera is not accurate in the case of non-spherical bubbles, due to several factors: (1) To extract the local gas holdup by the camera, one needs to assume the shape of bubbles, e.g., to be ellipsoidal, and get the volume of bubbles from their projection on the CCD plane. Obviously the bubble volume obtained in this way is not accurate for deformed bubbles. (2) When the major symmetry plane of bubbles (the symmetry plane that contains the major axes of an ellipsoidal bubble) is not vertical to the CCD plane (this is common, especially for small bubbles, which rotate continuously during their rise), the profile of bubbles obtained will be larger than the real value (refer to Figure 4-5). Moreover, as mentioned before, the local gas holdup cannot be determined in the 2D bubble column at relatively high gas holdup, as in bubble columns, due to the overlap of bubbles. Hence, the verification of the local gas holdup obtained by the probe was not conducted in the 2D bubble column.

As described before, the bubble chord lengths being pierced by the probe cannot be derived accurately by the camera in the 2D bubble column. However, the bubble chord length is obtained by the product of the bubble velocity, v, and the time interval that a

probe tip spent in that bubble, T_i: $L_i = v \cdot T_i$. Hence, it is reasonable to assert that after the validation of the bubble velocity and the time intervals that a probe tip spent in bubbles, the bubble chord lengths obtained by the probe are also indirectly validated.

In conclusion, the validation against video imaging shows that the bubble velocity distribution, mean bubble velocity, bubble chord length distribution, specific interfacial area, and local gas holdup obtained by the four-point optical probe are reliable. Hence, the probe is applied in bubble columns at different operating conditions to investigate bubble properties in systems of practical interest.

Chapter 5 Bubble Properties in Bubble Columns Obtained by the Four-Point Optical Probe

After validation of the four-point optical probe measurements in 2D systems, the probe was utilized in 3D bubble columns under specified operating conditions of interest to measure the bubble velocity distribution, bubble chord length distribution, local gas holdup, and specific interfacial area.

5.1 Experimental Setup

The configuration of the 16.2 cm (6.4") diameter stainless steel bubble column is shown in Figure 5-1. The setup was operated in the batch mode with tap water as the liquid phase and filtered, dry compressed air as the gas phase. The four-point probe measurements were conducted at different gas velocities and at atmospheric and high pressures. The operating conditions employed are listed in Table 5-1. Three axial positions, i.e., z/D= 1.7, 5.1, and 8.5, and seven radial positions, i.e., r/R=±0.9, r/R=±0.6, r/R=±0.3 and r/R=0, (where positive and negative values of r/R represent different sides along the diameter of the column in the plane of measurement, Figure 5-1), were selected for measurements of the local bubble properties. The optical probe must employ the fixed ports on the column wall. Due to the physical limitation of the column, i.e., the ports are all located on the same vertical plane (Figure 5-1), the radial measuring positions at each axial position are along one diameter and the measurements of the bubble properties were conducted at one single vertical plane and one angular position in the column. The configuration of the spargers used is shown in Figure 5-2 and Table 5-2.

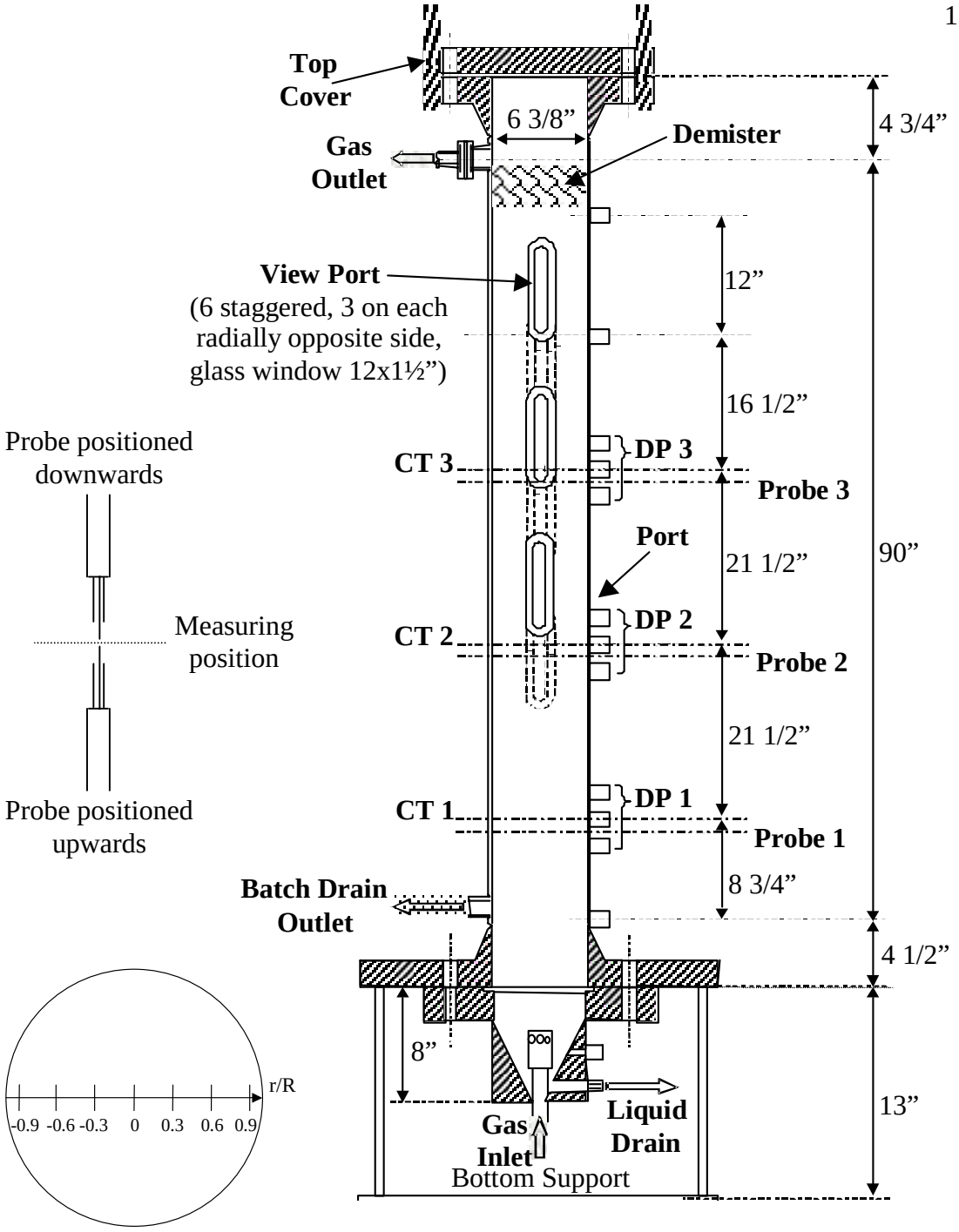

Figure 5-1. The Configuration of the Bubble Column

Table 5-1. Column Dimensions and Selected Operating Conditions

Column ID, D, cm (in.)	16.26 (6.4)	
Temperature, ^{o}C	20	
Dynamic liquid height, cm (in.)	180 (70.9)	
Probe vertical measurement levels from the distributors, z, cm (in.)	27.7 (10.9), 82.3 (32.4), 136.9 (53.9)	
z/D	1.7, 5.1, 8.5	
Probe radial measuring positions, r/R	±0.9, ±0.6, ±0.3, 0	
Liquid (Tap Water)	Batch	
Gas (Air)	Continuous	
Detailed Operating Conditions for Each Gas Distributor		
Sparger	Pressure, (MPa)	Ug, cm/s
#1 Cross Sparger (open area 0.1%)	0.1	30
#2 Perforated Plate (0.15%)	0.1	2, 8, 14, 30, 45, 60
#3 Perforated Plate (1.0%)	0.1, 0.4, 1.0	30

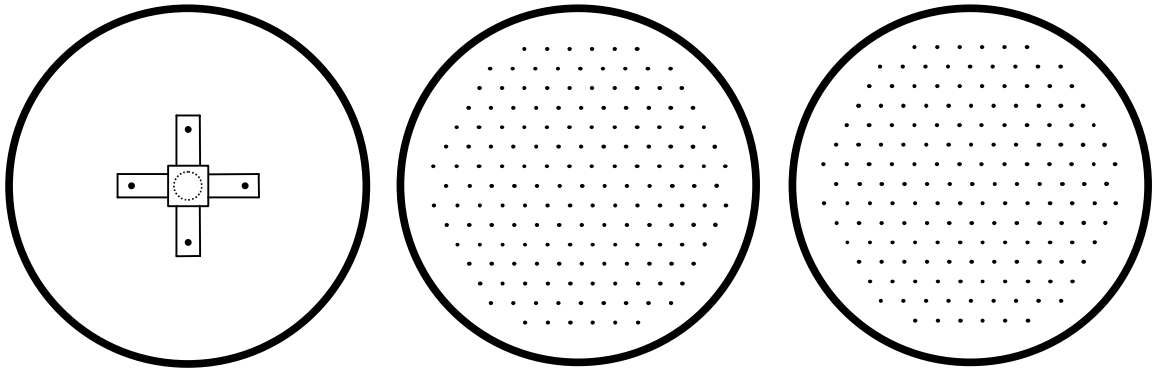

a) #1 Cross Sparger

b) #2 Uniform Perforated Plate (small hole)

c) #3 Uniform Perforated Plate (large hole, shown not to scale)

Figure 5-2. Sparger Configurations

Table 5-2. Sparger Configurations

Sparger	Number of holes N_H	Diameter of holes D_H, mm	Hole Pattern	Open Area %
#1	4	2.54	25.4 mm off center, facing down	0.100
#2	163	0.50	10 mm triangle pitch	0.156
#3	163	1.32	10 mm triangle pitch	1.09

The operating conditions were the same as those used for the CT and CARPT experiments conducted in CREL (Boon Cheng Ong, 2003). The axial measurement positions are a little different from those in the CT experiments (z/D= 2.1, 5.5, 9.0) because the optical probe must employ the fixed ports on the column wall, while the CT can be positioned freely anywhere along the axial direction. The operating principle of the four-point probe, discussed earlier, ensures that it accurately measures bubbles moving upwards when it is positioned downwards, and vice versa. Visual observation indicates that many bubbles move downwards in bubble columns in transition flow and churn-turbulent flow, especially in the wall zone. Hence, the four-point probe was positioned in two directions at each measuring site, i.e., upwards and downwards, and the probe tip was positioned at the same point when the probe was positioned upwards or downwards (Figure 5-1). In this way both bubbles moving upwards and those moving downwards can be measured, instead of only bubbles moving upwards as done in most other studies involving probes.

5.2 Comparison of the Gas Holdup Profile Obtained by Probe and by CT

The radial profiles of local gas holdup obtained by CT (data of Boon Cheng Ong, 2003, is used) and by the four-point optical probe were compared. If the gas holdup profile obtained by the two techniques matched well, and the integrated cross-sectional gas holdup matched the overall gas holdup obtained by the bed expansion height method within reasonable error, then one could claim that both the gas holdup profile obtained by CT and by the four-point optical probe method are reliable.

Figure 5-3 displays an example of the comparison of mean gas holdup radial profiles obtained by CT and the four-point optical probe at atmospheric pressure. Detailed results can be found in Appendix D. The value of the gas holdup obtained by the probe shown in Figures 5-3 and 5-4 is the mean of the values at the symmetric radial positions in the column along the single chord, i.e. for r/R=0.3 the gas holdup is the mean of the values obtained at r/R=±0.3. It can be seen that at atmospheric pressure the results of CT and the

probe match well, with relative error less than ±15% in most cases (refer to Table B-1). The cross-sectional gas holdup, $\overline{\varepsilon_g}$, was calculated from the radial profile of the gas holdup, $\varepsilon_g\left(\frac{r}{R}\right)$, as:

$$\overline{\varepsilon_g} = 2\int_0^1 \frac{r}{R}\cdot\varepsilon_g\left(\frac{r}{R}\right)\cdot d\left(\frac{r}{R}\right) \tag{5-1}$$

Equation (5-1) assumes that the holdup profile in a single plane measured by the probe is representative of the azimuthally averaged value by averaging the values obtained at equivalent + and – r/R locations.

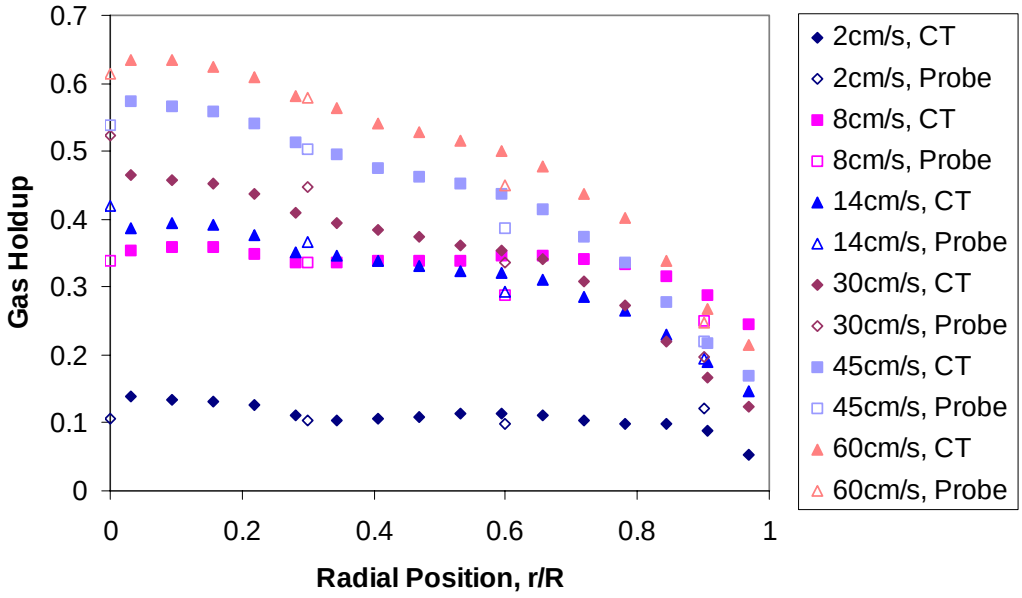

(a) z/D=5.1

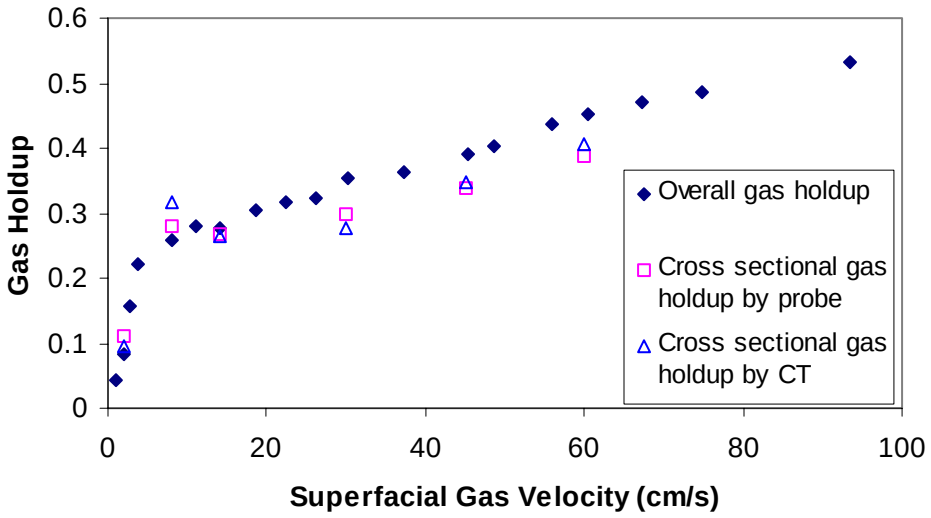

(b)

Figure 5-3. Comparison of Gas Holdup by CT and by Probe at Atmospheric Pressure (Sparger #2)

It can be seen from Figure 5-3b that the cross-sectional gas holdup obtained by CT and by the probe match the overall gas holdup pretty well at atmospheric pressure. Both of them are smaller than the overall gas holdup, with relative errors of –10%~-18%. Hence, at atmospheric pressure, both the CT and the four-point optical probe provide reasonable gas holdup values with negative systematic errors of acceptable magnitude for engineering estimates.

Figure 5-4 displays the comparison of gas holdup profiles obtained by CT and by the probe at both atmospheric and high pressures for sparger #3. It can be seen that for this sparger at atmospheric pressure the gas holdup profiles obtained by these two methods match well. At high pressures the gas holdup obtained by CT and by the probe obviously deviate from each other and the gas holdup obtained by the probe is always larger than that obtained by CT. From Table 5-3, it can be seen that at high pressure the relative error in the cross sectional gas holdup obtained by CT and the overall holdup can be as large as –37.2% (0.4MPa), while that obtained by the probe is still within the same range as at atmospheric pressure. Since the cross-sectional gas holdup obtained by the probe fits the

overall gas holdup better than that obtained by CT at high pressure, it is believed that the probe still gave reliable gas holdup measurements at high pressure. The reason for the large errors in the gas holdup obtained by CT at high pressure is still unknown and should be investigated. It should be noted that although CT holdup measurements and probe measurements were done at identical conditions in the same size column, the tap water used was different and the axial positions for measurements are about 2 inches apart. Water impurities are known to affect the gas holdup (Tang and Heindel, 2004).

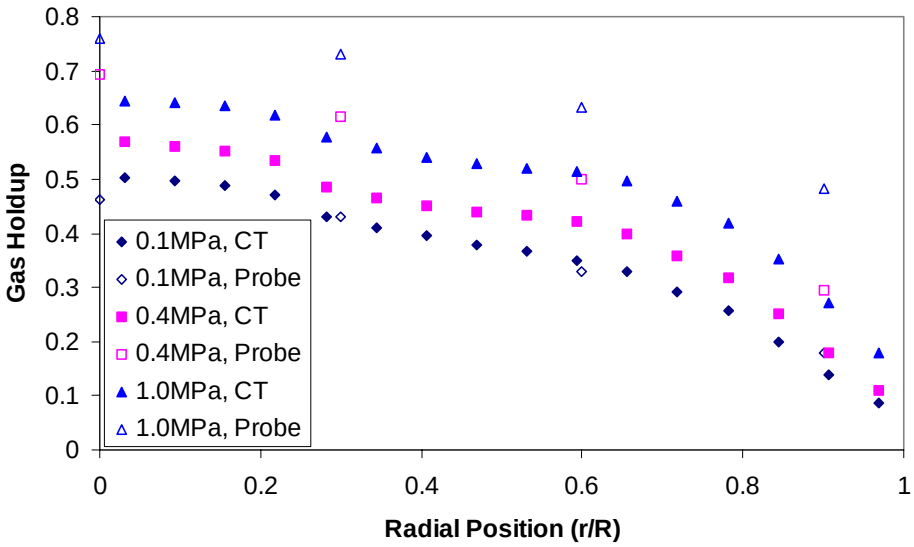

Figure 5-4. Comparison of Radial Profiles of Gas Holdup by CT and Probe at High Pressures (Sparger #3, 30 cm/s, z/D=5.1)

Table 5-3. Comparison of the Integrated Cross-Sectional Gas Holdup and the Overall Gas Holdup at High Pressures (Sparger #3, Ug=30 cm/s)

z/D	Overall ε_g	$\overline{\varepsilon_g}$ by CT	Error* (%)	$\overline{\varepsilon_g}$ by Probe	Error* (%)
P=0.1MPa					
5.1	0.328	0.281	-14.3	0.285	-13.0
P=0.4MPa					
5.1	0.534	0.335	-37.2	0.434	-18.7
P=1.0MPa					
5.1	0.672	0.426	-36.6	0.587	-12.7

* Error= $(\overline{\varepsilon_g} - \varepsilon_g)/\varepsilon_g \times 100\%$

5.3 The Effect of Superficial Gas Velocity

The superficial gas velocity, Ug, is one of the key operating variables that affects the hydrodynamics in bubble columns, including bubble properties. The effect of Ug on bubbles at atmospheric pressure in bubble columns was investigated in this study. Figure 5-5a shows the radial profiles of local gas holdup, $\varepsilon_{g,l}$, at different Ug and the changes of $\varepsilon_{g,l}$ with Ug at different radial positions. The error bars are also displayed. It is clear from Figure 5-5a that the radial profile of local gas holdup is flat at Ug=2 cm/s, which is bubbly flow. The local gas holdup profile is parabolic when Ug is larger than 8 cm/s, when the flow changes from transition flow to churn-turbulent flow. Furthermore, the higher the gas velocity, the steeper the parabolic profile. These observations are corroborated with the CT experimental results. It is also noticed that the bubble properties are not strictly symmetric in the radial direction in the range of measurements. Visual observation through the windows on the column wall indicates the asymmetry of the flow in the column. Possible causes for the asymmetry could be the bubble column alignment departure from verticality, lack of symmetry for the sparger used, and the coherent structure in the flow (Groen et al., 1996). In the following text, if the bubble properties are alike at symmetric radial positions then only bubble properties at one side are shown, e.g. if the bubble chord length distribution at r/R=0.9 and r/R=-0.9 is alike, so only the one at r/R=-0.9 is shown.

It is found that the radial profiles of both specific interfacial area (Figure 5-5b) and bubble frequency (the number of bubbles that hit the central tip of the probe per second) and their changes with Ug are similar to the radial profile of the local gas holdup. The similarity between these profiles is the result of the fact that local gas holdup, specific interfacial area and bubble frequency are strongly correlated. Speaking generally, an increase in bubble frequency leads to an increase in gas holdup and specific interfacial area.

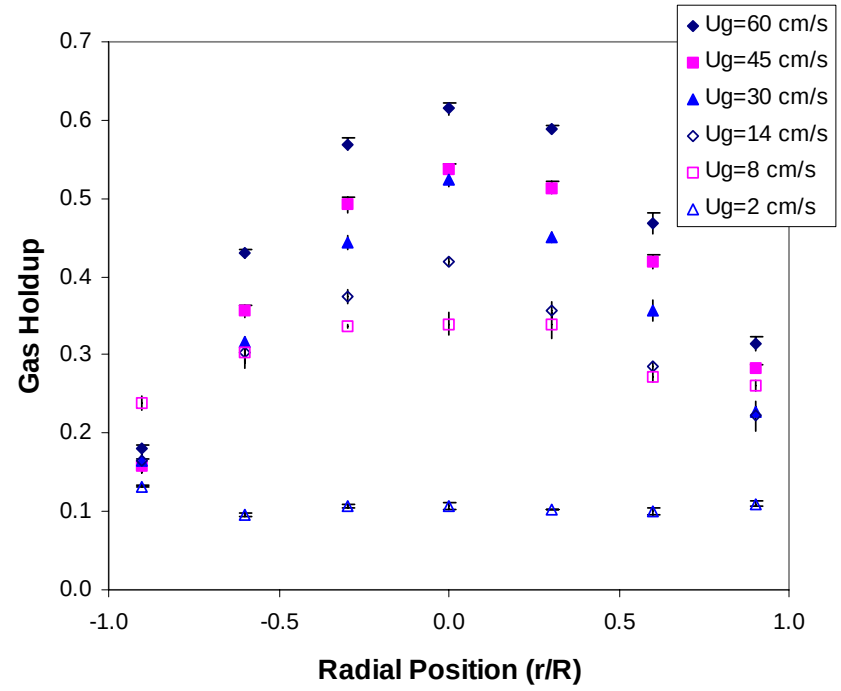

(a)

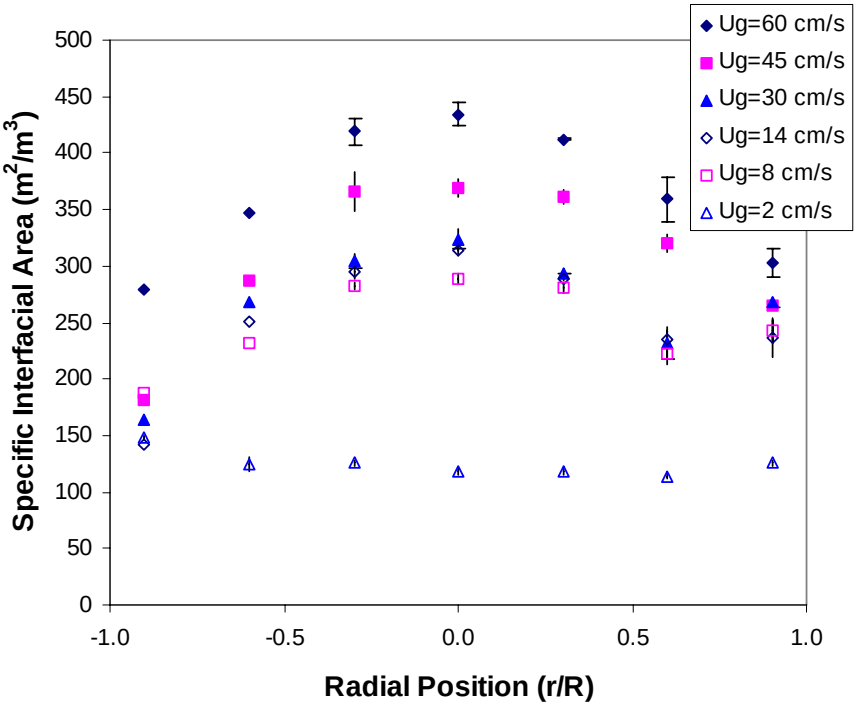

(b)

Figure 5-5. The Radial Profile of Local Gas Holdup and Specific Interfacial Area (Sparger #2, z/D=5.1)

The radial profiles of mean bubble velocity at different Ug are shown in Figure 5-6. The positive value of bubble velocity means that bubbles move upwards, while the negative value means that bubbles move downwards. The mean bubble velocity, $\overline{v_b}$, is the sum of the bubble velocities divided by the bubble numbers:

$$\overline{v_b} = \frac{\overline{v_{b,up}} \cdot N_{up} + \overline{v_{b,down}} \cdot N_{down}}{N_{up} + N_{down}} \qquad (5\text{-}2)$$

where N is the total number of bubbles measured by the four-point probe.

As expected, the radial profile of mean bubble velocity was flat at Ug=2 cm/s, which is bubbly flow, and it was parabolic when Ug was larger than 8 cm/s, when flow changes to transition flow and churn-turbulent flow (Figure 5-6a). Figure 5-6b shows that the mean bubble velocity was always positive and increased with Ug in the core of the column, and the rate of increase in the mean bubble velocity with Ug in the bubbly flow regime was faster than in the churn-turbulent flow regime. In the wall zone (r/R=±0.9), $\overline{v_b}$ was positive in bubbly flow (Ug = 2cm/s) and was small or even negative at Ug>8 cm/s. Above Ug of 14 cm/s, the magnitude of $\overline{v_b}$ increased slowly with Ug; in the range of Ug investigated (Ug = 2~60 cm/s) the minimum $\overline{v_b}$ was detected at Ug= 8cm/s, in the transition regime from bubbly flow to churn-turbulent flow, in the wall zone.

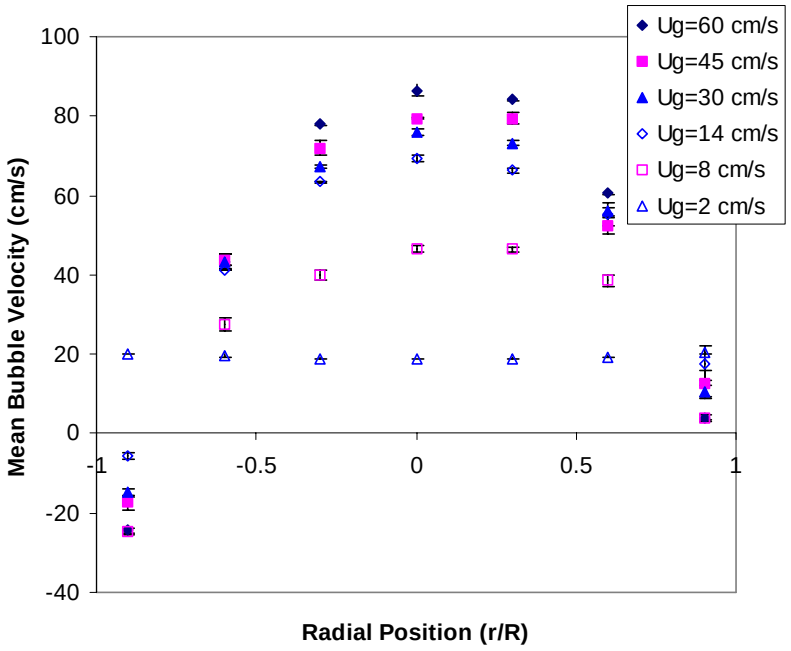

(a)

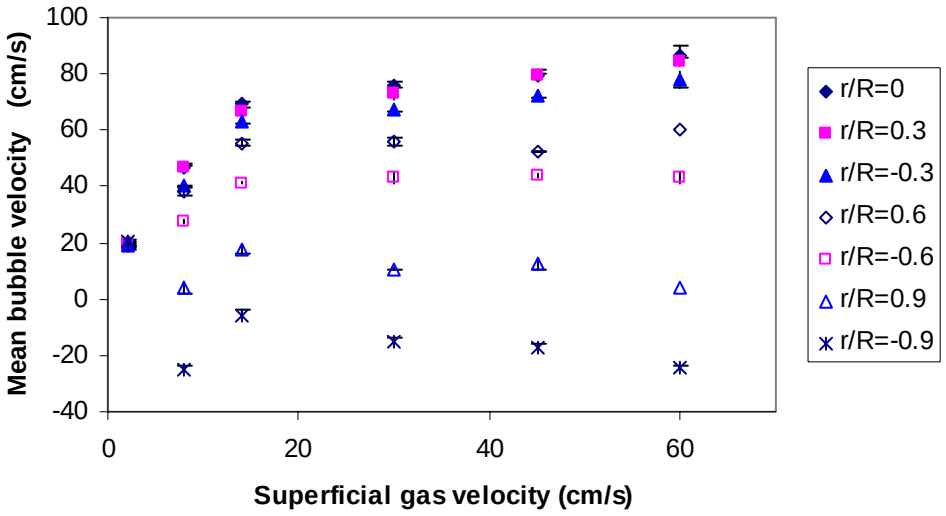

(b)

Figure 5-6. The Radial Profile of Mean Bubble Velocity and Its Change with Ug (Sparger #2, z/D=5.1)

The bubble velocity distribution in the wall zone (Figure 5-7, r/R=±0.9, z/D=5.1) obtained by the four-point optical probe clarifies the observed behavior for the mean

bubble velocity, $\overline{v_b}$. It should be noted that a large portion of bubbles of very low velocity cannot be measured by the probe. This is because it takes relatively long time for very slow bubbles to pass through the four tips of the probe. During this time interval if the flow field around the bubble changes, the bubble velocity also changes during its passage by the probe since bubbles move with liquid flow. In this case the velocity of the bubble determined by the four-point probe is a mean of the early slow velocity and the later high velocity. Hence, the four-point probe tends to underestimate the probability of bubbles of very low velocity. However, it should be noted that this bias is usually not significant because the vertical distance between the central tip and the other tips of the probe is about 2 mm, if the time scale of the flow field change is 0.1 s, then only bubbles with velocity lower than about 2 cm/s will be affected. Usually the percentage of bubbles with velocity as low as this is very low. The bias happens both for bubbles that move upwards and downwards, so the mean bubble velocity is not affected much by this bias. At Ug=2 cm/s all bubbles moved upwards (Figure 5-7a), and the peak in the bubble velocity distribution was thin and sharp. At Ug>8 cm/s, the bubble velocity distributions at r/R=-0.9 and r/R=0.9 were different. At r/R=-0.9, more bubbles moved downwards than upwards. At r/R=0.9, almost as many bubbles moved upwards as downwards. As a result, the radial profile of the mean bubble velocity was not symmetric at z/D=5.1 and the mean bubble velocity at r/R=-0.9 was smaller than that at r/R=0.9 (Figure 5-6a). When Ug increased from 8 cm/s to 14 cm/s (i.e., in the transition flow regime) the mean velocity of bubbles moving upwards increased greatly (from 9.45 to 20.9cm/s at r/R=-0.9 and from 12.4 to 28.3cm/s at r/R=0.9) while that of bubbles moving downwards increased mildly in magnitude (from –33.8 to -39.1cm/s at r/R=-0.9 and –28.2 to -34.6cm/s at r/R=0.9). This is because large bubbles, which have high velocity, arose in the transition flow regime (this is evident from an increase in the number of bubbles of high velocity in the bubble velocity distributions at Ug=8 cm/s and 14 cm/s, Figures 5-8b and 5-8c) and assembled in the central stream of the column. The velocity of bubbles moving downwards in the wall zone increased mainly due to the enhancement of the liquid recirculation caused by the appearance of large bubbles in the central stream. Hence, the velocity of bubbles moving upwards jumped and of bubbles moving

downwards increases only mildly in the transition flow regime. In churn-turbulent flow, at Ug>14cm/s, the percentage of bubbles moving downwards increased slowly with Ug in the wall zone.

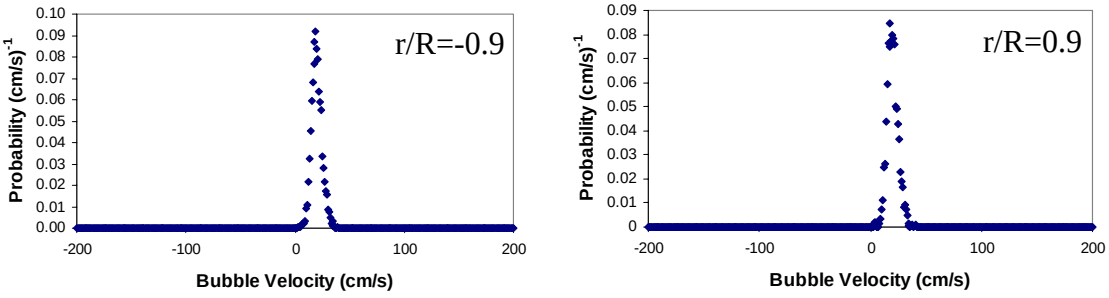

(a) Ug=2 cm/s

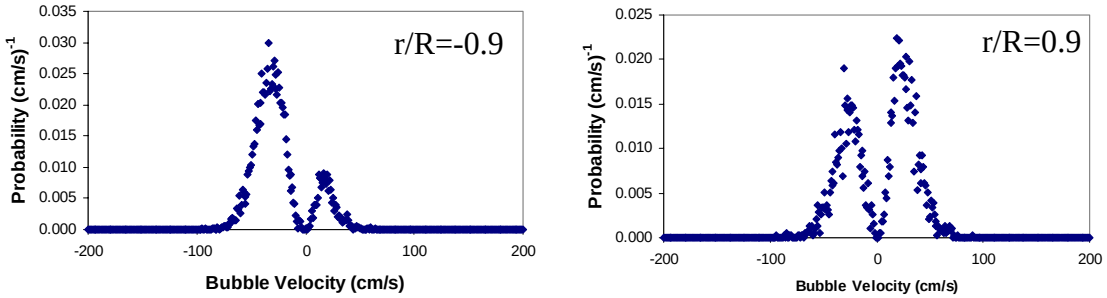

(b) Ug=8 cm/s

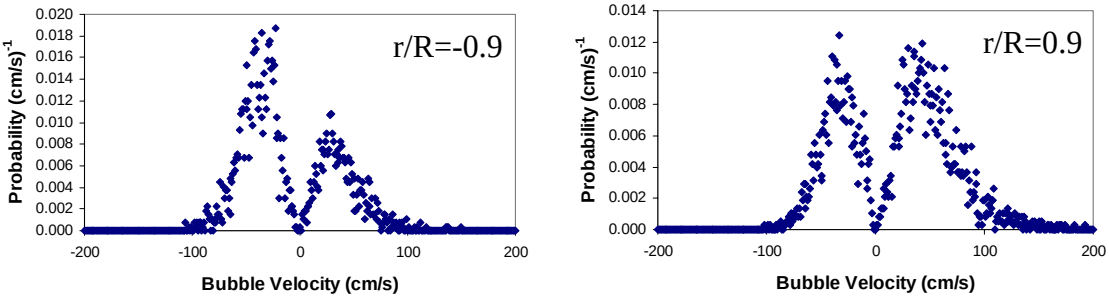

(c) Ug=14 cm/s

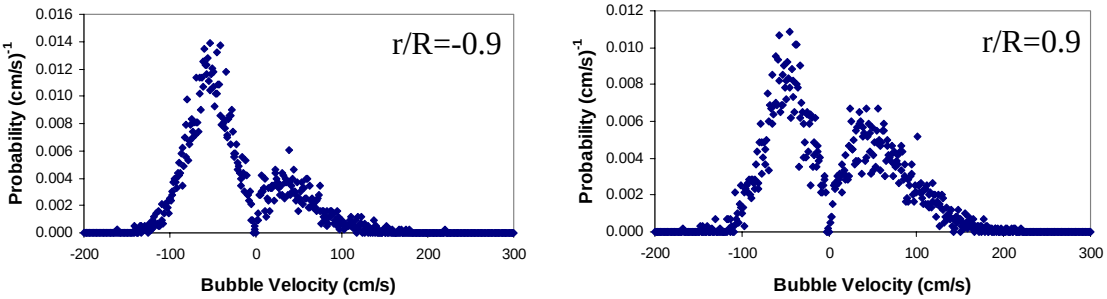

(d) Ug=60 cm/s

Figure 5-7. Bubble Velocity Distribution in the Wall Region at Different Superficial Gas Velocities (z/D=5.1, Sparger #2)

The bubble velocity distributions in the center of the bubble column (r/R=0, z/D= 5.1) at different Ug are shown in Figure 5-8. In contrast to the wall zone, most bubbles move upwards in the column center. The percentage of bubbles moving downwards increased with Ug, but even at Ug as high as 60cm/s, only a small percentage of bubbles moved downwards in the column center. Bubbles moving downwards in the column center may be small bubbles that exist in the wakes of large bubbles, which may have negative velocity due to liquid recirculation in the wakes. In churn-turbulent flow, the number of large bubbles increases with Ug, so there are more bubbles moving downwards being detected by the four-point probe. The bubble velocity distribution in the column center spreads more widely with increased Ug, and the magnitude of the mean velocity of bubbles moving upwards is much larger than that of bubbles moving downwards.

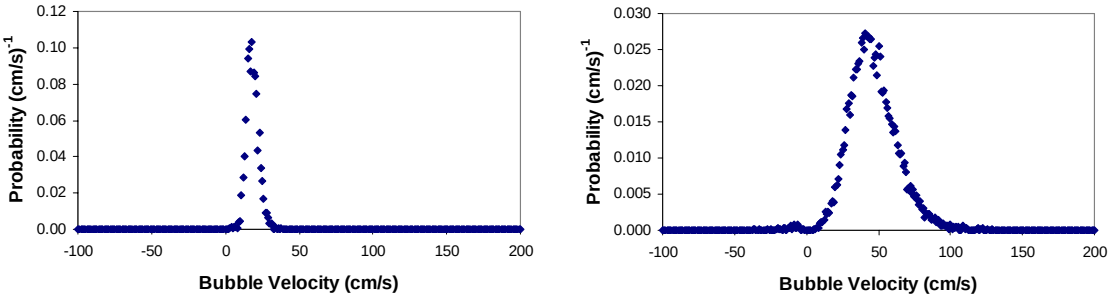

(a) Ug=2 cm/s **(b) Ug=8 cm/s**

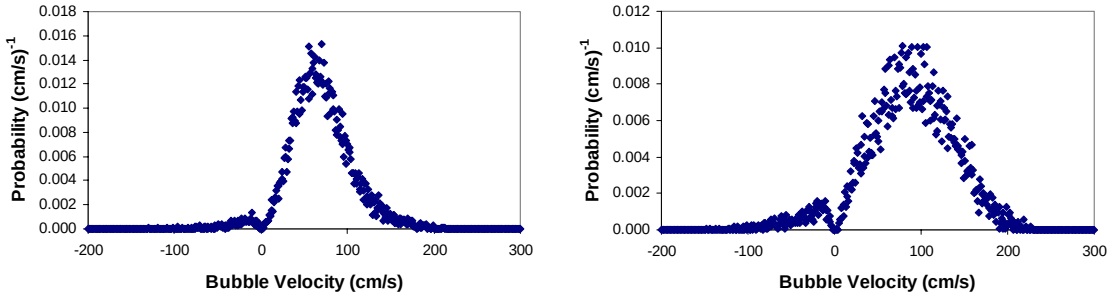

(c) Ug=14 cm/s **(d) Ug=60 cm/s**

Figure 5-8. Bubble Velocity Distribution at Different Superficial Gas Velocities (r/R=0, z/D=5.1, Sparger #2)

The bubble chord length distributions obtained by the four-point optical probe at different gas velocities in the wall zone (r/R=-0.9; the shape of bubble chord length distributions at r/R=0.9 are similar to that at r/R=-0.9.) and in the center (r/R=0) of the bubble column are displayed in Figure 5-9. At column center (r/R=0), the number of the bubbles used for the calculation of the bubble chord length distribution is over 10,000 at Ug≥8 cm/s and about 4,000 at Ug =2cm/s. In the wall region (r/R=-0.9), the number is over 5,000 and about 4,000, respectively. This large number of the bubbles available for the derivation of the bubble chord length distribution and mean bubble chord length makes the results reliable. It can be seen that in the column center the bubble chord length distribution spreads wider, and the probability for both small and large chord lengths increases with increased Ug (Figure 5-9a). In the wall zone (Figure 5-9b), the shape of the bubble chord length distribution does not change much with Ug when Ug ≥ 8 cm/s. The probability of small bubble chord length increases with Ug, while that of large bubble chord length does not change much with Ug. This is also because the large bubbles pass through the bubble column in the core of the central bubble stream, as described by Chen, Reese and Fan (1994), and seldom move into the wall zone, while small bubbles tend to enter the wall zone and move with the downwards liquid flow.

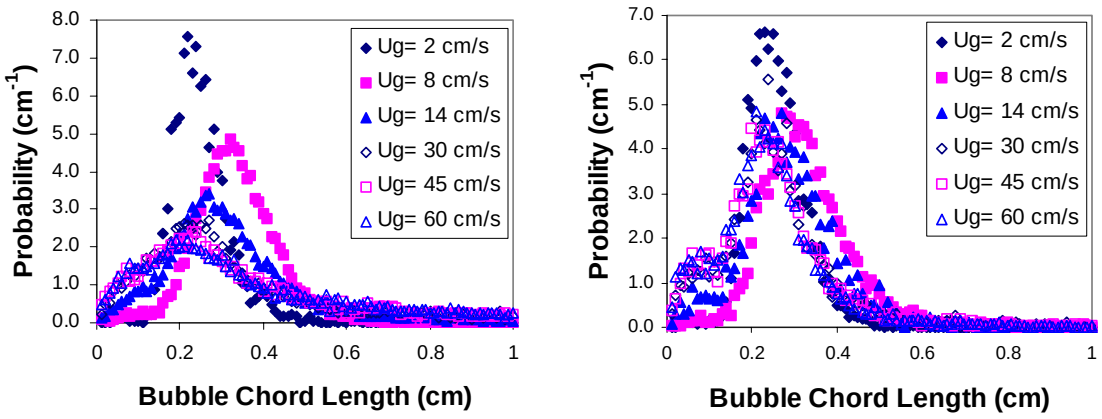

(a) r/R=0 **(b) r/R=-0.9**

Figure 5-9. Bubble Chord Length Distribution at Different Superficial Gas Velocities (Sparger #2, 0.1MPa, z/D=5.1)

The mean bubble chord length and the standard deviation of the bubble chord length distributions are plotted in Figure 5-10. The error bar for the mean bubble chord length is also shown. It can be seen that the mean and standard deviation of the bubble chord length distribution in the column center are almost identical to those in the wall zone at Ug=2 cm/s, where the central stream of large bubbles does not exist, and at Ug=8 cm/s, where the liquid recirculation starts, however, the number of large bubbles in the central stream is still small. When Ug ≥ 14 cm/s, the mean and standard deviation of the bubble chord length distribution in the column center are much larger than those in the wall zone due to the assembly of large bubbles in the central bubble stream. In the column center, the mean bubble chord length increases with Ug when Ug ≤ 30cm/s and decreases slightly with Ug when Ug ≥ 30 cm/s (Figure 5-10a); the standard deviation increases quickly between Ug = 8 cm/s and Ug = 30 cm/s and decreases slightly with Ug when Ug ≥ 30 cm/s. This is because in the transition flow regime and churn-turbulent flow regime, bubbles break and coalesce, and the number of both large and small bubbles increases and the bubble size distribution spreads wider than the relatively uniform bubble size distribution in bubbly flow. In the churn-turbulent flow regime the increase in the number of small bubbles is faster than that of large bubbles, so the mean bubble chord length

decreases slightly with Ug. In the wall zone, the mean bubble chord length increases with Ug when Ug ≤ 8cm/s and decreases somewhat with Ug when Ug ≥ 8 cm/s. The standard deviation keeps increasing with Ug in the range Ug=2 cm/s to 60 cm/s, but the rate of increase is much slower than that in the column center. This is also the consequence of the fact that the large bubbles gather in the column center, and mainly small bubbles exist in the wall zone of the column.

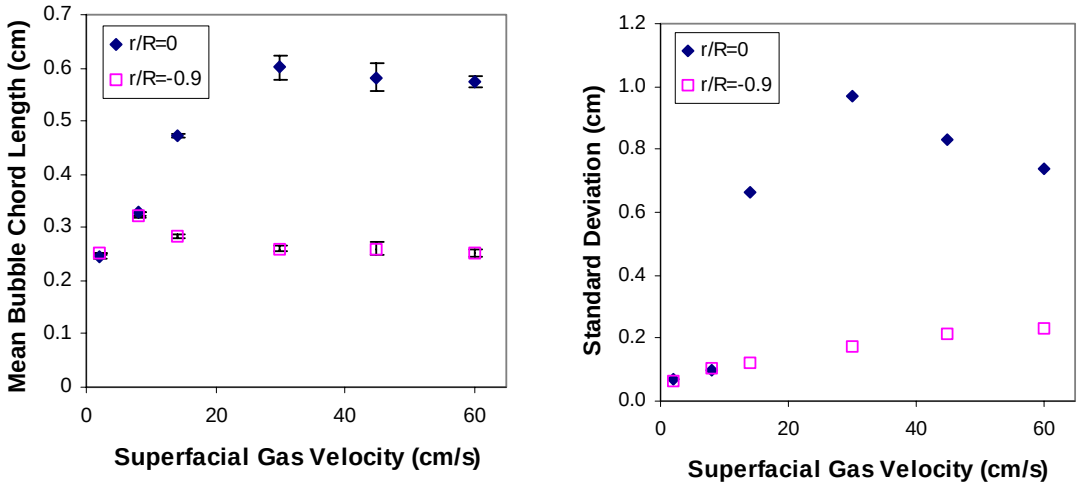

(a) **(b)**

Figure 5-10. The (a) Mean and (b) Standard Deviation of the Bubble Chord Length Distribution at Different Superficial Gas Velocities

Figure 5-11 shows the bubble velocity distribution and bubble chord length distribution at different radial positions in the bubble column (at radial positions r/R=0, -0.3, -0.6 and -0.9 only, the shape of the bubble velocity distribution and bubble chord length distribution at symmetric radial positions, r/R=0.3, 0.6 and 0.9, are alike). It can be seen from Figure 5-11a that the percentage of bubbles moving downwards increases from the column center to the wall zone; in the core of the column the change is slow, and bubbles moving upwards are in the majority, while in the wall zone bubbles moving downwards predominate. Since bubbles move with the liquid flow, this phenomenon is corroborated by research findings on liquid recirculation in bubble columns, which shows that the

transition from upflow to downflow for the liquid recirculation happens at r/R=0.6~0.7 (Boon Cheng Ong, 2003). As shown in Figure 5-11b, the bubble chord length distributions in the core of the column are alike in shape. A sudden change happens within the wall zone where the percentage of small bubble chord lengths increases greatly because mainly small bubbles exist in the wall zone of the column. Hence, it can be concluded that in churn-turbulent flow in the core of the column (r/R<0.6) the shape of the bubble velocity and bubble chord length distributions are alike, while in the wall zone they are very different from those in the core of the column.

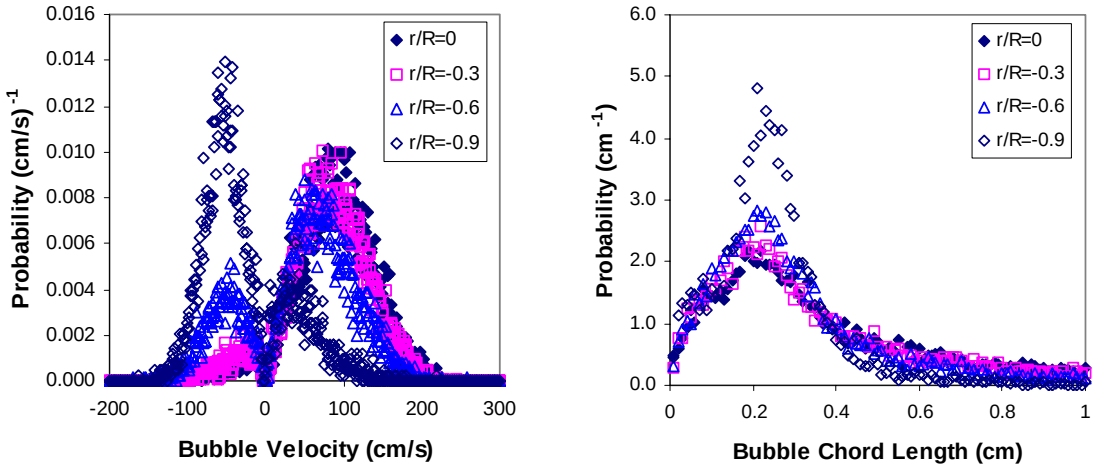

(a) **(b)**

Figure 5-11. Bubble Velocity and Bubble Chord Length Distribution at Different Radial Positions (Sparger #2, Ug=60 cm/s, z/D=5.1)

Figure 5-12 shows the relationship between the bubble velocity and the bubble chord length at the center of the column at different Ug. It should be noted that the bubble velocity is the sum of the liquid velocity and the bubble's slip velocity since bubbles move with the liquid flow in bubble columns. In other words, bubble size is not the only factor that affects the bubble velocity. In churn-turbulent flow, it is not even the decisive factor in some cases, e.g. many small bubbles have as high velocity as large bubbles (Figure 5-12c and d) because they exist in the wake of large bubbles and move with the large bubbles. As expected, the bubble velocity roughly increases with bubble size in

bubbly flow and it is much higher in churn-turbulent flow than in bubbly flow. In churn-turbulent flow, the velocity of a portion of small bubbles is as high as large bubbles (Figure 5-12d). This is because many small bubbles exist in the wake of large bubbles and hence move with the large bubbles. In a few cases, large bubbles have relatively low velocity. The possible reason is that large bubbles turn to vibrate seriously during movement, if the probe hits the part of a large bubble that is vibrating in the opposite direction of the bubble velocity, then the velocity detected by the probe will be much lower than the real velocity of the bubble. Besides, the flow field in bubble columns is very complicated and it affects the bubble velocity seriously. The simultaneous existence of down flow liquid stream may also decrease the velocity of some large bubbles.

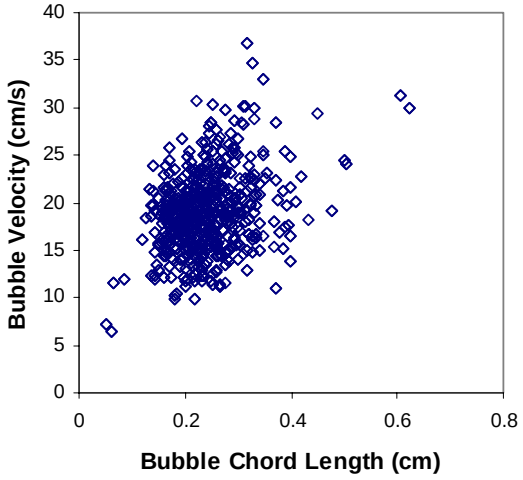

(a) Ug=2 cm/s

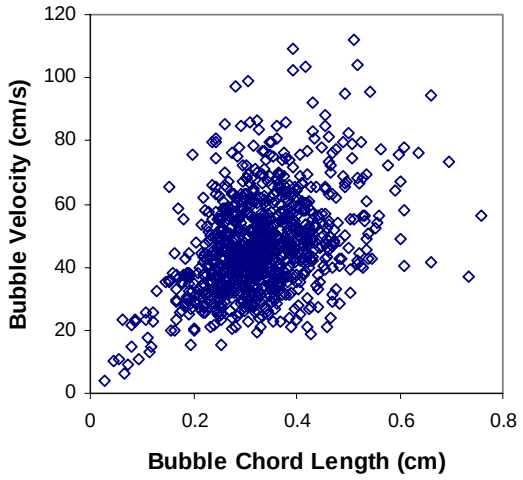

(b) Ug=8 cm/s

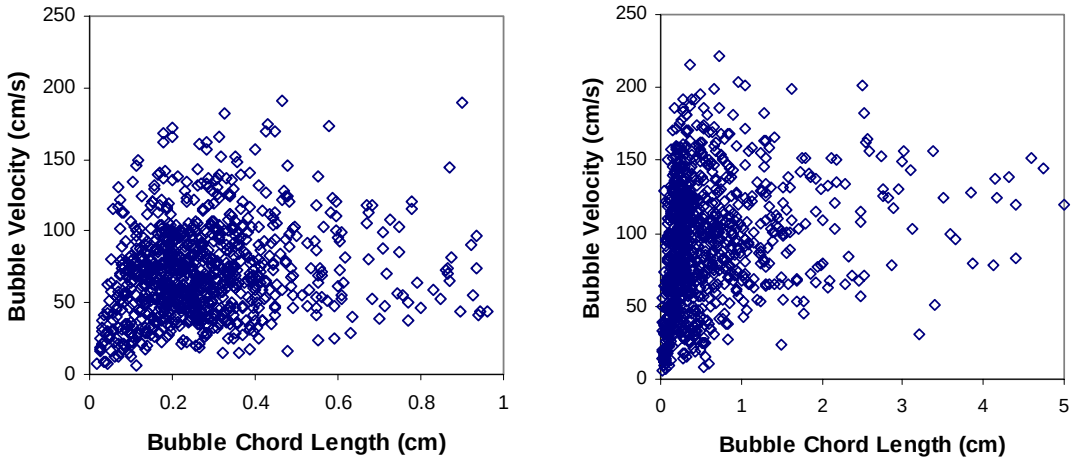

(c) Ug=14 cm/s **(d) Ug=60 cm/s**

Figure 5-12. Bubble Velocity vs. Bubble Chord Length (z/D=5.1, r/R=0)

5.4 The Effect of Pressure

Pressure is one of the key operating variables that affects the hydrodynamics in bubble columns. To investigate the pressure effect, bubble properties at 0.1MPa, 0.4MPa and 1.0MPa and at Ug=30cm/s were determined in this study. It can be seen from Figure 5-13 that both gas holdup and specific interfacial area increase greatly with pressure in the range of 0.1MPa to 1.0 MPa at Ug=30cm/s, and the increase is almost uniform across the column diameter. Furthermore, the increases in gas holdup and specific interfacial area when pressure increases from 0.1 MPa to 0.4 MPa are much larger than when pressure increases from 0.4 MPa to 1.0 MPa, i.e., the effect of pressure is weak when pressure increases from 0.4 MPa to 1.0 MPa, especially for the specific interfacial area (Figure 5-13b).

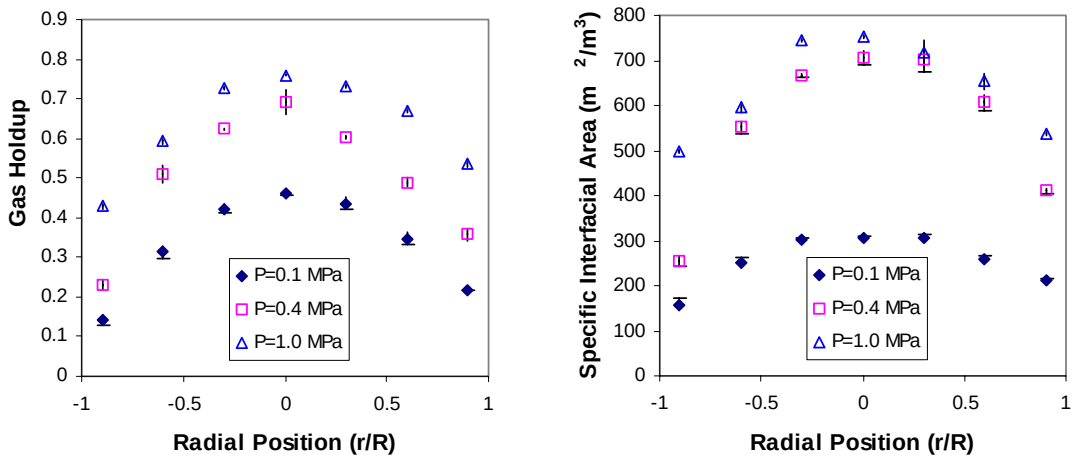

(a) **(b)**

Figure 5-13. Pressure Effect on (a) Gas Holdup and (b) Specific Interfacial Area (Sparger #3, 30 cm/s, z/D = 5.1)

In the studies conducted by LaNauze and Harris (1974) and Fan et al. (1999), it was shown that with increasing pressure, smaller and more frequent bubbles are formed at the gas sparger, which is attributed to the increased contribution of the gas momentum to the bubble formation process. According to the study by Igodawa et al. (1987), for sparger #3 and at Ug=30 cm/s, the bubble formation is in bubbling regime at 0.1MPa and it is in jetting regime at 0.4 and 1.0 MPa (Boon Cheng Ong, 2003). In the jetting regime, it was observed that smaller and more frequent bubbles are formed at a single orifice (Igodawa et al., 1987). This was proved by the bubble frequency in the sparger zone of the bubble column obtained by the four-point probe at different pressures, as shown in Figure 5-14a. It can be seen from Figure 5-14 that the bubble frequency increases greatly with pressure in the sparger zone and even beyond the sparger zone at z/D=5.1.

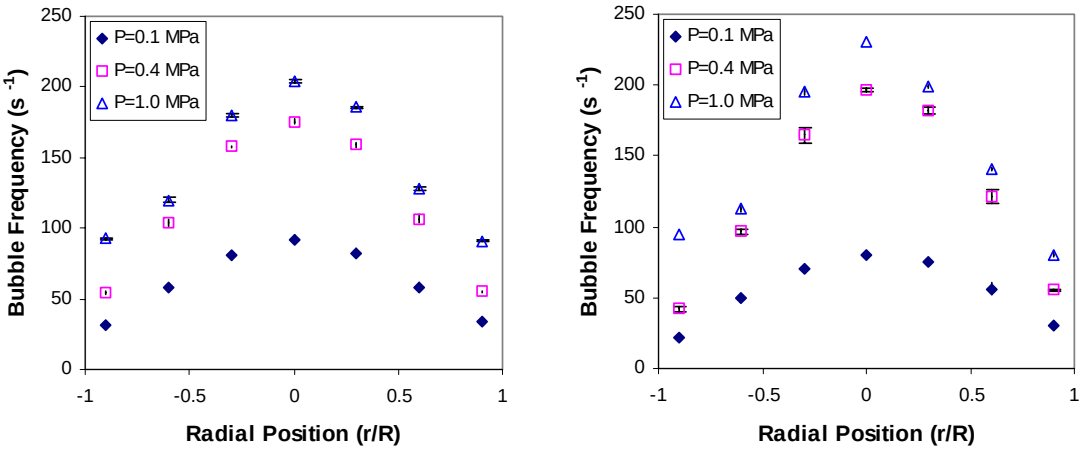

(a) z/D=1.7 **(b) z/D=5.1**

Figure 5-14. Pressure Effect on Bubble Frequency (Sparger #3, 30 cm/s)

In the core of the column, the mean bubble velocity also increases with pressure, but this increase is not as prominent as that of gas holdup and specific interfacial area (Figure 5-15). This is because on one hand the bubble size decreases with pressure; on the other hand, liquid recirculation is enhanced at high pressure (Boon Cheng Ong, 2003). These two factors have opposite effects on the mean bubble velocity: the former decreases the bubble velocity, because small bubbles have lower terminal velocity than large bubbles; the later increases the bubble velocity, since bubbles move with the liquid flow. These two factors somewhat counteract each other, so that the net effect of pressure on mean bubble velocity is weak. In the wall zone the downward movement of bubbles was obviously enhanced with the pressure. This is because the enhancement of the liquid recirculation dominates in the wall zone since there are no large bubbles there, thus the decrease of the bubble size with pressure was not as significant as in the core of the column. In short, at higher pressure the mean bubble velocity profile becomes more parabolic.

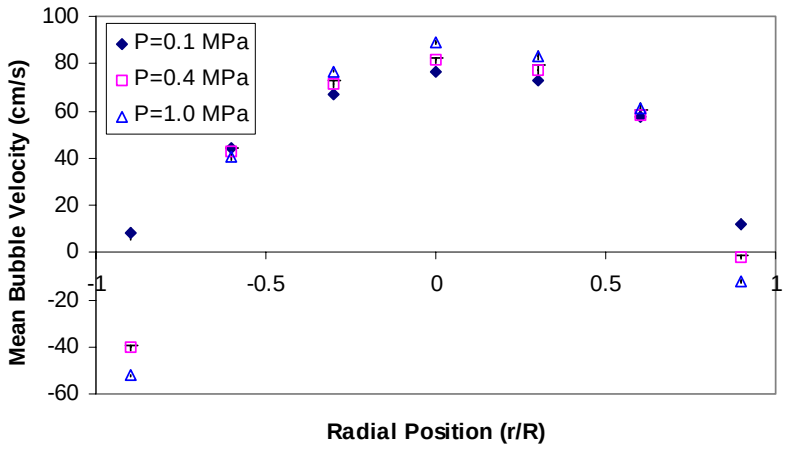

Figure 5-15. Pressure Effect on Mean Bubble Velocity (Sparger #3, 30 cm/s, z/D = 5.1)

It can be seen from Figure 5-16a that pressure does not affect the bubble velocity distribution very much in the column center. To a small extent, the percentage of bubbles moving downwards decreases with pressure, but the shape of the bubble velocity distribution is essentially identical. The situation is different in the wall zone, as shown in Figure 5-16b and 5-17c. In the wall zone, at r/R=-0.9 the percentage of bubbles that moved downwards increased greatly with pressure, so that the shape of the bubble velocity distribution changed notably with pressure. However, at r/R=0.9 the change of the shape of the bubble velocity distribution with pressure is not obvious. It is also noticed that in the column center the mean velocity of bubbles moving upwards increases somewhat with pressure, while that of bubbles moving downwards decreases. The opposite trend occurs in the wall zone. This means that the liquid recirculation is enhanced by pressure since bubbles move with the liquid flow in bubble columns. The same conclusion was reached in CARPT experiments at the same conditions by Boon Cheng Ong (2003) and in the literature (Jiang *et al.*, 1995; Fan *et al.*, 1999; Chen *et al.*, 1999b). This conclusion is in line with the analysis of the effect of pressure on the mean bubble velocity profiles reviewed before.

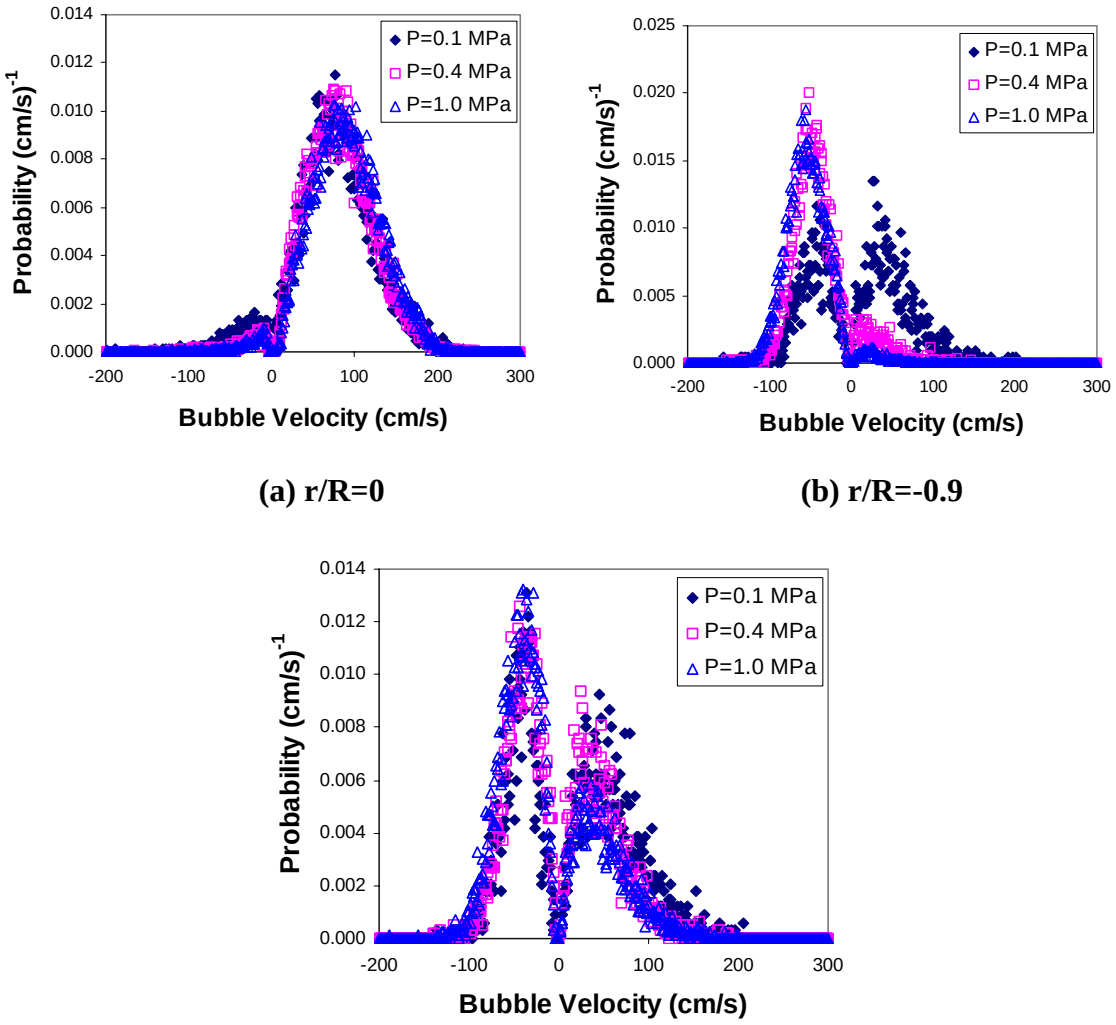

(a) r/R=0

(b) r/R=-0.9

(c) r/R=0.9

Figure 5-16. Pressure Effect on Bubble Velocity Distribution (Sparger #3, 30 cm/s, z/D = 5.1)

As shown in Figure 5-17, the shape of the bubble chord length distribution changes somewhat with pressure and the mean bubble chord length decreases in both the wall zone and the column center when the pressure changes from 0.1 MPa to 0.4 MPa. It is expected that the bubble size decreases with pressure (Fan *et al.*, 1999; Lin, Tsuchiya and Fan, 1998). Nevertheless, at pressure higher than 0.4 MPa, the mean bubble chord length stays almost identical and in some cases increases slightly with pressure. One explanation might be that when the number of large bubbles decreases with pressure, the number of

small bubbles in the wake of large bubbles also decreases. Furthermore, as expected, the mean bubble chord length in the column center is much larger than that in the wall zone, due to the assembly of large bubbles in the column center.

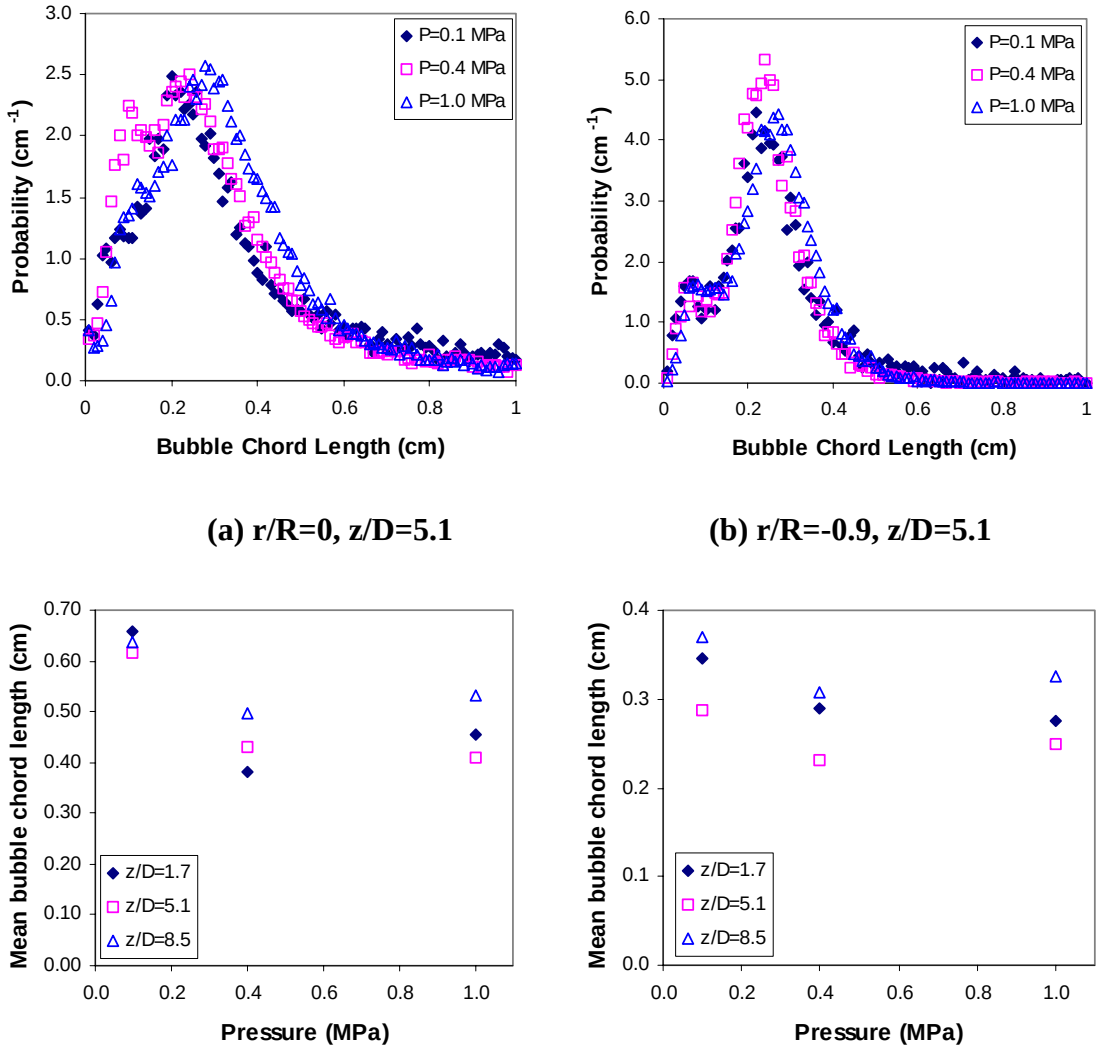

(a) r/R=0, z/D=5.1 **(b) r/R=-0.9, z/D=5.1**

(c) r/R=0 **(d) r/R=-0.9**

Figure 5-17. Pressure Effect on the Bubble Chord Length Distribution and Mean Bubble Chord Length (Sparger #3, 30 cm/s)

5.5 The Effect of Spargers

It has been reported that the configuration of the sparger, e.g., the number and size of the orifices, affects the generation of bubbles and subsequently may affect the hydrodynamics in bubble columns (LaNauze and Harris, 1974; Tsuge and Hibino, 1983; Idogawa *et al.*, 1987; Tsuge *et al.*, 1992; Yoo *et al.*, 1998; Snabre and Magnifotcham, 1998; Terasaka *et al.*, 1999; Hsu *et al.*, 2000). As shown in Figure 5-2 and detailed in Table 5-2, three spargers were used in this study: a cross sparger (sparger #1), a perforated plate with 0.15% open area (sparger #2), and a perforated plate with 1.0% open area (sparger #3).

It was found that, in the sparger zone (z/D=1.7), the bubble frequency increased in the order of sparger #1, sparger #3, and sparger #2, as shown in Figure 5-18. Sparger #1 and sparger #3, which are totally different in their hole numbers, hole sizes, and hole distributions, generate bubbles of relatively similar properties, e.g., bubble frequency, etc.

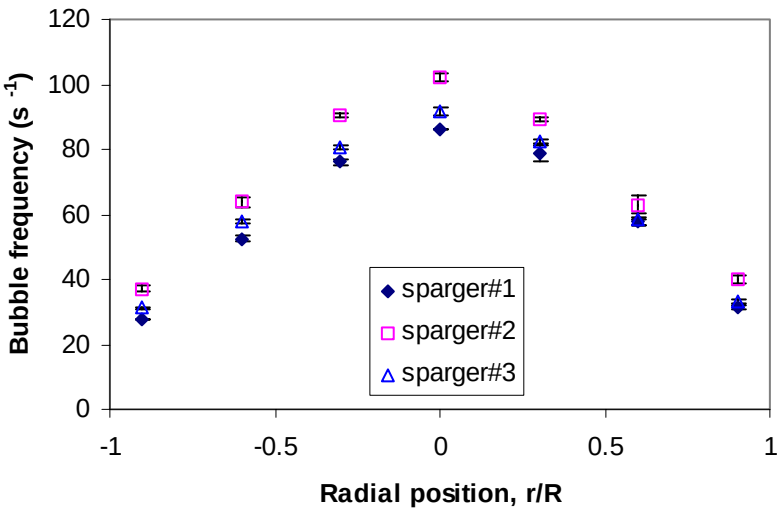

Figure 5-18. Sparger Effect on Bubble Frequency in the Sparger Zone (z/D=1.7, Ug=30cm/s, 0.1 MPa)

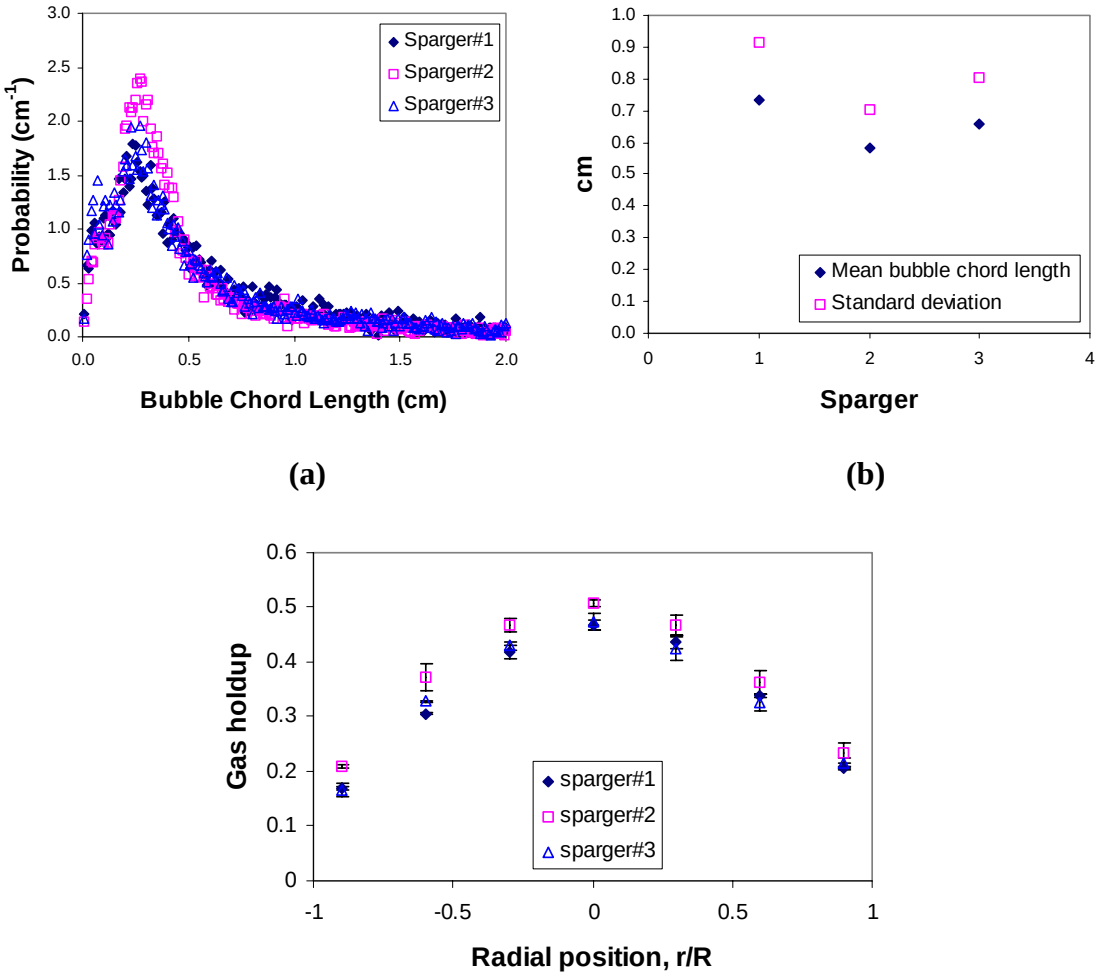

Figure 5-19. Sparger Effect on Bubble Chord Length Distribution and Local Gas Holdup (0.1MPa, 30 cm/s, z/D = 1.7, r/R=0)

Figure 5-19 shows the bubble chord length distributions in the column center in the sparger zone (z/D=1.7) for the three spargers. The distributions for sparger #1 and #3 are alike, except sparger #3 produced an additional peak at small values of bubble chord length. The bubble chord length distribution for sparger #2 has a higher probability density at small values of chord length. The mean bubble chord length and standard deviation of the bubble chord length distributions decreases in the order of sparger #1, sparger #3, and sparger #2 (Figure 5-19b). Consequently, the local gas holdup at z/D=1.7 increases in the same order, i.e., sparger #2 produced the highest local gas holdup and

sparger #1 and #3 gave almost the same gas holdup, as shown in Figure 5-19c. Some correlations have been developed for the estimation of the initial bubble size at the sparger (Ellenberger and Krishna, 1994; Leibson *et al.*, 1956; Wallis, 1969). The estimated initial bubble sizes based on these predictions are listed in Table 5-4 (Boon Cheng Ong, 2003). Obviously the initial bubble size by the prediction of Ellenberger and Krishna (1994) is too large. The initial bubble sizes predicted by Leibson *et al.* (1956) and Wallis (1969) are of the same order of magnitude as the mean bubble chord length obtained by the four-point probe. Although the bubble size increases with axial position in the sparger zone due to bubble coalescence so that the bubble size at the measuring position of the probe (z/D=1.7) is larger than at the sparger, the bubble size predicted by the proposition of Wallis (1969) for sparger #2 and #3 still seems to be too small. Furthermore, the initial bubble size increases in the order of sparger#1, sparger#2 and sparger#3 according to the prediction of Leibson *et al.* (1956), while the mean bubble chord length obtained by the probe (r/R=0) increases in the order of sparger#2, sparger#3 and sparger#1. Hence, the initial bubble size estimated by these predictions does not fit the experimental results in this study.

Table 5-4. Comparison of the Predicted Initial Bubble Size and Mean Bubble Chord Length Obtained by the Four-Point Optical Probe

Sparger	P MPa	Ug cm/s	Initial bubble size, cm			Mean chord length by probe*, cm	
			Ellenberge & Krishna, 1994	Leibson *et al.*, 1956	Wallis 1969	r/R=0	r/R=-0.9
1	0.1	30	14.3	0.41	0.52	0.731	0.357
2	0.1	30	3.25	0.42	0.1	0.582	0.265
3	0.1	30	3.25	0.48	0.25	0.659	0.368

* In the sparger zone, z/D=1.7.

The bubble velocity distributions in the sparger zone for different spargers are shown in Figure 5-20. It was found that sparger #1 and sparger #3 generated approximately the same bubble velocity distribution at different radial positions in the sparger zone (Figure 5-20a, 5-23b and 5-23c). Sparger #2 generated more bubbles moving downwards in the wall zone, especially at r/R=-0.9 (Figure 5-20b). This is also clear from the radial profiles

of the mean bubble velocity for different spargers (Figure 5-20d), where it can be seen that, for the three spargers used, the mean bubble velocity for sparger #2 is the smallest in the wall zone.

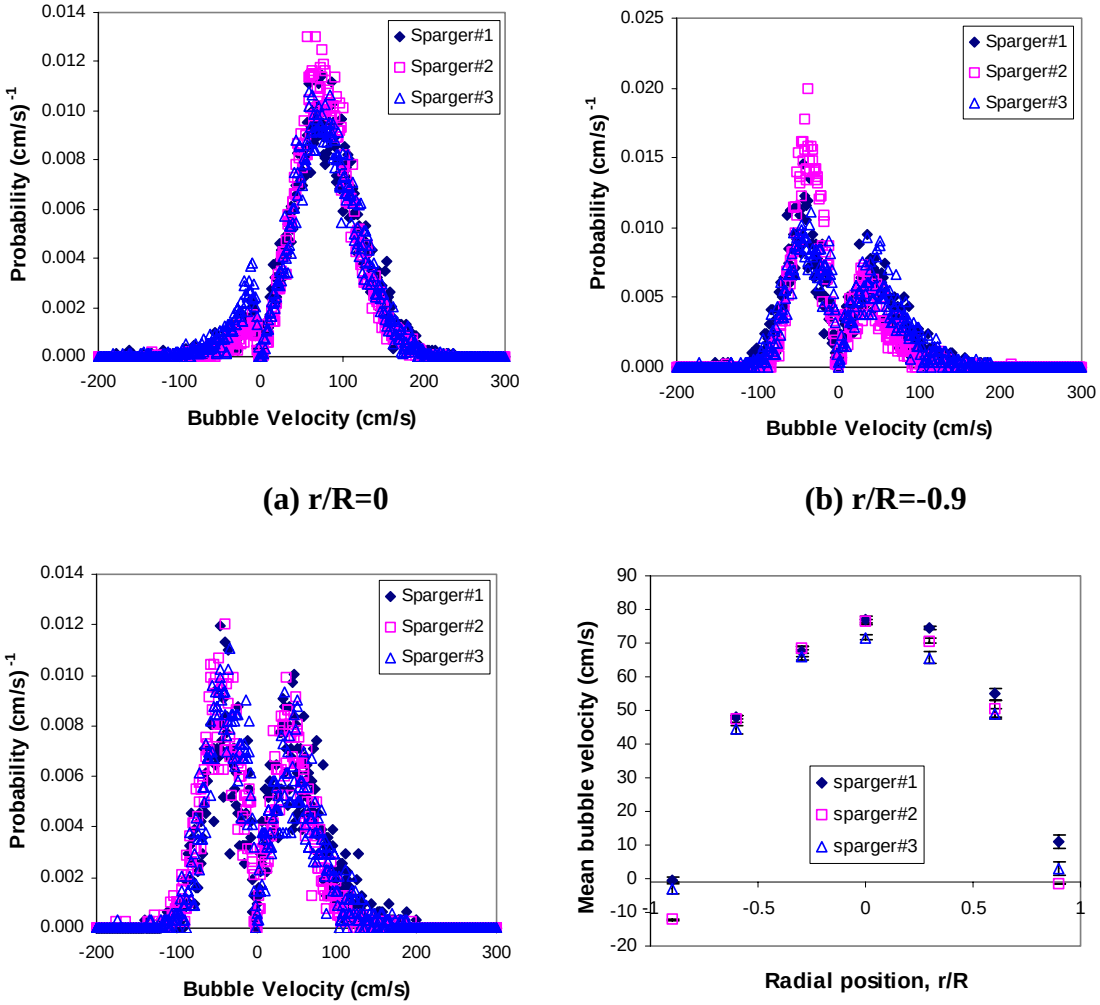

Figure 5-20. Sparger Effect on Bubble Velocity Distribution and Local Gas Holdup (0.1MPa, 30 cm/s, z/D = 1.7)

Sparger #2 also produced a higher specific interfacial area in the sparger zone than the other two spargers, as shown in Figure 5-21. This is in agreement with the radial profiles of the local gas holdup (Figure 5-19c) and bubble frequency (Figure 5-18), due to the correlation of these three variables.

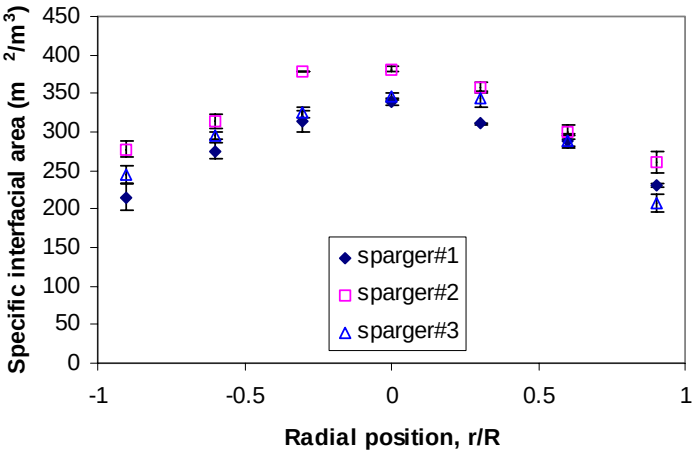

Figure 5-21. Sparger Effect on Specific Interfacial Area (0.1MPa, 30 cm/s, z/D = 1.7)

Earlier by CT and CARPT experiments Boon Cheng Ong (2003) found that deep in the churn-turbulent flow regime (Ug≥30cm/s) at atmospheric pressure there are small effects of the distributor on the radial gas holdup profile and liquid recirculation in the fully developed region (z/D≥5.5). The sparger effect on bubble properties in the fully developed region obtained by the four-point probe is shown in Figure 5-22. It can be seen that at atmospheric pressure, the sparger effect on the radial profile of gas holdup, bubble frequency, mean bubble velocity, and specific interfacial area is small at z/D=5.1. The exception is noted in the wall zone for mean bubble velocity and may be caused by the existence of coherent structures (Groen et al., 1996), which makes the flow field in the wall zone asymmetric and causes frequent changes in the flow direction. In other words, the radial profiles of the bubble frequency, the mean bubble velocity, and the specific interfacial area for the three spargers follow the same rule as the gas holdup profiles.

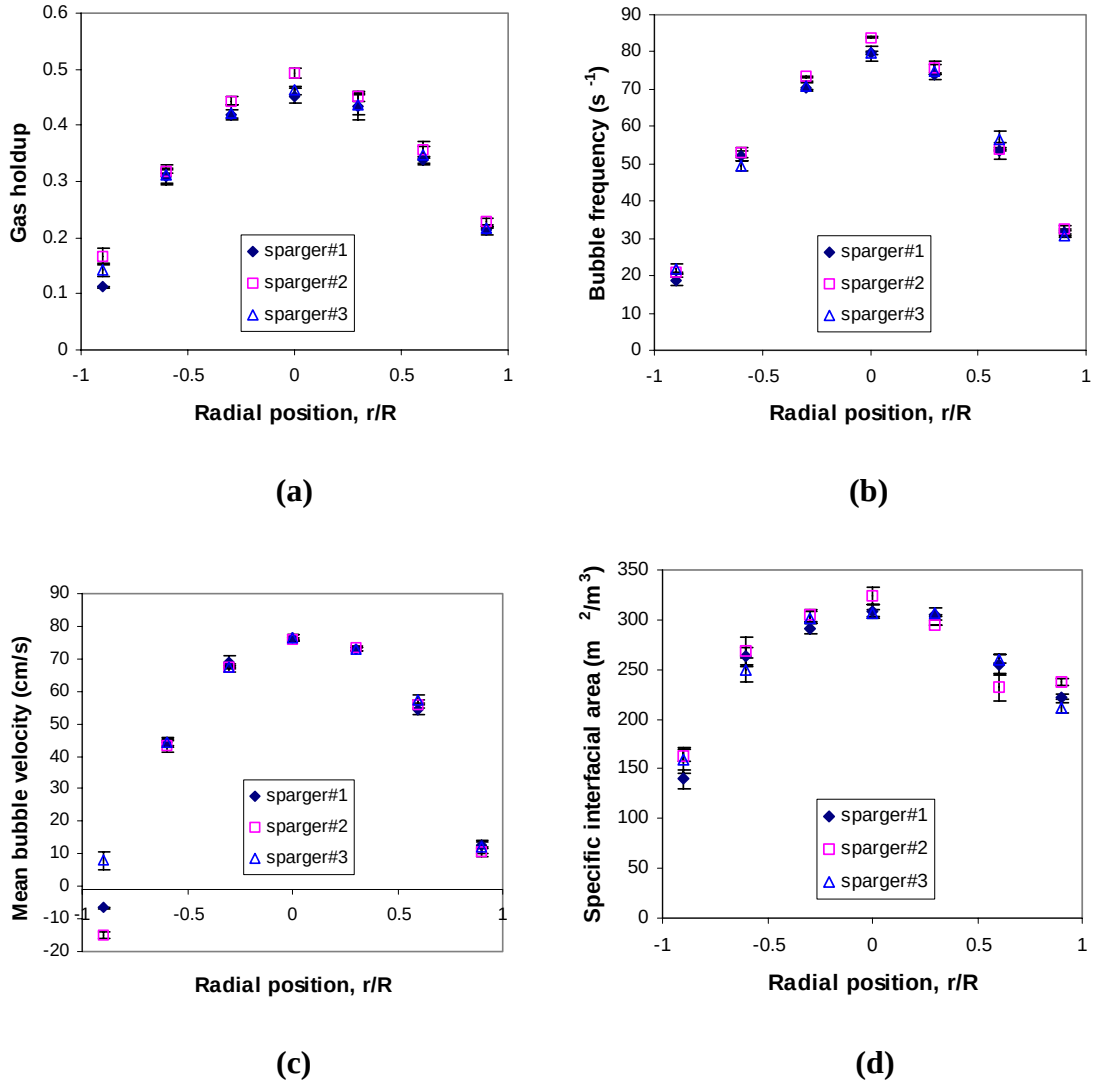

Figure 5-22. Bubble Properties at z/D=5.1 for Different Spargers

5.6 The Effect of Axial Position

In churn-turbulent flow, in the near sparger region, the bubble size continuously changes with respect to distance from the sparger and finally attains the equilibrium bubble size distribution, which is decided by the balance between bubble breakup and coalescence in bubble columns. The region where the bubble size changes is called the sparger region. The height of the sparger region depends on the configuration of the column and the sparger, the properties of the liquid and gas phase, and the operating conditions. It was

reported that the height of the sparger region in bubble columns is in the range of $1 \leq z/D \leq 5$ (Joshi et al., 1998). On the other hand, Shollenberger et al. (1997) reported sparger effect only up to 2.5 diameter heights in churn-turbulent flow. Beyond the sparger region, the gas holdup profile does not change with axial position in the bubble column. Besides the gas holdup profiles, the changes in other bubble properties with axial position were also investigated in this study.

At high pressure, it is observed that the gas holdup increases with the axial position in the column (Figure 5-23b and c), while at atmospheric pressure, when the other conditions are the same, the effect of axial position on the gas holdup profile was not obvious (Figure 5-23a). This result at high pressure is contrary to the findings at Sandia National Laboratory (Shollenberger, Torczynski and George, 2002). However, the liquid system used in their research was drakeoil, not water.

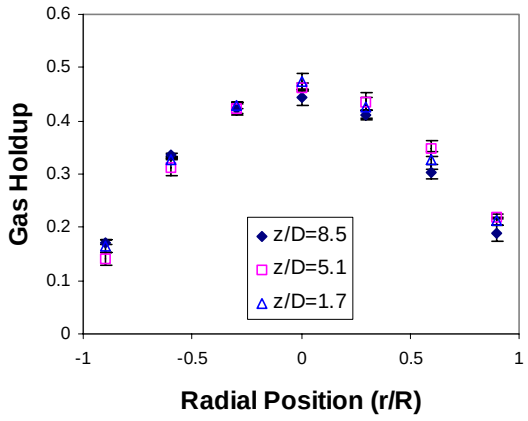

(a) 0.1MPa

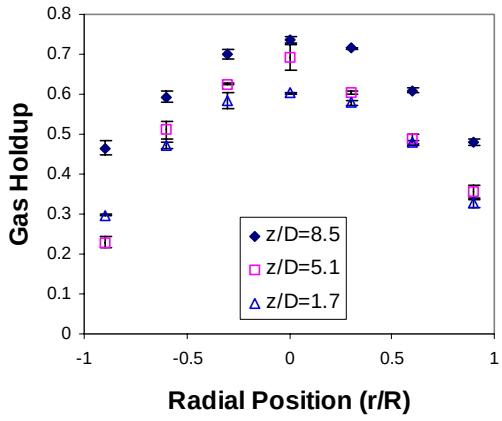

(b) 0.4MPa

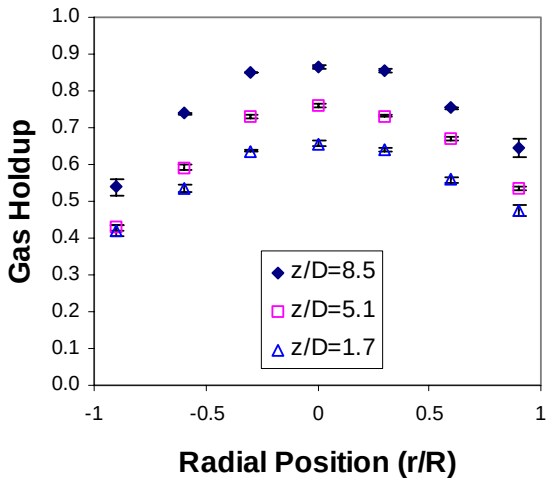

(c) 1.0MPa

Figure 5-23. Gas Holdup Profile at Different Axial Positions at High Pressure (Sparger #3, Ug=30 cm/s)

The reason for the increase in the gas holdup with the axial position at high pressure can be found by analyzing the holdup of large bubbles and small bubbles in the column center, as shown in Figure 5-24. The classification of bubbles into large and small ones is explained in detail later in Section 5.8. It can be seen that at atmospheric pressure the small bubble holdup decreases with axial position in the sparger zone and arrives at a constant value at z/D>5.1, while the large bubble holdup increases in the sparger zone and reaches its asymptotic value in the fully developed zone. This is because bubble coalescence leads to a decrease in the number of small bubbles and an increase in the number of large bubbles in the fully developed region. At high pressure, the small bubble holdup does not change much with the axial position, while the large bubble holdup keeps increasing in the axial direction.

The reason for this difference between atmospheric pressure and high pressures is unknown. One possibility is that an increase in pressure causes a decrease in the bubble size, and smaller bubbles are more stable than large bubbles (Fan, 1999) at the free surface. Hence, at high pressures bubbles accumulate in the upper zone of the column, leading to an increase in gas holdup in the axial direction. The effect of pressure on

bubble coalescence and breakage has not been reported in the literature. As shown later, the examination of the change of bubble frequency along the axial direction of the column supports this explanation.

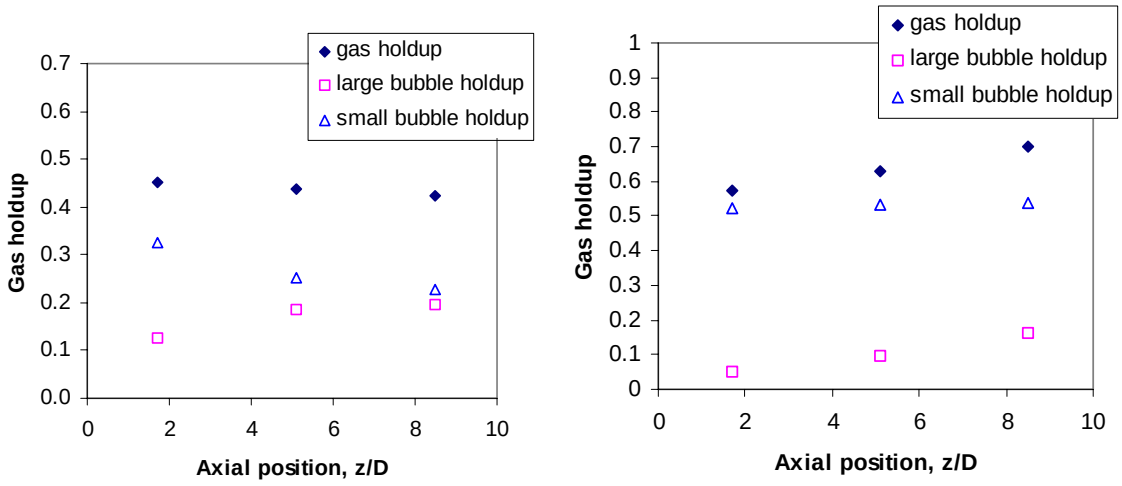

(a) 0.1 MPa

(b) 0.4 MPa

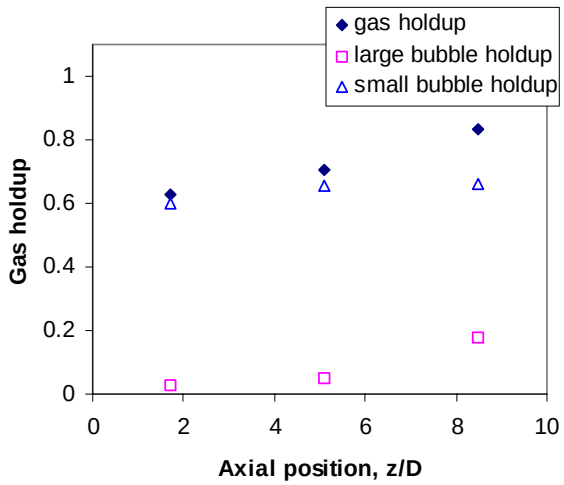

(c) 1.0 MPa

Figure 5-24. Large Bubble and Small Bubble Holdups (r/R=0)

At atmospheric pressure bubble frequency was higher in the sparger zone than in the upper zone of the column for the sparger used (Figure 5-25a). This supports the notion that bubble coalescence leads to a decrease in the number of small bubbles and an

increase in the number of large bubbles at atmospheric pressure. At high pressures, the opposite trend is true: the bubble frequency is lower in the sparger zone than in the upper zone of the column (Figure 5-25b and 5-30c). This fact supports the explanation for an increase in gas holdup in the axial direction at high pressure, i.e., the accumulation of bubbles in the upper zone of the column.

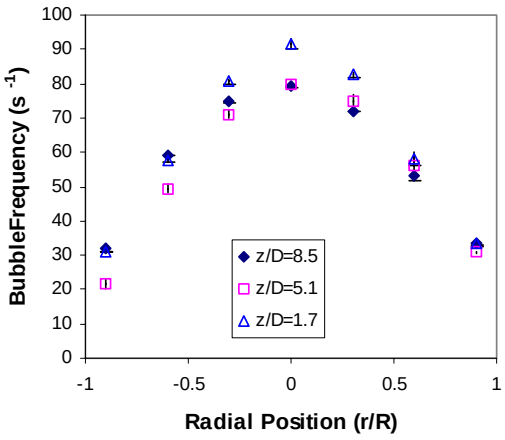

(a) 0.1MPa

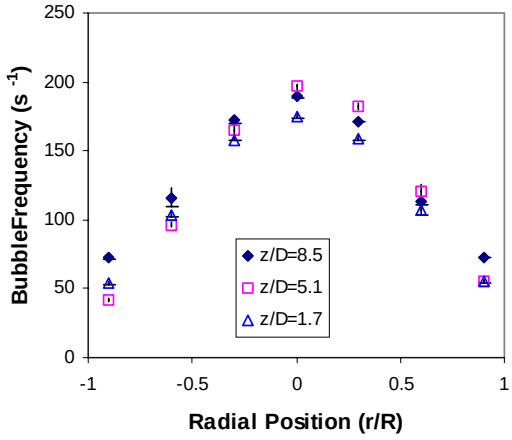

(b) 0.4MPa

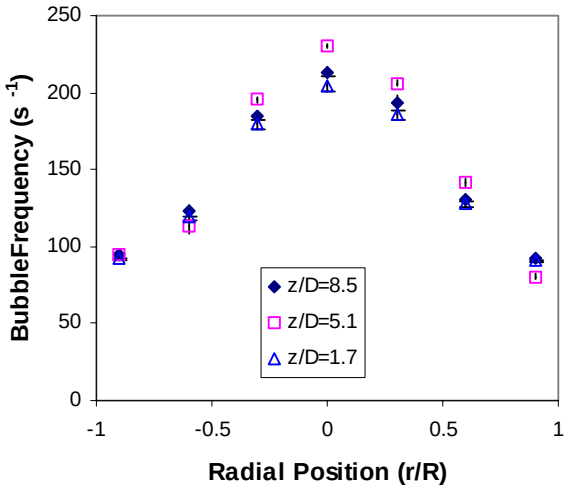

(c) 1.0MPa

Figure 5-25. Bubble Frequency Profile at Different Axial Positions (Sparger #3, Ug=30cm/s)

Figure 5-26 shows the bubble chord length distributions and mean bubble chord lengths at different pressures in the column center. The shape of the bubble chord length distributions is alike at different axial positions at high pressures (Figure 5-26a). The mean bubble chord length (Figure 5-26b) decreases slightly with axial position at atmospheric pressure, and it increases with axial position at 0.4 MPa and 1.0 MPa, which implies the enhancement of bubble coalescence due to the accumulation of bubbles in the upper zone of the column at high pressure. Furthermore, the mean bubble chord length decreases as pressure increases from 0.1 MPa to 0.4 MPa, as expected, but it does not change much at pressure higher than 0.4 MPa (Figure 5-26b).

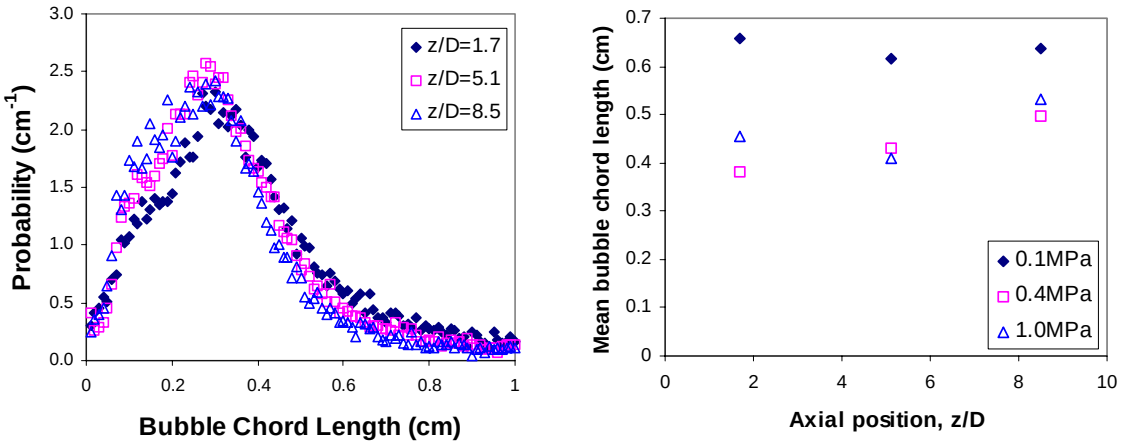

(a) 1.0 MPa **(b)**

Figure 5-26. Bubble Chord Length Distributions at High Pressure (r/R=0, Ug=30cm/s, sparger #3)

In bubbly flow and transition flow, the changes in the radial profile of specific interfacial area with axial position, as illustrated in Figure 5-27a, follow the same pattern as the gas holdup profile, since they are correlated. At high pressure, the specific interfacial area increased with axial position (Figure 5-27b and 5-26c), which was contrary to the situation at atmospheric pressure (Figure 5-27a). This is due to the obvious increase in the gas holdup (Figure 5-23) in the axial direction at high pressure.

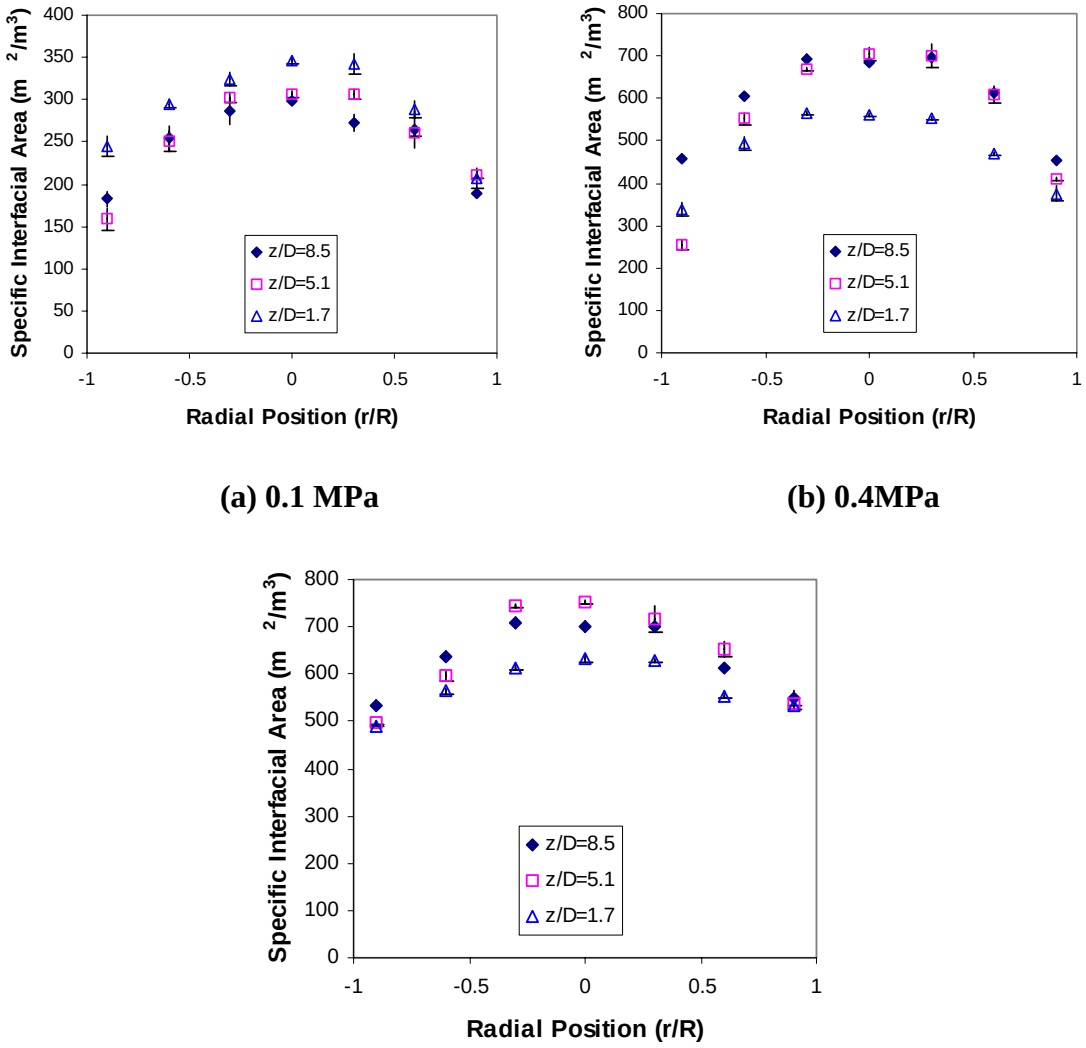

Figure 5-27. Specific Interfacial Area Profile at High Pressure

For the operating conditions employed in this study, the mean bubble velocity profile did not change much with axial position, except at low gas velocity (Ug =2 cm/s, shown in Figure 5-28). At Ug=2 cm/s the mean bubble velocity in the lower zone of the bubble column (z/D=1.7) was higher than that in the upper zone. This was possibly due to the large initial momentum of the bubbles jetting from the sparger and the lack of liquid recirculation at low gas velocity. This was not true when Ug ≥ 8 cm/s, i.e., in the transition and churn-turbulent region, where the mean bubble velocity in the core of the

column did not change much with axial position. The situation was the same at high pressure and for the other spargers. This means that in the transition and churn-turbulent regime the mean bubble velocity profile developed very fast in the axial direction; in other words, the sparger zone for the mean bubble velocity profile was small. In the wall zone, the mean bubble velocity was different at different axial positions in both bubbly flow and churn-turbulent flow. This change was due to the complexity of the flow field, i.e., the flow direction changed with time and the existence of flow cells (Groen et al., 1996).

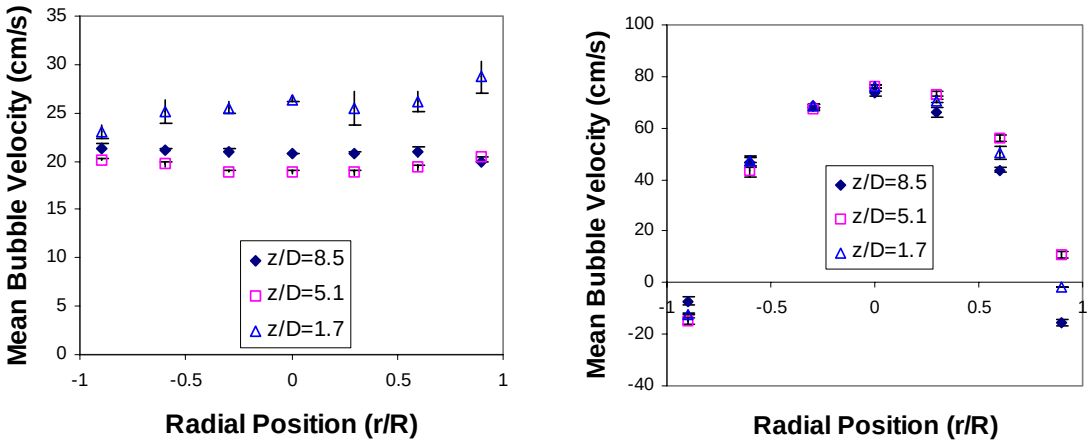

(a) Ug=2cm/s **(b) Ug=30 cm/s**

Figure 5-28. Mean Bubble Velocity Profile at Different Axial Positions (Sparger #2, 0.1MPa)

5.7 The Sauter Mean Bubble Diameter

Based on the local gas holdup and specific interfacial area obtained by the four-point probe, the Sauter mean bubble diameter, d_s, can be calculated with Equation (2-1). As discussed in Section 4.2, Equation (2-1) is accurate only for spherical bubbles. In bubble columns, although most bubbles are not spherical, the Sauter mean bubble diameter obtained with Equation (2-1) is still valuable for qualitative analysis. Actually it is widely used as a description of the magnitude of bubble size in bubble columns. Hence, this

parameter was also investigated in this study. The radial profiles of the Sauter mean bubble diameter at different gas velocities are shown in Figure 5-29. At Ug=2 cm/s, the radial profile of d_s is flat, which is reasonable for bubbly flow. At Ug=8 cm/s and 14 cm/s, the radial profile of d_s is roughly flat. At higher gas velocity, the profile becomes parabolic due to an increase in d_s in the column center and a decrease in the wall zone. This is true for churn-turbulent flow where large bubbles assemble in the central stream. It is also observed from Figure 5-29 that, unlike the radial profiles of gas holdup and specific interfacial area shown before, the radial profile of d_s is rather irregular, i.e., the variation is large so that the profile is not smooth. This lack of smoothness of the radial profile indicates that the error in the Sauter mean bubble diameter obtained by Equation (2-1) is large and is most likely due to different bubble shape in various regions.

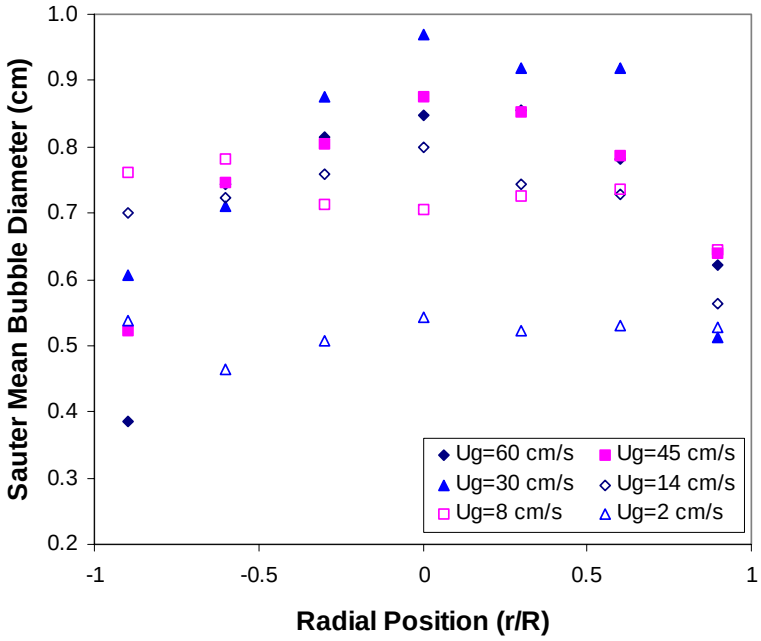

Figure 5-29. Sauter Mean Bubble Diameter at Different Ug (Sparger #2, 0.1 MPa, z/D=5.1)

As expected, the radial profile of the Sauter mean bubble diameter becomes flat at high pressure, and the value of d_s decreases greatly compared to the value at atmospheric pressure (Figure 5-30). Furthermore, d_s does not change much as the pressure changes

from 0.4 MPa to 1.0 MPa. This is consistent to the results for bubble chord length distribution as shown in Figure 5-26b. The above analysis indicates that while the Sauter mean bubble diameter is a valuable parameter to qualitatively describe the bubble size in bubble columns, it is subject to large errors.

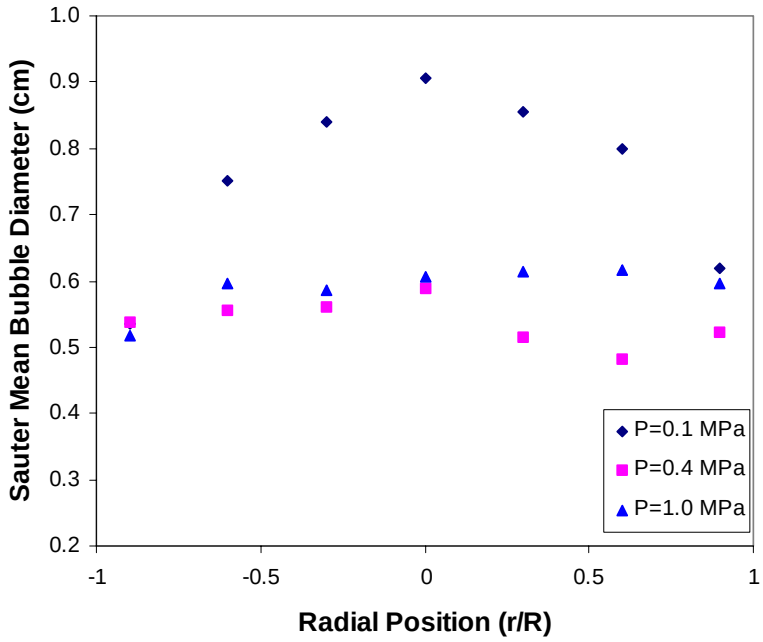

Figure 5-30. Sauter Mean Bubble Diameter at Different Pressures (Sparger #3, Ug=30cm/s, z/D=1.7)

5.8 The Bubble Size Distribution

Krishna, Wilkinson and van Dierendonck (1991) inferred from gas disengagement experiments that there are both large and small bubbles in churn-turbulent flow. They proposed that beyond a certain regime transition velocity, the small bubble holdup is constant and the large bubble holdup keeps increasing with the gas velocity, as illustrated in Figure 5-31. Such a bimodal bubble size distribution is a characteristic feature of the churn-turbulent flow regime, they claimed.

However, Deshpande, Dinkar and Joshi (1995) provided another explanation for the gas disengagement experimental results. They thought that the initial faster disengagement is due to internal liquid circulation and not due to the presence of very large bubbles, and, hence, they claimed that the bimodal bubble size distribution is not necessarily proven by the results of gas disengagement experiments. Since the bubble size distribution is important in modeling, design and scaleup of bubble columns, this must be clarified. To address this, the time based bubble chord length distribution, the large bubble holdup, and small bubble holdup obtained by the four-point probe were investigated.

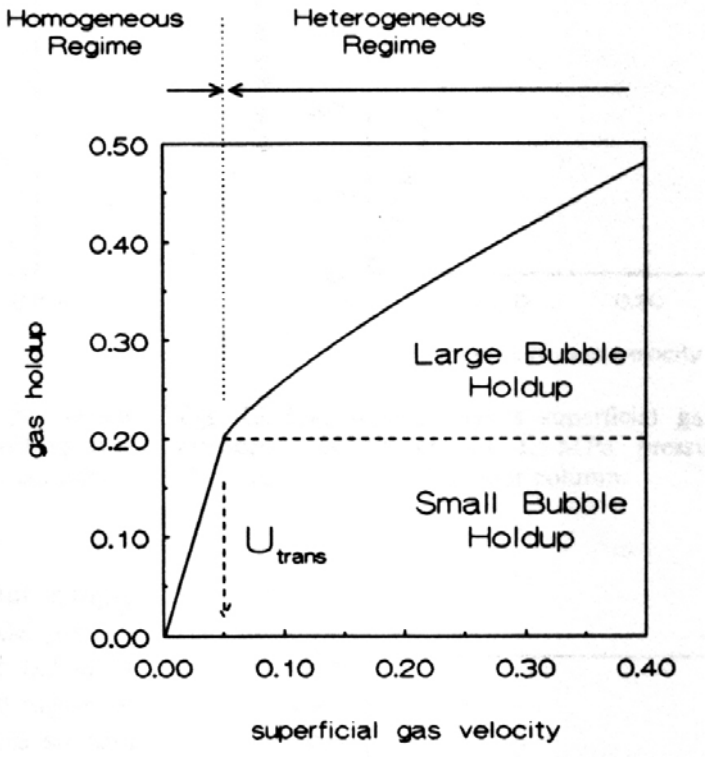

Figure 5-31. Gas Holdup Model in Bubble Columns Proposed by Krishna, Wilkinson, and van Dierendonck (1991)

It was necessary to classify bubbles into large and small based on an arbitrary criterion as to how long the probe tip resides in the bubble as indicated in Figure 5-32. At Ug=2cm/s, bubbly flow prevails in the column and there are few large bubbles. It can be seen in Figure 5-32 that the pdf of the bubble chord length ends at about t=0.02s at Ug=2 cm/s in

the center of the column at r/R=0, and actually this is true at all the radial positions. Hence, the criterion for distinguishing large and small bubbles is set to be t=0.02s. Based on this criterion, if the time interval that the probe tip spends in a bubble is larger than t = 0.02s, the bubble is classified as a large bubble; otherwise it is classified as a small bubble.

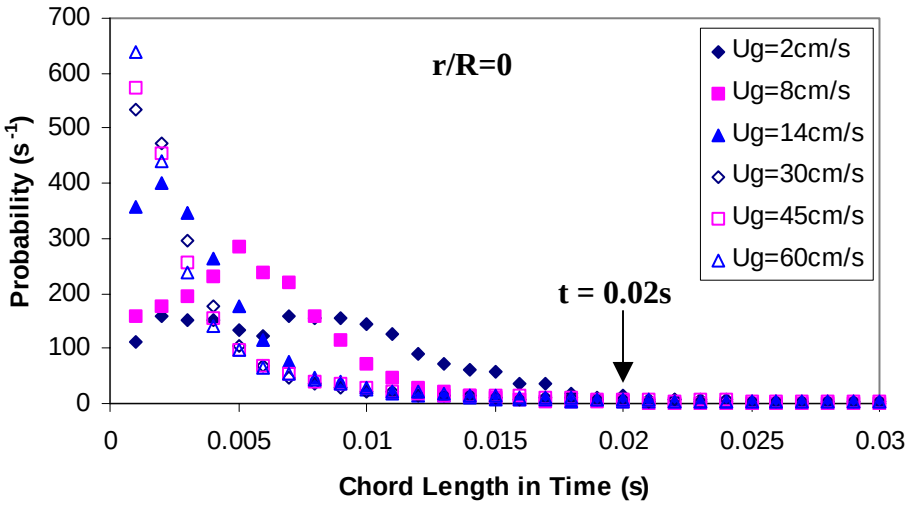

Figure 5-32. Time Based Bubble Chord Length Distribution Obtained by the Probe

Figure 5-33 shows the change of the local gas holdup, the large bubble holdup, and the small bubble holdup with superficial gas velocity at three radial positions, i.e., r/R=0, -0.6, -0.9, in the bubble column. The large bubble holdup is the contribution of the large bubbles to the gas holdup, which can be calculated as:

$$\varepsilon_L = \frac{\text{sum of time intervals larger than 0.02s}}{\text{Total measurement time}} \qquad (5\text{-}3)$$

The small bubble holdup can be obtained in the same way. It is shown in Figure 5-33 that in the core of the column (r/R=0, r/R=-0.6) both the small bubble holdup and the large bubble holdup increase with Ug in churn-turbulent flow, and the small bubble holdup increases faster. In the wall zone, the large bubble holdup in churn turbulent flow is low

and stays almost constant with an increase in Ug. Hence, the gas holdup model proposed by Krishna, Wilkinson, and van Dierendonck (1991) as shown in Figure 5-31 does not quite hold.

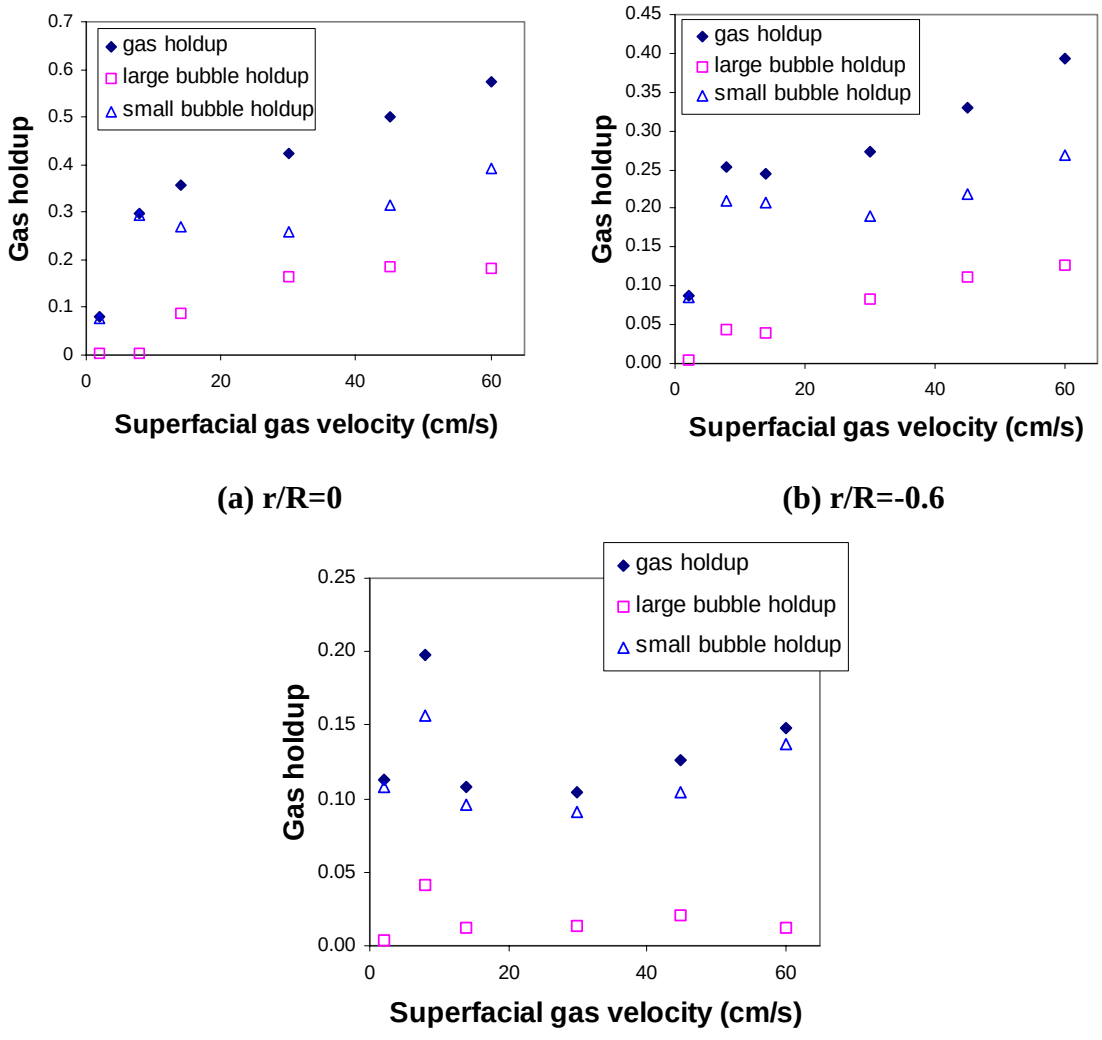

(a) r/R=0

(b) r/R=-0.6

(c) r/R=-0.9

Figure 5-33. Local Gas Holdup Obtained by the Probe

Figure 5-34 shows the contribution to the local gas holdup of the time intervals that the probe's central tip spends in bubbles. This is the volume based bubble chord length distribution in terms of time. It can be seen that the contribution of large bubble chord lengths to the local gas holdup increases with Ug, and becomes considerable at high Ug

in the core of the column (Figure 5-34a). In the wall zone, the large bubble holdup does not change much with Ug and is negligible even at Ug=60 cm/s (Figure 5-34b). Hence, it can be concluded that the volume based bubble size distribution is not bimodal. Rather, it is single modal in the range of operating conditions employed.

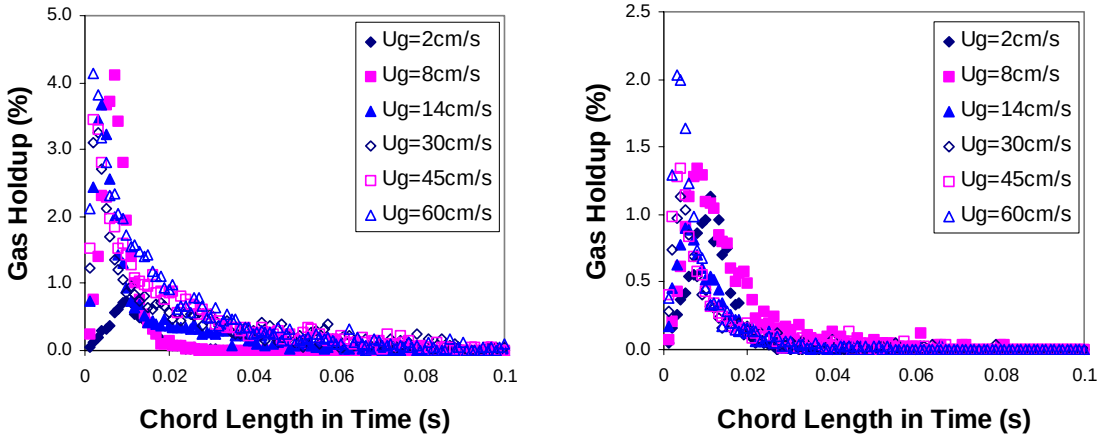

(a) r/R=0 **(b) r/R=-0.9**

Figure 5-34. Time Based Bubble Chord Length Distribution

The probe can detect only the bubble chord length distribution, and this is different from the bubble size distribution. For example, if the probe tip hits near the edge of a large bubble, a small chord length, which is possibly smaller than 0.02s, will be detected and this bubble will be classified as a "small" bubble according to the above criterion. However, the qualitative result obtained by the probe will not change due to the overwhelming number of small bubbles to large bubbles (Figure 5-32). Furthermore, it was found that a small change in this criterion does not change the shape of the gas holdup profiles shown in Figure 5-33. Hence, it is reasonable to expect that the bubble size distribution is also single modal in the range of operating conditions employed in this study, which cover both bubbly flow and churn-turbulent flow. A simulation as shown in Appendix D.4 also proves this.

The time based bubble chord length distribution and large and small bubble holdups at high pressure are shown in Figure 5-35. At high pressure the small bubbles contribute much more to the gas holdup than the large bubbles, and the small bubble holdup increases obviously with pressure, while the large bubble holdup decreases with pressure (Figure 5-35b). This is in line with the fact that the bubble size decreases with pressure. Hence, if the bubble size distribution is not bimodal at atmospheric pressure, neither is it at high pressure at the same gas velocity, due to the reduction of the number of large bubbles.

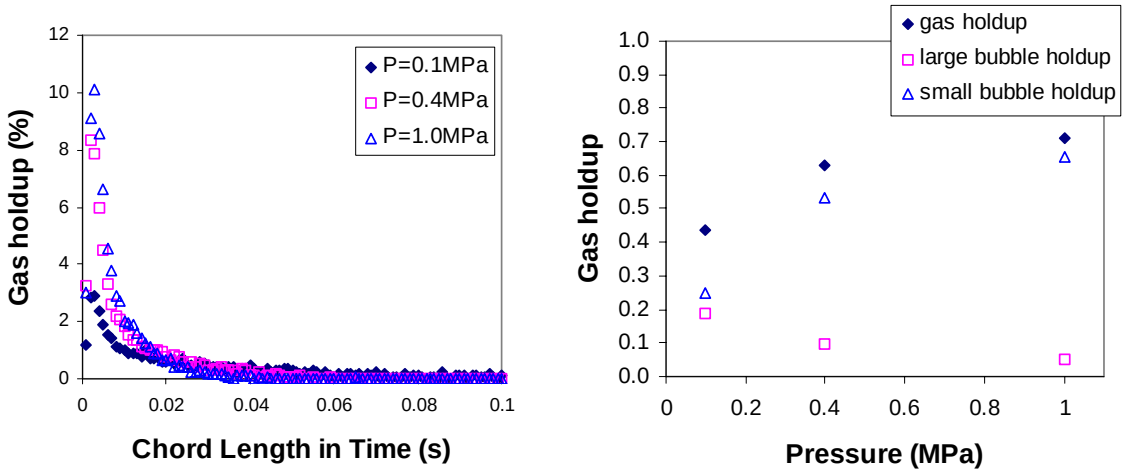

(a) **(b)**

Figure 5-35. Effect of Pressure on Time Based Bubble Chord Length Distribution and Gas Holdups (Sparger #3, Ug=30 cm/s, r/R=0, z/D=5.1)

As explained before, only when a bubble hits all the four tips of the probe, the bubble velocity and the bubble chord length can be obtained. The volume based bubble chord length distribution of these measured bubbles is a good analogue of that for the whole bubble population due to the fact that the bubbles hit the probe randomly. Some examples of the volume based bubble chord length distribution obtained by this means are shown in Figure 5-36. Actually Figure 5-36 shows the percentage of the sum of the bubble chord lengths pierced by the probe's central tip in each chord length class to the sum of all the bubble chord lengths pierced by the probe's central tip obtained by the four-point probe.

The shape of the distribution in Figure 5-36 is the same as the volume based bubble chord length distribution but in different scale. Actually the distribution in Figure 5-36 can be transferred to the volume based bubble chord length distribution can be obtained by multiplying the volume based local gas holdup (refer to Equation 4-10). However, the probe can only measure the time based gas holdup and the volume-based local gas holdup is unknown as explained in Section 4.3.

It can be seen that the volume based bubble chord length distributions have the same shape as time based bubble chord length distributions (Figure 5-34). Hence, the above analysis based on time based bubble chord length distribution is valid for volume based bubble size distribution. Therefore, while all the bubbles that hit the central tip of the four-point probe contribute to the local gas holdup, the volume based bubble chord length distribution obtained by the probe (Figure 5-36) utilizes only those bubbles whose velocity can be determined by the probe. On the other hand, the time based bubble chord length distribution utilizes the whole bubble population because every time interval that the probe's central tip spends in a bubble is employed in the derivation of the time based bubble chord length distribution. As described above, both of these distributions point to the same conclusion that the bubble size distribution is single modal in the range of operating conditions employed in this study.

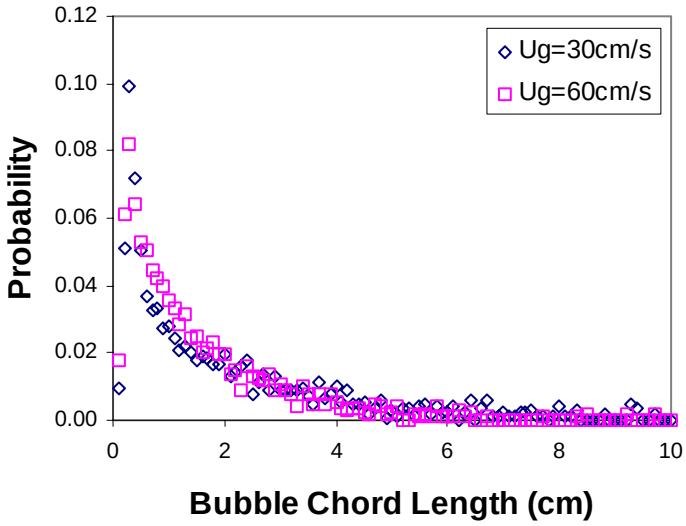

Figure 5-36. Volume Based Bubble Chord Length Distribution

5.9 The Mean Gas-Liquid Slip Velocity

The local gas-liquid slip velocity is defined as the relative velocity between the bubble and the surrounding liquid phase. This parameter is important in Computational Fluid Dynamics (CFD). When a bubble is moving in an infinite liquid phase, the slip velocity is equal to the bubble's terminal rise velocity. In bubble columns, in the homogeneous regime, the slip velocity is less than or equal to the bubble's terminal velocity, while in the heterogeneous regime, the slip velocity is larger than or equal to the bubble's terminal velocity (Fan and Tsuchiya, 1990).

By combining the local mean bubble velocity obtained by the four-point probe, $\overline{v_b}$, and the local mean liquid velocity, $\overline{v_l}$, obtained by CARPT (Boon Cheng Ong, 2003), the local mean gas-liquid slip velocity can be obtained as $v_s = \overline{v_b} - \overline{v_l}$. It is shown in Figure 5-37 that the bubble slip velocity increases from the column center towards the wall zone, and it reaches the maximum at r/R=0.6 at all the operating conditions studied. In the wall zone, i.e., at r/R=0.9, the slip velocity is much smaller than in the core of the column. As shown before in this study the bubble size in the wall zone is smaller than that in the core

of the column, and large bubbles usually have larger slip velocity than small bubbles. However, this is contrary to the observation that the slip velocity increases with r/R, since large bubbles tend to assemble in the central stream. Hence, in addition to the bubble size, there must be some other factors that affect the slip velocity, which, unfortunately, are unclear at present.

Figure 5-37a shows that the radial profiles of the mean slip velocity for the three spargers used in this study are almost identical. Figure 5-37b shows that, for sparger #2 at Ug=30cm/s and 45 cm/s, the slip velocity at different radial positions is identical. Finally Figure 5-37c shows that the slip velocity obviously decreases with pressure. This is in accord with the fact that the bubble size decreases with pressure.

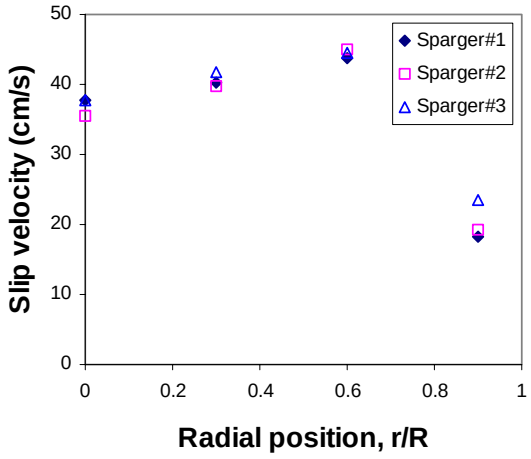

(a) P=0.1bar, Ug=30 cm/s

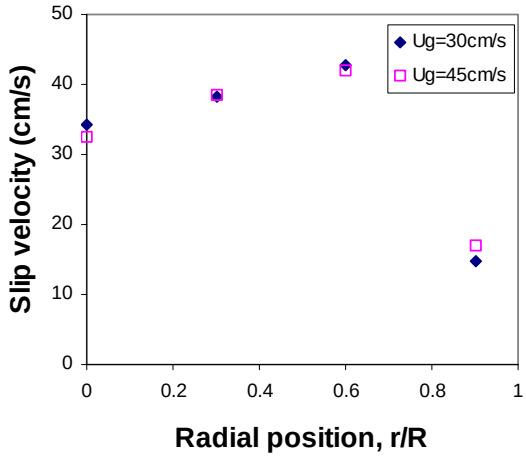

(b) P=0.1bar, sparger #2

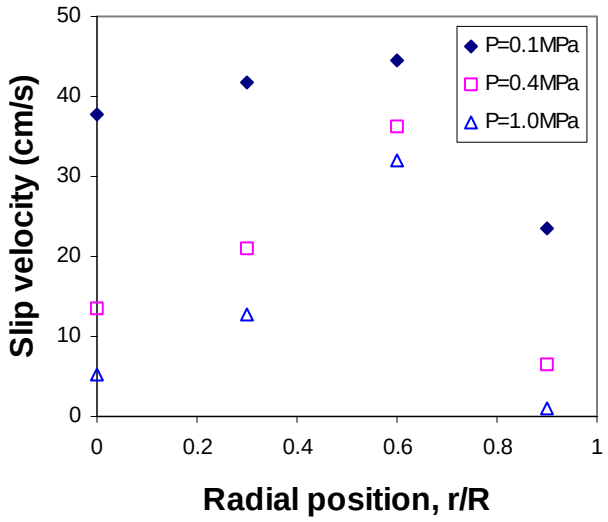

(c) Ug=30cm/s, sparger #3

Figure 5-37. Bubble Slip Velocity at Different Conditions

As mentioned before, the values of the mean gas-liquid slip velocity obtained by the four-point optical probe are valuable for CFD studies. However, such studies are beyond the scope of this study and will be followed up elsewhere.

Chapter 6 Conclusions and Future Work

The following conclusions can be derived from this study:

1. Two-point probes produce questionable results in systems having complex hydrodynamics, such as bubble columns, especially in transition and churn-turbulent flow regime.

2. The four-point optical probe and the new data processing algorithm is a practical tool for investigating bubble properties in bubble columns. By validation against video imaging, it was proved that the bubble velocity distribution, bubble chord length distribution, local gas holdup, and specific interfacial area obtained by the new four-point optical probe algorithm are reliable. Difficulties exist in the measurements of bubbles of very low velocity approximating to zero.

3. The four-point optical probe performed well both in bubbly flow and in highly churn-turbulent flow at superficial gas velocity up to 60 cm/s and pressure up to 1.0 MPa. Bubble properties at these conditions in a 6.4” bubble column were measured for the first time, which are valuable for CFD validation and for development of engineering models.

4. Some new findings about bubble properties in bubble columns are:

(1). In bubbly flow, the radial profiles of specific interfacial area, bubble frequency, and mean bubble velocity are all flat. With an increase in superficial gas velocity, Ug, these profiles became more parabolic. In the column center, the bubble chord length distribution spreads wider with an increase in Ug. The mean bubble chord length increases with Ug until it is in deep churn-turbulent flow and then remains almost identical with Ug. In the wall region, the bubble chord length distribution does not change much with Ug. The mean bubble chord

length in the wall region is much smaller than that in the column center, and it increases mildly with Ug between the bubbly flow and the transition flow regime, then decrease slightly with Ug.

(2). At very low gas velocity, e.g. 2 cm/s, all bubbles move upwards in bubble column. In churn-turbulent flow (Ug>8cm/s), some bubbles move downwards even in the column center. In the wall region, the number of bubbles moving downwards is equal to or even larger than that of bubbles moving upwards. The percentage of bubbles moving downwards increases slowly with Ug in both the wall region and in the core of the column. In the wall region, the bubbles moving downwards are dragged down by the liquid, while in the core of the column the flow direction is generally upwards most of the time, and the bubbles moving downwards most likely come from the wakes of large bubbles and large 3D flow structures.

(3). In bubbly flow, the bubble velocity distribution and bubble chord length distribution are alike at different radial positions, including the wall region. In churn-turbulent flow, in the core of the column the bubble velocity and chord length distributions are alike at different radial position, but in the wall region they are very different from the core of the column.

(4). With an increase in pressure, the global liquid recirculation is enhanced, and the radial profiles of specific interfacial area, bubble frequency, and mean bubble velocity become more parabolic. The gas holdup increases with the axial position, possibly due to the accumulation of bubbles at the upper zone of the column at high pressure. The pressure effect is strong at 0.1 MPa, but it becomes weaker at pressures higher than 0.4 MPa.

(5). Two of the three spargers used in this study, i.e. sparger#1 and sparger#3, generated similar bubble properties at the operating conditions employed,

although their configurations are totally different. Sparger#2 generates somewhat different bubble properties than the other two spargers, though not to a significant extent.

(6). In this study, the sparger effect disappears with an increase in the axial position in bubble column at z/D>5.1. However, at atmospheric pressure, the range of the sparger zone for the specific interfacial area is beyond z/D=5. Hence, the definition of the sparger zone based on gas holdup profiles may not apply to other bubble properties under some conditions. In other words, the range of the sparger zone for different bubble properties may be different.

(7). The Sauter mean bubble diameter cannot be calculated without assumptions that are not met and it is subject to large errors. Qualitatively it can be used for comparison of “mean” bubble size at different conditions.

(8). The bubble size distributions observed are single modal. Hence, the suggested bimodal bubble size distribution postulated for churn-turbulent flow was not detected.

(9). In this study, the mean gas-liquid slip velocity is almost identical for different spargers and at different superficial gas velocities in churn-turbulent flow, it decreases with pressure, due to a decrease in the bubble size.

Suggested future work to fully utilize the power of the four-point optical probe technique:

1. Use bubble properties data obtained by the four-point optical probe for validation and refinement of CFD codes.

2. Apply the four-point optical probe to a wider range of operating conditions, such as the superficial gas velocity, pressure, column diameter, and spargers, etc., to expand the

bubble properties data base and get a better understanding of the hydrodynamics in bubble columns. Besides, apply the four-point optical probe to multiphase reactors other than bubble column, e.g., stirred tank reactors.

3. Validate and apply the four-point probe in organic systems of industrial interest. In addition, apply the four-point probe at high temperature and pressure higher than 1.0 MPa. Exploit the potential of the probe technique to detect phase transition at supercritical conditions (see Appendix E).

4. Apply the probe in slurry bubble columns to test the durability of the probe against the collision of the particles. In the cases that the glass probe cannot stand long enough, e.g. systems with solid particles and high gas velocity, the plastic probe described in Appendix A should be used.

5. Commercialize the four-point probe technique to provide a tool which is simple and easy to use for the on site measurements of bubble properties, e.g. monitor the quality of the flow in multiphase reactors.

Appendix A The Plastic Fiber Optical Probe

An optical fiber probe made of plastic fibers (Polymethyl Meta Acrylate) was also developed in this research according to the methods employed by Saito and Mudde (2001). The fabrication of the plastic fiber probe is almost the same as that of the glass fiber probe, except that the tip of the plastic fiber is cut into a wedge of 30^{o} (Figure 3.14a), which is the optimal angle determined by trail and error, instead of being made conical with a flame as in the case with the glass fiber.

The plastic probe has the advantage over the glass probe that the size is small since there isn't any protective cladding cover on it (the outer diameter of plastic fibers used is 0.25mm, compared with 0.6mm for glass fibers). The smaller size of the probe reduces the disturbance of the probe to the flow field and makes the probe detects smaller bubbles. Furthermore, it is much more durable than the glass fiber probe due to the flexibility of the plastic fiber. Therefore, the plastic probe may be more suitable for use in slurry bubble columns where the glass probe may be broken by the particles in turbulent motion.

It can be seen from Figure 3.14b that the output voltage of the plastic fiber probe is low when the tip is in a bubble, and it is high when the tip is in the liquid phase, which is contrary to that of a glass fiber probe. This is determined by the characteristic of the photoelectric multiplier used. The processing of the responses is the same as that for the glass optical probe.

The disadvantages of the plastic fiber probe are: (1) It cannot endure high temperature (the permanent usage temperature of the plastic fiber used is 75^{o}C). (2) Some organic solution may do harm to the plastic fiber, this limits its application in organic systems. And (3) the flexibility of the fiber makes it tremble in turbulent flow, this will cause

errors in measurements. Moreover, the response of the plastic probe to a bubble is slower than that of a glass probe. This makes the front edge of its response to a bubble more inclined than that of a glass probe (Figure A-1).

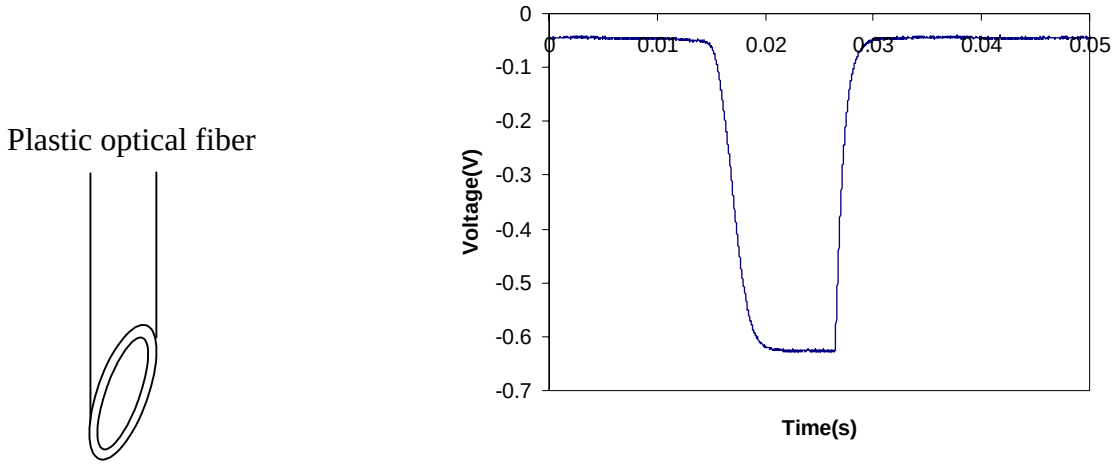

(a) The Wedge-Shaped Fiber Tip **(b) Response of a Single Fiber To a Bubble**

Figure A-1. The Tip Shape and the Response of a Single Plastic Optical Fiber to a Bubble Passage

Appendix B Derivation of the Transformation Matrix

The derivation of the transform matrix, $\underline{\underline{A}}$, in Equation (3-13) is shown as follows.

As shown in Figure 3-14, the xyz coordinate system was transformed to the x'y'z' system with z'-axis in the direction of the bubble velocity vector. This transformation can be accomplished with two rotations of the coordinate axes in xyz system: rotate angle φ around z axis and then rotate angle θ around y axis. Hence the rotation matrix, $\underline{\underline{A}}$, can be obtained as (Glassner, 1990):

$$\underline{\underline{A}} = \begin{bmatrix} \cos\theta & 0 & -\sin\theta \\ 0 & 1 & 0 \\ \sin\theta & 0 & \cos\theta \end{bmatrix} \cdot \begin{bmatrix} \cos\varphi & \sin\varphi & 0 \\ -\sin\varphi & \cos\varphi & 0 \\ 0 & 0 & 1 \end{bmatrix} = \begin{bmatrix} \cos\theta\cos\varphi & \cos\theta\sin\varphi & -\sin\theta \\ -\sin\varphi & \cos\varphi & 0 \\ \sin\theta\cos\varphi & \sin\theta\sin\varphi & \cos\theta \end{bmatrix} \quad \text{(B-1)}$$

Appendix C The Natural Frequency of the Optical Probe

To check the possibility of resonance of the glass optical probe in multiphase flow, the natural frequency of the probe was calculated.

The formula for the natural frequency is (Condon and Odishaw, 1967):

$$f = \frac{1}{2L}\sqrt{\frac{E}{\rho}} \qquad \text{(C-1)}$$

where f is the natural frequency, L and ρ are the length and the density of the object (probe), and E is the Youngs modulus of the material of which the object (probe) is made.

The physical properties of the glass optical fiber used in this study are: L≈1.5cm, ρ=2.203 g/cm^3, and E=5.8×10^9 Kg/m^2. Hence, the natural frequency of the optical fiber is about 54 KHz, which is much higher than the bubble frequency in multiphase systems (usually in the range of 0~1000 Hz). Hence, the glass optical probe used in this study does not resonate in the bubble column flows.

Appendix D Additional Bubble Properties in Bubble Columns Obtained by the Four-Point Optical Probe

D.1 Comparison of the Gas Holdup Profile Obtained by Probe and by CT

Figure D-1 and Table D-1 show that at atmospheric pressure the gas holdup profiles obtained by the four-point optical probe and CT match well.

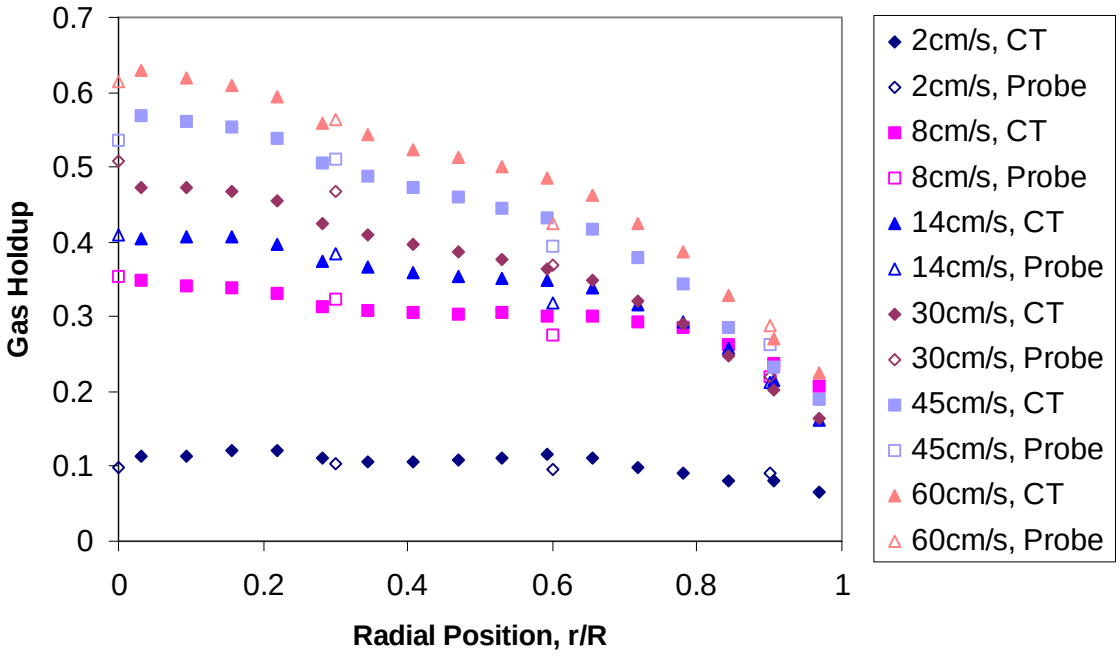

(a) Sparger #2, 0.1MPa, z/D=1.7

Figure D-1. Comparison of Radial Profiles of Gas Holdup by CT and by Probe

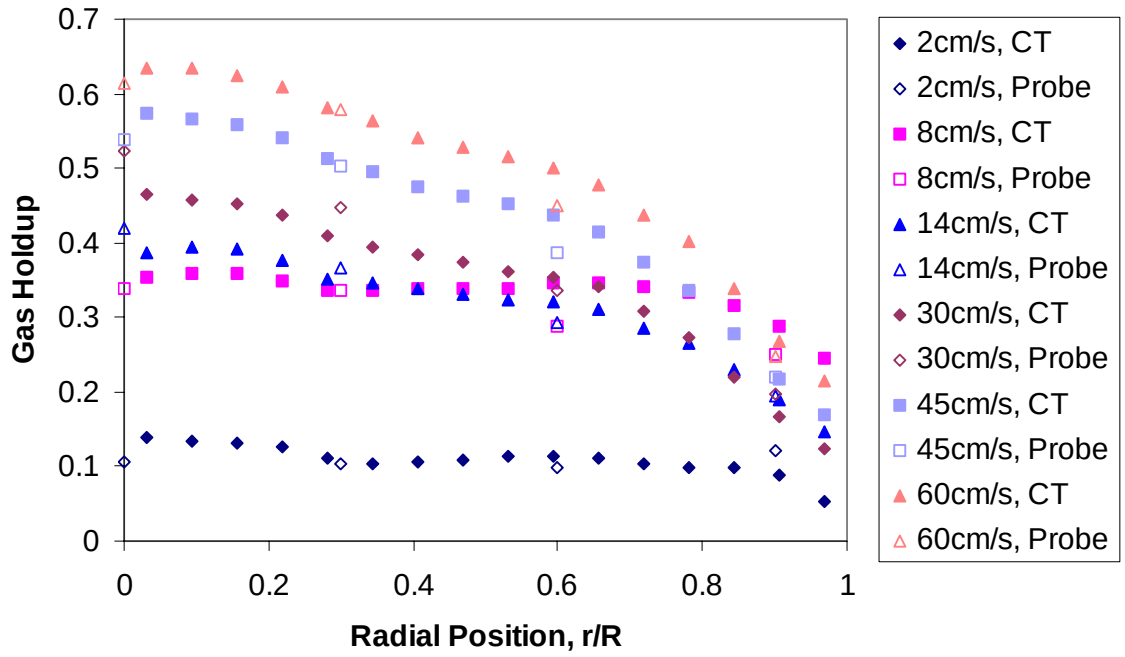

(b) Sparger #2, 0.1MPa, z/D=5.1

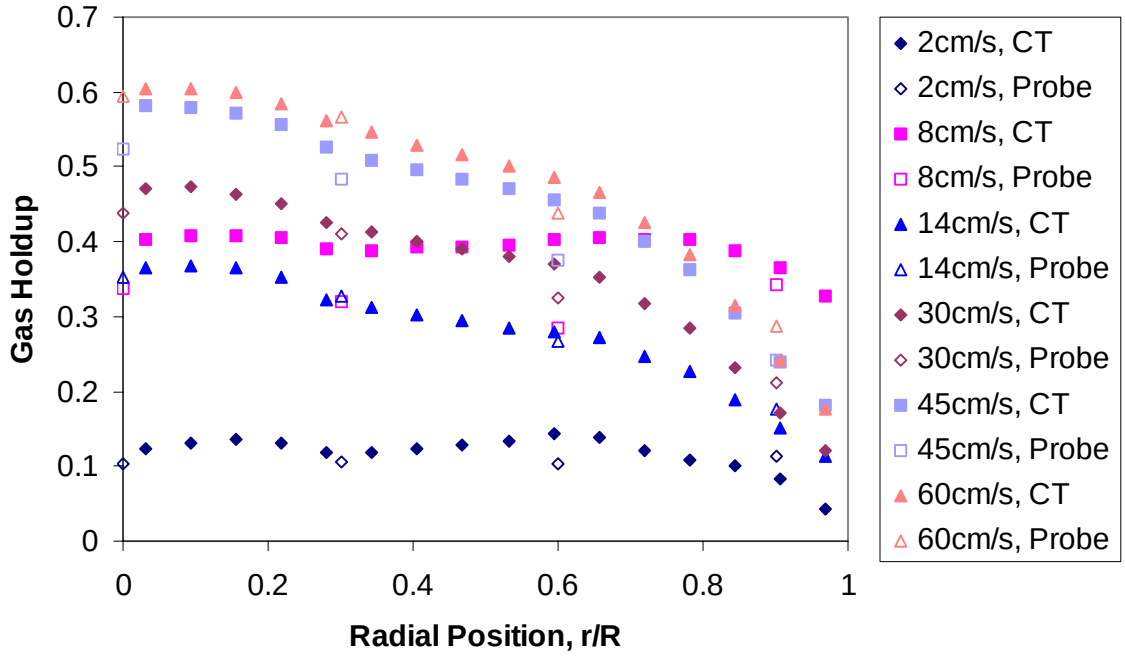

(c) Sparger #2, 0.1MPa, z/D=8.5

Figure D-1. (continued) Comparison of Radial Profiles of Gas Holdup by CT and by Probe

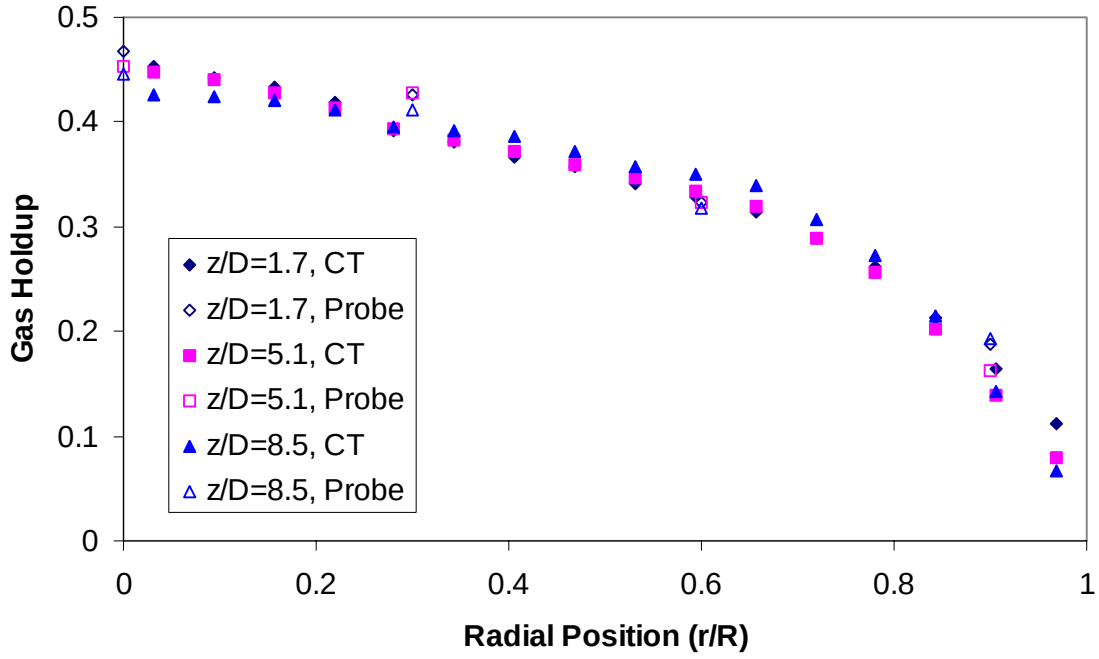

(d) Sparger #1, 0.1MPa, Ug=30cm/s

Figure D-1. (continued) Comparison of Radial Profiles of Gas Holdup by CT and by Probe

Table D-1. Comparison of the Local Gas Holdup Obtained by CT and by Probe

Radial position r/R	z/D=1.7			z/D=5.1			z/D=8.5		
	CT	Probe	Error* (%)	CT	Probe	Error* (%)	CT	Probe	Error* (%)
Sparger #1, P=0.1MPa, Ug=30 cm/s									
0	0.454	0.467	-2.96	0.448	0.453	-1.02	0.426	0.446	-4.54
0.3	0.392	0.427	-8.19	0.393	0.427	-7.90	0.396	0.411	-3.76
0.6	0.328	0.322	1.77	0.335	0.323	3.49	0.350	0.318	10.2
0.9	0.163	0.188	-13.0	0.140	0.162	-14.0	0.142	0.193	-26.5
Sparger #2, P=0.1MPa, Ug=30 cm/s									
0	0.473	0.507	-6.78	0.464	0.524	-11.4	0.470	0.437	7.46
0.3	0.424	0.468	-9.40	0.409	0.447	-8.57	0.425	0.410	3.64
0.6	0.365	0.368	-0.88	0.353	0.337	4.88	0.370	0.324	14.2
0.9	0.201	0.221	-8.81	0.166	0.197	-15.9	0.170	0.212	-19.6
Sparger #2, P=0.1MPa, Ug=45 cm/s									
0	0.568	0.537	5.91	0.574	0.538	6.74	0.582	0.524	11.2
0.3	0.505	0.510	-0.95	0.512	0.503	1.89	0.525	0.484	8.60
0.6	0.431	0.394	9.44	0.437	0.388	12.7	0.455	0.376	21.0
0.9	0.231	0.261	-11.4	0.216	0.273	-20.6	0.238	0.242	-1.71

Table D-2 and D-3 show that at high pressure the gas holdup obtained by the optical probe is always higher than that by CT, and the cross-sectional gas holdup obtained by the optical probe matches the overall gas holdup better than that by CT. Hence, at high pressure gas holdup obtained by the optical probe is still reliable. The reason for the large discrepancy in the gas holdup obtained by CT at high pressure is still unknown and is to be investigated.

Table D-2. Comparison of the Local Gas Holdup Obtained by CT and by Probe (Sparger #3, Ug=30 cm/s, z/D=5.1)

Radial position r/R	P=0.1MPa			P=0.4MPa			P=1.0MPa		
	CT	Probe	Error* (%)	CT	Probe	Error* (%)	CT	Probe	Error* (%)
0	0.504	0.463	8.81	0.569	0.692	-17.9	0.643	0.760	-15.4
0.3	0.430	0.430	0.03	0.485	0.614	-20.9	0.577	0.730	-21.0
0.6	0.350	0.330	5.84	0.420	0.499	-15.8	0.513	0.631	-18.7
0.9	0.140	0.180	-22.2	0.179	0.293	-38.8	0.271	0.482	-43.8
Mean	---	---	-1.9	---	---	-23.4	---	---	-24.7

* Error= $(\varepsilon_{g,\,CT} - \varepsilon_{g,\,Probe})/\ \varepsilon_{g,\,Probe} \times 100\%$

Table D-3. Comparison of the Integrated Cross-Sectional Gas Holdup and the Overall Gas Holdup

z/D	Overall ε_g	$\overline{\varepsilon_g}$ by CT	Error* (%)	$\overline{\varepsilon_g}$ by Probe	Error* (%)
Sparger #1, P=0.1MPa, Ug=30 cm/s					
1.7	0.315	0.276	-12.5	0.285	-9.4
5.1		0.268	-14.9	0.275	-12.8
8.5		0.276	-12.4	0.283	-10.2
Sparger #2, P=0.1MPa, Ug=30 cm/s					
1.7	0.353	0.311	-11.8	0.325	-7.9
5.1		0.290	-17.7	0.299	-15.2
8.5		0.300	-14.8	0.293	-16.9
Sparger #2, P=0.1MPa, Ug=45 cm/s					
1.7	0.391	0.367	-6.1	0.360	-7.9
5.1		0.362	-7.3	0.361	-7.6
8.5		0.382	-2.1	0.340	-12.9
Sparger #3, P=0.1MPa, Ug=30 cm/s					
5.1	0.328	0.281	-14.3	0.285	-13.0
Sparger #3, P=0.4MPa, Ug=30 cm/s					
5.1	0.534	0.335	-37.2	0.434	-18.7
Sparger #3, P=1.0MPa, Ug=30 cm/s					
5.1	0.672	0.426	-36.6	0.587	-12.7

* Error= $(\overline{\varepsilon_g} - \varepsilon_g)/\varepsilon_g \times 100\%$

D.2 The Effect of Superficial Gas Velocity

Figure D-2 show the radial profiles of the bubble frequency at different Ug and its change with Ug. The radial profile of bubble frequency is flat in bubbly flow (Ug=2cm/s), and it is parabolic at Ug ≥ 8cm/s. From D-2b, it is obvious that the bubble frequent increases with Ug at all radial positions in the column.

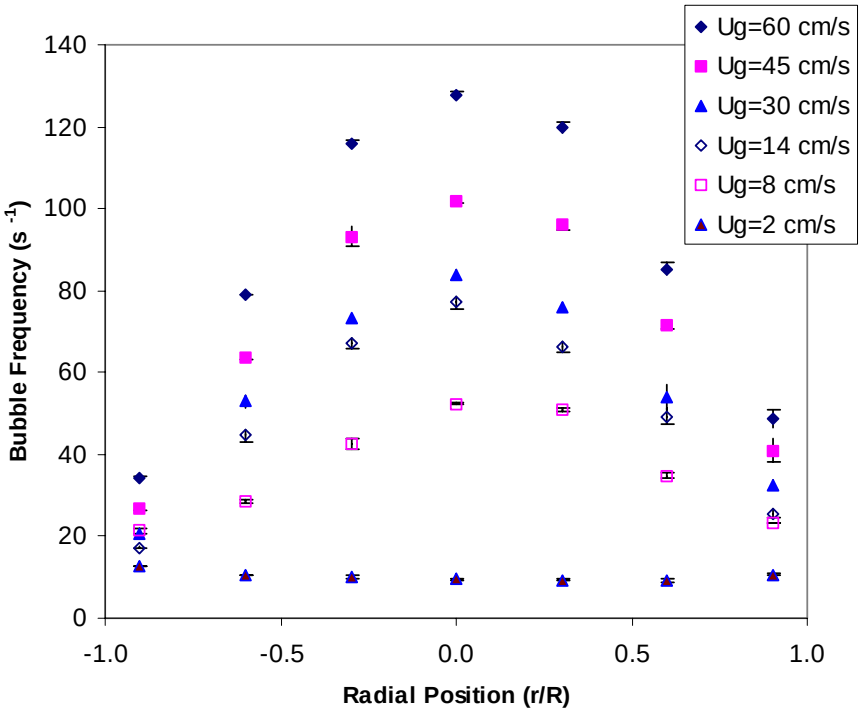

(a)

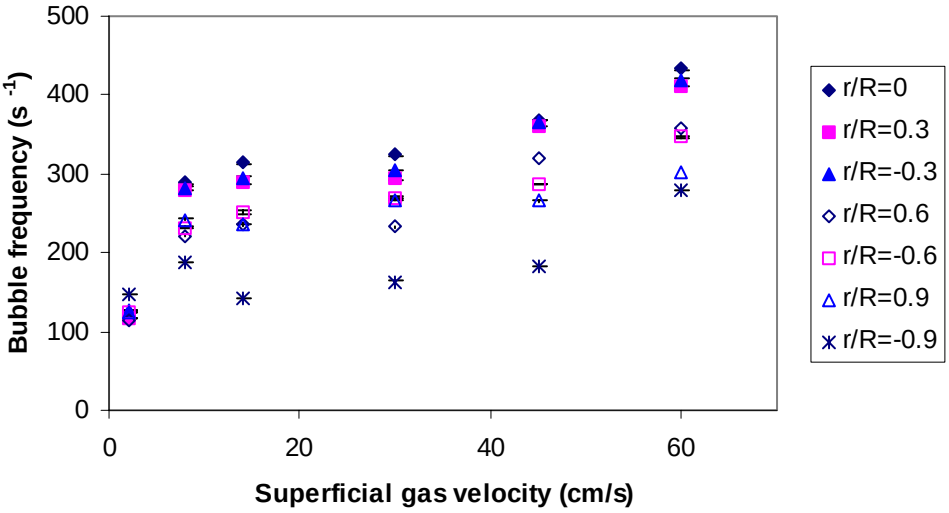

(b)

Figure D-2. The Radial Profile of Bubble Frequency

(Sparger #2, z/D=5.1)

Figure D-3 shows the comparison of the bubble velocity distributions obtained by two-point probes (use the central tip and one of the three peripheral tips of the four-point probe, e.g., Tip0 and Tip1 as shown in Figure 3-21) and by four-point probes. In bubbly flow (Ug=2 cm/s), as expected by the simulation (Figure 3-3a), the bubble velocity distribution obtained by two-point probe has higher pdf value at high value of velocity than by the four-point probe. This is more obvious in transition flow regime (Ug=8 cm/s, Figure D-3b). In churn-turbulent flow, the two-point probe cannot distinguish bubbles that move upwards and downwards, and it detects many bubbles of unreasonably high velocity (Figure D-3c and d). This is because at high gas holdup, due to the large number of bubbles in the bubble column, sometimes different bubbles hit the two tips of the two-point probe almost simultaneously. The algorithm for the two-point probe considers this case the same as the case when the same bubble hits the two tips successively, and thus derives a very high bubble velocity. For four-point probe, the probability that several different bubbles hit the four tips of the probe almost simultaneously is very low. Furthermore, because the probe has more tips, more information about the bubbles that hit the probe can be derived so that many cases can be distinguished and discarded if

needed. This is illustrated by the bubble velocity distribution obtained by the four-point probe in highly churn-turbulent flow (Figure D-3b). Hence, it is experimentally established that the bubble velocity distribution obtained by two-point probes is not reliable, especially in transition and churn-turbulent flow regime.

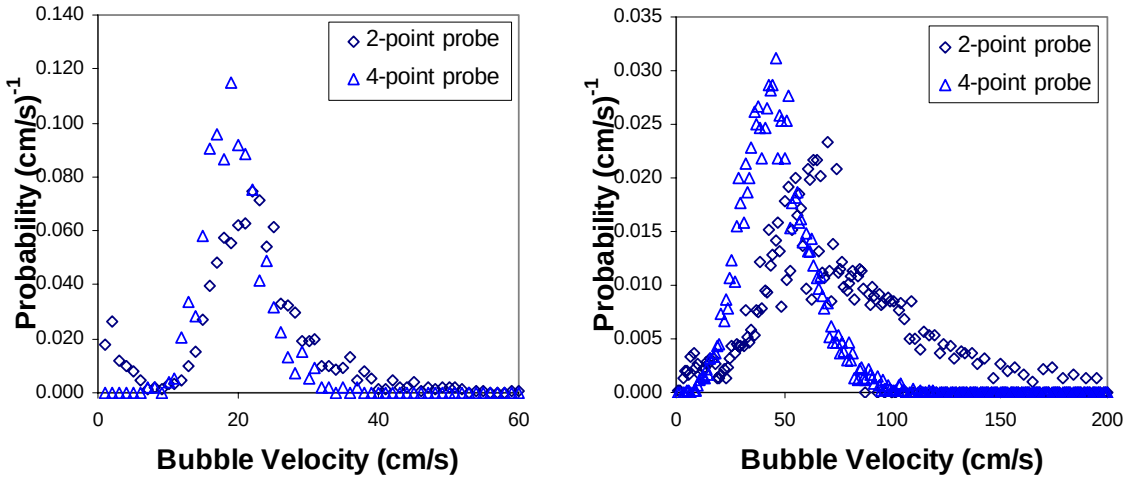

(a) Ug=2 cm/s **(b) Ug=8 cm/s**

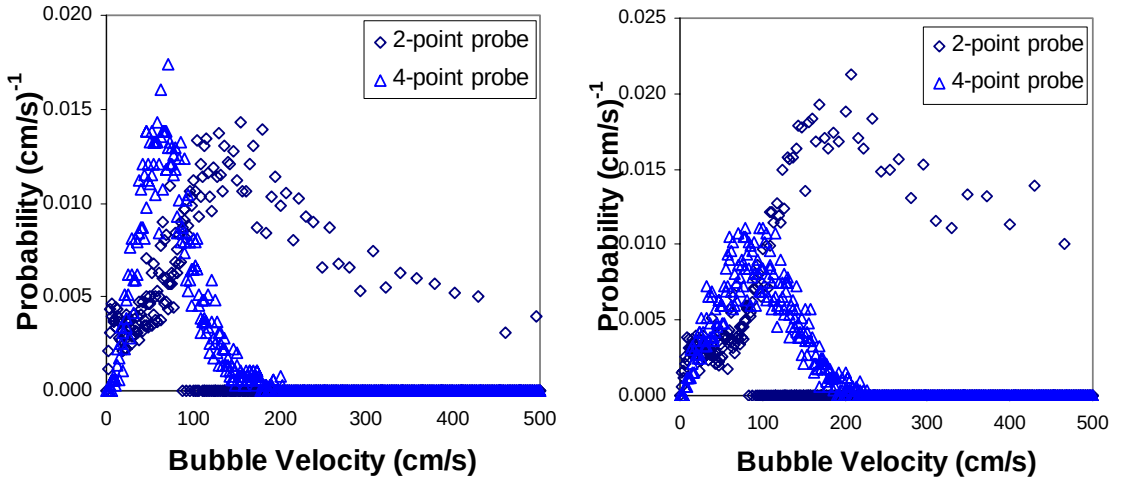

(c) Ug=14 cm/s **(d) Ug=60 cm/s**

Figure D-3. Comparison of the Bubble Velocity Distribution Obtained by Two-Point Probe and Four-Point Probe (r/R=0, z/D=5.1, Sparger #2)

Table D-4 displays the statistical parameters of the bubble velocity distribution illustrated in Figure 5-7 and 5-8. It shows the increase of the velocity of both bubbles moving upwards and downwards with Ug.

Table D-4. Statistical Parameters of the Bubble Velocity Distribution

Ug (cm/s)	Whole		Upwards Bubbles		Downwards Bubbles	
	Mean velocity (cm/s)	Standard deviation σ, (cm/s)	Mean velocity (cm/s)	Standard deviation σ, (cm/s)	Mean velocity (cm/s)	Standard deviation σ, (cm/s)
r/R=0						
2	18.9	4.22	18.9	4.22	---	---
8	46.6	17.5	47.1	16.6	-15.8	16.9
14	69.4	35.7	72.0	32.3	-28.2	21.8
30	76.0	45.1	81.5	38.0	-36.1	24.9
45	82.1	48.0	88.2	40.6	-34.8	24.2
60	86.6	51.2	93.8	42.1	-37.6	27.1
r/R=-0.9						
2	20.1	4.80	20.1	4.80	---	---
8	-24.8	23.7	20.6	9.45	-33.8	12.9
14	-10.8	41.7	38.2	20.9	-39.1	17.3
30	-12.2	51.5	47.8	28.9	-46.9	20.5
45	-17.3	54.5	51.0	31.7	-50.9	22.4
60	-27.0	53.8	49.6	32.6	-55.1	25.0
r/R=0.9						
2	20.4	4.94	20.4	4.94	---	---
8	3.94	30.8	28.4	12.4	-28.2	13.2
14	17.8	49.3	52.7	28.3	-34.6	17.2
30	10.7	58.8	60.8	33.4	-42.4	21.5
45	12.5	64.3	65.6	37.4	-47.1	22.0
60	3.76	65.7	64.8	38.4	-50.4	24.5

D.3 The Effect of Pressure

Table D-5 displays the statistical parameters of the bubble velocity distribution illustrated in Figure 5-14. It shows the increase of the velocity of both bubbles moving upwards and downwards with pressure.

Table D-5. Pressure Effect on the Mean and Standard Deviation of the Bubble Velocity Distribution

r/R	Pressure (MPa)	Whole Bubbles		Upward Bubbles		Downward Bubbles	
		Mean (cm/s)	Standard Deviation (cm/s)	Mean (cm/s)	Standard Deviation (cm/s)	Mean (cm/s)	Standard Deviation (cm/s)
-0.9	0.1	7.92	54.5	49.8	30.2	-46.0	21.4
	0.4	-40.5	33.2	32.7	23.0	-49.3	21.0
	1.0	-52.2	27.7	31.5	20.4	-55.1	22.9
0	0.1	76.4	47.1	83.2	38.7	-35.7	26.9
	0.4	81.3	42.4	84.3	38.6	-30.3	23.8
	1.0	88.9	42.2	91.3	38.9	-28.1	23.9
0.9	0.1	2.94	55.3	55.2	32.2	-41.3	22.3
	0.4	-2.21	51.5	48.9	30.3	-41.5	20.7
	1.0	-12.6	52.8	52.2	32.0	-45.3	22.2

D.4 Transformation from Bubble Size Distribution to Bubble Chord Length Distribution

Digital simulations were conducted to clarify whether a single modal bubble chord length distribution implies a single modal bubble size distribution. Figure D-4 shows examples of the bubble chord length distribution obtained by the four-point optical probe in a bubble column in churn-turbulent flow.

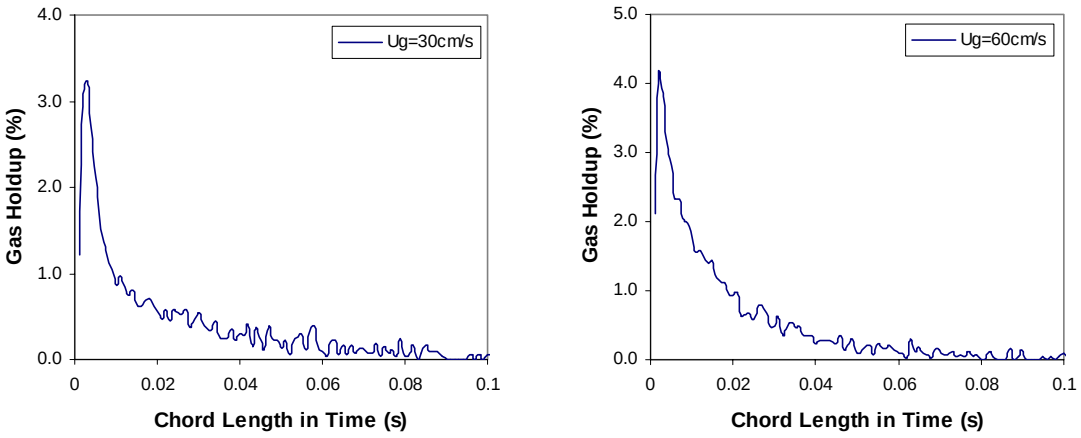

(a) **(b)**

Figure D-4. Volume Based Bubble Chord Lengths Distribution Obtained by Four-Point Optical Probe (r/R=0, z/D=5.1)

To derive the bubble size distribution from the bubble chord length distribution, the bubble shape needs to be assumed. The assumptions made for the simulation are: (1) the bubbles are ellipsoidal, (2) the probe hits the bubble leading surface randomly, i.e. the probability that the probe tip hits every single point on the bubble leading edge is identical.

When he probe tip randomly hits a bubble with minor axis, a, the chord length obtained will range from 0 to a. The probability density function (pdf) of bubble chord length distribution obtained is (Clark and Turton, 1988):

$$P(y) = \frac{y}{2a^2} \qquad 0 \le y \le a \qquad \text{(D-1)}$$

Assume that the bubble size (length of minor axis) distribution is bimodal, for small bubbles it is log-normal distribution and for large bubbles it is normal distribution, the bubble size distribution and bubble chord length distribution calculated are shown in Figure D-5.

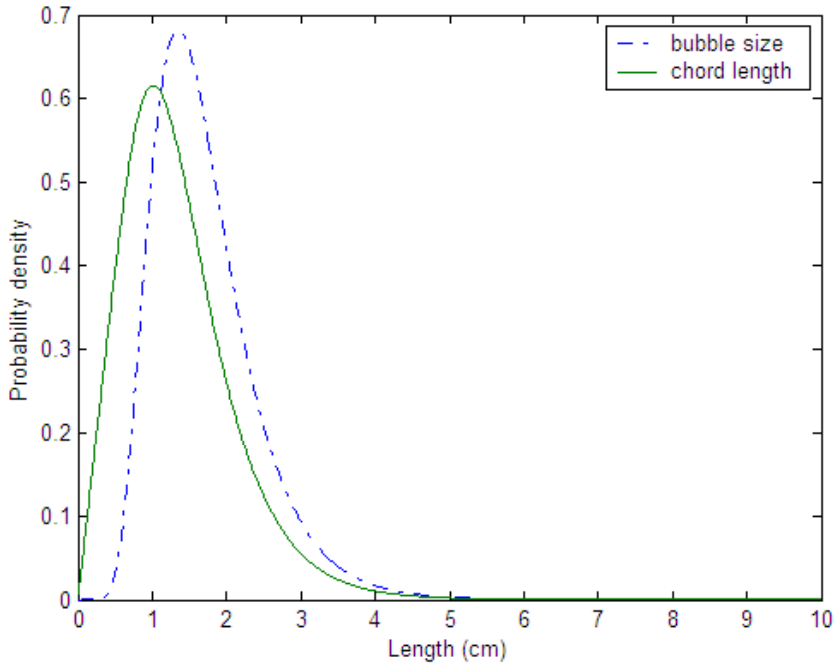
bubble size
chord length
Probability density
Length (cm)
0
0.1
0.2
0.3
0.4
0.5
0.6
0.7
0
1
2
3
4
5
6
7
8
9
10

(a)

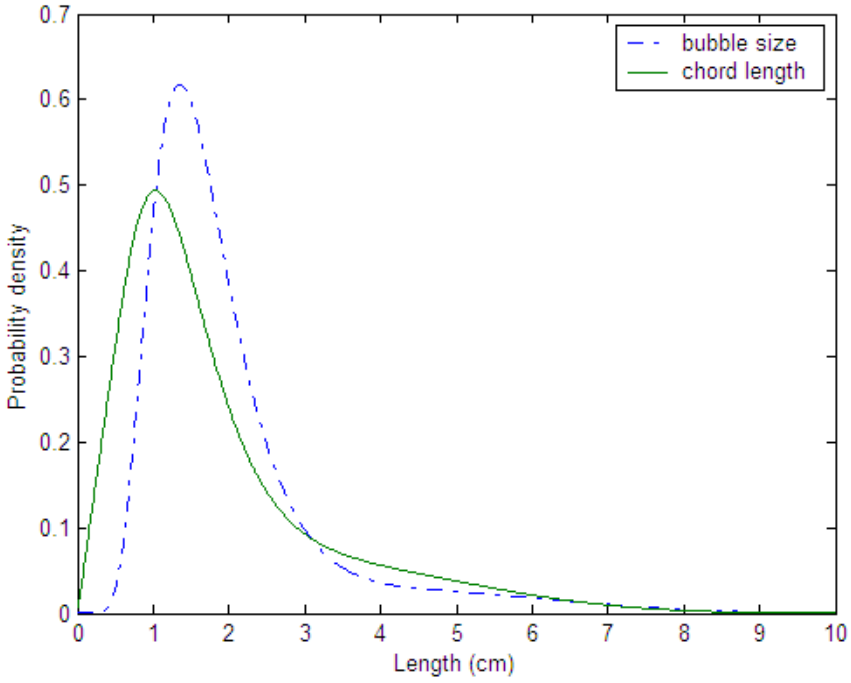
bubble size
chord length
Probability density
Length (cm)
0
0.1
0.2
0.3
0.4
0.5
0.6
0.7
0
1
2
3
4
5
6
7
8
9
10

(b)

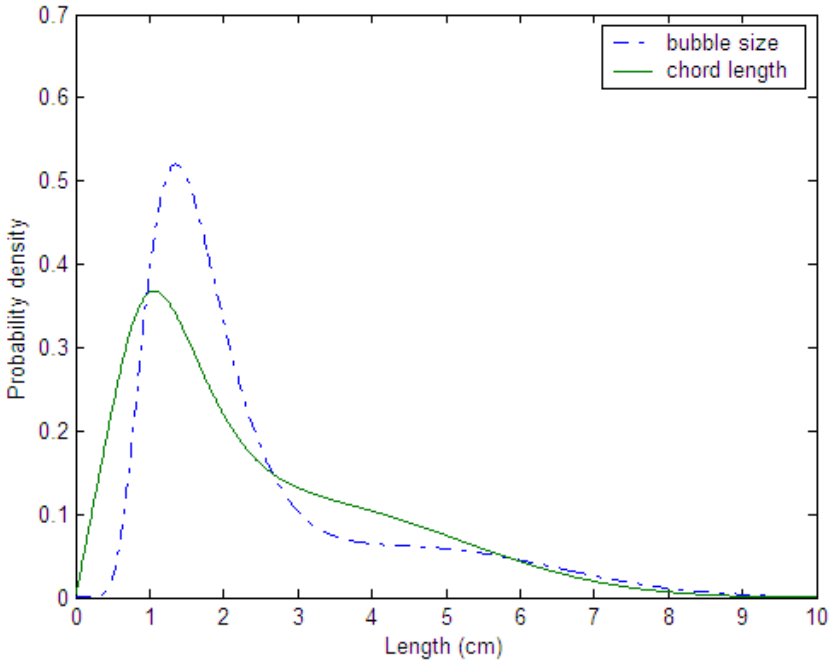

(c)

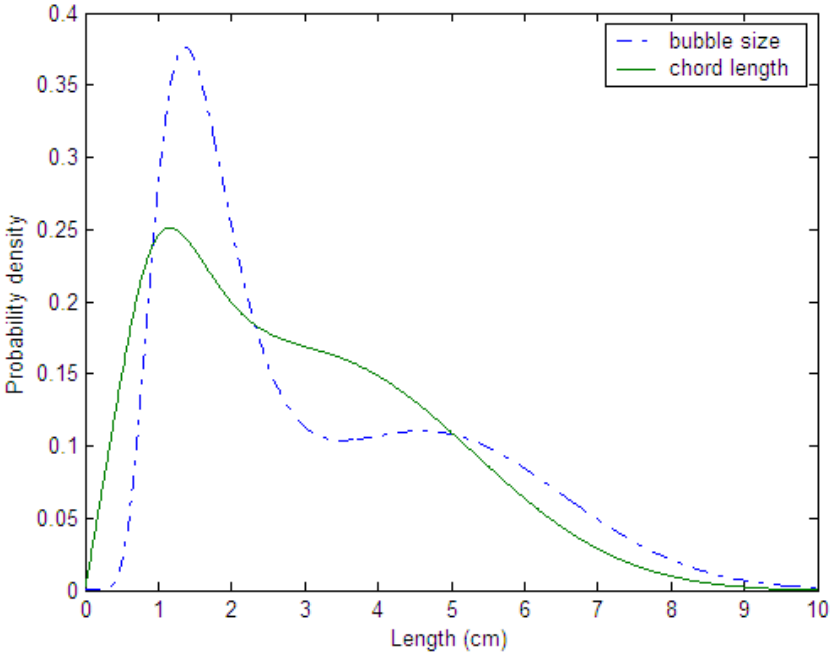

(d)

Figure D-5. The Bubble Size and Chord Length Distribution Calculated

In Figure D-5 from (a) to (d), the percentage of large bubbles in the whole bubble population increased. It is evident that when the bubble size distribution is bimodal, it is impossible for the bubble chord length distribution to have the shape shown in Figure D-4. Hence, it is reasonable to conclude that the bubble chord length distributions obtained by the four-point optical probe in a bubble column, as shown in Figure D-4, infer single modal bubble size distributions at superficial gas velocity up to 60 cm/s.

D.5 Summary

Table D-6. Change of Bubble Properties with Operating Conditions

	Bubble velocity	Chord length	Specific interfacial area	Gas holdup
Superficial Gas Velocity, Ug ↑	↑	↑→	↑	↑
Pressure ↑	↑	↓	↑	↑
Radial position, r/R ↑ Atmospheric pressure	↓	↓	↓	↓
Axial position, z/D ↑ Atmospheric pressure	→	↓→	→	→
Axial position, z/D ↑ High pressure	→	↓→	↑	↑

↑ : increase; ↓ : decrease; → keep almost identical; ↑→ : increase firstly and then keep almost identical.

Appendix E Testing of Phase Transition At Subcritical and Supercritical Conditions Using Four-Point Optical Probe

The objective of this study is to evaluate the suitability of the four-point optical probe and the algorithm for data processing in stirred autoclave reactors and minireactors (this work was supported by the National Science Foundation Engineering Research Centers Program, Grant EEC-0310689). In addition, the suitability of such probe to provide transition information from two to single phase systems in expanded solvents will be assessed. This information is necessary for evaluation of the medium and the selection of the reactor type for the pilot plant and commercial implementation of the test bed reaction systems under investigation.

The principle of the optical probe as explained in Section 3.2 makes it suitable for the detection of the transition of the n-decane-CO_2 system from two phases to one phase (expanded solvent) with the increase in the pressure. The probe is going to be tested in a 1 liter autoclave stirred reactor (Figure E-1) using organic liquid (n-decane) with sparged carbon dioxide. At subcritical condition, the CO_2 will form bubbles in the n-decane phase and these bubbles can be detected by the optical probe. At supercritical conditions, the CO_2 is miscible with organic solvent. Hence, there should be no bubbles detected. By this means, the transition from two phases to expanded solvent (CO_2 supercritical phase systems) can be determined by the optical probe. The experimental conditions will be just above the critical temperature of CO_2 (31^oC), e.g. 35^oC. The operating pressure will be 0.1 to 10 MPa. Above 31^oC and 7.28 MPa, the CO_2 will be in supercritical condition. Hence, 35^oC and 0.1~10 MPa include the critical point of CO_2.

It has been proved experimentally that the four-point optical probe worked efficiently at high pressure up to 10 MPa at about 40^{o}C in the n-decane-CO_2 system.

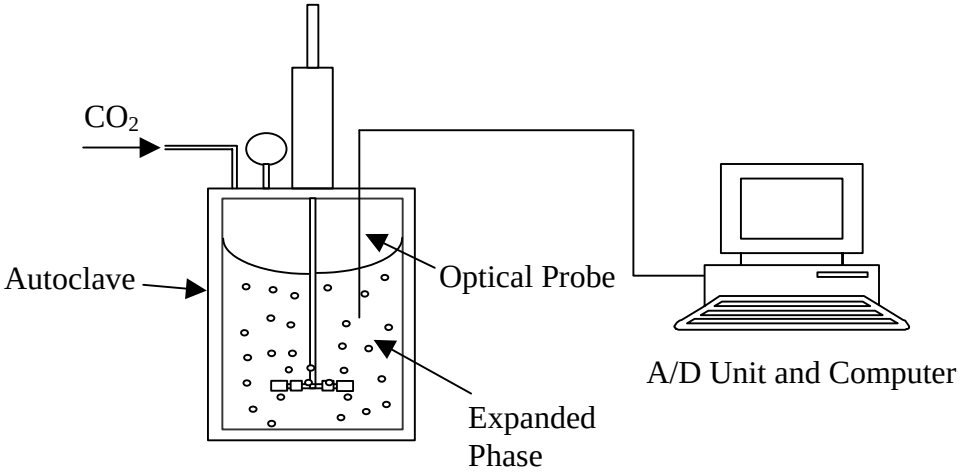

Figure E-1. Setup for the Detection of Phase Transition at Subcritical and Supercritical Conditions

Appendix F Derivation of The Bubble Size and Aspect Ratio

An algorithm to derive the length of the bubble's minor axis and the bubble's aspect ratio based on the assumption that bubbles are ellipsoidal is suggested in Section 3.3 (Equation 3-20). Unfortunately, the validation of the probe's measurements in a 2D bubble column (Figure 4-5) conducted in this study shows that the proposed algorithm based on solution of Equations (3-20a-d) does not give an accurate estimate of both aspect ratio and bubble size (Figure F-1). As illustrated in Figure F-1, the algorithm always underestimates the bubble aspect ratio (Figure F-1a) and overestimates the length of the bubble's major axis (Figure F-1b). Furthermore, it is very sensitive to changes of the bubble chord lengths obtained by the probe, i.e., small changes in the bubble chord lengths may cause large variations in the calculated bubble size and aspect ratio. As a result, this method is not recommended to investigate the bubble size and aspect ratio in bubble columns.

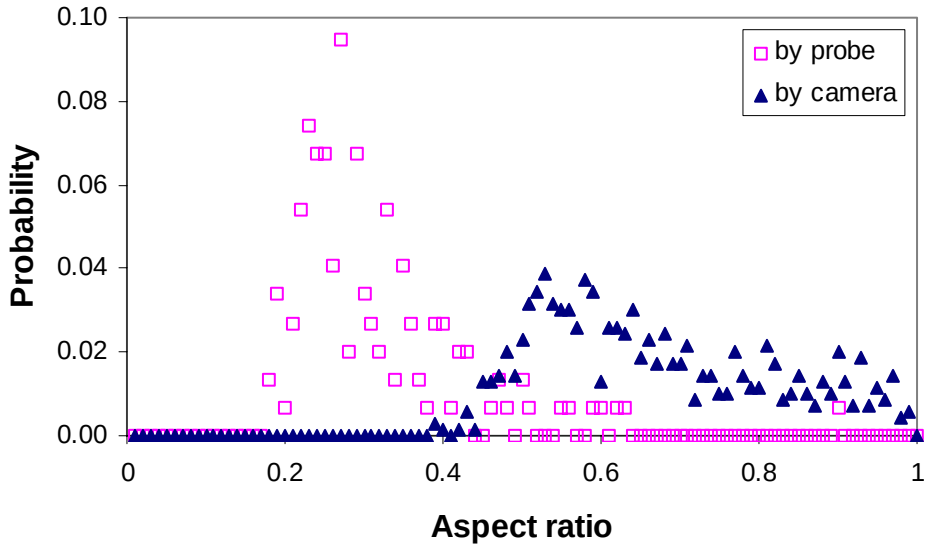

(a)

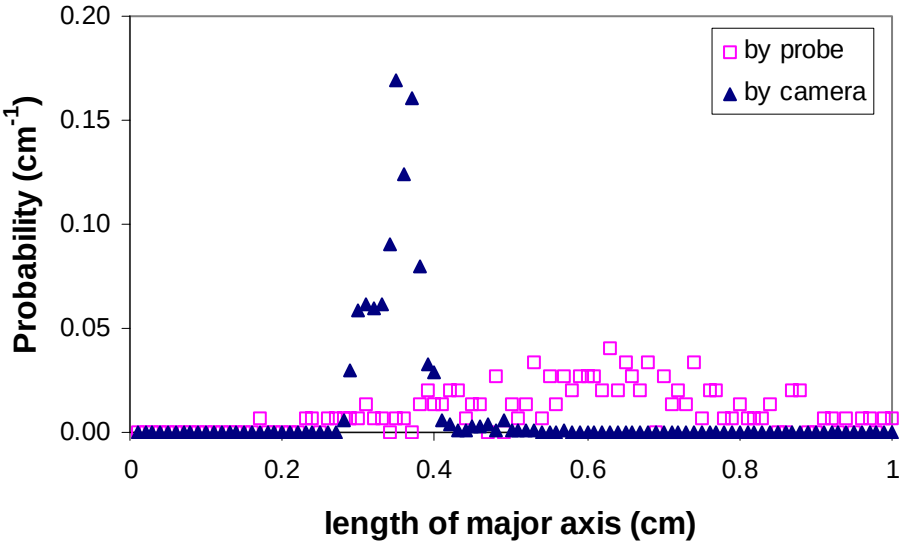

(b)

Figure F-1. Comparison of Bubble's Aspect Ratio and the Length of Major Axis Obtained by Camera and by Four-Point Optical Probe (mean bubble velocity 32.2 cm/s, mean bubble size 0.23cm)

References

1. Abuaf N., Jones O. C., Zimmer G. A. (1978). "Optical probe for local void fraction and interface velocity measurements", *Rev Sci Instrum*, 49: 1090-1094

2. Akita K. and Yoshida F. (1973). "Gas holdup and volumetric mass transfer coefficient in bubble columns. Effect of liquid properties", *Ind Eng Chem Process Des Dev*, 12: 76-80

3. Bach H. F. and Pilhofer T. (1978). "Variation of Gas Holdup in Bubble Columns with Physical Properties of Liquids and Operating Parameters of Columns", *Ger Chem Eng*, 1:270

4. Batchelor G. K., "An introduction to fluid dynamics", Cambridge U Press, London (1967), 474-481

5. Bhaga D., Weber M. E. (1981). "Bubbles in viscous liquids: shapes, wakes and velocities", *J Fluid Mech*, 105: 61-85

6. Bruce C. A. (1985). "Probability and random processes: a first course with applications", 2nd edition, J. Wiley, New York.

7. Burgess J. M., Calderbank P. H. (1975). "The measurement of bubble parameters in two-phase dispersions I: the development of an improved probe technique", *Chem Eng Sci*, 30: 743-750

8. Cartellier A. (1998). "Measurement of gas phase characteristics using new monooptical fiber probes and real time signal processing", *Nucl Eng Des*, 184: 393-408

9. Chabot J., Lee S. L. P., Soria A., De Lasa H. I. (1992). "Interaction Between Bubbles and Fiber Optic Probes in a Bubble Column", *Can J Chem Eng*, 70: 61-68

10. Chanson H. (1997). "Air bubble entrainment in open channels: flow structure and bubble size distributions", *Int J Multiphase Flow*, 23: 193-203

11. Chen J., Gupta P., Degaleesan S., Al-Dahhan M. H., Dudukovic M. P. and Toseland B. A. (1998). "Gas Holdup Distributions in Large-Diameter Bubble Columns Measured by Computed Tomography." *Flow Meas. Instrum.*, 9(2): 91-101

12. Chen J., Li F., Degaleesan S., Gupta P., Al-Dahhan M. H., Dudukovic M. P. and Toseland B. A. (1999a), "Fluid Dynamic Parameters in Bubble Columns with Internals." *Chem Eng Sci*, 54: 2187-2197.

13. Chen J., Kemoun A., Al-Dahhan M. H., Dudukovic M. P., Lee D. J., Fan L-S. (1999b). "Comparative hydrodynamics study in a bubble column using computer-automated radioactive particle tracking (CARPT)/computed tomography (CT) and particle image velocimetry (PIV)", *Chem Eng Sci*, 54: 2199-2207

14. Chen R. C., Reese J., Fan L-S. (1994). "Flow structure in a three-dimensional bubble column and three-phase fluidized bed", *AIChE J*, 40: 1093

15. Choi K. H., Lee W. K. (1990). "Comparison of probe methods for measurement of bubble properties", *Chem Eng Comm*, 91: 35-47

16. Clark N. N. and Turton R. (1988). "Chord length distribution related to bubble size distributions in multiphase flows", *Int J Multiphase Flow*, 14: 413-424

17. Condon E. U., Odishaw H. (1967). "Handbook of physics", 2nd Ed., McGraw-Hill Book Co., New York.

18. Daly J. G., Patel S. A., Buckur D. B. (1992). "Measurement of gas holdups and Sauter mean bubble diameters in bubble column reactors by dynamic gas disengagement method", *Chem Eng Sci*, 47(13-14): 3647-3654

19. Danckwerts P. V. (1970). "Gas-Liquid Reactions", McGraw-Hill Book Co., New York.

20. Darton R. C., Harrison D. (1974). "The rise of single gas bubbles in liquid fluidized beds", *Trans I Chem E*, 52: 301-306

21. Davis B. H. (2002). "Overview of reactors for liquid phase Fischer-Tropsch synthesis." *Catalysis Today*, 71(3-4): 249-300

22. Deckwer W., Louisi Y., Zaidi A., Ralek M. (1980). "Hydrodynamic properties of the Fischer-Tropsch slurry process", *Ind Eng Chem Process Des Dev*, 19: 699-708

23. De Lasa H. I., Lee S. L. P., Bergougnou M. A. (1984). "Bubble measurement in three-phase fluided beds using a U-shape optical fiber", *Can J Chem Eng*, 62: 165-169

24. De Swart J. W. A., Krishna R. (1995). “Effect of particles concentration on the hydrodynamics of bubble column slurry reactors”, *Chem Eng Res Design, Trans Ind Chem Eng*, 73: 308-313

25. Deshpande N. S., Dinkar M., Joshi J. B. (1995). “Disengagement of the gas phase in bubble columns”, *Int J Multiphase Flow*, 21: 1191-1201

26. Domenico C., Damiano V., Roberto B., Maurizio M., Eiman Abu B. (1999). “A study on coalescence and breakage mechanisms in three different bubble columns”, *Chem Eng Sci*, 54: 4767-4777

27. Ellenberger, J. and Krishna, R. (1994). “A Unified Approach to the Scale-Up of Gas-Solid Fluidized Bed and Gas-Liquid Bubble Column Reactors”, *Chem Eng Sci*, 49**:** 5391-5411

28. Eisenberg B., Ansel L. L., Fiato R. A., Bauman R. F., “Advanced gas conversion technology for remote natural gas utilization”, GPA Convention, New Orleans, LA 1994

29. Fan L-S., Tsuchiya K., “Bubble wake dynamics in liquids and liquid-solid suspensions”, Butterworth-Heinemann, 1990

30. Fan L-S., Yang G. Q., Lee D. J., Tsuchiya K., Luo X. (1999), “Some aspects of high-pressure phenomena of bubbles in liquids and liquid-solid suspensions”, *Chem Eng Sci*, 54: 4681-4709

31. Farag H. I., Hjarbo K., Mejdell T., Hjarbo K., Ege P., Lysberg M., Grislingaas A., De Lasa H. I. (1997), “Fiber Optic and Capacitance Probes in Turbulent Fluidized Beds”, *Chem Eng Comm*, 157: 73-107

32. Frijlink J. J. (1987). “Physical aspects of gassed suspension reactors”, Ph. D. Thesis, Delft University of technology, the Netherlands.

33. Glassner A. S. (1990). “Graphics gems”, Academic Press, Boston.

34. Groen J. S., Oldeman R. G. C., Mudde R. F., van der Akker H. E. A., “Coherent structures and axial dispersion in bubble column reactors”, Chem Eng Sci, 51(1996): 2511-2520

35. Grunn D. J., Al-Doori H. H. (1985). “The measurements of bubbles flows in fluidized beds by electrical probe”, *Int J Multiphase Flow*, 11: 535-551

36. Guet S., Fortunati R. V., Mudde R. F., Ooms G. (2003). “Bubble velocity and size measurement with a four-point optical fiber probe’, *Part Part Syst Charact*, 20(2003): 219-230

37. Haberman W. L., Morton R. K. (1953). “An experimental investigation of the drag and shape of air bubbles rising in various liquids”, David W. Taylor Model Basin Report 802, Navy Dept., Washington DC

38. Harmathy, T. Z. (1960), “Velocity of large drops and bubbles in media of infinite or restricted extent”, *AIChE J*, 6: 281-288

39. Heijnen J. J., Van't Riet K. (1984), “Mass transfer, mixing and heat transfer phenomena in low viscosity bubble column reactors”, *Chemical Engineering Journal* (Amsterdam, Netherlands), 28(2): B21-B42

40. Hibiki T., Ishii M. (2002). “Interfacial Area Concentration of Bubbly Flow Systems” , *Chem Eng Sci*, 57: 3967-3977

41. Hibino S., “The behavior of single bubbles”, in Advances in Chemical Engineering 3: Dynamics of bubbles and Drops (Soc Chem Eng Japan, eds.), Chap. 2, 3-26, Nikkan Kogyo Shinbun, Tokyo, Japan 1969

42. Hills, J. H.; Darton, R. C. (1976). “The rising velocity of a large bubble in a bubble swarm”, Trans Inst Chem Eng, 54(4): 258-264

43. Hikita H., Asai S., Tanigawa K., Segawa K., Kitao M. (1980), “Gas hold-up in bubble columns”, *Chemical Engineering Journal* (Amsterdam, Netherlands), 20(1): 59-67

44. Hsu S. H., Lee W. H., Yang Y. M., Chang C. H. and Maa J. R. (2000). “Bubble Formation at an Orifice in Surfactant Solutions Under Constant-Flow Conditions”, *Ind Eng Chem Res*, 39: 1473-1479

45. Idogawa K., Ikeda K., Fukuda T. and Morooka S. (1987). “Formation and Flow of Gas Bubbles in a Pressurized Bubble Column with a Single Orifice or Nozzle Gas Distributor”, *Chem Eng Comm*, 59: 201-212

46. Idogawa K. (1997). “Methods for measurement of gas hold-up and gas bubble diameter in a high-pressure bubble column”, *Kagaku Kogaku*, 61: 781-782

47. Iguchi M., Nakatani T., Kawabata H. (1997). “Development of a multineedle electroresistivity probe for measuring bubble characteristics in molten metal baths”, *Metallurgical and Materials Transactions B*, 28: 409-416

48. Jager B., Espinoza R. (1995). “Advances in low temperature Fisher-Tropsch synthesis”, Catal Today, 23(1): 17-28

49. Jamialahmadi M., Muller-Steinhagen H. (1993). “Effect of superficial gas velocity on bubble size, terminal bubble velocity and gas hold-up in bubble columns”, *Dev Chem Eng Miner Process*, 1: 16-31

50. Jiang P., Lin T-J., Luo X., Fan L-S. (1995). “Flow visualization of high pressure (21 MPa) bubble column: bubble characteristics”, *Chem Eng Res Des*, 73: 269-274

51. Joshi J. B., Veera U. P., Parasad C. V., Phanikkumar D. V., Deshphande N. S., Thakre S. S. and Thorad B. N. (1998). “Gas Holdup Structure in Bubble Column Reactors.” *PINSA*, 64A(4): 441-567

52. Kataoka I., Ishii M., Serizawa A. (1986). “Local formulation and measurements of interfacial area concentration in two-phase flow”, *Int J Multiphase flow*, 12(4): 505-529

53. Kemoun A., Cheng Ong B., Gupta P., Al-Dahhan M. H. and Dudukovic M. P. (2001). “Gas Holdup in Bubble Columns at Elevated Pressure Via Computed Tomography”, *Int J Multiphase Flow*, 27(5), 929-946

54. Kiambi S. L., Duquenne A. M., Bascoul A. and Delmas H. (2001). “Measurements of local interfacial area: application of bi-optical fiber technique”, *Chem Eng Sci*, 56: 6447-6453

55. Kreischer B. E., Moritomi H., Fan L-S. (1990). “Wake solids holdup characteristics behind a single bubble in a three-dimensional liquid-solid fluidized bed”, *Int J Multiphase Flow*, 16: 187-200

56. Krishna R., Wilkinson P. M., van Dierendonck L. L. (1991). “A model for gas holdup in bubble columns incorporating the influence of gas density on flow regime transitions”, *Chem Eng Sci*, 46: 2491-2496

57. Kuncova G., Zahradnik J., Mach J. (1993). “Light Transmission Probe Connected with Spectrophotometer HP-8452 for local Measurements in Bubble Columns”, *Chem Eng Sci*, 48: 1013-1018

58. Kulkarni A. A., Joshi J. B., Kumar V. R., Kulkarni B. D. (2001). "Simultaneous Measurement of Holdup Profiles and Interfacial Area Using LDA in Bubble Columns: Predictions by Multiresolution Analysis and Comparison with Experiments", *Chem Eng Sci*, 56: 6437-6445

59. LaNauze, R. D. and Harris, I. J., (1974). "Gas Bubble Formation at Elevated System Pressures", *Trans Instn Chem Engrs*, 52(4): 337-348

60. Lans R. G. J. M. van der, van der Lans, R. G. J. M., "Hydrodynamics of a bubble column loop reactor", Doctoral dissertation, Delft University of Technology, 1985.

61. Lee S. L., De Lasa H. I., Bergougnou M. A. (1986). "A U-shape fiber optic probe to study three-phase fluidized beds", *Part Sci Technol*, 4: 61-71

62. Lee S. L., Soria A., De Lasa H. I. (1990). "Evolution of bubble length distributions in three phase fluidized beds", *AIChE J*, 36: 1763-1767

63. Leibson, I., Holcomb, E. G., Cacoso, A. G., and Jacmic, J. J. (1956). "Rate of Flow and Mechanics of Bubble Formation from Single Submerged Orifices", *AIChE J*, **2** (3): 296-306

64. Letzel H. M., Schouten J. C., Krishna R., van den Bleek C. M. (1997). "Characterization of regimes and regime transitions in bubble columns by chaos analysis of pressure signals", *Chem Eng Sci*, 52: 4447-4459

65. Lim K. S., Agarwal P. K. (1992). "Bubble velocity in fluidized beds: the effect of non-vertical bubble rise on its measurement using submersible probes and its relationship with bubble size", *Powder Technology*, 69: 239-248

66. Lin T-J., Tsuchiya K., Fan L-S. (1998). "Bubble flow characteristics in bubble columns at elevated pressure and temperature", *AIChE J*, 44: 545-560

67. Lin T. J., Juang R. C., Chen Y. C., Chen C. C. (2001). "Predictions of flow transitions in a bubble column by chaotic time series analysis of pressure fluctuation signals. " *Chem Eng Sci*, 56(3): 1057-1065

68. Liu W., Clark N. N., Karamavruc A. I. (1996). "General method for the transformation of Chord-length data to a local bubble-size distribution", *AIChE J*, 42: 2713-2720

69. Liu W., Clark N. N., Karamavruc A. I. (1998). “Relationship between bubble size distribution and Chord-length distribution in heterogeneously bubbling systems”, *Chem Eng Sci*, 53: 1267-1276

70. Luewisutthichat W., Tsutsumi A., Yoshida K. (1997a). “Bubble characteristics in multi-phase flow systems: bubble sizes and size distribution”, *J Chem Eng Jpn*, 30: 461-466

71. Luewisutthichat W., Tsutsumi A., Yoshida K. (1997b), “Chaotic hydrodynamics of continuous single-bubble flow systems”, *Chem Eng Sci*, 52: 3685-3691

72. Luo X., Yang G., Lee D. J., Fan L-S. (1998). “Single bubble formation in high pressure liquid-solid suspensions”, *Powder Technol*, 100: 103-112

73. Manabu I., Hirotoshi K., Keiji N., Zen-Ichiro M. (1995). “Measurement of bubble characteristics in a molten iron bath at 1600°C using an electroresistivity probe”, *Metall Mater Trans B*, 26B: 67-74

74. Marques J. J. P., Bouard R. (1999). “Bubbles in a gas-solid fluidized bed. Photographic characterization”, *Tech Mod*, 91: 20-24

75. Matsuura A., Fan L-S. (1984). “Distribution of bubble properities in a gas-liquid-solid fluized bed”, *AIChE J*, 30: 894-903

76. Mihai M., Pincovschi I. (1998). “Experimental study of bubble size distribution in a bubble column”, *Sci Technol Environ Prot*, 5: 34-41

77. Mikkilineni S., Knickle H. N., “The effect of gas distributors on holdup and flow pattern in bubble columns”, Part. Multiphase Processes, [Proc. Int. Symp. Workshop] (1987), Meeting Date 1985, Publisher: Hemisphere, Washington D C, 3: 127-145

78. Miyahara T., Hamanaka H., Takino T., Akagi Y., Okada K. (1997). “Gas holdup, gas-liquid interfacial area and mass transfer coefficient in external-loop airlift bubble column containing low density particles”, *J Chem Eng Japan*, 30: 958-961

79. Mudde R. F., Bakker R. A., van der Akker H. E. A. (1992). “Noise analysis of transmitted light beams for determining bubble velocity and gas holdup profiles in a bubble column”, *Chem Eng Sci*, 47: 3631-3638

80. Mudde R. F., Saito T. (2001). “Hydrodynamical similarities between bubble column and bubbly pipe flow”, *J Fluid Mech*, 437: 203-228

81. Olmos E., Gentric C., Vial Ch., Wild G., Midoux N. (2001). “Numerical simulation of multiphase flow in bubble column reactors. Influence of bubble coalescence and break-up.” *Chem Eng Sci*, 56(21-22): 6359-6365

82. Ong, Boon Cheng (2003). “Experimental Investigation of Bubble Column Hydrodynamics: Effect of Elevated Pressure and Superficial Gas Velocity”, Ph. D. Thesis, Washington University in Saint Louis.

83. Patel S. A., Daly J. G., Bukur D. B. (1990). “Bubble-size distribution in Fischer-Tropsch-derived waxes in a bubble column”, *AIChE J*, 36: 93-105

84. Rajarathinam P., Nafis A. (1996). “Size distribution of bubbles generated by fine-pore spargers”, *J Chem Eng Jpn*, 29: 1030-1034

85. Reuter H. (1966). “The nature of bubbles in gas- and liquid-fluidized beds”, *Chem Eng Progr Symp Ser*, 62: 92-99

86. Rowe P. N., Widmer A. J. (1973). “Variation in shape with size of bubbles in fluidized beds”, *Chem Eng Sci*, 28(3): 980-981

87. Saberi S., Shakourzadeh K., Bastoul D., Militzer J. (1995). “Bubble Size and Velocity measurement in Gas-Liquid Systems: Application of Fiber Optic Technique to Pilot Plant Scale”, *Can J Chem Eng*, 73: 253-257

88. Saito T., Mudde R. F. (2001). “Performance of 4-tip optical fiber probe and bubble characterizations by the probe in turbulent bubbly flow”, *ICMF2001*

89. Sanaullah K., Zaidi S. H., Hills J. H. (2001). “A study of bubbly flow using resistivity probes in a novel configuration”, *Chem Eng J*, 83: 45-53

90. Saxena A. C., Rao N. S., Saxena, S. C. (1990). “Bubble Size Distribution in Bubble Columns”, *Can J Chem Eng*, 68: 159-161

91. Shollenberger K. A., Torczynski J. R., Adkins D. R., O’Hem T. J., Jackson N. B. (1997). “Gamma-densitometry tomography of gas holdup spatial distribution in industrial scale bubble columns”, *Chem Eng Sci*, 52: 2037-2048

92. Shollenberger K. A., Torczynski J. R., George, D. L. (2002). “Gas distribution in air/water and air/oil bubble-column flows”, FED (American Society of Mechanical Engineers) [257-2] (A, Proceedings of the 2002 ASME Joint U.S.-European Fluids Engineering Conference), 641-648

93. Snabre P. and Magnifotcham F. (1998). “I. Formation and Rise of a Bubble Stream in a Viscous Liquid”, *Eur Phys J B*, 4: 369-377

94. Spicka P., Martins A., Dias Madalena M., Lopes Jose Carlos B. (1999). “Hydrodynamics of gas-liquid flow in 2D packed/unpacked rectangular reactor”, *Chem Eng Sci*, 54: 5127-5137

95. Stegeman D., Knop P. A., Wijnands A. J. G., Westertern K. R. (1996). “Interfacial area and gas holdup in a bubble column reactor at elevated pressures”, *Ind Eng Chem Res*, 35: 3842-3847

96. Tang C., Heindel T. J. (2004). “Time-dependent gas holdup variation in an air-water bubble column”, *Chem Eng Sci*, 59: 623-632

97. Tadaki T. and Maeda S. (1963). “Size of bubbles from perforated plates”, *Kagaku Kogaku*, 27(6): 402-406

98. Terasaka K, Hieda Y. and Tsuge H. (1999). “SO_2 Bubble Formation from an Orifice Submerged in Water”, *J Chem Eng Japan*, 32(4): 472-479

99. Tsuge H. and Hibino S. (1983). “Bubble Formation From An Orifice Submerged In Liquids”, *Chem Eng Comm*, 22: 63-79

100. Tsuge H., Nakajima Y. and Terasaka K. (1992). “Behavior of Bubbles Formed from a Submerged Orifice Under High System Pressure”, *Chem Eng Sc*., 47(13/14): 3273-3280

101. Vazquez G., Cancela M. A., Riverol C., Alvarez E. and Navaza J. M. (2000). “Determination of Interfacial Areas in a Bubble Column by Different Chemical Methods”, *Ind Eng Chem Res*, 39: 2541-2547

102. Vince M. A., Breed H., Krycuk G. and Lahey R.T. Jr. (1982). “Optical probe for high-temperature local void fraction determination”, *Applied Optics*, 21: 886-892

103. Wallis, G. B. (1969). “One-Dimensional Two-Phase Flow”, McGraw Hill, New York.

104. Wilkinson P. M. and van Dierendonck L. L. (1990). “Comments on Studies on Gas Holdup in a Bubble Column Operated at Elevated Temperatures”, *Ind Eng Chem Res*, 29: 927

105. Wilkinson P. M., Haringa H. (1994), “Mass transfer and bubble size in a bubble column under pressure”, *Chem Eng Sci*, 49: 1417-1427

106. Wu Q., Ishii M. (1999). “Sensitivity study on double-sensor conductivity probe for the measurement of interfacial area concentration in bubbly flow”, *Int J Multi Flow*, 25: 155-173

107. Xue J., Al-Dahhan M., Dudukovic M. P. (2003), Mudde R. F. “Bubble Dynamics measurements using Four-Point Optical Probe”, *Canadian Journal of Chemical Engineering*, 81: 375-381

108. Yang G. Q., Luo X., Lau R., Fan L-S. (2000). “Heat-transfer characteristics in slurry bubble columns at elevated pressures and temperatures”, *Ind Eng Chem Res*, 39: 2568-2577

109. Yoo D. H., Terasaka K. and Tsuge H. (1998). “Behavior of Bubble Formation at Elevated Pressure”, *J Chem Eng Japan*, 31(1): 76-82

110. Yu Y. H., Kim S. D. (1988). “Bubble Characteristics in the Radial Direction of the Three-Phase Fluidized Beds”, *AIChE J*, 34: 2069-2077

111. Zou R., Jiang X., Li B., Zu Y. and Zhang L. (1988). “Studies on Gas Holdup in a Bubble Column Operated at Elevated Temperatures”, *Ind Eng Chem Res*, 27:1910